

5-1-2021

Behavior of Aged Reinforced Concrete Columns Under High Sustained Concentric and Eccentric Loads

Wenchen Ma

Follow this and additional works at: <https://digitalscholarship.unlv.edu/thesesdissertations>



Part of the [Civil Engineering Commons](#)

Repository Citation

Ma, Wenchen, "Behavior of Aged Reinforced Concrete Columns Under High Sustained Concentric and Eccentric Loads" (2021). *UNLV Theses, Dissertations, Professional Papers, and Capstones*. 4174. <http://dx.doi.org/10.34917/25374066>

This Dissertation is protected by copyright and/or related rights. It has been brought to you by Digital Scholarship@UNLV with permission from the rights-holder(s). You are free to use this Dissertation in any way that is permitted by the copyright and related rights legislation that applies to your use. For other uses you need to obtain permission from the rights-holder(s) directly, unless additional rights are indicated by a Creative Commons license in the record and/or on the work itself.

This Dissertation has been accepted for inclusion in UNLV Theses, Dissertations, Professional Papers, and Capstones by an authorized administrator of Digital Scholarship@UNLV. For more information, please contact digitalscholarship@unlv.edu.

BEHAVIOR OF AGED REINFORCED CONCRETE COLUMNS UNDER HIGH
SUSTAINED CONCENTRIC AND ECCENTRIC LOADS

By

Wenchen Ma

Bachelor of Science in Civil Engineering
Beijing Jiaotong University
2014

Master of Science in Civil Engineering
Northeastern University
2016

A dissertation submitted in partial fulfilment
of the requirements for the

Doctor of Philosophy - Civil and Environmental Engineering

Department of Civil and Environmental Engineering and Construction
Howard R. Hughes College of Engineering
The Graduate College

University of Nevada, Las Vegas
May 2021



Dissertation Approval

The Graduate College
The University of Nevada, Las Vegas

April 30, 2021

This dissertation prepared by

Wenchen Ma

entitled

Behavior of Aged Reinforced Concrete Columns Under High Sustained Concentric and Eccentric Loads

is approved in partial fulfillment of the requirements for the degree of

Doctor of Philosophy - Civil and Environmental Engineering
Department of Civil and Environmental Engineering and Construction

Ying Tian, Ph.D.
Examination Committee Chair

Kathryn Hausbeck Korgan, Ph.D.
Graduate College Dean

Nader Ghafoori, Ph.D.
Examination Committee Member

Samaan Ladkany, Ph.D.
Examination Committee Member

Ryan Sherman, Ph.D.
Examination Committee Member

Zhiyong Wang, Ph.D.
Graduate College Faculty Representative

ABSTRACT

Time-Dependent Behavior of Aged Reinforced Concrete Columns Subjected to High Sustained Loads

By

Wenchen Ma

Dr. Ying Tian, Examination Committee Chair, Professor

Department of Civil and Environmental Engineering and Construction

University of Nevada, Las Vegas

Columns are critical components resisting the collapse of a reinforced concrete (RC) frame structure subjected to high sustained loads. Research on columns under sustained high stresses is very limited. At material level, past creep tests were focused either on concrete with ages less than 90 days or under a sustained stress less than 70% of short-time strength. At structural component scale, virtually no experimental data can be found for the response of axially loaded RC columns subjected to high sustained loads exceeding 75% of column short-time strength with loading age greater than 200 days. Even if a few experiments were conducted to examine the sustained eccentrically loaded columns under high sustained loads, the experiments were conducted predominantly within three months of concrete casting. The goals of this research were to (1) understand the behavior of aged reinforced concrete frame columns with ages greater than 200 days and under high sustained loads no less than 75% of short-time loading capacity caused by sustained concentric and eccentric loading, (2) examine the effects of

transverse reinforcement ratio on the creep behavior of RC columns, (3) examine and explore a numerical method based on an existing nonlinear creep model for aged concentrically loaded concrete columns under high sustained stresses.

To achieve the research goals, thirteen columns were tested after 209 to 629 days of concrete casting. The sustained loading lasted 2 to 120 days. Test variables included sustained load level, eccentricity ratio, and transverse reinforcement ratio. Eight of the thirteen columns were subjected to concentric loads. Among them, one plain concrete and one RC column, as control specimens, were tested to failure in a short time; two plain concrete and four RC columns were subjected to sustained concentric loads ranging from 76% to 98% of code-defined nominal short-time strength. No concentrically loaded column failed even the sustained load was as high as 98% of column short-time strength. Five RC columns were tested under sustained eccentric loading. These columns were initially loaded to cause the bending moment at the column mid-height to reach 77% to 100% of nominal flexural capacity after considering axial force-moment interactions. The columns showed high resistance to large sustained loads, and only one eccentrically loaded column failed during sustained eccentric loading. For concentrically loaded columns subjected to 98% code-defined nominal short-time strength, higher transverse reinforcement ratio decreased concrete creep during the early stage of sustained concentric loading but diminished over time. For eccentrically loaded columns, higher transverse reinforcement ratio increased flexural stiffness and resulted in lower creep deformation, thereby reducing failure risk due to second order effects.

A numerical method for predicting concrete column creep under high axial sustained stresses and older loading ages is explored based on existing creep models. The experimental results of short column tests were compared with the predictions.

ACKNOWLEDGEMENTS

I would like to express my sincere gratitude to Dr. Ying Tian, my dissertation supervisor. His technical guidance was crucial for my Ph.D. research. Gratitude is extended to Dr. Nader Ghafoori, Dr. Ryan Sherman, Dr. Samman Ladkany, and Dr Zhiyong Wang for their advice and serving on my dissertation committee.

I would like to thank the support from the Department of Civil and Environmental Engineering and Construction, the Graduate College and the Graduate & Professional Student Association at the University of Nevada, Las Vegas.

I would like to thank my father, Yong Ma. for his constant support and advice, and my mother, Rongxin Gao for her selfless devotion to our family and growth.

I would like to offer special thanks to the late development technician, Peter Faught, for his selfless devotion to our experiment.

The financial support from the National Science Foundation under Grant No. 1762362 and 1760915 are gracefully acknowledged.

Wenchen Ma

May 2021

TABLE OF CONTENTS

ABSTRACT.....	iii
ACKNOWLEDGEMENTS.....	v
LIST OF TABLES.....	x
LIST OF FIGURES.....	xi
CHAPTER 1 INTRODUCTION.....	1
1.1 Collapse of Reinforced Concrete Buildings under Sustained Load.....	1
1.2 Concrete Creep under Sustained Load.....	4
1.3 Research Justification.....	7
1.4 Research Goal, Approach, and Objectives.....	8
1.5 Research Contribution.....	9
1.6 Literature Review.....	10
1.6.1 Parameters Affecting Concrete Creep.....	10
1.6.2 Tests of Concrete Material under High Sustained Load.....	12
1.6.3 Existing Concrete Creep Models.....	19
1.6.3.1 Models for Linear Creep.....	19
1.6.3.2 Models for Nonlinear Creep.....	23
1.6.4 Experimental Studies for RC Columns under Sustained Concentric Loading.....	31
1.6.5 Experiments of RC Columns under Sustained Eccentric Loading.....	36
1.7 Research Tasks.....	44
CHAPTER 2 PROTOTYPE STRUCTURE DESIGN AND ANALYSES.....	46
2.1 Prototype Building Design.....	46
2.1.1 Objectives.....	46
2.1.2 Elastic Analysis of Prototype Structure.....	47
2.1.3 Structural Design Results.....	49
2.1.3.1 Beam Design.....	49
2.1.3.2 Column Design.....	50
2.1.3.3 Slab Design.....	52

2.2 Nonlinear Analysis of Prototype Structure.....	54
2.2.1 Analysis Procedure	54
2.2.2 Element Type and Material Property	55
2.2.3 Analysis Results of the Intact Prototype Structure Without Column Loss.....	58
2.3 Nonlinear Analysis of Prototype Structure with an Interior Column Loss	59
CHAPTER 3 EXPERIMENTAL PROGRAM.....	62
3.1 Introduction.....	62
3.2 Test Matrix.....	62
3.2.1 Test Variables and Matrix for Concentric Loading	62
3.2.2 Test Variables and Matrix for Eccentric Loading	64
3.3 Specimen Geometry and Reinforcing Details	65
3.4 Specimen Fabrication	69
3.4.1 Formwork	69
3.4.2 Concrete Mix	70
3.4.3 Specimen Pouring and Curing.....	70
3.5 Material Mechanical Properties	71
3.5.1 Steel Reinforcing Bars.....	71
3.5.2 Concrete Compressive Strength	73
3.6 Test Setup and Instrumentation for Concentric Loading Tests	75
3.6.1 Test Setup	75
3.6.2 Loading Approach and Procedure	81
3.6.3 Instrumentation	82
3.7 Test Setup and Instrumentation for Eccentric Loading Tests.....	84
3.7.1 Test Setup	84
3.7.2 Loading Procedure.....	90
3.7.3 Instrumentation	90
CHAPTER 4 EXPERIMENTAL RESULTS OF COLUMNS SUBJECTED TO CONCENTRIC SUSTAINED LOADING	92
4.1 Introduction.....	92
4.2 Behavior of Plain Concrete Columns	92
4.2.1 Plain Concrete Specimen under Short-Term Loading.....	92

4.2.2 Plain Concrete Specimen under Sustained Loading	93
4.2.2.1 Loading History	93
4.2.2.2 Axial Strain History and Creep Coefficient.....	95
4.2.2.3 Stress-Strain Response and Failure Mode	97
4.3 Experimental Results of Reinforced Concrete Columns	98
4.3.1 RC Specimen under Short-Term Loading	98
4.3.2 RC Specimens under Sustained Loading.....	101
4.3.2.1 Loading history	101
4.3.2.2 Axial Strain History and Creep Coefficient.....	103
4.3.2.3 Load-Strain Response and Failure Mode.....	108
4.3.2.4 Transverse Strain and Poisson's Ratio History	111
CHAPTER 5 EXPERIMENTAL RESULTS OF COLUMNS SUBJECTED TO SUSTAINED ECCENTRIC LOADING	115
5.1 Introduction.....	115
5.2 Loading History	115
5.3 Load-Strain Relationship and Strain History.....	118
5.4 Deflection at Column Mid-height and Load-Deflection Relationship	122
5.5 Axial Load - Mid-Height Moment Response	126
5.6 Moment - Curvature Response	129
5.7 Creep for Deflection and Curvature	132
5.8 Concrete Transverse Strain History	135
5.9 Poisson's Ratio.....	137
5.10 Damage and Failure Modes	139
CHAPTER 6 NUMERICAL SIMULATIONS OF COLUMN NONLINEAR CREEP DUE TO SUSTAINED CONCENTRIC LOADING.....	141
6.1 Introduction.....	141
6.2 Strain of Concrete and Reinforcing Bars Due to Shrinkage.....	141
6.3 Short-Time Loading Capacity of RC Columns Subjected to Concentric Loading	145
6.4 Simulations of Column Creep under High Sustained Concentric Loading.....	149
6.4.1 Simulating Creep of Plain Concrete Columns.....	149
6.4.2 Simulating Creep of Reinforced Concrete Columns	157

CHAPTER 7 SUMMARY AND CONCLUSIONS	165
7.1 Summary	165
7.2 Conclusions.....	167
7.2.1 Concentric Loading	167
7.2.2 Eccentric Loading	168
7.2.3 Numerical Simulations of Column Nonlinear Creep.....	169
7.3 Suggestions for Future Research	170
APPENDIX A COMPRESSIVE STRENGTH OF CYLINDRICAL CONCRETE SPECIMENS	172
APPENDIX B CONCRETE MIX DETAILS.....	173
REFERENCE.....	174
CURRICULUM VITAE.....	183

LIST OF TABLES

Table 1.1	Parameter range for four linear creep models	20
Table 1.2	Values of coefficient s	22
Table 1.3	Summary of sustained loading tests by Viest et al. (1956)	38
Table 1.4	Test results of columns under sustained eccentric loading (Green and Breen, 1969)	40
Table 1.5	Properties of slender columns tested by Jenkins (2015) under sustained eccentric loading	43
Table 2.1	Concrete Damage Plasticity parameters	56
Table 2.2	Calculated equivalent stress-strain relationship for roof beams	58
Table 2.3	Calculated equivalent stress-strain relationship for floor beams	58
Table 3.1	Testing matrix of columns under concentric loading	64
Table 3.2	Testing matrix of columns under eccentric loading.....	65
Table 3.3	Concrete mix proportions	70
Table 3.4	Summary of tensile test results for steel reinforcing bars	72
Table 3.5	Concrete cylinder compressive strength over time	73
Table 4.1	Specific loading details for Specimens P77 and P90.	94
Table 4.2	Characteristic concrete strains of Specimens P77 and P90	96
Table 4.3	Loading details for Specimens C76A, C76B, C98A, and C98B	102
Table 4.4	Characteristic concrete strains for Specimens C76A, C76B, C98A and C98B.....	105
Table 5.1	Loading details for Specimen E98A17, E100B17, E99A17, E77A25, and E92A25	116
Table 5.2	Concrete strain at characteristic loading stages of eccentrically loaded columns.	121
Table 5.3	Mid-height moment at characteristic loading stages of eccentrically loaded columns	128
Table 5.4	Curvature at characteristic loading stages of eccentrically loaded columns	131
Table 5.5	Poisson's ratio at characteristic loading stages of eccentrically loaded columns.	138
Table 6.1	Concrete and reinforcement strains due to shrinkage	143
Table 6.2	Calculated and measured loading capacity of RC specimens	149

LIST OF FIGURES

Figure 1.1	Collapse of Sampoong Department Store (Park, 2012).	2
Figure 1.2	Collapse of Hotel New World in Singapore.....	3
Figure 1.3	Collapse of Zumrut apartment building (Kaltakci et al., 2013).	4
Figure 1.4	Column damage in Konya caused by creep effect (Kaltakci et al., 2007).	4
Figure 1.5	Concrete strength and strain under creep effect (reproduced from Rüsçh, 1960).....	5
Figure 1.6	Loading rate effects to concrete strain (reproduced from Rüsçh, 1960).	6
Figure 1.7	Summary of creep data from Northwestern University's database and four literature.	13
Figure 1.8	Concrete creep under high sustained stresses measured by Shah and Chandra (1970).....	14
Figure 1.9	Concrete creep under high sustained stresses measured by Awad and Hilsdorf (1971).....	15
Figure 1.10	Concrete creep under high sustained stresses measured by Smadi et al. (1985 and1986).	16
Figure 1.11	Concrete creep and creep recovery of high-, medium-, and low-strength concrete under sustained compressive stress: (a) $\sigma_c / f_c' = 0.7$ and (b) $\sigma_c / f_c' = 0.4$ (Smadi et al., 1985 and1986)..	17
Figure 1.12	Concrete creep data under high sustained stresses measured by Irvani and MacGregor (1998).... ..	18
Figure 1.13	Concrete creep data under high sustained stresses (Irvani and MacGregor, 1998).	18
Figure 1.14	Response of concrete under uniaxial compressive stresses: short- and long-term stress-longitudinal strain diagram according to Rüsçh (1960).	25
Figure 1.15	Instantaneous pre- and post-peak longitudinal strains' inelastic strain capacity (Tasevski et al., 2019).....	25
Figure 1.16	Three stages of creep: primary (I), secondary (II), and tertiary (III) (Tasevski et al., 2019).	27
Figure 1.17	Illustration of solidification theory employed by Mazzotti and Savoia (2003).....	28
Figure 1.18	Schematic of concrete nonlinear creep model proposed by Luzio and Cusatis (2012).....	30

Figure 1.19	Schematic illustration of nonlinear creep model proposed by Wei et al. (2016)	30
Figure 1.20	Sustained loading approach for columns (Richart and Brown, 1934).....	32
Figure 1.21	Reinforcement details for a short RC column tested by Jenkins (2015).	33
Figure 1.22	Test setup for sustained loading of short columns (Jenkins, 2015).....	34
Figure 1.23	Comparison of measured creep in plain and reinforced concrete columns under sustained axial loading (Jenkins, 2015).	34
Figure 1.24	Configuration and reinforcement details of RC columns subjected to sustained loading (Eom et al., 2018).....	35
Figure 1.25	Axial deformation time-history of two RC columns under sustained concentric loading (Eom et al. 2018).....	36
Figure 1.26	Details of specimens tested by Viest et al. (1956).....	37
Figure 1.27	Loading frames for sustained load tests by Viest et al. (1956).	37
Figure 1.28	Columns tested by Green and Breen (1969) under sustained eccentric loading: (a) specimen dimension, and (b) axial load versus moment at the beginning of sustained loading. ...	39
Figure 1.29	Sustained loading test of a RC frame by Furlong and Ferguson (1966).	41
Figure 1.30	Concrete compressive strain in short columns subjected to sustained eccentric loading (Jenkins, 2015).	42
Figure 1.31	Test setup for sustained eccentric loading of slender columns (Jenkins, 2015).....	43
Figure 1.32	Sustained eccentric loading response of slender columns tested by Jenkins (2015): (a) axial load vs. center deflection, (b) center deflection time history, and (c) axial force vs. moment.....	44
Figure 1.33	Research procedure	45
Figure 2.1	Prototype RC frame building: (a) 3D view and (b) floor plan.	46
Figure 2.2	Internal force envelopes of the prototype structure.	48
Figure 2.3	Slab moment intensity distribution about x-axis (unit: kip-in/in)... ..	48
Figure 2.4	Interior floor beam design (unit of dimension: in)... ..	49
Figure 2.5	Roof beam design (unit of dimension: in).....	50
Figure 2.6	Axial force envelope of Frame 3.....	51
Figure 2.7	Moment envelope of Frame 3.....	51
Figure 2.8	Column cross section: (a) top and 3rd floor and (b) 1st and 2nd floor (unit of dimension: in.).	52
Figure 2.9	Reinforcement distribution of slab: (a) top reinforcement and (b) bottom reinforcement. (unit of dimension: in.).....	53

Figure 2.10 Analysis procedure (unit of dimension: ft).....	55
Figure 2.11 Stress-strain relationship of concrete ($f'_c = 5500$ psi).....	56
Figure 2.12 Stress-strain relationship of steel reinforcement ($f_y = 60000$ psi).	57
Figure 2.13 Beam material property assignment (unit of dimension: ft).....	59
Figure 2.14 Axial force in prototype structure without column loss (unit: lb).....	59
Figure 2.15 Beam material property assignment after column loss (unit of dimension: ft).	60
Figure 2.16 Axial load in prototype structure after the loss of Column C3 (unit: lb)..	60
Figure 2.17 Moment and axial load of top floor columns next to Column C3 (unit of dimension: in.).....	61
Figure 3.1 Column cross section. (unit of dimension: in.).....	66
Figure 3.2 Reinforcement layout for (a) Specimens C76A, C98A, and CS and (b) Speicmens C76B and C98B.....	67
Figure 3.3 Reinforcement layout for (a) Specimens E98A17, E99A17, E77A25, and E92A25, and (b) Speicmens E100B17.....	68
Figure 3.4 Tensile stress-strain response of steel reinforcement.	72
Figure 3.5 Concrete compressive strength versus age.....	74
Figure 3.6 Compressive stress-strain relationship for three concrete cylinders at an age of 481 days... ..	75
Figure 3.7 Test setup for concentric loading (unit: in.)... ..	76
Figure 3.8 Loading frame for columns under concentric loading... ..	77
Figure 3.9 Column end regions for concentric loading tests.	78
Figure 3.10 Disk spring details... ..	80
Figure 3.11 Two specimens installed prior to concentric loading tests.....	80
Figure 3.12 Test setup for eccentric loading (unit: in.).....	85
Figure 3.13 Loading frame for columns under sustained eccentric loading.....	87
Figure 3.14 End region of columns under sustained eccentric loading... ..	87
Figure 3.15 Confinement provided at column ends.....	88
Figure 3.16 Lateral support at column upper end... ..	88
Figure 3.17 Two specimens installed prior to sustained eccentric loading test.....	89
Figure 4.1 Load-strain relationship of Specimen PS during short-time loading test.....	93
Figure 4.2 Loading history of plain concrete Specimens P77 and P90... ..	94
Figure 4.3 Strain history of plain concrete Specimens P77 and P90.....	95

Figure 4.4	Creep coefficient during sustained concentric loading for Specimens P77 and P90...	96
Figure 4.5	Stress-strain relationship of plain concrete specimens P77 and P90 under concentric loading.....	97
Figure 4.6	Plain concrete specimens after failure.....	98
Figure 4.7	Load strain response of CS.....	99
Figure 4.8	Load versus Poisson's ratio response of Specimen CS.....	101
Figure 4.9	Loading history of Specimens C76A, C76B, C98A, and C98B....	102
Figure 4.10	Strain history of Specimens C76A, C76B, C98A, and C98B....	104
Figure 4.11	Creep coefficient during sustained loading for Specimens C76A, C76B, C98A, and C98B.....	107
Figure 4.12	Load-strain response of Specimens C76A, C76B, C98A, and C98B... ..	109
Figure 4.13	RC column specimens after failure.	111
Figure 4.14	Transverse strain history of concrete cover during sustained concentric loading for Specimens C76A, C76B, C98A, and C98B.....	112
Figure 4.15	Poisson's ratio history during sustained loading for Specimens C76A, C76B, C98A, and C98B.. ..	114
Figure 5.1	Loading history of column specimens subjected to sustained eccentric loading....	117
Figure 5.2	Load-strain relationship of Specimens E100B17, E99A17, E77A25, and E92A25....	119
Figure 5.3	Strain history at compression face of Specimens E100B17, E99A17, E77A25, and E92A25.....	120
Figure 5.4	Mid-height deflection history of column specimens subjected to sustained eccentric loading.....	123
Figure 5.5	Load-deflection relationship of column specimens subjected to sustained eccentric loading.....	125
Figure 5.6	Axial load-moment response of column specimens subjected to sustained eccentric loading.....	127
Figure 5.7	Moment-curvature relationship of column specimens subjected to sustained eccentric loading.....	130
Figure 5.8	Creep coefficient of columns with $e/h = 0.17$	133
Figure 5.9	Creep coefficient of columns with $e/h = 0.25$	134
Figure 5.10	Concrete transverse strain history of column specimens subjected to sustained eccentric loading....	136

Figure 5.11 Time history of Poisson’s ratio in Specimens E100B17, E99A17, E77A25, and E92A25.....	138
Figure 5.12 Failure modes of column specimens subjected to eccentric loading.....	140
Figure 6.1 Conceptual view of restrained shrinkage behavior of a RC component....	144
Figure 6.2 Stress-strain relationship for confined and unconfined concrete for Specimen C76B....	147
Figure 6.3 Comparison of predicted and measured creep strains with two different methods defining sustained stress ratio for Specimens P77 and P90.....	152
Figure 6.4 Comparison of predicted and measured creep strains for Specimen P77.....	155
Figure 6.5 Comparison of predicted and measured creep strains for Specimen P90.....	156
Figure 6.6 Variation of axial forces resisted by concrete and longitudinal reinforcement during sustained loading of Specimens C76A, C76B, C98A, and C98B.....	158
Figure 6.7 Comparison of predicted and measured creep strains for Specimens C76A and C76B.....	162
Figure 6.8 Comparison of predicted and measured creep strains for Specimens C98A and C98B.....	163

CHAPTER 1

INTRODUCTION

1.1 Collapse of Reinforced Concrete Buildings under Sustained Load

Building collapse can be initiated by the loss of loading capacity in a primary structural component, resulting in the failure of surrounding elements, which in turn cause a failure propagation. Globally, a total of 38,363 people lost their lives due to collapse of structures between 2001 and 2015 (Factly News, 2019). In the U.S., 172 structural failures occurred in low-rise and multistory buildings from 1989 to 2000 (Wardhana and Hadipriono, 2003). Of these, 94% of the failures ended up with partial or total collapse and 45% were attributed to design or construction error, overloading, or material deficiency. Most collapses happened under sustained load rather than due to earthquake or wind load. Another study (Eldukair and Ayyub, 1991) reported 604 failures in the U.S. from 1975 to 1989, excluding those due to natural hazard. Of those, 78% were caused by technical errors and 86% were related to reinforced concrete (RC) structures. The failures resulted in 416 deaths. In contrast, according to United States Geological Survey (USGS), earthquakes only led to 68 deaths in the U.S. since 1990. These data highlight the likelihood of structural failure under sustained load in the U.S., where building design and construction have been rigorous.

Well-engineered RC buildings generally have a good performance under normal loading conditions. However, faulty design, construction errors, material deterioration, and overloading can occur. Additionally, abnormal loading such as impact, flood, and blast may also happen. Either case of human error or abnormal loading can lead to sustained high stresses and failure of key structural components. The initial local failure may not result in an immediate failure propagation. The building is able to find an alternative load path; however, elements along that

path may be under sustained high stresses due to load redistribution. This causes the building to exhibit early warning signs such as concrete cracking or large deformation. If the warning signs are ignored, collapse may occur.

Figure 1.1 shows the collapse of the Sampoong Department Store in South Korea in 1995. The building was a 5-story RC flat-plate building (Park, 2012). Due to under-designed slab thickness and overload, a punching failure was initiated from an interior slab-column connection at the roof, resulting in a progressive collapse of the building that killed 501 people. Several days before the collapse, civil engineers who examined the building realized that the building was at risk of collapse. Cracks radiated from one column to the slab on the fifth floor due to the vibration from air conditioning unit on the roof. The cracks were further widened five hours prior to the collapse. Eventually, all floors in the south wing progressively collapsed in less than 25 seconds (Wearne, 2000).



Figure 1.1 Collapse of Sampoong Department Store (Park, 2012).

Hotel New World in Singapore, a six-story RC frame building, collapsed on March 15, 1986, as shown in Figure 1.2. The collapse trapped 50 people beneath the rubble; 17 people were

rescued, whereas 33 people were killed (The New York Times, 1986). Investigations revealed that the structural engineer had considered the building's live load in the design but the building's dead load was completely neglected. What is more, the building owner added a total of 100 tons load throughout the years not considered in the original design (Thean et al., 1987). The extra loads included a strong room for a bank in the building, 3 air-conditioned towers, and heavy duty glazed ceramic tiles on building surface. Sixteen hours before the building collapse, a nightclub hostess observed persistent cracking in one of the supporting columns, an early sign of incoming failure.



before collapse (MustShare News, 2016)



after collapse (Asiaone News, 2016)

Figure 1.2 Collapse of Hotel New World in Singapore.

Two RC buildings collapsed under sustained loads in Turkey. The Diyarbakir Hicret Apartment experienced a total collapse in 1983, causing 93 death. The Konya Zumrut Apartment collapsed in 2004 (Figure 1.3), causing 92 death. Both buildings suffered initiating column failures believed to be due to concrete creep under sustained gravity loads. Two similar cases of column failure due to concrete creep were found in Konya, Turkey (Kaltakci et al., 2007), as shown in Figure 1.4.



before collapse



after collapse

Figure 1.3 Collapse of Zumrut apartment building (Kaltakci et al., 2013).



Altinbasak apartment building



Sirinyurt apartment building

Figure 1.4 Column damage in Konya caused by creep effect (Kaltakci et al., 2007).

1.2 Concrete Creep under Sustained Load

The failure of a RC structural component under sustained loads is most likely related to concrete creep, a long-term deformation under sustained loading. Water within the hardened cement paste is forced to move as a result of the applied load (Theconstructor.org). This moisture movement is the primary cause of creep deformation. Creep is affected by many parameters, including stress level, short-time strength, loading age, temperature, aggregate type and size, water-cement ratio, geometry, and relative humidity (Bažant, 1975; Bažant and Chern, 1985; Iravani and MacGregor, 1998; Mazzotti and Savoia, 2002). Concrete creep is fundamentally

caused by progressive propagation of internal microcracks (Shah and Chandra, 1970). Stress level is the most crucial parameter governing concrete creep behavior. If the sustained stress σ_c is less than $0.4f_c'$ (f_c' = short-time cylinder compressive strength of concrete), creep strain is linear with respect to stress. Nonlinearity presents at higher stresses. When the sustained stress is less than $0.7f_c'$, microcracks grow slowly. Nonlinear creep presents at higher stresses when the applied stress is greater than $0.70f_c'$. When the stress is greater than $0.8f_c'$, concrete experiences failure in a short time, preceded by a rapid microcrack growth and a sharp increase in volume expansion. Of importance to the structural behavior of a RC component is the stress-strain response of concrete. As an example, Figure 1.5 shows the response of concrete strain versus time of failure at different stress levels (Rüsch 1960). The short-time concrete compressive strength was $f_c' = 5000$ psi and the sustained loads were applied at a concrete age of 56 days. It is seen that higher stress level leads to shorter failure time.

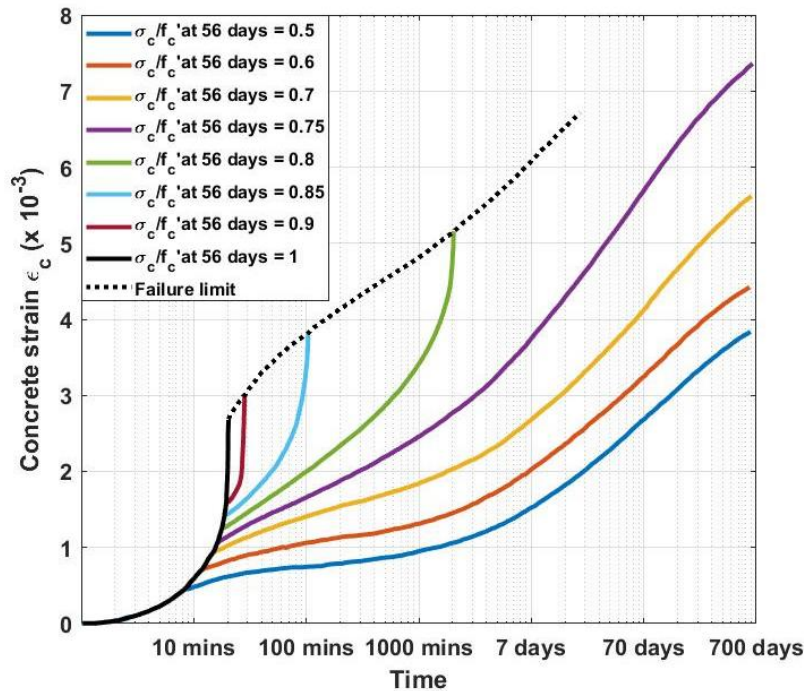


Figure 1.5 Concrete strength and strain under creep effect (reproduced from Rüsch, 1960).

It is also known that concrete strength under a sustained load is less than that tested under a load monotonically increased in a short time. This is of fundamental importance in the design of RC structures since it means a reduction in safety margin with regard to short-time concrete strength. This situation can be illustrated by Figure 1.6 (Rüsch, 1960), which shows a relationship between the ratio of stress σ_c to f'_c and total strain after loading at an age of 56 days. The leftmost curve shows normalized stress-strain response of concrete loaded for 20 minutes until failure. The lower right line indicates the creep deformation of concrete experiencing an extremely low loading rate. The two other curves correspond to a loading time between 20 minutes to infinity. The top dashed line shows decreasing strength with increasing load duration, which demonstrates a reduction in concrete strength due to reduced loading rates. It can be extrapolated from the failure stress under the very low loading rate that concrete compressive strength under sustained loading could be around 80% of its short-time loading capacity.

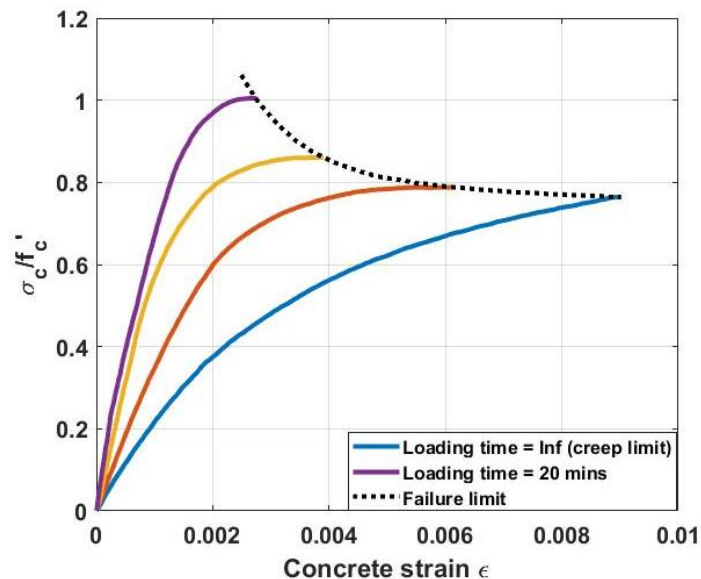


Figure 1.6 Loading rate effects to concrete strain (reproduced from Rüsch, 1960).

1.3 Research Justification

Building resistance to progressive collapse was a major research thrust in structural engineering community especially after the collapse of the World Trade Center in 2001. To evaluate the robustness of a structure against progressive collapse, one well-accepted approach is to examine whether the structure can develop an alternative load path to continue carrying gravity loads after the local failure of one or more critical components. This threat-independent approach formed the basis of past research and is adopted in the existing guidelines for progressive collapse analysis (DoD, 2013; GSA, 2003). Accordingly, research on the collapse resistance of RC frame buildings (e.g. Sasani et al., 2007; Yi et al., 2008; Su et al., 2009; Qian and Li, 2012; Orton and Kirby, 2013; Dat and Hai, 2013; Xiao et al. 2015) has focused primarily on the capability of beams and slabs in bridging over one or more failed columns. However, no effort was found to understand the near-collapse response of RC frame buildings under high sustained loads.

In many actual RC building collapse cases, as described previously, the gravity loads should have changed little prior to the final large-scale failure. Therefore, the collapse happened under sustained loads and the evolution from local damage to global collapse was time-dependent. It can be hypothesized that under sustained loading, nonlinear creep of concrete under high stresses as well as the resulting load redistribution can lead to local failure of members and then a partial or complete collapse of the structure.

Columns are critical components resisting collapse of a RC frame structure subjected to extreme loading conditions. As stated previously, construction faults, design mistakes, and over loading all can cause sustained high stresses in a column. Moreover, the load redistribution after the loss of a column also can lead to high stresses in the neighboring columns. It is not clear how

sustained high stresses lead to a local column failure nor how the local failure evolves into a collapse. Research on columns under sustained high stresses is very limited, likely because of the long-lasting belief that creep is mainly a serviceability issue. At material scale, although decades of research efforts have been made on creep of concrete material, they focused either on the properties of concrete in early ages (normally less than 60 days) or concrete under a sustained stress less than 70% of short-time compressive strength. At structural component level, virtually no experimental data can be found for the response of axially load RC columns subjected to high sustained loads exceeding 70% of short-time strength with loading age greater than 200 days. Even if a few experiments were conducted to examine the sustained eccentrically loaded columns under high sustained loads, such test data remain rare. The lack of knowledge of RC columns under sustained high stresses, the critical role of column, and the high consequence of building collapse necessitate this research.

1.4 Research Goal, Approach, and Objectives

This study is a portion of a joint research effort to explore the near-collapse behavior of RC frame and flat-plate buildings under sustained gravity loads, involving the University of Nevada, Las Vegas and the University of Missouri – Columbia. The overall goal is to understand the behavior of RC frame columns under high sustained stresses caused by sustained axial loads no less than 75% of column short-time loading capacity.

The understanding of experimental data generated from this fundamental research would permit developing reliable predictive models used for understanding the complex, system-scale damage evolution process in a near-collapse RC frame structure under high sustained gravity loads. To achieve the goal, a series of experiments were design and conducted with the following

objectives:

- Characterize the behavior of RC columns under high sustained axial loading.
- Examine the effects of column transverse reinforcement on creep behavior and examine the existing constitutive models for concrete with nonlinear creep.
- Characterize the behavior of RC columns under high sustained eccentric loading.

1.5 Research Contribution

Research on axial loading response of RC columns under high sustained stresses is very limited on both material and structural component scales. Past studies of concrete creep effects on structural performance focused mainly on serviceability. Almost no experimental data can be found for the response of either plain concrete or RC columns subjected to sustained loads exceeding $0.7f_c'$ and with a loading age greater than 100 days. Data for eccentrically loaded RC columns under high sustained stress are also rare. Very few nonlinear creep models have been developed and they were not extensively validated. Moreover, the effects of confinement provided by transverse reinforcement on concrete nonlinear creep are largely unknown.

The experimental data generated by this study will help understand RC structures' behavior near collapse and improve the existing model to predict concrete creep under high sustained loads. The findings obtained from the project would (1) permit a better understanding of column failures under sustained high stresses caused by various abnormal conditions and the possibility of progressive collapse of the whole structure, (2) enable more reliable methods to evaluate the structural reliability under abnormal events such as component failures due to human errors, and (3) identify critical damage in buildings and thus permit more prudent evacuation, rescue, and stabilization decisions by interpreting the early warning signs.

1.6 Literature Review

1.6.1 Parameters Affecting Concrete Creep

Concrete creep is affected by many parameters. Among them, sustained applied stress level, loading age, concrete short-time compressive strength, temperature, relative humidity, loading history, and aggregate type and size have the greatest influence on the concrete creep.

Sustained stress level applied — If the sustained stress σ_c is less than $0.4f_c'$, creep strain is in general linear with respect to stress (ACI Committee 209, 2008). Nonlinearity presents at higher stresses. Once the stress is greater $0.75f_c'$, the material suffers tertiary creep, characterized by an accelerated strain rate ($\ddot{\epsilon} > 0$) (Zhou, 1992). When the stress is greater than $0.8f_c'$, concrete experiences a rapid microcrack growth and a sharp increase in volume expansion (Shah and Chandra, 1970). When sustained stress attains to approximately $0.85f_c'$, stress-strain curve of concrete bifurcates (Challamel et al., 2005). Concrete will experience a high strain rate prior to failure when $\sigma_c > 0.85f_c'$.

Loading age — Greater loading age reduces both total and creep strains at failure and elongates failure time. Because gel quality in concrete improves with time, creep is greater when concrete with a young gel is loaded. Two types of concrete aging, including short-term chemical aging and long-term non-chemical aging, decreases concrete creep rate (Bažant et al., 2004). Short-term chemical aging is caused by the slow process, in which new solids are produced during the chemical reactions of cement hydration and deposited on the walls of capillary pores. Short-term chemical aging ceases at room temperatures after about one year. Long-term non-chemical aging can be demonstrated by decreased creep rate with increased loading age, even if the creep caused by cement hydration is nearly ceased. This phenomenon was explained by microprestress relaxation (Bažant et al., 1997), although a long-term increase of bonding

between cement paste and aggregate due to “polymerization” in calcium silicate hydrates (C-S-H) may also play a role (Bažant and Prasannan, 1989).

Short-time compressive strength (f_c') — If $\sigma_c / f_c' \geq 0.4$, creep strain decreases with increasing f_c' for at least 60 days (Smadi et al., 1985). However, if $\sigma_c \geq 0.9f_c'$, total strain becomes greater with increasing f_c' (Smadi et al., 1986). In general, the ratio of sustained load strength to f_c' increases as f_c' increases. High-strength concrete ($f_c' > 60$ MPa) has a higher creep-stress proportionality limit (about $0.65f_c'$) than low- and medium- strength concretes ($0.45f_c'$). This means that high-strength concrete may be loaded up to $0.65f_c'$ without causing significant crack formation. On the other hand, the period of sustained loading up to failure is generally longer for high-strength concrete than that for low- and medium-strength concretes. Iravani and MacGregor (1998) reported that, for concrete with $f_c' = 65$ MPa, the sustained strength can be 0.7 to $0.75 f_c'$; for $f_c' = 95$ MPa concrete, the sustained strength can be 0.75 to $0.8 f_c'$; for concrete with f_c' higher than 105 MPa, the sustained strength can be 0.85 to $0.9 f_c'$.

Temperature — Temperature-induced creep is unrecoverable. Creep rate is increased under temperature increase, because it accelerates bond breakage and affects bond restoration. However, once temperature reaches a certain value, higher temperature accelerates the chemical process of cement hydration, thereby increasing concrete aging and reducing creep rate (Bažant et al., 2004). Overall, the former effect prevails. For instance, Geymayer (1970) stated that a temperature increase from 0 °C to at least up to 50 °C increases creep by more than 100%. Nevertheless, creep may not increase when the temperature is increased from 50 °C to 100 °C.

Relative humidity — Change in humidity induces free hygrometric strain, which is caused by the changes in capillary tension, surface tension, and disjoining pressure (Bažant et al., 2004). Hygrometric strain is reduced by moisture movement into and out of cement gel pores

(Deryagin, 1963). Environmental humidity variations lead to a non-uniform stress distribution on concrete, causing crack diffusion and affecting concrete pore humidity (Bažant and Oh, 1983). The pore humidity plays a similar role in concrete aging. Both the hydration and creep processes are slowed down by decreased pore humidity.

Loading history — Shah (1970) stated that sustained stress has a strengthening effect on concrete creep. This phenomenon is probably caused by increased van der Waals' force, which intensifies attraction among the particles of hydrated cement paste. Because of this beneficial effect, sustained loading was found to be less damaging than cyclic loading.

Aggregate type and size —According to Carlos et al. (2010), the modulus of elasticity of aggregate significantly affects concrete creep. Aggregate with higher elasticity modulus offers higher creep resistance. Both the strength and elastic modulus of concrete increase as the proportion of limestone aggregate in concrete increases. Additionally, well-graded, coarser aggregate with low-void content decreases creep deformation.

1.6.2 Tests of Concrete Material under High Sustained Load

The collapse of a RC building under sustained loads is most likely caused by concrete material failure due to nonlinear creep increasing continuously. Assessments of concrete creep require experimental results at high stresses. Nevertheless, these results are very scarce so that the relationship between nonlinear creep and damage as well as failure mechanism cannot be effectively clarified. For instance, in a well-cited concrete creep experimental database produced by Northwestern University (Wendner et al., 2015), only 50 out of 1439 data sets exist for concrete subjected to sustained stresses σ_c greater than or equal to 75% of short-time strength f_c' . Figure 1.7 shows the applied stress level versus loading time of the test data given in this

database as well as those provided in four literature to be reviewed in this section. Overall, only 111 of 1500 tests considered a stress ratio greater than 0.75 and only 84 of the 1500 specimens were loaded after 200 days of concrete casting. It is noteworthy that no experiment shown in Figure 1.7 was performed both under a stress ratio greater than 0.75 and after a concrete age of 200 days.

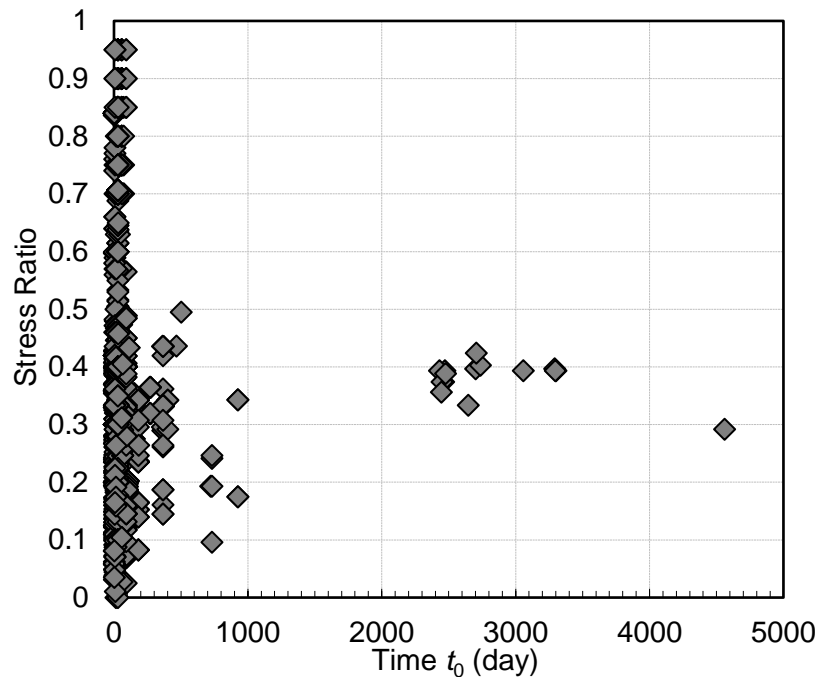


Figure 1.7 Summary of creep data from Northwestern University's database and four literature.

Tests by Shah and Chandra (1970)

Shah and Chandra tested six 2 in. x 2 in. x 6 in. concrete prismatic specimens subjected to sustained concentric stresses of 60, 70, 80, and 90% of 28-day cylinder compressive strength (average strength = 4580 psi). The concrete age of loading was between 28 and 30 days. Concrete failure process under sustained loading was studied. Both longitudinal and lateral strains were measured. Figure 1.8 summarizes the creep deformation data obtained in this study. All the four specimens subjected to $\sigma_c / f_c' \geq 0.80$ failed within 100 minutes during the

sustained loading. The other two specimens subjected to lower sustained stresses were loaded up to 4 hours. It was concluded that crack growth under sustained stress results from stress corrosion. Stress corrosion is influenced significantly by free moisture presence and allows crack tip to be corroded faster due to concrete material deterioration. Additionally, sustained stress has a strengthening effect on concrete creep when comparing with cyclic loading. This phenomenon is because concrete under sustained load intensifies attraction among the particles of hydrated cement paste so that creep strain under sustained load is less than under cyclic loading.

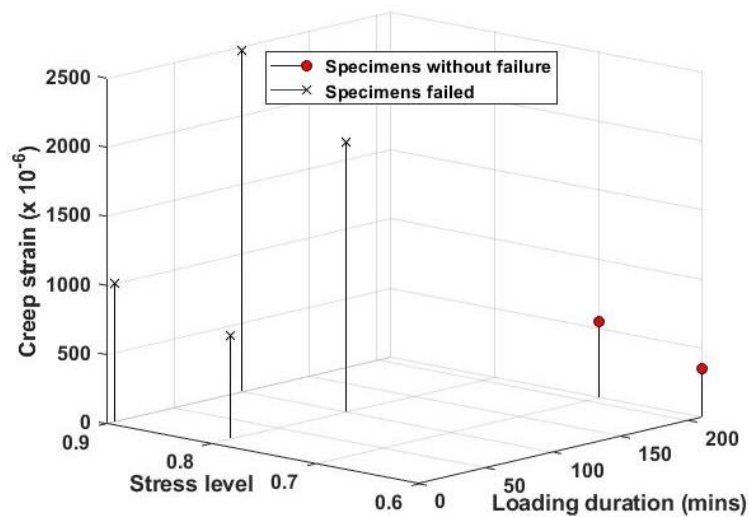


Figure 1.8 Concrete creep under high sustained stresses measured by Shah and Chandra (1970).

Tests by Awad and Hilsdorf (1971)

Thirty 4x4x12 in. concrete prismatic specimens were tested to investigate strength and deformation characteristics of plain concrete subjected to high sustained concentric compressive stresses. Deformations were recorded in both longitudinal and transverse directions. The specimens were divided into three groups based on loading age. In each group, three sustained load levels were considered: $\sigma_c / f_c' = 0.85, 0.9$ and 0.95 , where f_c' is concrete short-time

strength at the start of sustained loading. Eight specimens, with an average f_c' of 2330 psi were loaded after 7 days of concrete pouring. Twelve specimens were loaded at an age of 28 days when the average f_c' was 3690 psi. Ten specimens were loaded at an age of 90 day when the average f_c' was 4522 psi. Figure 1.9 shows the measured creep failure strain data, all specimens were failed within 4 days. It was found that, when the sustained stress was lower, the failure strain under sustained loads was higher. Moreover, if concrete was loaded at an older age, the longitudinal strain at failure for $\sigma_c / f_c' \leq 0.9$ was higher.

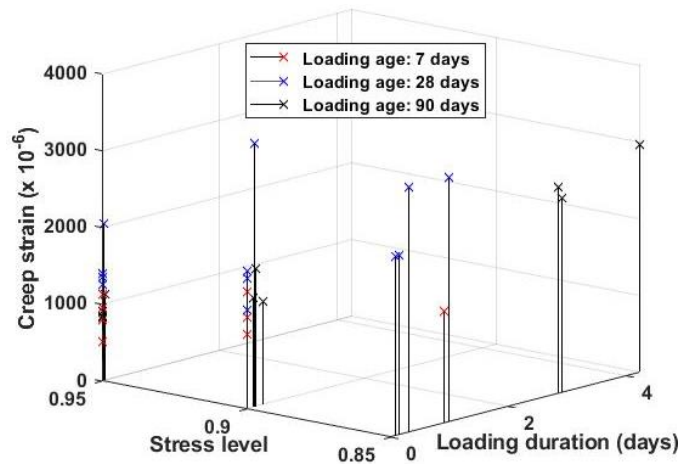


Figure 1.9 Concrete creep under high sustained stresses measured by Awad and Hilsdorf (1971).

Tests by Smadi et al. (1985 and 1986)

Smadi et al. (1985 and 1986) conducted sustained concentric loading tests of forty-four 4 x 8 in. cylinder specimens. The objective was to determine the effects of concrete strength and applied stress level on total deformation, creep deformation, normalized creep, and creep recovery. Based on 28-day compressive strength, three groups of specimens were tested, including high strength concrete ($f_c' = 8,000$ to $10,000$ psi), medium strength concrete ($f_c' = 5,000$

to 6,000 psi), and low strength concrete ($f_c' = 3,000$ to 4,000 psi). The sustained stresses were of 40, 60, 70, 75, 80, 85, 90 and 95% of concrete ultimate strength. The age of loading ranged from 28 to 30 days. Figure 1.10 shows the measured creep deformation data. For specimens with $\sigma_c / f_c' \geq 0.85$, the measurements were taken up to 4 hours; for $\sigma_c / f_c' < 0.85$, the specimens were loaded up to 60 days. Under the same σ_c / f_c' , the creep strain of high-strength concrete was lower than that of medium- and low-strength concrete. At very early ages after loading (i.e., within one day), the total strain at the same stress level was greater when concrete f_c' was higher; however, at later ages this was not the case anymore, as shown in Figure 1.11. Additionally, the total strain recovery was approximately proportional to the previously applied stress and was greater if concrete f_c' was higher.

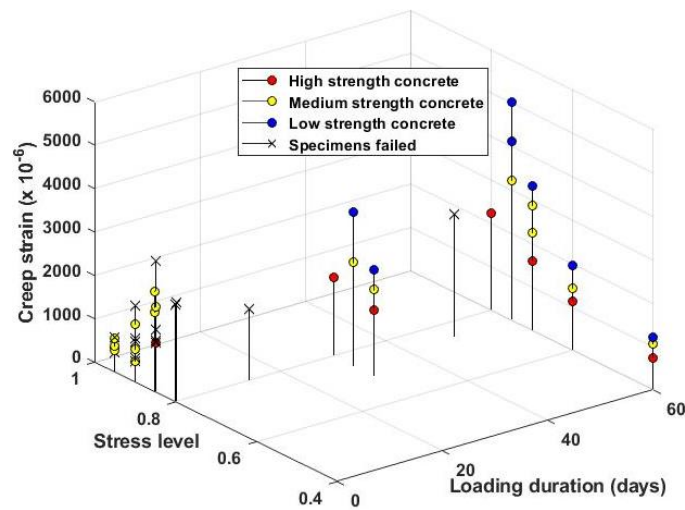


Figure 1.10 Concrete creep under high sustained stresses measured by Smadi et al (1985 and 1986).

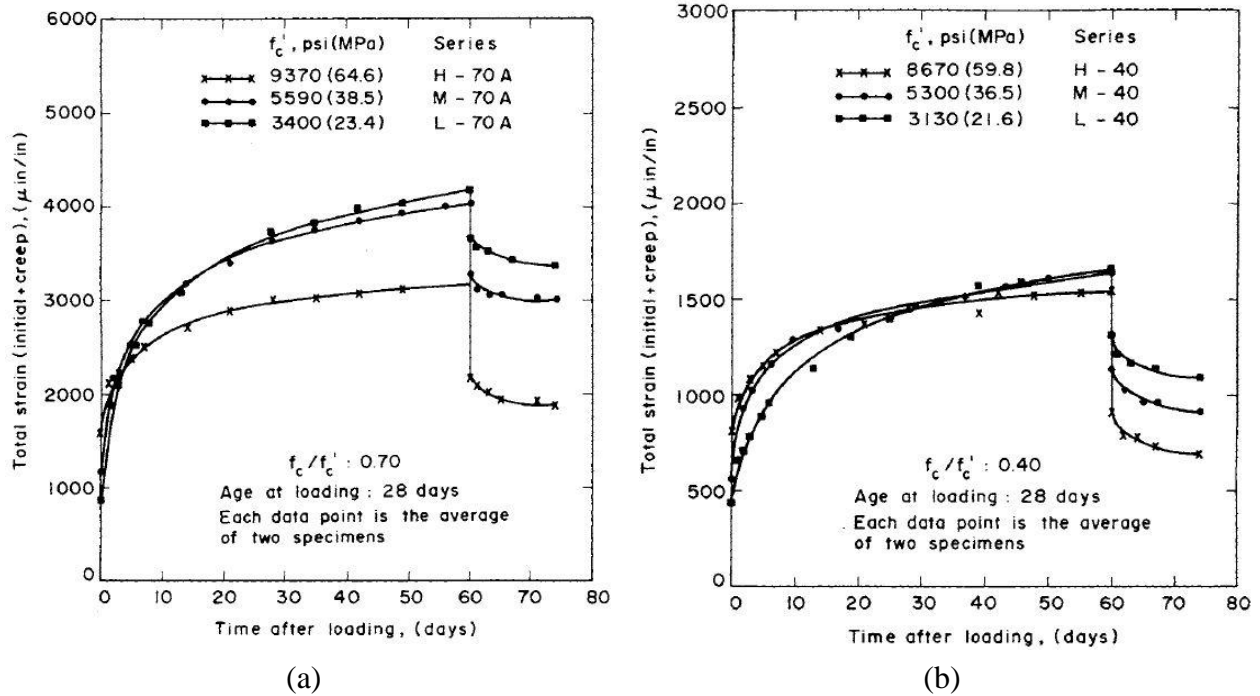


Figure 1.11 Concrete creep and creep recovery of high-, medium-, and low-strength concrete under sustained compressive stress: (a) $\sigma_c / f_c' = 0.7$ and (b) $\sigma_c / f_c' = 0.4$ (Smadi et al., 1985 and 1986).

Tests by Irvani and MacGregor (1998)

Sustained loading tests were carried out on twenty-nine 100 x 200 mm concrete cylinders to study compressive strength under high sustained stresses. The specimens were subjected to sustained stresses for 3 months if no failure occurred. Two groups of concrete cylinders were tested under long-term loading: 20 tests were loaded under concentric loading and 9 tests were loaded under eccentric loading with an eccentricity of 10% of diameter. The loading age was 56 days, when concrete short-time strength was measured as $f_c' = 65$ to 120 MPa (9,425 to 17,400 psi). Sustained stresses ranged from 70 to 95% of the short-time strength. The tests examined whether strength reduction is as great for high-strength concrete as for normal-strength concrete. Figure 1.12 summarizes measured extreme fiber creep strain data. The following observations were made: (1) The ratio of sustained load strength to short-time strength of high-strength

concrete increased as the compressive strength increased; (2) as shown in Figure 1.13, small eccentricity slightly improved the sustained load strength ratios of high-strength concrete by approximately 5%; (3) during the initial loading to the sustained stress in a short time, nonlinearity in stress-strain response appears at a greater ratio of stress to the short-time strength.

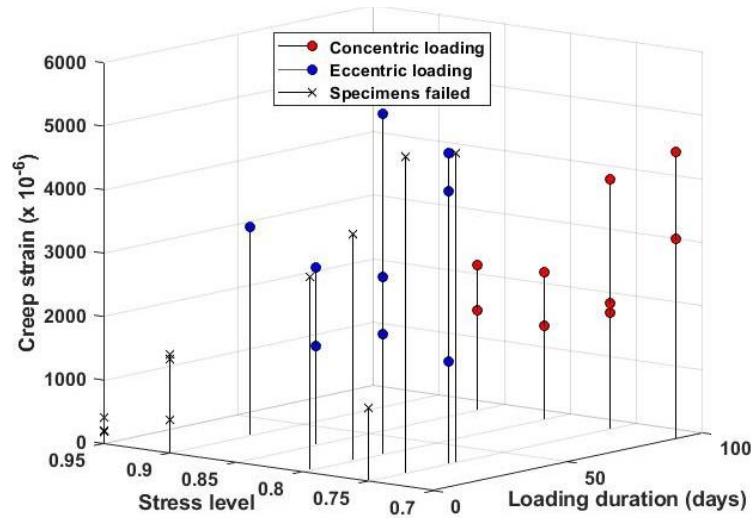


Figure 1.12 Concrete creep data under high sustained stresses measured by Iravani and MacGregor (1998).

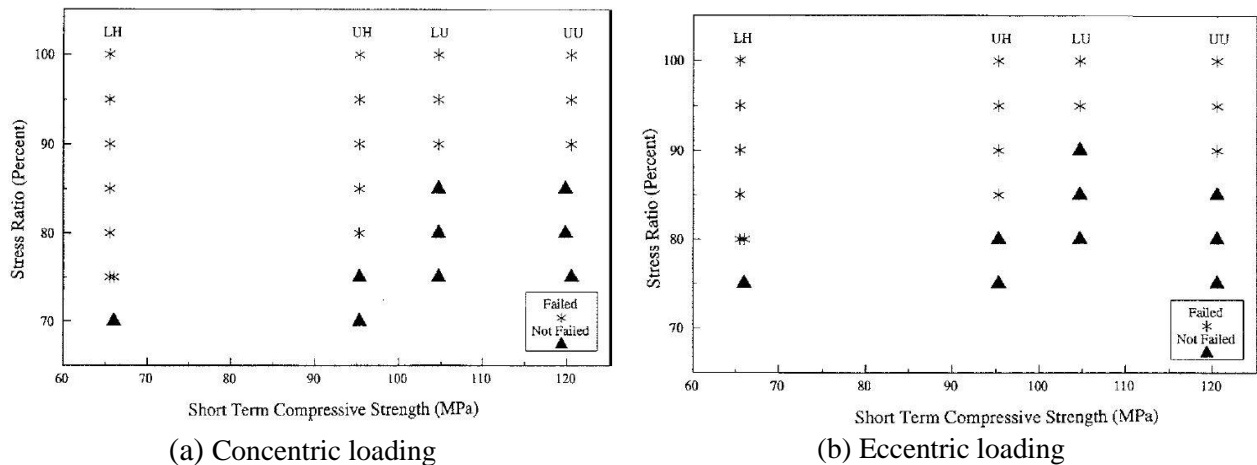


Figure 1.13 Concrete creep data under high sustained stresses (Iravani and MacGregor, 1998).

1.6.3 Existing Concrete Creep Models

1.6.3.1 Models for Linear Creep

Four linear creep models are frequently cited to predict the long-term creep strain of concrete under low level of sustained stresses (0 to 40% of concrete ultimate stress), including ACI 209 model (ACI Committee 209, 1992), B3 model (Bažant and Baweja, 1995 and 2000), CEB MC90-99 model (Muller and Hillsdorf, 1990; CEB, 1999) and GL2000 model (Gardner and Lockman, 2001). These models were calibrated with typical composition concretes, excluding concrete containing silica fume, fly ash contents greater than 30%, or natural pozzolans. The individual model's applicable range for different input variables are listed in Table 1.1, where f_{cm28} is concrete mean compressive cylinder strength at 28 days, a/c is aggregate-cement ratio, t_c is age of concrete (in days) when drying starts at end of moist curing, and t_0 is age of concrete at loading (in days). Five basic assumptions were normally adopted: (1) shrinkage and creep are additive; (2) creep may be considered approximately proportional to stress; (3) creep can be separated into basic creep and drying creep; (4) differential shrinkage and creep or shrinkage and creep gradients can be neglected; and (5) Restrained stresses caused by concrete swelling and autogenous shrinkage during curing phase are negligible. Basic creep, measured on specimens sealed condition, is considered a material constitutive property and independent of the specimen size and shape. Drying creep is the remaining strain after removing shrinkage, elastic and basic creep strains from the total strain of identical specimens in a drying condition.

Table 1.1 Parameter range for four linear creep models

Input variables	ACI 209	B3	CEB MC90	GL2000
f_{cm28} (psi)	—	2,500 to 10,000	2,175 to 17,400	2,320 to 11,900
a/c	—	2.5 to 13.5	—	—
Cement content (lb/yd ³)	479 to 752	270 to 1215	—	—
w/c	—	0.35 to 0.85	—	0.4 to 0.6
Relative humidity, %	40 to 100	40 to 100	40 to 100	20 to 100
Type of cement	I or III	I, II, III	I, II, III	I, II, III
t_c (moist cured)	≥ 1 day	≥ 1 day	< 14 days	≥ 1 day
t_c (steam cured)	1 to 3 days	—	—	—
t_0	≥ 7 days	$t_0 \geq t_c$	> 1 day	$t_0 \geq t_c \geq 1$ day

ACI 209 model (ACI, 1992)

The ACI 209 model (1992) predicts total concrete strain, including creep and shrinkage strains. Only the formulation of creep strain in this model is described herein. This model defines a compliance function $J(t, t_0)$ that represents the total stress-dependent strain caused by a unit stress, as shown in Equation (1.1).

$$J(t, t_0) = \frac{1 + \phi(t, t_0)}{E_{cm t_0}} \quad (1.1)$$

where $E_{cm t_0}$ is concrete modulus of elasticity at the time of loading (t_0 , in days); and $\phi(t, t_0)$ is a creep coefficient defined in Equation (1.2) as the ratio of the creep strain at t (concrete age, in days) to elastic strain at the start of loading at the age of t_0 (in day).

$$\phi(t, t_0) = \frac{(t - t_0)^\psi}{d + (t - t_0)^\psi} \cdot \phi_u \quad (1.2)$$

where $t - t_0$ is time since application of load; ϕ_u is an ultimate creep coefficient. For standard conditions, in the absence of specific creep data for local aggregates and conditions, the average value for ϕ_u is proposed as 2.35; $d = 10$ and $\psi = 0.6$ are recommended average values.

B3 model (Bazant and Baweja, 2000)

B3 model is the most updated method developed at Northwestern University for predicting concrete shrinkage and creep. The B3 model is simpler and is better theoretically justified than the previous models (Bazant and Baweja, 2000). The model has some restrictions, as shown in Table 1.1. Additionally, B3 model is restricted to service stresses (no more than $0.45f_{cm28}$). An average compliance function $J(t, t_0)$ is expressed using Equation (1.3). $J(t, t_0)$, evaluated at concrete age t and caused by an uniaxial constant stress applied at age t_0 , includes instantaneous deformation and drying creep.

$$J(t, t_0) = q_1 + C_0(t, t_0) + C_d(t, t_0, t_c) \quad (1.3)$$

where q_1 is an instantaneous strain due to unit stress (at a time of about 10^{-9} second); $C_0(t, t_0)$ is a compliance function for basic creep; $C_d(t, t_0, t_c)$ is additional compliance function for drying creep.

CEB MC90 model (1999)

CEB MC90 model (Muller and Hilsdorf, 1990; CEB, 1999) involves similar concepts to the ACI 209 model. The CEB MC90 model gives a hyperbolic change with time for creep and shrinkage. The model also uses an ultimate value corrected according mixture proportioning and environment conditions. The CEB model does not require any input regarding curing duration and condition; however, it considers average relative humidity and member size. The compliance function $J(t, t_0)$ in this model is expressed as Equations (1.4) and (1.5).

$$J(t, t_0) = \frac{1}{E_{cm28}} [\eta(t_0) + \phi_{28}(t, t_0)] = \frac{1}{E_{cm0}} + \frac{\phi_{28}(t, t_0)}{E_{cm28}} \quad (1.4)$$

$$E_{cm0} = E_{cm28} \cdot \exp\left[\frac{s}{2} \{1 - (28/t_0)^{0.5}\}\right] \quad (1.5)$$

where E_{cm28} is mean modulus of elasticity of concrete when loading starts at age t_0 ; $\phi_{28}(t, t_0)$ is 28-day creep coefficient (dimensionless) expressed using Equations (1.6) through (1.10); coefficient s should be taken from Table 1.2.

Table 1.2 Values of coefficient s

f_{cm28}	Type of cement	s
$\leq 60\text{MPa}$	III (rapid hardening high-strength cement)	0.2
	I (normal or rapid hardening cements)	0.25
	II (slowly-hardening cement)	0.38
$\geq 60\text{MPa}$	All types	0.2

$$\phi_{28}(t, t_0) = \phi_0 \cdot \beta_c(t - t_0) \quad (1.6)$$

$$\phi_0 = \phi_{RH}(h) \beta(f_{cm28}) \beta(t_0) \quad (1.7)$$

$$\phi_{RH}(h) = \left[1 + \frac{1 - h / h_0}{\sqrt[3]{0.1[(V/S)/(V/S)_0]}} \left(\frac{3.5 f_{cm0}}{f_{cm28}} \right)^{0.7} \right] \left(\frac{3.5 f_{cm0}}{f_{cm28}} \right)^{0.2} \quad (1.8)$$

$$\beta(f_{cm28}) = 5.3 / (f_{cm28} / f_{cm0})^{0.5} \quad (1.9)$$

$$\beta(t_0) = 1 / [0.1 + (t_0 / t_1)^{0.2}] \quad (1.10)$$

where h is relative humidity of the ambient environment expressed as a decimal; $h_0 = 1$; V/S is volume-surface ratio; $(V/S)_0 = 2$ in.; $f_{cm0} = 1450$ psi; $t_1 = 1$ day.

GL2000 model (2004)

The latest GL2000 model (Gardner 2004) was minorly modified from the original model developed by Gardner and Lockman (2001). The modifications include some coefficients and strength development with time. The model presents a design procedure for calculating the creep

of normal-strength concretes. The 28-day specified concrete strength, concrete strength at loading, element size, and relative humidity are needed for this model. The effects of element size, represented by V/S ratio, are reflected in Equations (1.11) and (1.12). Aggregate stiffness is taken into account. The compliance expression is based on the modulus of elasticity at 28 days instead of the modulus elasticity at the age of loading. This model includes a term for drying before loading, which is applied to both basic and drying creeps. The compliance function $J(t, t_0)$ is identical to that of the MC90 model (Equation (1.4)); however, the expression of $\phi_{28}(t, t_0)$ is modified as Equation (1.11). The GL2000 can be used regardless of chemical admixtures or mineral by-products in concrete, casting temperature, or curing regime.

$$\phi_{28}(t, t_0) = \Phi(t_c) \left[2 \frac{(t-t_0)^{0.3}}{(t-t_0)^{0.3} + 14} + \left(\frac{7}{t_0} \right)^{0.5} \left(\frac{(t-t_0)}{(t-t_0) + 7} \right)^{0.5} + 2.5 \cdot (1 - 1.086h^2) \left(\frac{t-t_0}{(t-t_0) + 0.12(V/S)^2} \right)^{0.5} \right] \quad (1.11)$$

where $\Phi(t_c)$ is the correction term for the effect of drying before loading and expressed as Equation (1.12).

$$\Phi(t_c) = \left[1 - \left(\frac{(t_0 - t_c)}{(t_0 - t_c) + 0.12(V/S)^2} \right)^{0.5} \right]^{0.5} \quad (1.12)$$

where t_c is concrete age when drying starts or end of moist curing (in days).

1.6.3.2 Models for Nonlinear Creep

The damaging effect of high sustained stress on concrete compressive strength has been recognized and studied since the 1950s. The methods for modeling concrete nonlinear creep and associated damage can be categorized into three types. The first type was developed based on material damage development (Hellesland and Green, 1972; Carol and Murcia, 1989; Mazzotti and Savoia, 2003; Bockhold and Stangenberg, 2004; El-Kashif and Maekawa, 2004; Challamel

et al., 2005; Ruiz et al., 2007; Tasevski et al., 2018 and 2019). The second type was based on fracture mechanics (Whittmann and Zaitsev, 1972; Zhou, 1992; Zijl et al., 2001; Barpi and Valente, 2002; Luzio G. Di, 2009). The third type theory had a physical basis in micromechanics of aging process, which amalgamates a microplane model and a modified solidification-microprestress theory and considering the temperature and humidity effects on concrete creep. This category of modeling method was originated from Bažant et al. (2004) and further modified by Luzio and Cusatis (2012) and Wei et al. (2016). Four prominent models, developed by Tasevski et al. (2018 and 2019), Mazzotti and Savoia (2003), Luzio and Cusatis (2012), and Wei et al. (2016), are described herein. Because the model proposed by Tasevski et al. (2018 and 2019) is employed in this study, more details are given in the description.

Tasevski et al. (2018 and 2019)

In this nonlinear creep model, the total strains of concrete loaded at time t_0 is described as

$$\varepsilon_c \left(t, \frac{\sigma_c}{f_c} \right) = \varepsilon_{c0} \left(t_0, \frac{\sigma_c}{f_c} \right) + \Delta\varepsilon_{cs}(t, t_0) + \Delta\varepsilon_{cc} \left(t, t_0, \frac{\sigma_c}{f_c} \right) \quad (1.13)$$

where f_c is uniaxial compressive strength of concrete at the age of loading; the first term on the right-hand of the equation is an instantaneous pre-peak strain, which is indicated by the short-time stress-strain response shown in Figure 1.14; the second term corresponds to shrinkage strain defined using Equation 1.14; the third term is creep strain, which is divided into primary creep (ε_{cc1}), secondary creep (ε_{cc2}), and tertiary creeps (ε_{cc3}), as shown in Equation (1.15).

$$\varepsilon_{cs}(t, t_s) = -3.64 \times 10^{-5} (1 - e^{-0.2\sqrt{t}}) - \frac{6.99 \times 10^{-4}}{\sqrt{\frac{224}{t-t_s} + 1}} \quad (1.14)$$

where t_s is concrete age at demoulding (in days); after concrete has been loaded, t_s in Equation

(1.14) shall be replaced by t_0 to calculate the change in shrinkage strain.

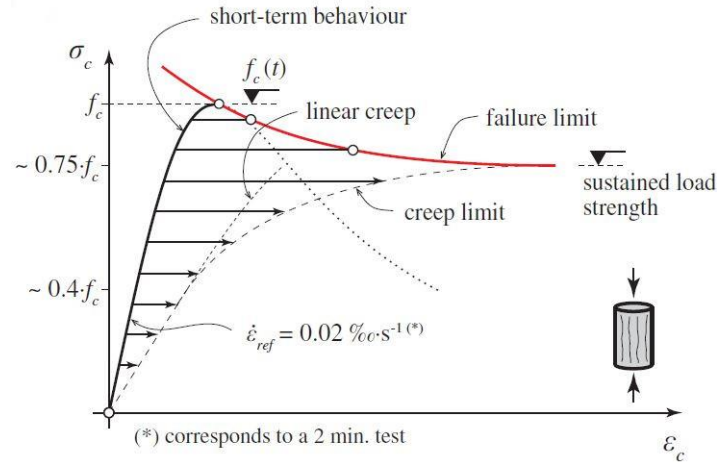


Figure 1.14 Response of concrete under uniaxial compressive stresses: short- and long-term stress-longitudinal strain diagram according to Rüschi (1960).

$$\epsilon_{cc}(t, t_0, \frac{\sigma_c}{f_c}) = \epsilon_{cc,1}(t, t_0) + \epsilon_{cc,2}(t, t_0, \frac{\sigma_c}{f_c}) + \epsilon_{cc,3}(t, t_0, \frac{\sigma_c}{f_c}, \frac{\epsilon_{in}}{\epsilon_{in,av}}) \quad (1.15)$$

The primary creep strain, ϵ_{cc1} , is calculated by Equation (1.16), where ϵ_{c0} is an instantaneous prepeak strain, as shown in Figure 1.15, and φ_{lin} is a linear creep coefficient φ_{lin} (not associated to material damage) defined using Equation (1.17).

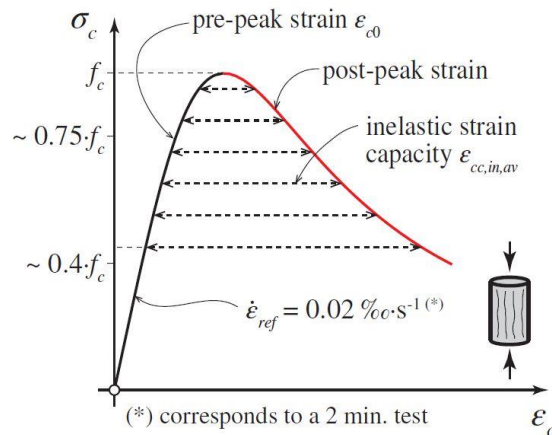


Figure 1.15 Instantaneous pre- and post-peak longitudinal strains' inelastic strain capacity

(Tasevski et al., 2019).

$$\varepsilon_{cc,1}(t, t_0) = \varphi_{lin}(t, t_0)\varepsilon_{c0} \quad (1.16)$$

$$\varphi_{lin}(t, t_0) = \frac{3.24}{0.1+t_0^{0.2}} \left(\frac{t-t_0}{682+t-t_0} \right)^{\frac{1}{2.3+\frac{3.5}{\sqrt{t_0}}}} + \frac{3}{0.1+t_0^{0.2}} \left(\frac{t-t_0}{395+t-t_0} \right)^{\frac{1}{2.3+\frac{3.5}{\sqrt{t_0}}}} \quad (1.17)$$

The secondary creep strain, ε_{cc2} , is associated with material damage due to micro-cracking and evaluated by Equation (1.18). The coefficient η in this equation is expressed using Equation (1.19) (Ruiz et al. 2007), where the coefficient η_τ takes into account nonlinear creep strains developed with time and is defined using Equation (1.20).

$$\varepsilon_{cc,2}(t, t_0, \frac{\sigma_c}{f_c}) = (\eta - 1)\varepsilon_{cc,1}(t, t_0) \quad (1.18)$$

$$\eta\left(\frac{\sigma_c}{f_c}, t, t_0\right) = 1 + 2\eta_\tau(t, t_0) \left(\frac{\sigma_c}{f_c(t)}\right)^4 \quad (1.19)$$

$$\eta_\tau(t, t_0) = \left(1 - \log\left(\frac{t-t_0}{t_m + t - t_0}\right)\right)^n \quad (1.20)$$

where constant values of $t_m = 100$ days and $n = 0.75$ can be assumed. Noted that, η_τ approaches unity as t approaches infinity. Consequently, Equation (1.19) takes the form originally suggested by Ruiz et al. (2007) for nonlinear creep strains after a long time.

Tertiary creep strain, ε_{cc3} , is associated with micro-crack coalescence and material damage. ε_{cc3} is evaluated by Equation (1.21), which considers the ratio of developed-to-available inelastic strains ($\varepsilon_{cc,in}/\varepsilon_{cc,in,av}$) and stress level. $\varepsilon_{cc,in,av}$ is total inelastic strain capacity indicated in Figure 1.15. $\varepsilon_{cc,in}$ is nonlinear creep strain, which is equal to total strain minus shrinkage, instantaneous and linear creep strains.

$$\varepsilon_{cc,3} \left(t, t_0, \frac{\sigma_c}{f_c}, \frac{\varepsilon_{cc,in}}{\varepsilon_{cc,in,av}} \right) = \gamma \left(\frac{\sigma_c}{f_c}, \frac{\varepsilon_{cc,in}}{\varepsilon_{cc,in,av}} \right) \varepsilon_{cc,2} \left(t, t_0, \frac{\sigma_c}{f_c} \right) \quad (1.21)$$

For low ratios of $\varepsilon_{cc,in} / \varepsilon_{cc,in,av}$, tertiary creep strain is a negligible; however, tertiary creep strain increases at a growing rate when failure is approached. When $\sigma_c / f_c(t) \geq 0.75$, the parameter γ in Equation (1.21) is calculated as

$$\gamma = \frac{1}{2} \left(\frac{\varepsilon_{cc,in}}{\varepsilon_{cc,in,av}(t)} \right)^\alpha \quad (1.22)$$

According to this assumption, γ is zero for stress levels below an assumed threshold of $\sigma_c / f_c = 0.75$ for possible tertiary creep. The parameter α , taken as 4, governs the shape of the tertiary creep curve. At failure, $\varepsilon_{cc,in} = \varepsilon_{cc,in,av}$, resulting in $\varepsilon_{cc,3} = 0.5\varepsilon_{cc,2}$. This relationship is consistent with the hypothesis of $\varepsilon_{cc,2} = (2/3)\varepsilon_{cc,in,av}$ and $\varepsilon_{cc,3} = (1/3)\varepsilon_{cc,in,av}$ (Ruiz et al., 2007), as shown in Figure 1.16.

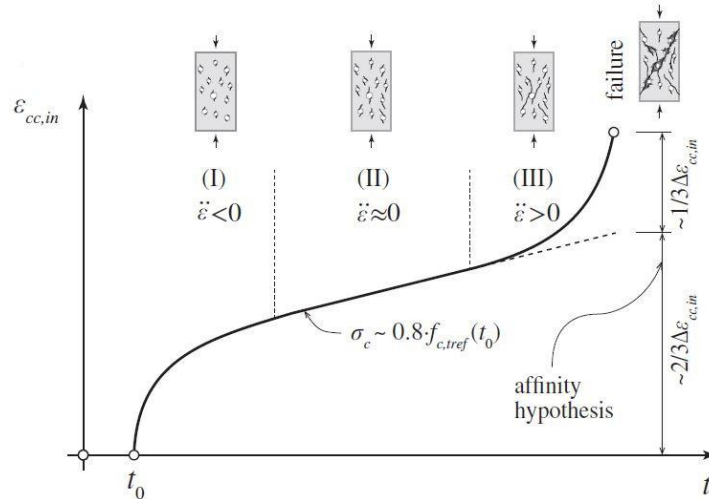


Figure 1.16 Three stages of creep: primary (I), secondary (II), and tertiary (III) (Tasevski et al., 2019).

Mazzotti and Savoia (2003)

Claudio and Marco (2003) proposed a model for concrete creep damage, which considers the effects of both nonlinear viscous strain evolution and crack nucleation and propagation at high stresses. The effect of concrete strength variation with time is also considered. Based on strain splitting assumption for creep and damage contributions, concrete creep is modeled by a modified version of solidification theory as shown in Figure 1.17. The model covers the entire range of creep behavior, including viscoelastic behavior under low stresses, nonlinear creep not accompanied by significant concrete damage under medium-level stresses, and tertiary creep leading eventually to a failure under high stresses.

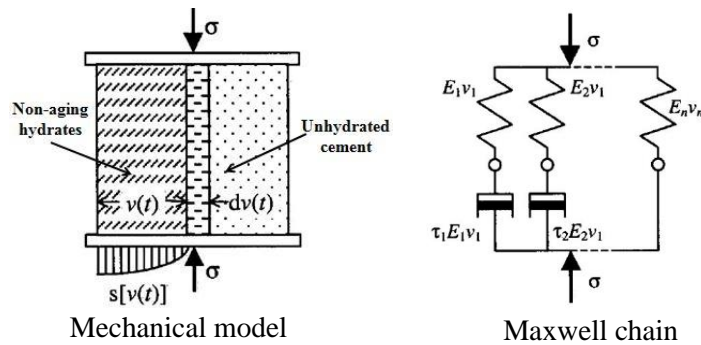


Figure 1.17 Illustration of solidification theory employed by Mazzotti and Savoia (2003).

To implement this model, an iterative exponential algorithm was provided to numerically perform time integration of nonlinear equations. This algorithm is an efficient time step numerical integration algorithm first developed by Bažant and Chern (1985). The stability and accuracy of the proposed algorithm was verified by experiments. As indicated by the numerical results, this algorithm is nearly insensitive to time discretization and equal time intervals in the log scale can be used to cover the full time range from early to late ages after loading.

Luzio and Cusatis (2012)

This nonlinear creep model, entitled solidification-microprestress-microplane (SMM) model, was developed based on the constitutive model initially proposed by Bažant (2004) and formulated using a strain rate format shown in Equation (1.23). The model combines a microplane model and a solidification-microprestress theory. Included in the model are nearly all crucial concrete behaviors, such as creep, shrinkage, thermal deformation, and cracking from the initial curing to several years of age. The creep strain is taken primarily as two portions. The first portion is age-dependent viscoelastic behavior under variable hygro-thermal conditions and described based on a solidification-microprestress theory. The second portion is cracking/damage behavior defined by an age-dependent microplane model, in which the model parameters are assumed to depend on variables including temperature, humidity and concrete aging caused by the progress of nano- and micro-sclae chemical reactions. Concrete aging effects are mainly reflected in concrete stiffness, concrete strength in both tension and compression, and fracture energy. The fracture energy increases with concrete age, whereas concrete creep decreases with concrete age. Concrete age also affects concrete behavior relevant to heat transfer and moisture diffusion. Figure 1.18 schematically shows the proposed model.

$$\dot{\epsilon} = \dot{\epsilon}^i + \dot{\epsilon}^v + \dot{\epsilon}^f + \dot{\epsilon}^d + \dot{\epsilon}^s + \dot{\epsilon}^t \quad (1.23)$$

where $\dot{\epsilon}^i$ is instantaneous strain rate, $\dot{\epsilon}^v$ is viscoelastic strain rate, $\dot{\epsilon}^f$ is purely viscous strain rate, $\dot{\epsilon}^d$ is inelastic strain rate due to cracking and damage, $\dot{\epsilon}^s$ and $\dot{\epsilon}^t$ are hygral and thermal strains due to variations of relative humidity and temperature, respectively.

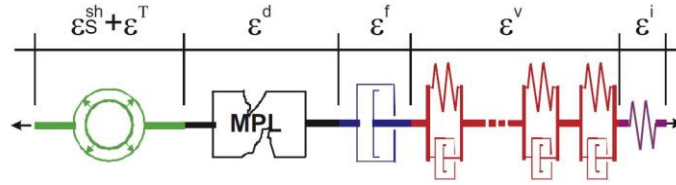


Figure 1.18 Schematic of concrete nonlinear creep model proposed by Luzio and Cusatis (2012).

Wei et al. (2016)

This model is a modified version of Bažant’s model (2004). The model combines ε^v and ε^d in Equation (1.23) into a single term ε^{eV} , as shown in Equation (1.24). Moreover, this model introduces an adjusting factor to account for the effects of temperature and humidity on microprestress relaxation rate. At last, revisions are made in the numerical approach of simulating concrete creep. Figure 1.19 shows major concept of the model. The solidification part of microprestress-solidification theory explains creep aging effect, which leads to an increasing volume fraction of non-aging hydration products as shown in Figure 1.19 (a). Temperature and humidity changes result in unbalanced chemical potential, and hence microprestress and creep rate change.

$$\varepsilon = \varepsilon^i + \varepsilon^{eV} + \varepsilon^f + \varepsilon^{sh} + \varepsilon^T \tag{1.24}$$

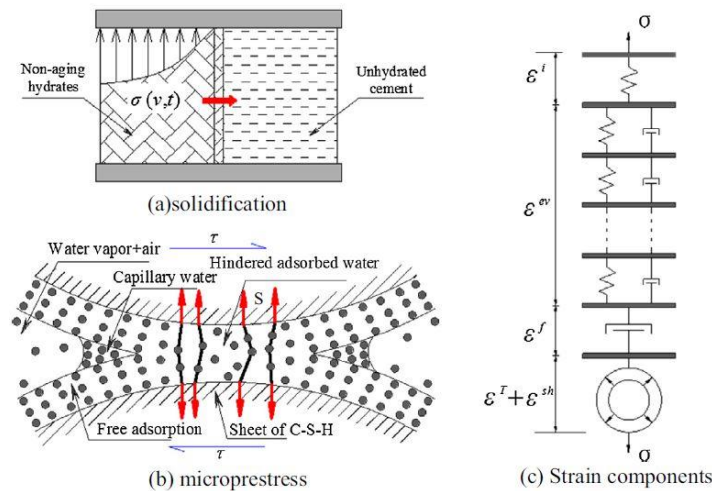


Figure 1.19 Schematic illustration of nonlinear creep model proposed by Wei et al. (2016).

1.6.4 Experimental Studies for RC Columns under Sustained Concentric Loading

Very limited experimental studies have been conducted on RC columns under sustained axial (concentric) loading especially for columns with square cross sections. However, the existing data indicate high sustained concentric load can fail RC columns. Two series of axial loading experiments, one on columns with circular cross sections and the other one on columns with square cross sections, are described as follows.

Richart and Brown (1934)

Totally 66 circular columns, including 60 RC and 6 plain concrete columns, were tested under sustained loads for one year. Each column has an 8.25-in. diameter and was 60-in. long. Three levels of target 28-day concrete strength (2000, 3500 and 5000 psi) were considered in the RC columns. However, the actual concrete strength at the time of testing was not reported. Longitudinal reinforcement ratios were approximately $\rho = 1.5, 4$ and 6% . Transverse reinforcement ratios of spirals were $\rho_t = 1.2$ and 2% . The yield strengths of longitudinal reinforcement and spirals were 45.6 and 49.4 ksi, respectively. All the columns were first moisture-cured for 56 days and then loaded in air of laboratory or moist room. The sustained loads ranged from 0.24 to $0.42P_0$, where P_0 is the axial loading capacity of columns calculated by Equation (1.25).

$$P_0 = 0.85f'_c(A_g - A_{st}) + A_{st}f_y \quad (1.25)$$

where A_g is gross sectional area of column; A_{st} is total area of longitudinal reinforcement; f'_c is 28-day concrete strength; and f_y is yield strength of steel reinforcement.

Figure 1.20 shows the testing device for applying loads on the columns. Two companion columns with identical design were confined between bearing plates by four 1-in. diameter steel

rods. The target tension force in these rods was maintained by four calibrated coil springs. The load was applied to the columns by tightening nuts on the four rods until a pre-determined compressive deformation of each spring was reached. Spring deformation was measured so that the compression force in the springs was adjusted after load release due to column creep.

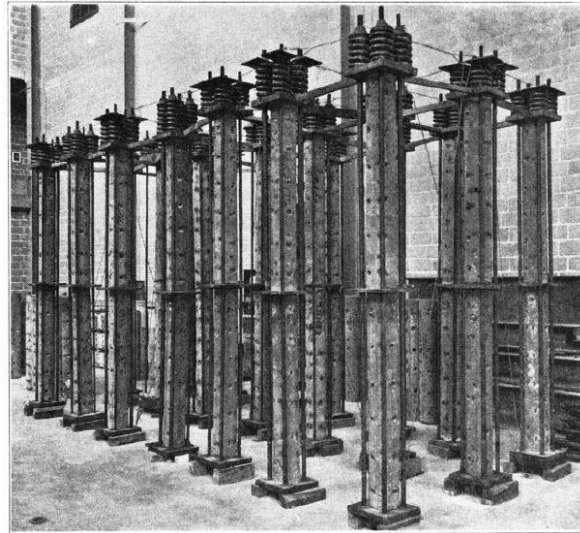


Figure 1.20 Sustained loading approach for columns (Richart and Brown, 1934).

No specimen was failed during the one-year sustained loading. Some of the columns were then tested under axial compression to failure in a short time. The following findings were made: (1) Column long-term deformation was a function of longitudinal reinforcement ratio. Both the deformation and change in steel stress were the least for columns with $\rho = 6\%$ but were greatest for the columns with $\rho = 1.5\%$. (2) Environmental condition had a strong influence of column sustained loading response. The creep deformations for air-stored columns were large, causing the secant modulus of elasticity to reduce by 75%; however, for moist-stored columns, the modulus reduction was only 20%. (3) The initial strains in the columns had no effect upon the ultimate load. (4) Concrete stress at the ultimate load was on average 85% of cylinder strength for air-stored columns and 64% for moist-stored columns.

Jenkins (2015)

Two 6.125 in. x 6.125 in. x 24 in. square columns were tested. One of them was plain concrete column. The other one was a RC column reinforced by four No. 3 bars ($f_y = 72.9$ ksi) with a longitudinal reinforcement ratio of $\rho = 1.2\%$. Figure 1.21 shows reinforcement details of the RC column. These specimens had identical concrete strength of $f'_c = 5980$ psi at the time of loading (50 days after concrete curing). The two short columns were subjected to sustained loading for 365 days. The load level was $0.55P_0$ calculated by Equation (1.25) for the plain concrete column and $0.48P_0$ for the RC column.

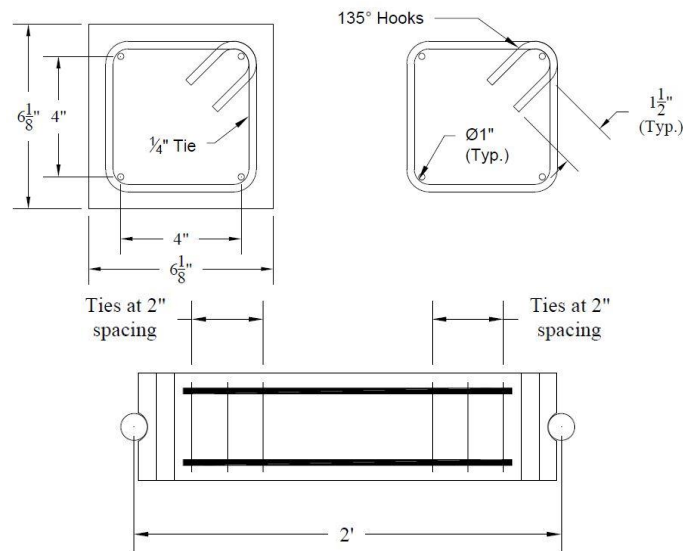


Figure 1.21 Reinforcement details for a short RC column tested by Jenkins (2015).

Figure 1.22 shows the loading frame, by which the specimens were horizontally situated and tested. Note that what the figure shows is associated with eccentric loading tests (described in the next section) performed by the same researcher. However, identical loading approach was used for axial loading, except that the columns were positioned at the center. The test setup consisted of three steel plates and four high-strength post-tensioning bars ($d = 1.25$ in). A roller

plate was attached to the frame plate and the end plate attached to specimen had the same level. Hydraulic loading rams were used to apply loads to the columns up to the predetermined level. Once the load was applied, hex nuts were then tightened to resist the post-tensioning force in the rods. The force applied to the column was increased periodically to consider time-dependent losses resulting from concrete creep. Neither of the two columns subjected to one-year sustained loading failed. Figure 1.23 shows measured axial strain time history. Compared with the plain concrete column, the RC column had significantly decreased creep rates due to the presence of longitudinal reinforcement.

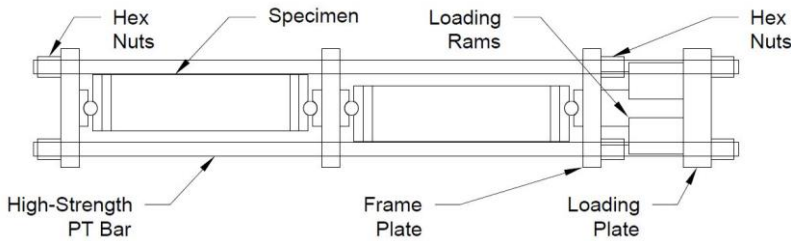


Figure 1.22 Test setup for sustained loading of short columns (Jenkins, 2015).

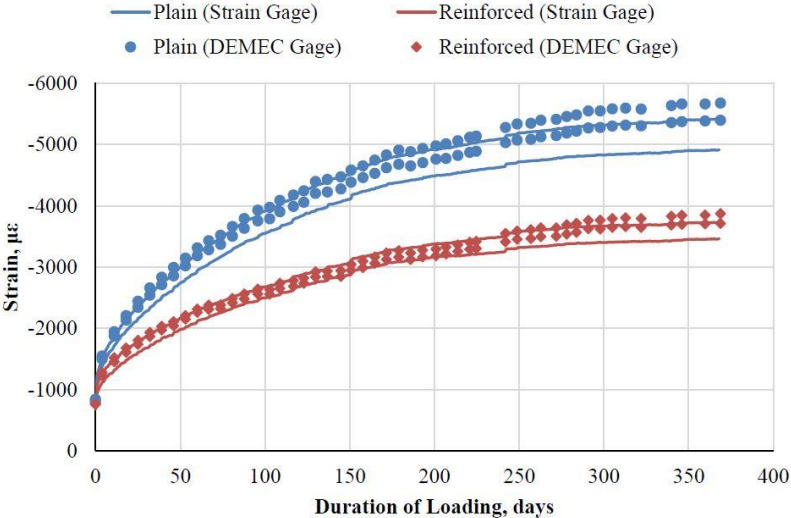


Figure 1.23 Comparison of measured creep in plain and reinforced concrete columns under sustained axial loading (Jenkins, 2015).

Eom et al. (2018)

Two RC columns were tested under sustained axial loading. Figure 1.24 shows specimen configuration and reinforcing details. Fabricated together with a pedestal, the RC column had a 950-mm height and a 200 mm x 300 mm cross section. Each column was longitudinally reinforced by six 17.5-mm diameter bars with a yield strength of $f_y = 400$ MPa. Tie hoops made of 10.4-mm diameter bars were placed at a spacing of 100 mm. The longitudinal and transverse reinforcement ratios were $\rho = 2.4$ and $\rho_t = 1.27\%$, respectively. The 28-day concrete strength was $f'_c = 47.3$ MPa.

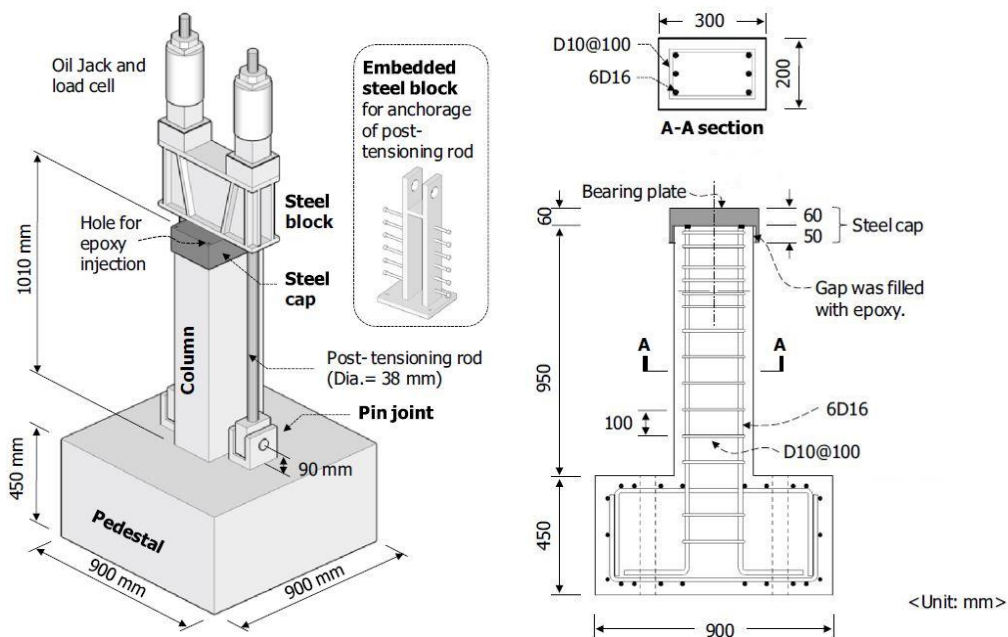


Figure 1.24 Configuration and reinforcement details of RC columns subjected to sustained loading (Eom et al., 2018).

Two sustained load levels based on Equation (1.25), $0.15P_0$ and $0.30 P_0$, were applied to the columns at an age of 37 days after concrete placement and lasted for 64 days. As shown in Figure 1.25, sustained load was applied by two post-tensioning high-strength steel rods ($d = 38$ mm) and a steel beam placed on column top. No failure occurred in the two columns during the

sustained loading. As shown by the blue color lines in Figure 1.25, it was found that the increasing rates of long-term deformations rapidly decreased with loading time.

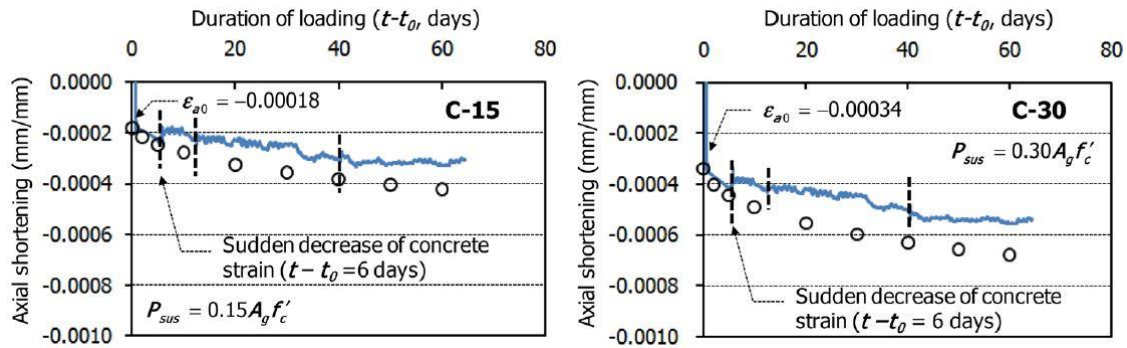


Figure 1.25 Axial deformation time-history of two RC columns under sustained concentric loading (Eom et al. 2018).

1.6.5 Experiments of RC Columns under Sustained Eccentric Loading

Experimental investigations of RC columns under sustained eccentric loading were more common than columns under sustained concentric loading. Representative experimental studies are selected and described as follows.

Viest et al. (1956)

Viest et al. (1956) reported sustained eccentric loading tests of 19 RC columns. Test variables include eccentricity, concrete strength, and sustained load level. The columns had the same size and were identically reinforced. Each specimen was 20 in. long and 5 in. x 5 in. in cross section. The corresponding height-to-depth ratio (H/h) was 4. A 10-in. capital was used at each end to accommodate the applied loads, as shown in Figure 1.26. The reinforcement contained four No. 4 bars ($f_y = 43.3$ ksi) and seven 3/16-in. ties spaced at 4 in. The longitudinal reinforcement ratio and transverse reinforcement ratio were $\rho = 3.2\%$ and $\rho_t = 0.44\%$, respectively. Extra reinforcement was provided in the capitals. The concrete cover thickness for

the longitudinal reinforcement was 0.5 in. Eccentricity, e , was defined as the distance from section center to the line of load. Small and moderate initial eccentricity, with eccentricity ratios of e/h ranging from 0.25 to 0.73, were considered, where h is section depth in the plane of bending. Load was applied to the columns through two 1/2 in. rollers. Each roller was placed in a triangular groove of a steel plate attached to column top and bottom. The sustained loads were maintained by coil springs as shown in Figure 1.27. The sustained loads ranged from 82 to 95% of the estimated ultimate load under short-time loading.

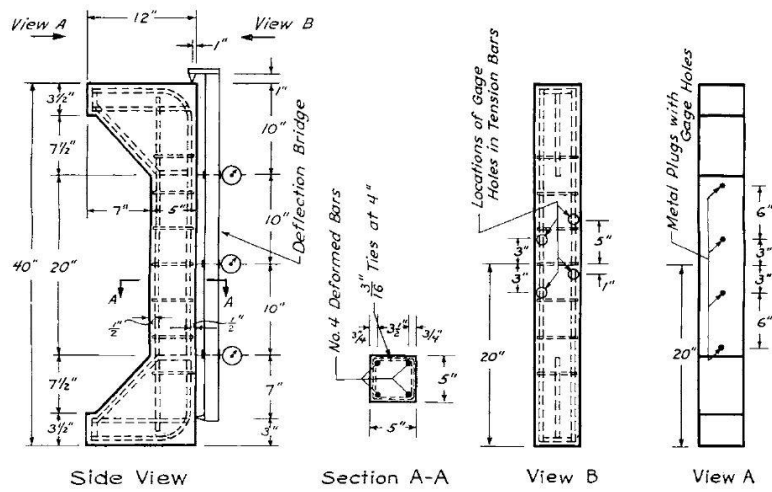


Figure 1.26 Details of specimens tested by Viest et al. (1956).

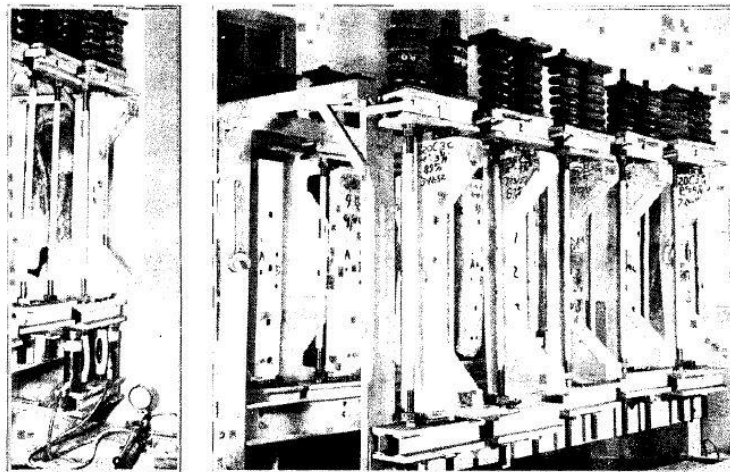


Figure 1.27 Loading frames for sustained load tests by Viest et al. (1956).

Table 1.3 summarizes the test data. Six columns, indicated by SU in Table 1.3, were failed by sustained loading in a period of 1.5 hr to 151 days. The remaining columns, indicated by SU+FA in Table 1.3, were subjected to sustained loads for 217 to 933 days. It was thought that these columns would never fail under the sustained loads. They were then loaded to failure in a short time. On average, the tested columns had a sustained loading capacity of about 90% of the ultimate load for short-time loading, regardless of concrete strength and eccentricity. The lowest and highest failure sustained loads were 82.6% and 94% of short-time failure loads, respectively.

Table 1.3 Summary of sustained loading tests by Viest et al. (1956)

Col. No.	Concrete strength (psi)	Initial eccentricity, e (in.)	Age (days) at		At failure			Type of loading
			Loading	Failure	Load (kips)	Steel strain (10^{-6})	Concrete strain (10^{-6})	
Columns with moderate eccentricities								
20B3a	2350	3.63	35	540	25	2850	6300	SU+FA
20B4a	2660	3.63	34	547	24.3	3130	7500	SU+FA
20B4b	1800	3.81	83	541	22	2700	4500	SU+FA
35B3a	4610	2.5	47	75	43.7	4000	6250	SU
35B4a	4640	2.5	48	199	43.4	3100	6500	SU
35B3b	4710	2.25	274	274	43.1			SU
35B4b	4760	2.25	271	936	47.3	2080	4200	SU+FA
50B3a	5420	2.25	40	592	57	2800	5350	SU+FA
50B4a	5680	2.25	41	589	51	5070	6780	SU+FA
50B3b	4740	2.5	52	490	49.5	3140	5880	SU+FA
50B4b	5320	2.5	52	124	41.3	3800	5760	SU
Columns with small eccentricities								
20C3a	3470	1.25	40	98	52.5	1100	6300	SU
20C4a	2900	1.25	34	602	53	1960	8720	SU+FA
20C3b	1820	1.75	43	48	32.4	1540	5420	SU
20C4b	1770	1.75	43	479	32	2850		SU+FA
20C3c	2380	1.25	50	948	51.2	1330	5940	SU+FA
20C4c	2810	1.25	82	1052	48.4	1600	6600	SU+FA
35C3b	4330	1.75	90	601	47.4	2400	7250	SU+FA
35C4b	4120	1.75	87	545	57	2450	6970	SU+FA

Green and Breen (1969)

Sustained loading responses of 10 eccentrically loaded RC columns were experimentally investigated. Figure 1.28(a) shows the details of a typical specimen. The stem portion of a column had a height-to-depth (H/h) ratio of 13. The 6 in. x 4 in. sections were longitudinally reinforced by four No. 3 bars ($\rho = 1.8\%$) and transversely by 12 gage wire ($d = 0.081$ in) at a spacing of 4 in ($\rho_t = 0.1\%$). The yielding strength of No. 3 bars were about 60 ksi. The average concrete strength at initial loading was 4190 psi. Eccentricity and sustained load level were the major test variables. The loading system consisted of a pair of coil springs, knife edges, ram, and strands.

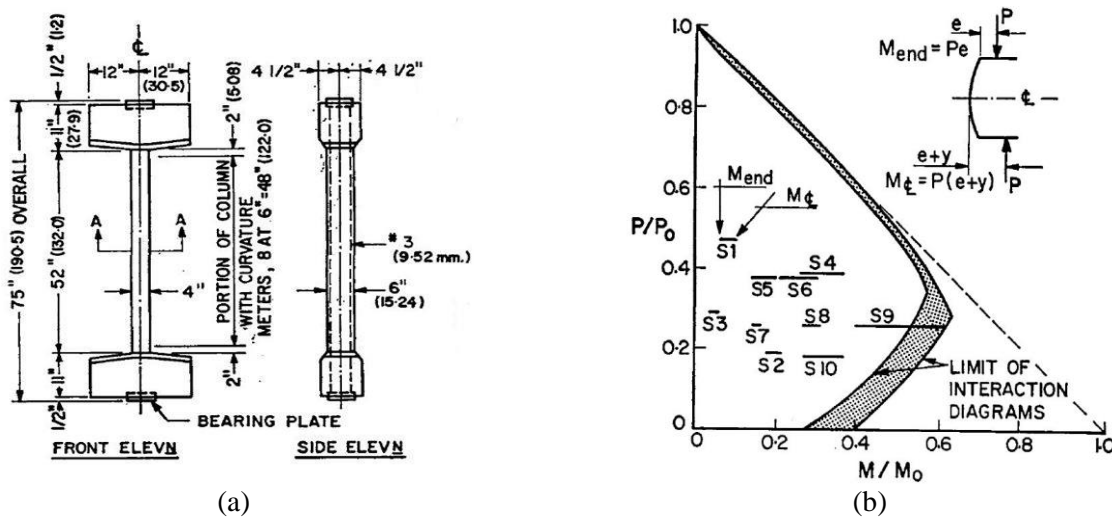


Figure 1.28 Columns tested by Green and Breen (1969) under sustained eccentric loading: (a) specimen dimension, and (b) axial load versus moment at the beginning of sustained loading.

The average specimen age at initial loading was 49 days with a maximum deviation of 7 days. The specimens were initially loaded to a predetermined level. The load was then maintained using coil springs and regulated to within 3% of the desired level. Table 1.4 gives the major test results, including the values of sustained axial load (P), sustained load level (P/P_0), end eccentricity ratio (e/h), and moments at column end (M_{end}) and mid-height (M_{CL}). In this

table, t_s is loading duration. Figure 1.28(b) shows normalized axial force-moment interaction diagrams, where the initially applied axial load, end moment, and moment at column mid-height (considering 2nd order effects) are indicated. The combination of sustained axial load and end moments induced failure in two columns (S4 and S6) within 2 months of loading. These columns were loaded to $P/P_0 = 0.38$ and had e/h ratios greater than 0.15. Additionally, the specimens continued deforming with time even if no failure occurred within 1.5 years. For the columns with $P/P_0 > 0.25$, the curvature after 1.5 years typically exceeded four times the initial curvature.

Table 1.4 Major test results of columns under sustained eccentric loading (Green and Breen, 1969)

Specimen No.	P (kips)	P/P_0	e/h	M_{end} (kip-in.)	M_{CL}/M_{end} (at $t_s = 0$)	M_{CL}/M_{end} (at $t_s = 500$ days)
S1	53	0.47	0.038	7.9	1.49	4.95
S2	27.5	0.19	0.246	27.5	1.23	1.8
S3	42.5	0.29	0.038	6.4	1.23	1.86
S4	42	0.38	0.178	30.4	1.45	3*
S5	41.5	0.38	0.106	17.2	1.45	2.88
S6	36.5	0.36	0.156	23.3	1.38	43*
S7	29	0.26	0.148	17.4	1.15	1.51
S8	30	0.26	0.269	33	1.18	2.02
S9	30	0.26	0.42	51	1.55	NA*
S10	18	0.175	0.42	30.6	1.36	1.62

*: at time of last reading prior to failure (days)

Furlong and Ferguson (1966)

As shown in Figure 1.29, a rectangular frame was symmetrically loaded to examine the sustained loading response of RC columns. The columns had a cross section 4 in. x 6 in. and a clear height of $H = 60$ in., leading to a height-to-depth ratio of $H/h = 15$. Each column was reinforced with four No. 3 bars ($\rho = 1.8\%$) with a yield strength of 50.7 ksi. The concrete compressive strength was 4800 psi. Loads were applied simultaneously to the columns and the beam, causing a single curvature in the columns. The ratio α between the forces applied to the

columns and the beams was 0.0244. The eccentricity ratio was $e/h = 0.141$. The frame was loaded to 60% of its estimated capacity at an age of 32 days. The loads were maintained for 102 days. No failure occurred. The frame was then loaded to failure in about 3 hours. The failure load was 78.5 kips. The test indicated that the ultimate strength of the frame was not altered by the previously applied sustained load.

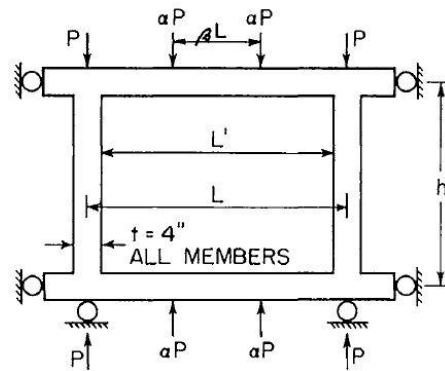


Figure 1.29 Sustained loading test of a RC frame by Furlong and Ferguson (1966).

Jenkins (2015)

Four short columns and twelve slender columns having an identical cross section were tested under sustained eccentric loading for 375 days. The four short columns had a dimension of 6.125" x 6.125" x 24" ($H/h = 3.92$) and tested using the loading frame shown in Figure 1.22. Two of them were plain concrete columns. One was loaded with an eccentricity ratio of $e/h = 0.1$ to $0.35P_0$, while another one was loaded with $e/h = 0.25$ to $0.21P_0$. The two RC short columns were loaded to $0.30P_0$ and $0.18P_0$ with eccentricity ratios of 0.10 and 0.25, respectively. The material properties, longitudinal and transverse reinforcement layout, loading age, loading duration and test setup were the same as those described in Section 1.6.4 for concentric sustained loading tests performed by Jenkins (2015). None of the short columns failed by the end of sustained loading. Figure 1.30 shows the measured concrete compressive strain at column mid-height. It was

believed that eccentricity ratio did not influence column creep rate because it is affected only by the stress at the extreme compressive fiber.

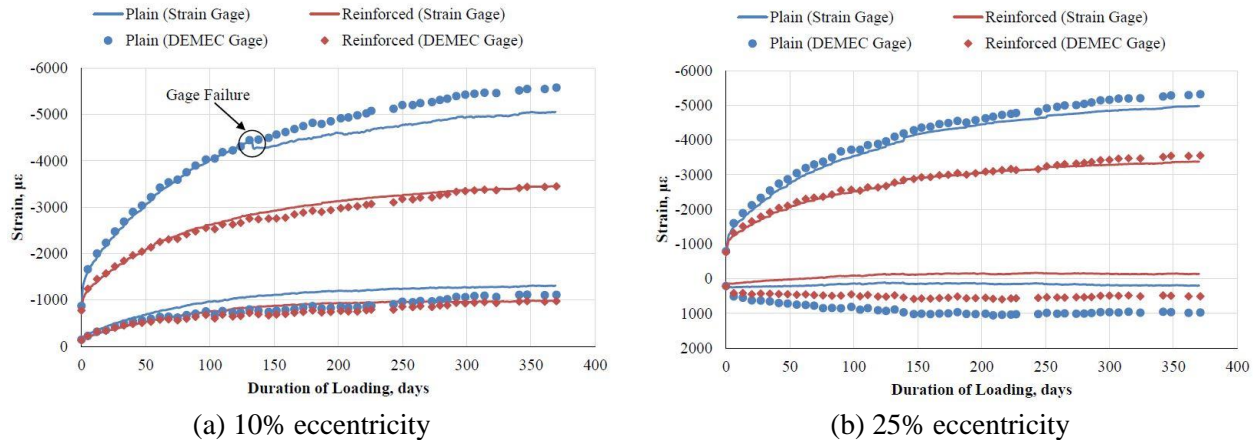


Figure 1.30 Concrete compressive strain in short columns subjected to sustained eccentric loading (Jenkins, 2015).

For the slender RC columns, six of them were 6-ft. long ($H/h = 11.8$) and six were 10.5-ft. long ($H/h = 20.6$). Reinforcement ratio, slenderness ratio, eccentricity, and axial load level were test variables. Each column was longitudinally reinforced by four No. 3 bars ($\rho = 1.2\%$) or four No. 5 bars ($\rho = 3.3\%$). The middle portion of each column was reinforced in the transverse direction by 0.25-in diameter ties at a spacing of 6 in. ($\rho_t = 0.4\%$). The steel reinforcement property was the same as that described in Section 1.6.4 for the concentric sustained loading tests conducted by Jenkins (2015).

The slender columns were tested at a concrete age of 50 days and loaded for 100 days using the test setup shown in Figure 1.31. If no failure occurred by then, the columns were subject to short-time loading until failure. Table 1.5 shows the slender column properties. Two columns, R3-40-25-LT(2) and R3-70-10-LT(2) marked by an asterisk, failed under sustained load within 100 days. Figure 1.32 shows the sustained loading responses in terms of axial force,

moment, and center deflection for the six columns reinforced by four No. 3 bars. The tests indicated that longitudinal reinforcement aided the long-term stability of the columns. None of the columns with No. 5 bars failed under sustained loading. Additionally, most columns presented a ductile failure mode, even for the columns with the lower eccentricity of $e/h = 0.10$.

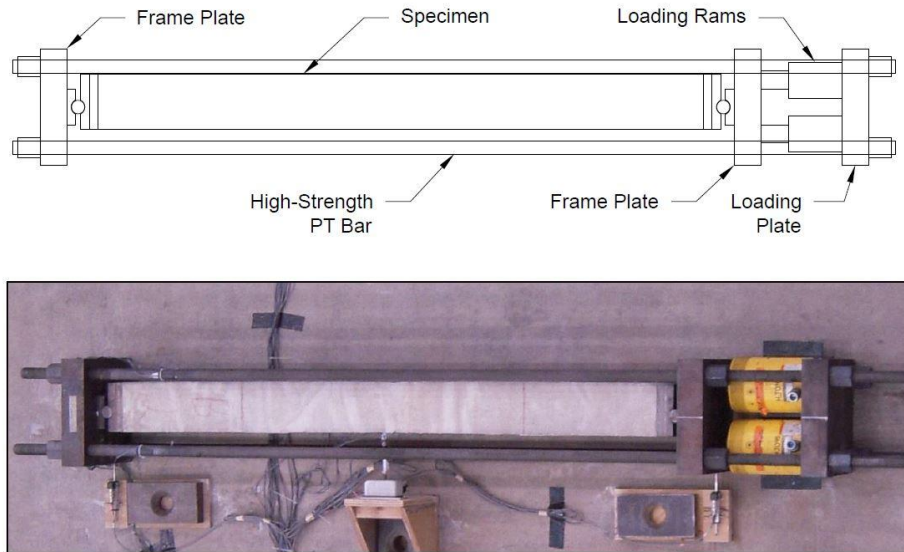


Figure 1.31 Test setup for sustained eccentric loading of slender columns (Jenkins, 2015).

Table 1.5 Properties of slender columns tested by Jenkins (2015) under sustained eccentric loading

Column ID	Reinforcement	Height-to-depth ratio, H/h	Eccentricity ratio, e/h	Sustained load, P/P_0	f'_c at initial loading
R3-40-10-LT	4 No. 3	11.75	10%	36.5%	6630
R3-40-25-LT(1)			32%	6630	
R3-40-25-LT(2)*		25%	31%	5710	
R3-70-10-LT(1)		20.6	10%	27.4%	6630
R3-70-10-LT(2)*			31%	5710	
R3-70-25-LT			25%	13.7%	6630
R5-40-10-LT	10%		36.5%	5710	
R5-40-25-LT(1)	4 No. 5	11.75	25%	32%	5710
R5-40-25-LT(2)			34.5%	5930	
R5-70-10-LT(1)		20.6	10%	27.4%	5710
R5-70-10-LT(2)			30%	5800	
R5-70-25-LT			25%	13.7%	5710

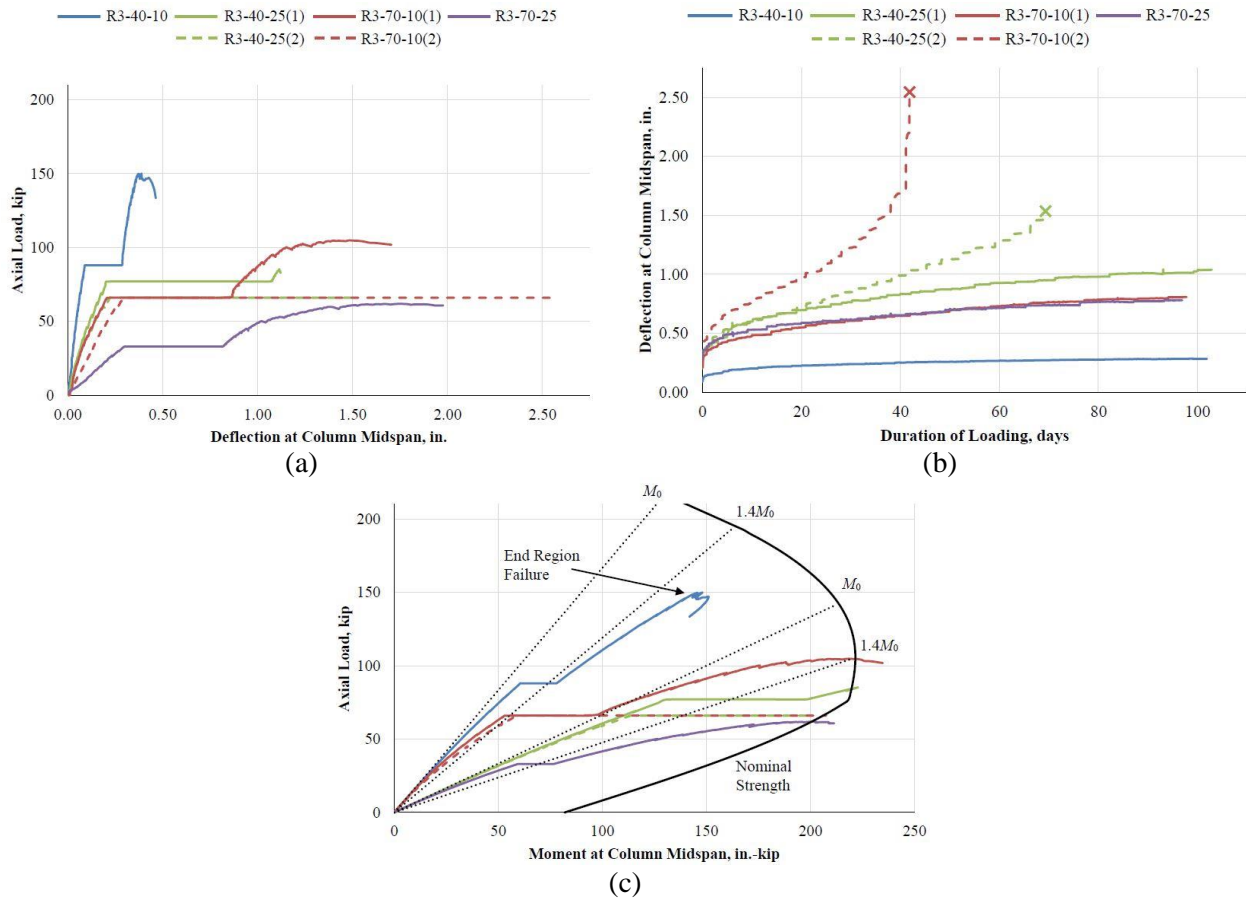


Figure 1.32 Sustained eccentric loading response of slender columns tested by Jenkins (2015): (a) axial load vs. center deflection, (b) center deflection time history, and (c) axial force vs. moment.

1.7 Research Tasks

The present research follows the six stages shown in Figure 1.33. In the first stage, relevant papers related to concrete creep, creep model, and columns under sustained concentric and eccentric loads were reviewed. The second stage focused on experimental design. This stage mainly includes three steps: (1) prototype structure design, (2) specimen design based on the prototype structure design, (3) and test setup design for both concentric and eccentric loading tests. The specimens and test setup were then fabricated in Stage 3. In stage 4, eight concentric axial loading short column experiments and five eccentrically loaded longer columns were tested.

The test results were analyzed and interpreted in Stage 5. In stage 6, a nonlinear creep model was examined based on the experimental results of short column tests obtained in Stage 5 are compared with the creep predicted in Stage 6.

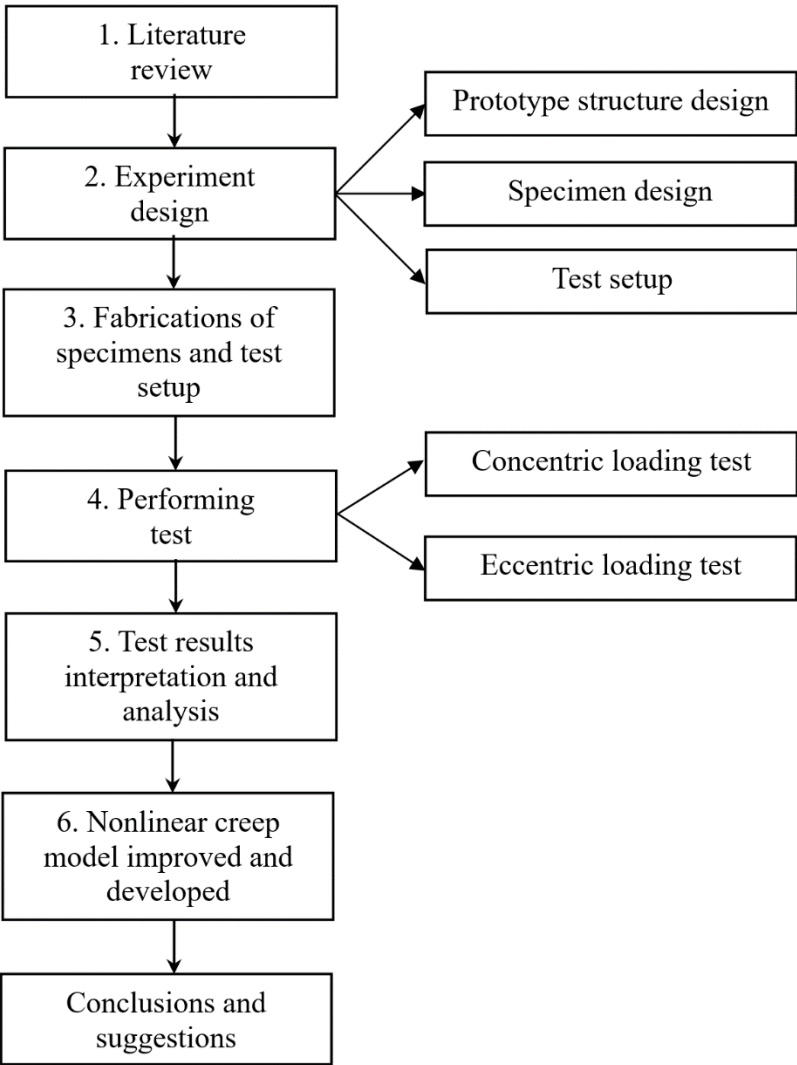


Figure 1.33 Research procedure.

CHAPTER 2

PROTOTYPE STRUCTURE DESIGN AND ANALYSES

2.1 Prototype Building Design

2.1.1 Objectives

A four-story building, shown in Figure 2.1, was designed following ASCE 7-16 (2016) and ACI 318-19 (2019). The building, assumed with office occupancy, was located in a non-seismic region and gravity loads governed structural design. It had five bays in each direction with a 28 ft center-to-center span length. The story height was 14 ft at the first floor and 12 ft at all other floors.

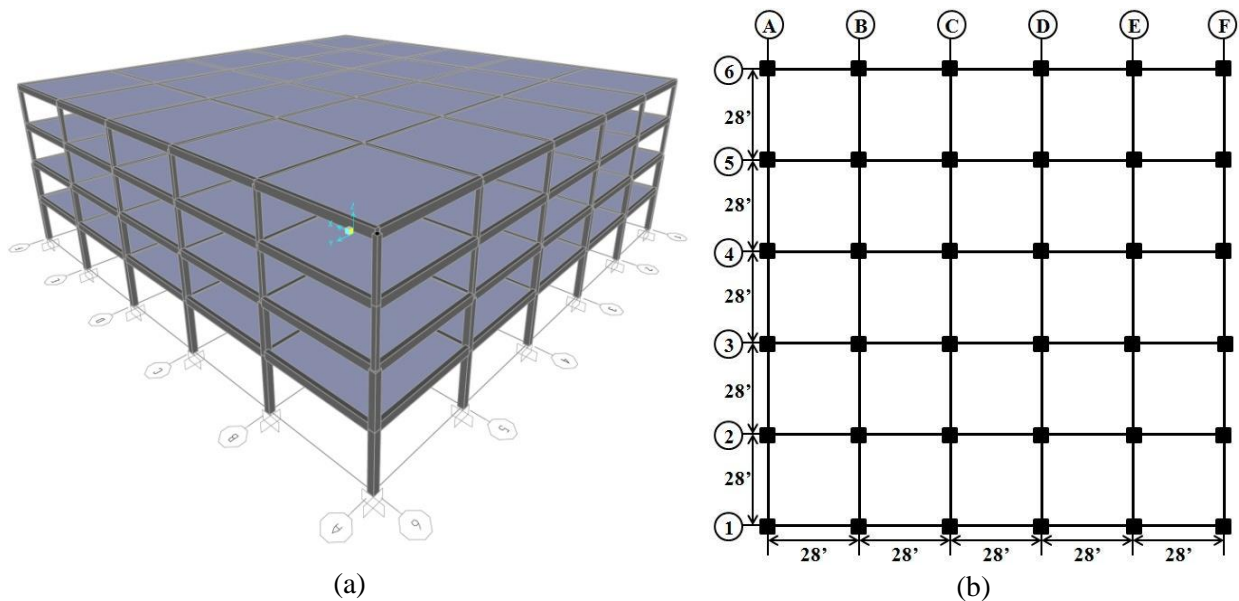


Figure 2.1 Prototype RC frame building: (a) 3D view and (b) floor plan.

The structural system of this building was cast in place two-way slabs with beams spanning between supports on all sides. It was assumed that moment can be fully transferred between the slabs and the beams. The purposes of designing this prototype structure were to: (1)

Determine the dimension and the distribution of longitudinal and transverse reinforcement of RC column specimens to be tested in the experiments described in Chapters 3, 4, and 5. The dimension of the column specimens was reduced proportionally using a scale factor of 0.5 in both structural level and material level (concrete aggregate size was reduced with the same scale) according to the prototype structure. (2) Determine the load eccentricity ratio (e/h) for the eccentrically loaded column specimens based on the simulation results of the whole prototype structure after one interior column loses load-bearing capacity, as described in Section 2.4.

2.1.2 Elastic Analysis of Prototype Structure

For design purpose, elastic analyses of the prototype structure were performed using software SAP2000 (2014). The design was governed by a vertical load combination of 1.2 x dead load + 1.6 x live load based on IBC (2018). The dead load included a 112.5 psf self-weight of 9-in. thick RC slab for all floors and a superimposed dead load of 17 psf for the roof and 20 psf for the floor. The superimposed dead loads accounted for partition walls, floor finishes, tiles, water proofing, cable wires, plumbing pipes, etc. The live loads were 20 psf for the roof and 50 psf for the floor according to ASCE 7-16 (2016). All members were assumed to be constructed with Grade 60 steel reinforcement and concrete with a cylinder compressive strength 5500 psi. The maximum size of concrete aggregate was assumed to be 0.75 in. The load combinations considered dead load plus different kinds of live load patterns. The internal force (moment, shear force, and axial force) envelopes were determined from the elastic analyses, as shown in Figures 2.2. Moment existed in the concrete slab with respect to both x- and y- directions because of the fixed connections between the slabs and beams. Because the structure was symmetric, the moment intensity distribution was symmetric as well. Therefore, only the envelope of slab

bending moment intensity in x-axis is shown in Figure 2.3.

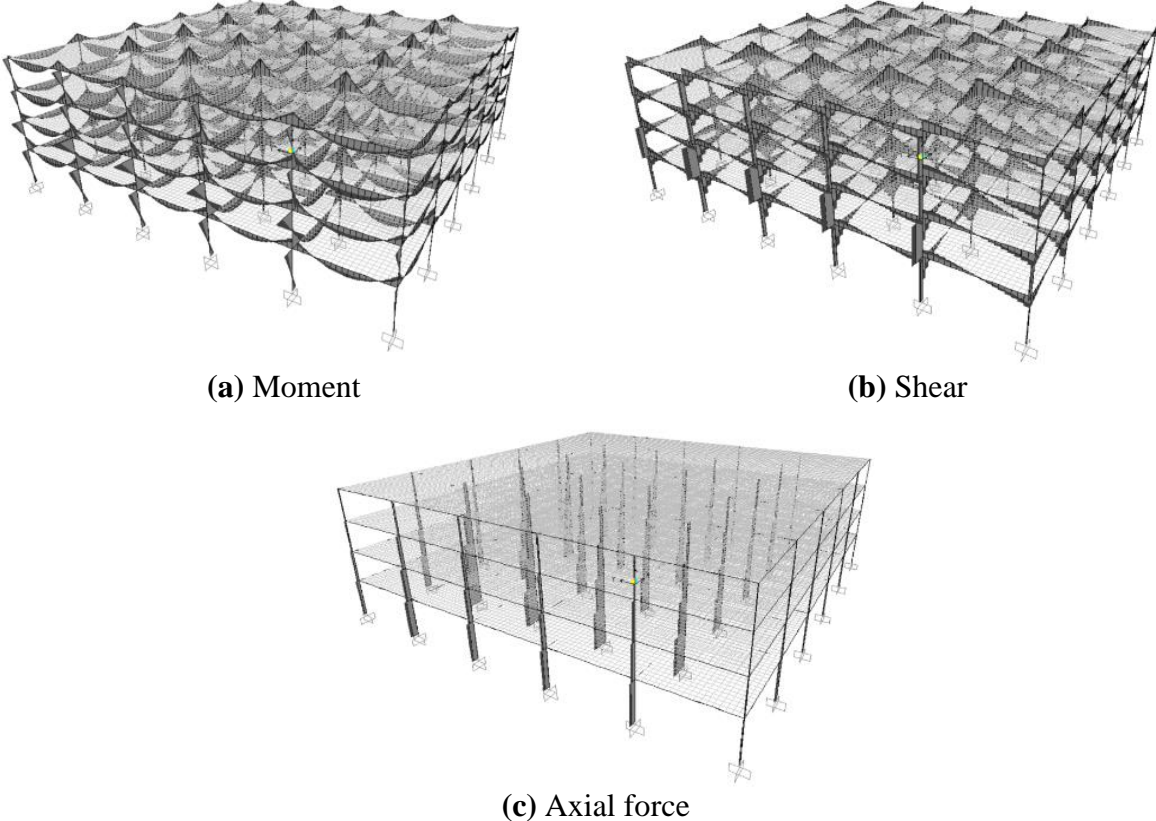


Figure 2.2 Internal force envelopes of the prototype structure.

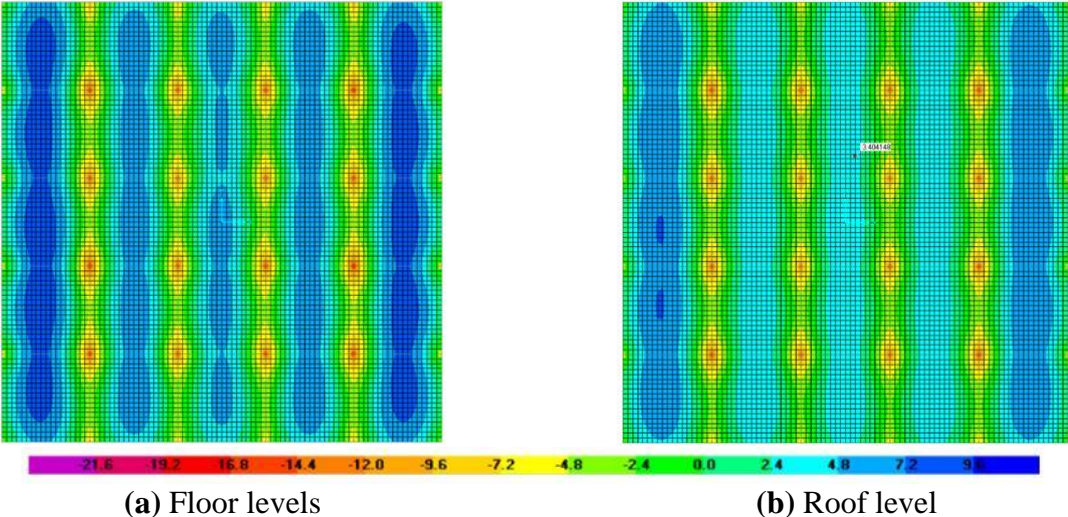


Figure 2.3 Slab moment intensity distribution about x-axis (units: kip-in/in).

2.1.3 Structural Design Results

2.1.3.1 Beam Design

The governing positive and negative moments for the interior floor beams were 1187 kip-in and 2396 kip-in, respectively. The maximum shear appeared in the interior beam was 45.2 kips. For simplicity, all the interior floor beams were designed with the same dimension and steel reinforcement layout. The beam design based on the highest moment and shear demands in the floor level is shown in Figure 2.4. The concrete cover of the beam cross section was 1.5 in. for all sides. No.3 ties with a diameter of 0.375 in. were chosen. The spacing of ties was 20 in. in the middle portion of the beams (within a length of 24 ft). At both ends of a beam within a length of 15 in., the spacing of ties was changed to 7.5 in. The interior beam design based on the maximum moment and maximum shear in the floor levels is shown in Figure 2.4.

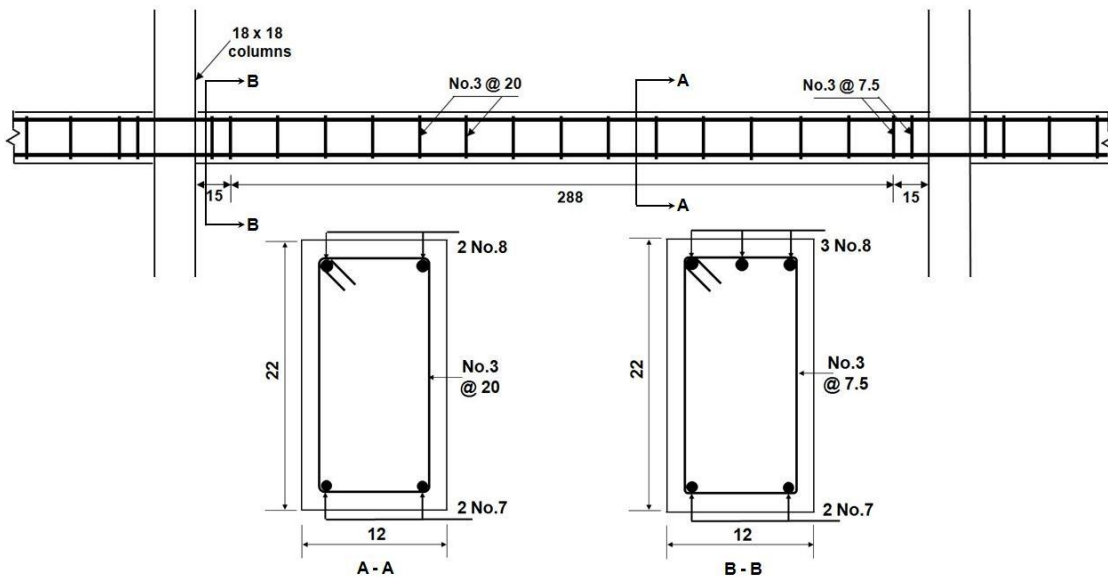


Figure 2.4 Interior floor beam design (unit of dimension: in.).

Because both the dead and live loads applied on the roof were lower than those at the floor levels, the interior beam design for the roof was adjusted and is shown in Figure 2.5. The

maximum positive and negative moments for the roof beams were 850 kip-in and 1903 kip-in. The maximum shear existed in the roof beams was 29.1 kips. For simplicity, all the interior roof beams were designed with the same dimension as that of the floor beams. Both the longitudinal and shear reinforcement layout were slightly modified based on the moment and shear envelopes of the roof beams and their clear span length.

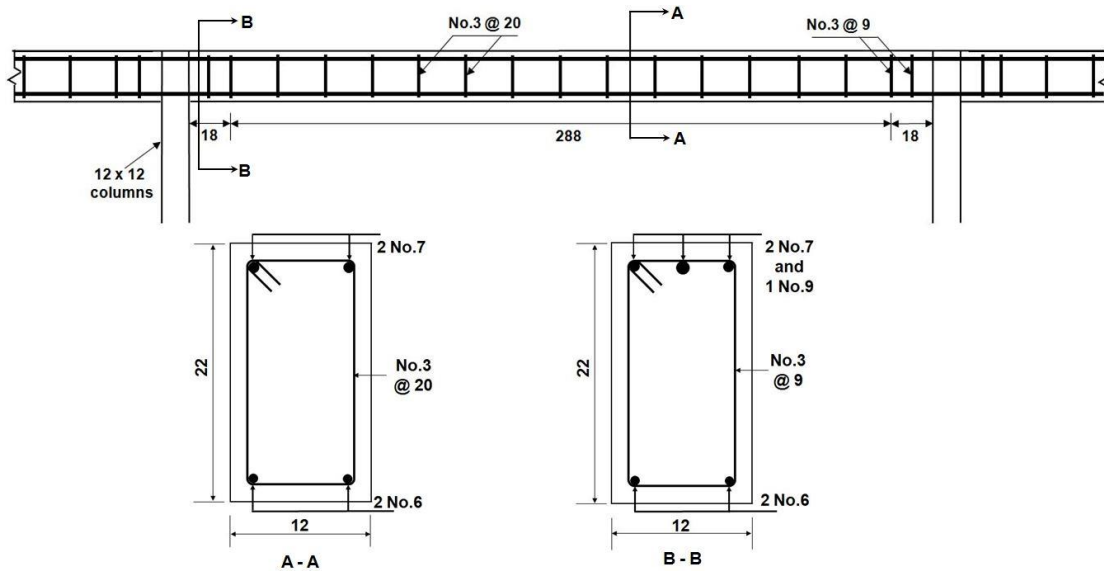


Figure 2.5 Roof beam design (unit of dimension: in.).

2.1.3.2 Column Design

Two column sizes were used in the prototype structure. The columns at the top and third floors were 12 in. square, whereas those at the 1st and 2nd floors were 18 in. square. Based on the elastic analysis, the maximum shear force (V_u) in the 1st and 2nd interior floor columns was 12 kips, appearing at the exterior column of the top floor in Frame 3. For the columns at the first and second floors, the maximum shear force was 28.5 kips, appearing at the exterior column in the second floor. According to ACI 318-19 (2019) for RC columns subjected to both axial load and shear force, the nominal shear strength (V_n) provided by concrete was 10.5 kips for the

columns in the top and 3rd floors, and 28.1 kips for the columns in the 1st and 2nd floors. The nominal shear strength provided by concrete were close to the maximum shear force existing in the prototype structure. Therefore, the maximum shear reinforcement spacing permitted by ACI 318-19 (2019) was chosen. For the roof and 3rd floor columns, No.3 ties with 12 in. spacing were used. For the 1st and 2nd floor columns, No.3 ties with 16 in. spacing were used. The axial load and moment envelopes for the columns of Frame 3 are shown in Figures 2.6 and 2.7, respectively. For the columns at the roof and 3rd floor, the column with maximum axial load was appeared at 3B on the 3rd floor. The maximum axial load was 359 kips, and the maximum moment for this column was 95.7 kip-in. Column 3A on the 3rd floor had the maximum moment of 182 kip-in, the axial load for this column was 286 kips.

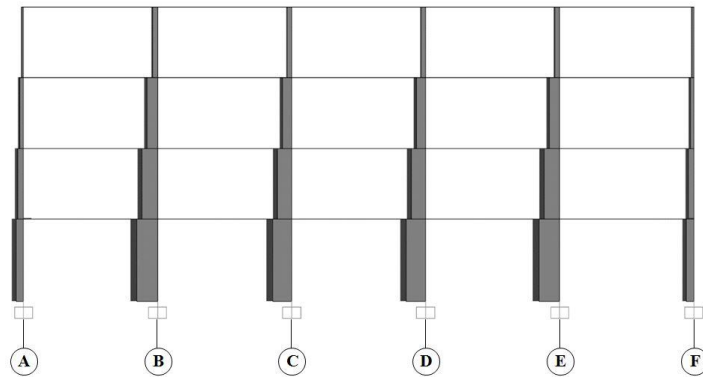


Figure 2.6 Axial force envelope of Frame 3.

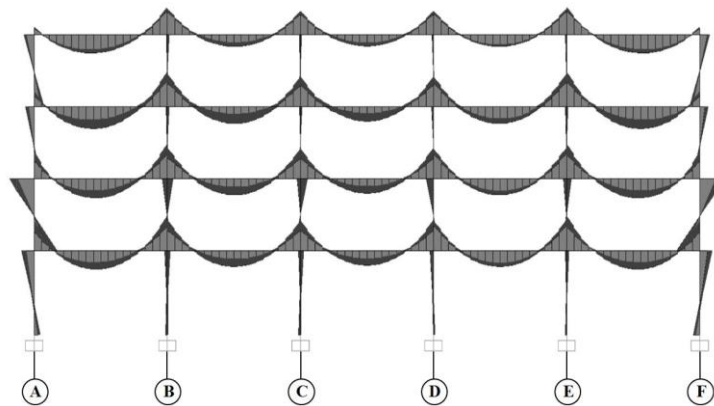


Figure 2.7 Moment envelope of Frame 3.

For the 1st and the 2nd floor, the column with maximum axial load was located at 3B on the first floor. The maximum axial load was 751 kips, and the moment for this column was 120 kip-in. The column with maximum moment was located at 3A on the 2nd floor. The maximum moment was 612 kip-in, and the axial force for this column was 440 kips. Based on the elastic analysis results, the columns at the 3rd and roof floor were designed with 4 No.6 bars with a reinforcement ratio of $\rho = 1.22\%$. The columns at the 1st and 2nd floor were designed with 4 No.8 bars with $\rho = 0.98\%$, as shown in Figure 2.8.

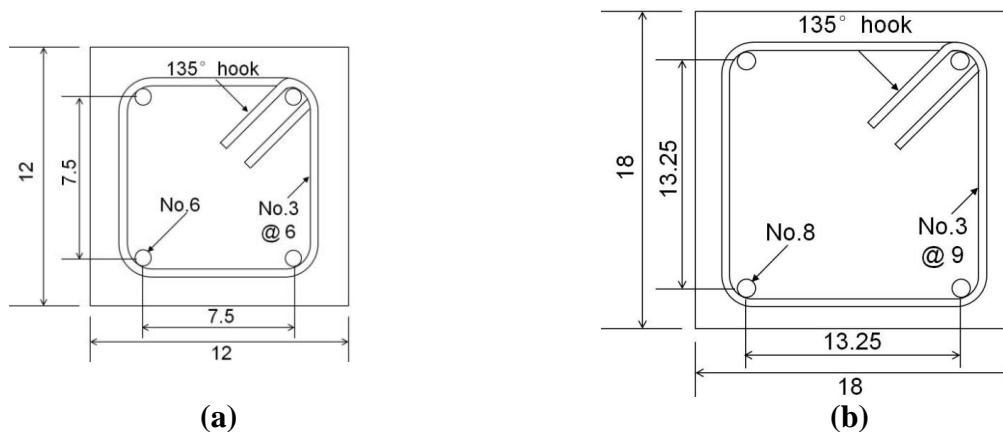


Figure 2.8 Column cross section: (a) top and 3rd floor and (b) 1st and 2nd floor (unit of dimension: in.).

2.1.3.3 Slab Design

Based on ACI 318-19 (2019), the minimum thickness of non-prestressed two-way slabs with beams spanning between supports on all sides in this prototype structure was 8.91 in; thus, a 9-in. slab thickness was considered. The thickness of slab concrete cover was chosen as 0.75 in. The slab was divided into a 7-ft wide column strip and a 14-ft wide middle strip. ACI 318-19 (2019) specifies the minimum reinforcement for concrete slab as $A_{s,min} = 0.0018A_g$, where A_g is gross area of concrete slab section. The equivalent steel reinforcement distribution is 0.194 in²/ft (No.4 @ 12 in). The slab reinforcement design was performed for an interior slab panel shown in

the shade region in Figure 2.9. The maximum positive moment intensity of this slab was $M_{\max+} = 7.07$ kip-in/in for the roof and $M_{\max+} = 8.78$ kip-in/in for the floors. The maximum negative moment intensity was $M_{\max-} = 8.06$ kip-in/in for the roof and $M_{\max-} = 9.26$ kip-in/in for the floors. For simplicity, all the interior slab panels in the prototype structure were designed with the same reinforcement distribution. Reinforcement using No.5 @ 12 in. was designed for the whole slab. The curtailment of slab reinforcing bars shown in Figure 2.9 was determined based on the detailing rules specified by ACI 318-19 (2019).

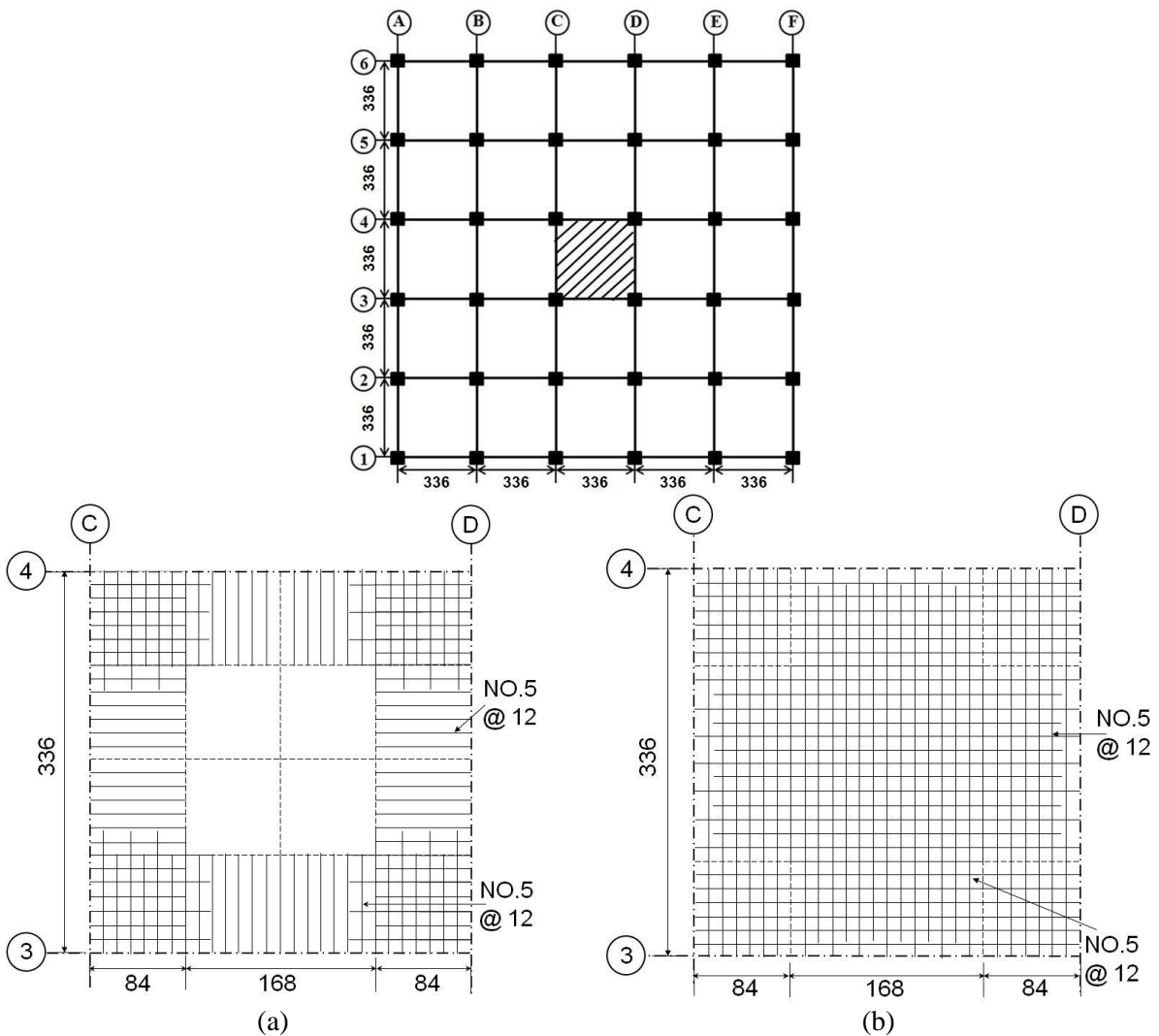


Figure 2.9 Reinforcement distribution of slab: (a) top reinforcement and (b) bottom reinforcement. (unit of dimension: in.).

2.2 Nonlinear Analysis of Prototype Structure

The Alternate Load Path Method recommended by the DoD guideline (2009) was an easy method to estimate the redundancy of a structure. For buildings classified in Occupancy Category II, the DoD guideline (2009) specifies several load-bearing elements to be removed when using this method, including the removals of (1) an interior column (Column C3 in Figure 2.1 (b)), (2) an exterior column (Column C1 in Figure 2.1(b)), and (3) a corner column (Column A1 in Figure 2.1(b)) at the first story. This study investigates the internal force redistribution of the prototype structure after the interior Column C3 was removed at the first level. The load conditions and boundary conditions were the same as the elastic analysis of the prototype structure: (1) the dead loads were applied on all spans and slab panels of the whole structure, (2) live load patterns were considered, and (3) all supports and all connections between structural members were fixed.

2.2.1 Analysis Procedure

To simulate the effects of removing a column, the analyses were conducted using an equivalent approach shown in Figure 2.10. All the load applied to the prototype structure were unchanged. The interior column was deleted from the original model, and the previous determined column axial load was applied as reaction forces in the opposite direction at the location of the removed column, as shown in the middle part of Figure 2.10. In this way, the structure without this column had load conditions identical to that in the original prototype structure. Finally, the loss of Column C3 was modeled by applying column end forces to cancel the axial load of Column C3, as shown in the bottom part of Figure 2.10.

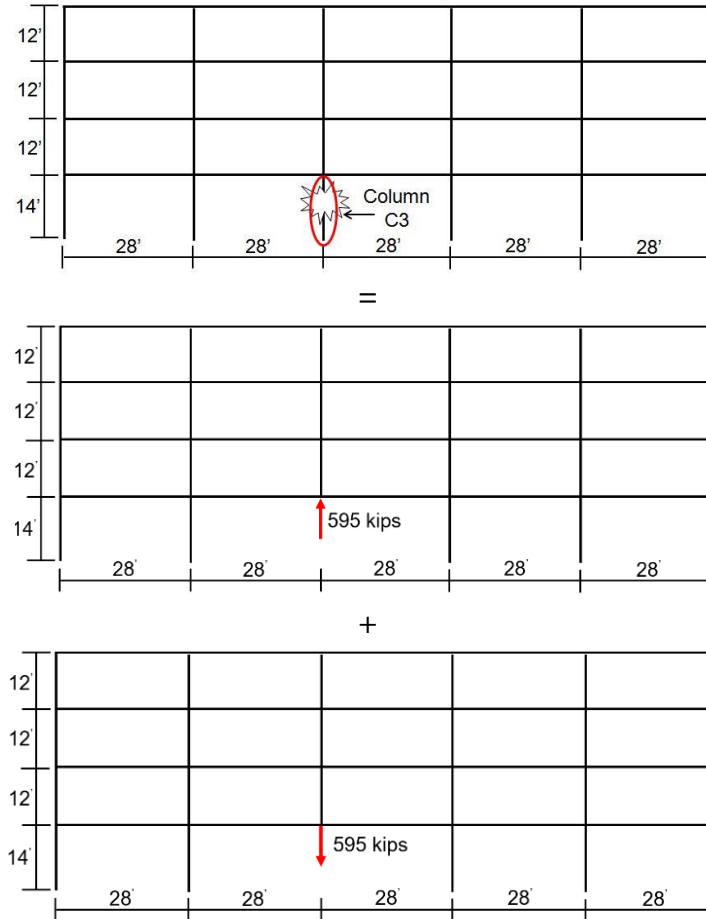


Figure 2.10 Analysis procedure (unit of dimension: ft).

2.2.2 Element Type and Material Property

After removing Column C3, the beams connected to the removed column and the slab panels around the removed column behave inelastically. For nonlinear analysis of the structure with RC floor slabs, ABAQUS (2014) was chosen as a modeling platform. Due to the high computational cost of system-level nonlinear analysis of the whole structure, solid elements are excluded in this study. The slabs were modeled using shell elements. Both the beams and columns were modeled using beam elements to reduce the cost of analyses.

Concrete short-time strength was assumed to be $f'_c = 5500$ psi, and the elastic modulus of concrete was 4030 ksi. Concrete Poisson's ratio was assumed to be equal to 0.2. The concrete

damaged plasticity parameters were defined, as shown in Table 2.1. Figure 2.11 shows the assumed stress-strain curve of concrete under uniaxial loading. The strain went up to around 0.00244 when the maximum stress was reached, then decrease linearly to 0.00324. The tensile strength of concrete ($f_t = 110$ psi) was assumed to be 2% of concrete compressive strength.

Table 2.1 Concrete Damage Plasticity parameters

Dilation Angle	Eccentricity	f_{b0}/f_{c0}	K	Viscosity Parameter
30	0.1	1.16	0.667	0

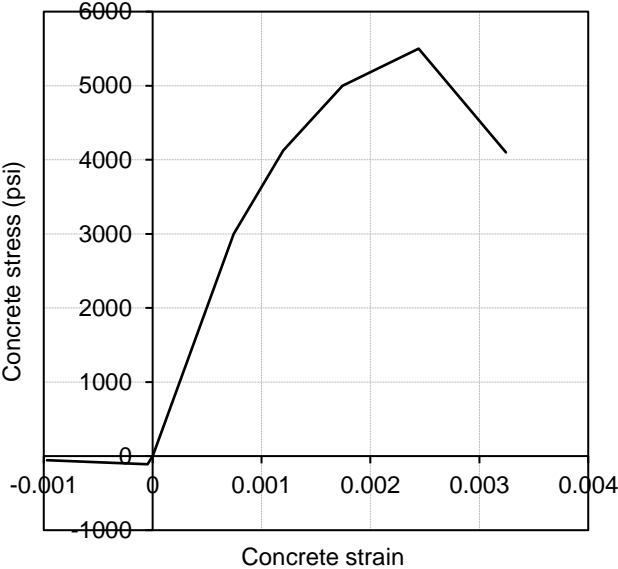


Figure 2.11 Stress-strain relationship of concrete ($f'_c = 5500$ psi).

Grade 60 steel reinforcement was used in finite element analysis. The elastic modulus of steel reinforcement was 29000 ksi, and steel Poisson's ratio was assumed to equal 0.3. Figure 2.12 shows the assumed bilinear stress-strain relationship of steel reinforcement (Grade 60). The strain hardening begins at about 0.00207, and the ultimate strain reaches to 0.122. The strain hardening ratio for Grade 60 reinforcement was assumed to be equal to 0.86%.

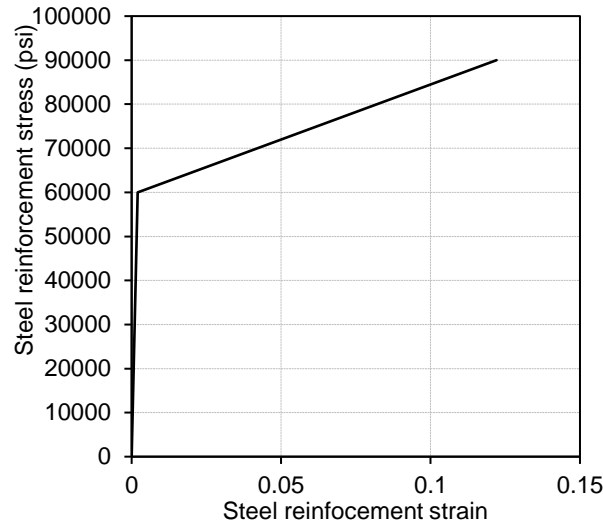


Figure 2.12 Stress-strain relationship of steel reinforcement ($f_y = 60000$ psi).

For all the columns, the concrete material was assumed to be elastic because, following the removal of Column C3, the remaining columns are unlikely to yield. For the slabs in the prototype structure, the material property of concrete and steel reinforcement were defined based on the stress-strain relationship shown in Figures 2.11 and 2.12. Because the concrete property can only be defined by the stress-strain relationship in ABAQUS, the material properties for the interior beams were modeled with an equivalent method. The method was based on the calculated curvature and moment from the beam cross-section, as shown in Figures 2.4 and 2.5. The cracking moment (M_{cr}), yield moment (M_y), and ultimate moment (M_u) were calculated by a trilinear moment-curvature relationship based on the conventional approach for RC beams recommended by Park and Paulay (1975). The cracking strain (ϵ_{cr}), yield strain (ϵ_y), and ultimate strain (ϵ_u) were then calculated by the cracking curvature ϕ_{cr} , yield curvature ϕ_y , and ultimate curvature ϕ_u . The equivalent stresses were assumed to be proportional to the calculated cracking moment (M_{cr}), yield moment (M_y), ultimate moment (M_u). The interior beam stress-strain relationship defined in the finite element model were summarized in Tables 2.2 and 2.3.

Table 2.2 Calculated equivalent stress-strain relationship for roof beams

	Roof (+) M (kip- in)	Equivalent Stress (psi)	Equivalent strain	Roof (-) M (kip- in)	Equivalent Stress (psi)	Equivalent Strain
Cracking moment	538	556	0.000132	538	556	0.000132
Yield moment	973	1005	0.000485	2349	2427	0.000835
Ultimate moment	1002	1035	0.003000	2435	2516	0.003000

Table 2.3 Calculated equivalent stress-strain relationship for floor beams

	Floor (+) M (kip- in)	Equivalent Stress (psi)	Equivalent Strain	Floor (-) M (kip- in)	Equivalent Stress (psi)	Equivalent Stress (psi)
Cracking moment	538	556	0.000132	538	556	0.000132
Yield moment	1184	1223	0.000568	2720	2810	0.000905
Ultimate moment	1193	1232	0.003000	2822	2915	0.003000

2.2.3 Analysis Results of the Intact Prototype Structure Without Column Loss

After the material properties of all structural members were determined, the finite element (FE) analysis of the whole prototype building was performed to determine the axial load in the supporting Column C3. The material properties of beams were assigned, as shown in Figure 2.13. The red parts indicate that the stress-strain curve of beams was equivalently defined based on the calculated flexural response of beams under negative moment. The blue parts indicate the stress-strain curve of beams was equivalently defined based on the flexural response of beams under positive moment. The slab reinforcement distribution was assigned in rebar layers in the modeling in the same way as the steel reinforcement layout shown in Figure 2.9. The axial load of the prototype structure determined from the analysis is shown in Figure 2.13. Based on the analysis result, the axial load of the Column C3 at the first floor before its removal was 595 kips.

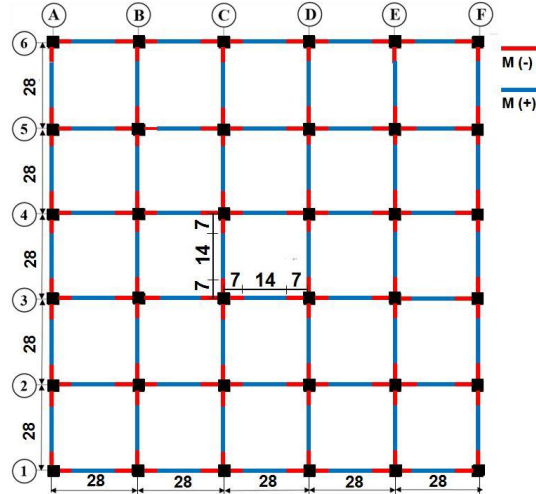


Figure 2.13 Beam material property assignment (unit of dimension: ft).

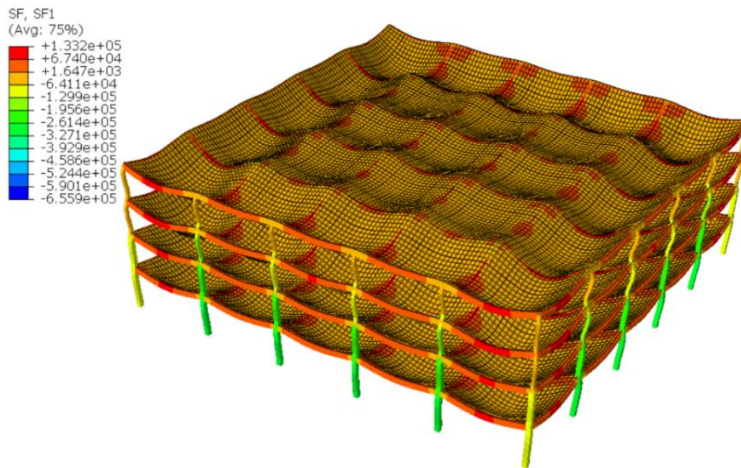


Figure 2.14 Axial force in prototype structure without column loss (unit: lb).

2.3 Nonlinear Analysis of Prototype Structure with an Interior Column Loss

After Column C3 at the first floor was removed, loads on the prototype structure were redistributed. The behavior of beams connected to the removed column and the slab panels around the removed column entered inelastic stage. The material property assigned to the beams connected to the removed column is shown in Figure 2.15. The definition of red and blue parts in Figure 2.15 was the same as in Figure 2.13. The material property of all other members was defined the same as in Section 2.4.3. Then, the analysis of the prototype structure following the

removal of Column C3 at the first floor was performed. Figure 2.16 shows the axial load diagrams of the prototype structure with the loss of Column C3.

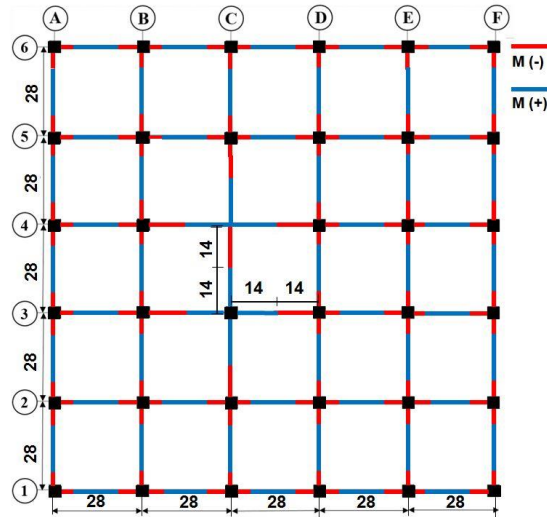


Figure 2.15 Beam material property assignment after column loss (unit of dimension: ft).

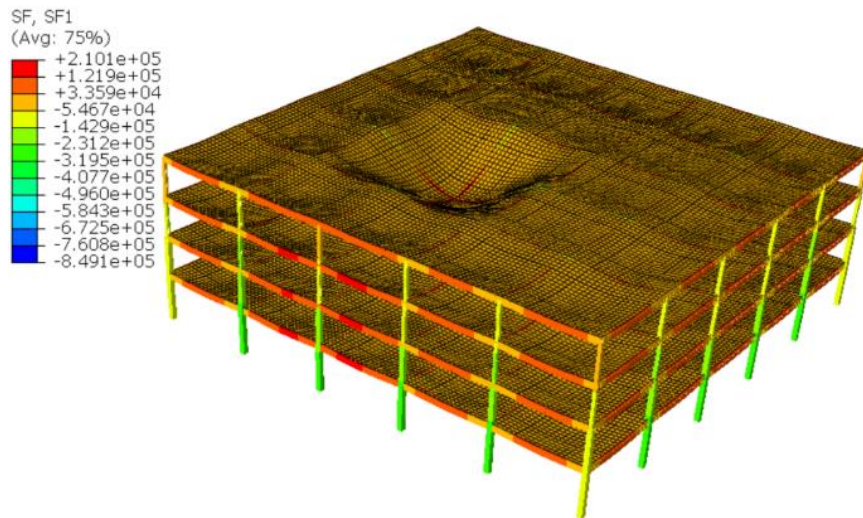


Figure 2.16 Axial load in prototype structure after the loss of Column C3 (unit: lb).

According to the analysis result shown in Figure 2.16, the maximum moment of columns appeared at the top end of Column D3 in the top floor, as shown in Figure 2.17. The maximum moment of Column D3 was 957.9 kip-in., and the corresponding axial load was 186.1 kips,

leading to an eccentricity of $e = 5.14$ in. and an eccentricity ratio of $e/h = 0.428$. For the top floor Column B3 situated on the left side of the removed column, the maximum moment and axial load were 762 kip-in and 193.7 kips, respectively; the corresponding eccentricity was $e = 3.93$ in., and the eccentricity ratio was $e/h = 0.328$. The column specimens described in Chapter 5 were eccentrically loaded with a single curvature, and the height to depth ratio for these specimens was $H/h = 10.8$. However, the height to depth ratios of Column B3 and Column D3 in the single curvature portion (between the top end and zero moment section) were 8.7 and 8.6 for Columns B3 and D3, respectively. Based on the column eccentricity ratio determined from the prototype structure and the column length-to-depth ratio in single curvature, the largest eccentricity ratio employed in the experiments was chosen as 0.25.

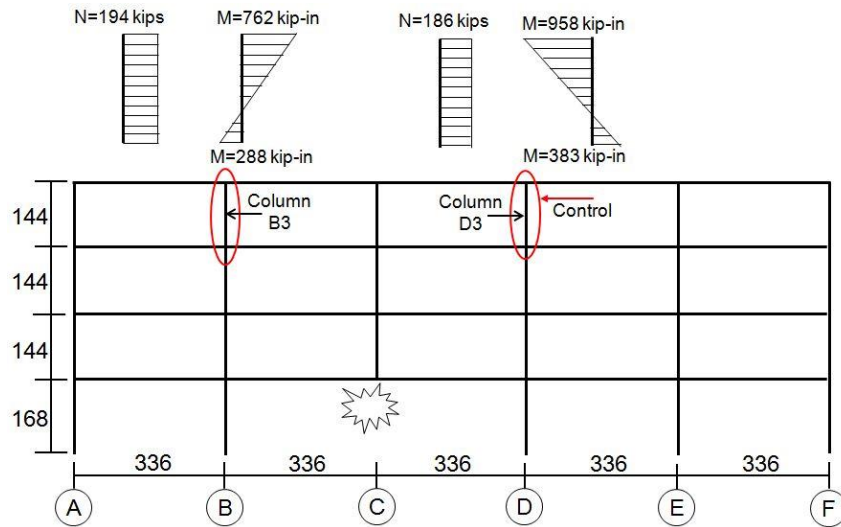


Figure 2.17 Moment and axial load of top floor columns next to Column C3 (unit of dimension: in.).

CHAPTER 3

EXPERIMENTAL PROGRAM

3.1 Introduction

The experimental program was designed to investigate the behavior of columns made of normal strength concrete and under high sustained stresses. As stated previously in Chapter 1, the major objectives of the experiments were to: (1) characterize the behavior of RC columns under different levels of high sustained concentric loading, (2) characterize the behavior of RC columns under different levels of high sustained eccentric loading, and (3) identify the effects of confinement on concrete creep and sustained loading response of RC columns.

A total of 13 column specimens were tested. For concentric loading, the experiments were conducted on 3 plain concrete and 5 RC square short columns with a length-to-width ratio of $H/h = 3.6$. For eccentric loading, the experiments were carried out on 5 slender ($H/h = 10.8$) RC columns. This chapter describes the test matrix, setup, loading approach, and instrumentation.

3.2 Test Matrix

3.2.1 Test Variables and Matrix for Concentric Loading

Sustained load level and transverse reinforcement ratio were the two major test variables. Two load levels (about 76% and 98% of column short-time loading capacity) and two transverse reinforcement ratios ($\rho_t = 0.26\%$ and 0.78%) were considered. According to the literature described in Chapter 1, nonlinear creep, the focus of this study, presents when the sustained compressive stress in concrete exceeds 60% of its short-time strength. The 76%- and 98%- levels of sustained loading were used to obtain test data needed for examining an existing nonlinear

concrete model suggested by Tasevski et al. (2019). The 98%-level loading was also used to detect the possible failure of RC columns under high sustained long-term loads. Even if maximum tie spacing for the test specimens per ACI 318-19 (2019) was 6 in., the ACI spacing requirement is not based on the need of maintaining column long-term loading capacity.

Eight short square columns, with a length-to-width ratio of $H/h = 3.6$ (H is column height and h is cross section size), were constructed and tested under sustained concentric loading in the Structural Engineering Laboratory at the University of Nevada, Las Vegas. The specimens included 3 plain concrete columns, which provided the information about fundamental material behavior under high sustained stresses needed to interpret the test results of reinforced concrete columns. Table 3.1 shows a test matrix. In the specimen designations, P and RC stand for plain concrete and reinforced concrete, respectively. The following number (e.g. 77) represents the percentage sustained load ratio α to indicate the level of sustained load. For the plain concrete columns, α is defined as the ratio of average sustained load N_{sus} to the short-time axial loading capacity determined based on the test result of Specimen PS; for the RC columns under concentric loading, α is the ratio of N_{sus} to the nominal axial strength defined by ACI 318 (2019). The letters A and B following the number denote specimens with transverse reinforcement at a spacing of 6 and 2 in., respectively. Specimens PS and CS, serving as control specimens, were subjected to short-time loading to failure without experiencing sustained loads. Table 3.1 provides the loading condition, reinforcing pattern, age at loading (days), duration of sustained load t_d (days), and concrete cylinder compressive strength measured at the beginning and end of each test. The concrete cylinder compressive strength was determined by testing at least three cylinders at different concrete ages. f_c' was constant between 219 and 318 days and then slightly decreased by 7.9% after 474 days of concrete casting.

Table 3.1 Testing matrix of columns under concentric loading

Specimen	Loading condition	Column property	Age at loading (days)	Duration of sustained load t_d (days)	f'_c (psi) at t_0	f'_c (psi) at $t_0 + t_d$
PS	short-time	Plain concrete	209	—	4316	4316
P77	sustained	Plain concrete	238	22	4316	4316
P90	sustained	Plain concrete	317	22	4316	4198
C76A	sustained	trans. reinf. @ 6 in.	268	47	4316	4316
C76B	sustained	trans. reinf. @ 2 in.	268	47	4316	4316
C98A	sustained	trans. reinf. @ 6 in.	348	120	4198	3974
C98B	sustained	trans. reinf. @ 2 in.	354	120	4198	3974
CS	short-time	trans. reinf. @ 6 in.	478	—	3978	3978

3.2.2 Test Variables and Matrix for Eccentric Loading

Five longer RC columns with a length-to-width ratio of $H/h = 10.8$ were tested under eccentric sustained loading. The sustained load level, eccentricity, and transverse reinforcement ratio were the test variables. These specimens had a cross section size and longitudinal reinforcement layout identical to those of the eight short columns tested under concentric loading. As shown in Table 3.2, the specimens included four RC columns with a lower transverse reinforcement ratio of $\rho_t = 0.26\%$ and one RC column with a higher transverse reinforcement ratio of $\rho_t = 0.78\%$. Three of the specimens were loaded with an eccentricity of $e = 1$ in., resulting in an eccentricity ratio of $e/h = 0.17$; the remaining two columns were loaded with an eccentricity of $e = 1.5$ in. ($e/h = 0.25$). In the specimen designations, E stands for eccentric loading. The subsequent number (e.g. 98) represents the percentage ratio of column mid-height moment at the end of initial short-time loading to the unfactored nominal short-time moment capacity, $M_{u,ACI}$, defined after considering axial force-moment interaction based on the ACI 318-19 (2019). The letters A and B following the number denote specimens with transverse reinforcement at a spacing of 6 and 2 in., respectively. The last number (e.g. 17) represents the percentage eccentricity ratio. Table 3.2 provides the eccentricity, reinforcing pattern, age at

loading (days), duration of sustained load t_d (days), and concrete cylinder compressive strength measured at the beginning and end of each test. Beyond $t = 468$ days, the average cylinder strength varied in a narrow range; thus, f'_c was considered as constant until $t = 657$ days when the last column test was finished.

Table 3.2 Testing matrix of columns under eccentric loading

Specimen	Eccentricity	Transverse Reinforcement	Age at loading (days)	Duration of sustained load t_d (days)	f'_c (psi) at t_0	f'_c (psi) at end of loading
E98A17	1 in.	trans. reinf. @ 6 in.	547	22	3978	3978
E99A17	1 in.	trans. reinf. @ 6 in.	604	3	3978	3978
E100B17	1 in.	trans. reinf. @ 2 in.	603	11	3978	3978
E77A25	1.5 in.	trans. reinf. @ 6 in.	628	28	3978	3978
E92A25	1.5 in.	trans. reinf. @ 6 in.	629	11/17	3978	3978

3.3 Specimen Geometry and Reinforcing Details

Large-scale structural tests are preferred due to the possible size effect: concrete creep may increase with the decrease of specimen size expressed as a volume/surface (V/S) ratio (Bažant, 1975). Large-scale experiments also reduce the impact of geometric imperfectness in either specimen dimension or loading position. However, large-scale tests are difficult to perform, especially when a high sustain stress in columns needs to be maintained. Thus, the specimens were constructed at a 1/2-scale in this study, which still required maintaining a sustained load of nearly 150 kips over 120 days in some tests. The test scale was identical to that considered by Jenkins (2015) at Purdue University but greater than that by Viest et al. (1956) and Green and Breen (1969).

The columns in the top floor of a building contain less longitudinal reinforcement than the lower floors and thus more vulnerable to excessive creep deformation and failure induced by high sustained loads. For this reason, the top floor columns were experimentally simulated. As

described in Chapter 2, the cross section of top floor columns in the prototype building was 12 in. square. Based on the chosen scale factor, the cross section of the test specimens was 6 in. square. The length of the short columns under concentric loading was chosen as 21 in. After measuring the size of formwork (described later), the actual cross section size was 5.91 in. (150 mm) square and the length was 21.26 in. (540 mm). The length of the slender columns subjected to sustained eccentric loading was chosen as 64 in., which was based on the considered scale factor, the column length of 12 ft. at the top floor of the prototype building, and the actual formwork size.

All the short and longer RC column specimens were identically reinforced by four No.3 bars in the longitudinal direction to simulate a reinforcement ratio of $\rho = 1.26\%$ in the prototype columns. Because the actual bar diameter was measured as $d = 9$ mm, D9 rather than No. 3 was used in the following discussions to denote the size of longitudinal bars. The actual longitudinal reinforcement ratio, evaluated using the entire gross sectional area, was 1.13%. Figure 3.1 shows the cross-sectional property of the column specimens. The center distance between the longitudinal reinforcements was 3.55 in. in each direction.

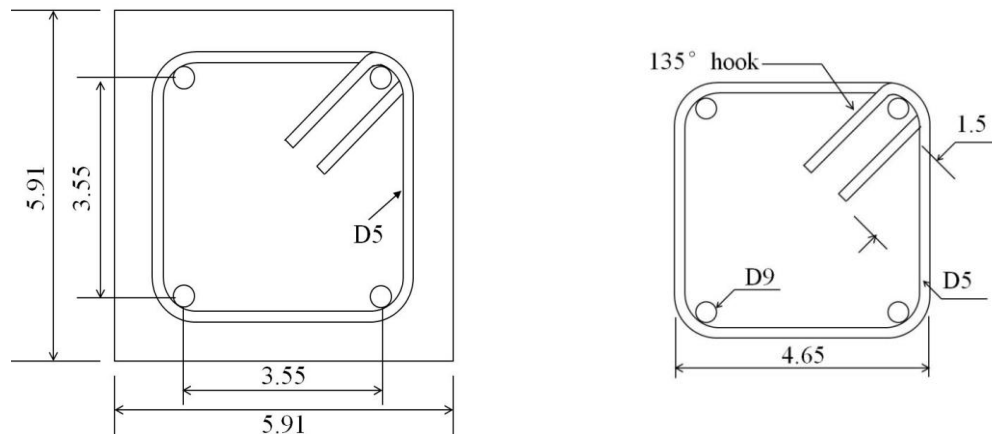


Figure 3.1 Column cross section. (unit of dimension: in.).

It is desirable if the failure of a column can occur in the middle portion of a specimen, where concrete and steel strains were measured. To avoid failure in the column end regions, they

were strengthened by four 6-in. long D16 ($d = 16$ mm, nominally No. 5) reinforcements tied with the four D9 longitudinal bars. Because the concrete cover, as opposed to the core, was expected to reach failure first, no extra transverse reinforcement was used for the strengthening purpose. A706 Grade 60 deformed carbon-steel, conforming to ASTM A615 (2012), was used for the longitudinal reinforcement. The reinforcing bars for each size were obtained from the same heat of steel. As shown in Figure 3.1, closed hoops were used as column transverse reinforcement. The hoops were made of 0.20-in. (5-mm) diameter carbon steel wires and bent into a 4.625 in. square shape. The hoops had 135 degrees, 1.5-in. long standard hooks designed according to ACI 318-19 (2019). The nominal clear concrete cover for the transverse reinforcement was 0.64 in. All the ties were fastened to the longitudinal reinforcement and spaced with a tolerance of 0.25 in. Figures 3.2 and 3.3 show the typical reinforcement layout for the short column specimens subjected to concentric loading and longer columns subjected to eccentric loading, respectively.

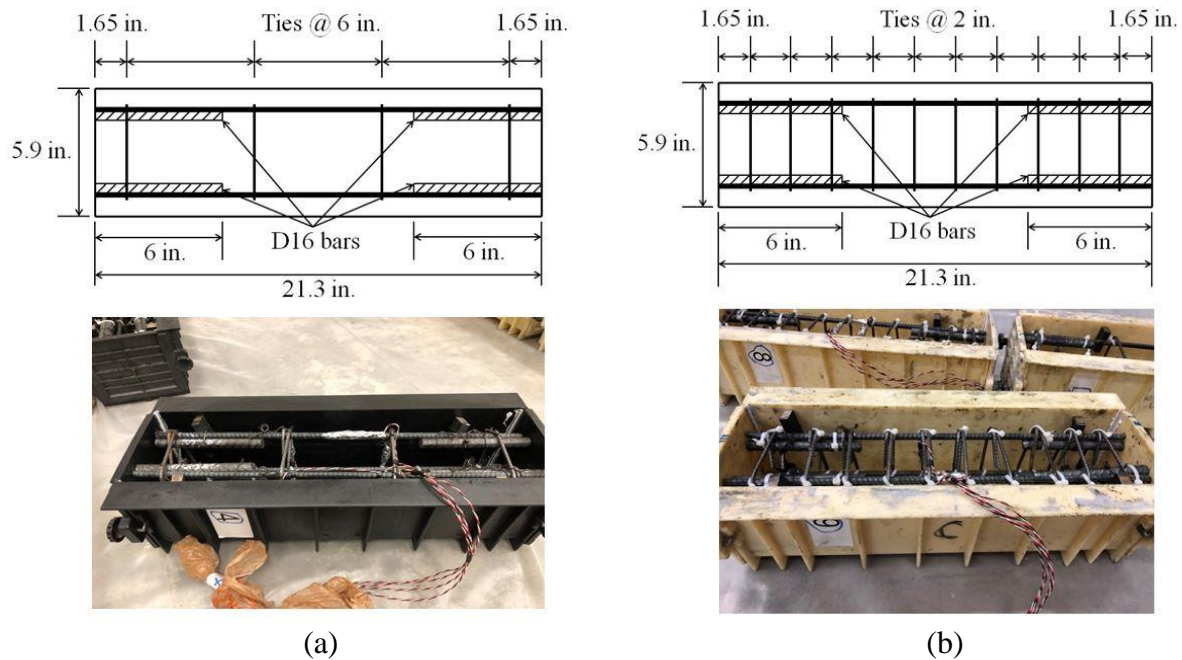
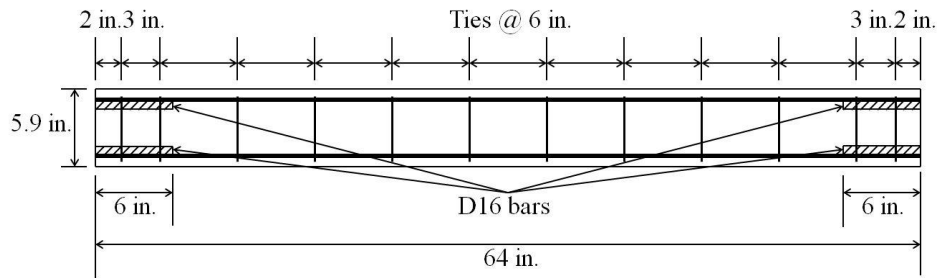
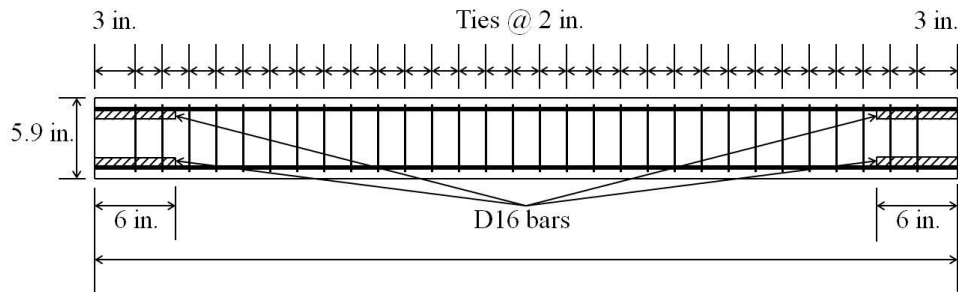


Figure 3.2 Reinforcement layout for (a) Specimens C76A, C98A, and CS and (b) Specimens C76B and C98B.



(a)



(b)

Figure 3.3 Reinforcement layout for (a) Specimens E98A17, E99A17, E77A25, and E92A25, and (b) Specimens E100B17.

Tie spacing of transverse reinforcement was 6 in. for concentrically loaded specimens C76A, C98A, and PS, and all eccentrically loaded specimens except for E100B17. For concentrically loaded Specimens C76B and C98B and eccentrically loaded Specimen E100B17, the transverse reinforcement spacing was 2 in. The corresponding volumetric transverse reinforcement ratios were $\rho_t = 0.26\%$ and $\rho_t = 0.78\%$. Totally four and ten ties were used for the columns subjected to sustained concentric loading with lower and higher transverse reinforcement ratios, respectively. For the eccentrically loaded columns, totally twelve ties were

used for E98A17, E99A17, E77A25, and E92A25 and thirty ties for E100B17.

3.4 Specimen Fabrication

3.4.1 Formwork

Commercially available plastic molds, with a dimension of 5.91 in. x 5.91 in. x 21.3 in. (150 mm x 150 mm x 540 mm), were used as formworks for the short column specimens. The formworks, together with the steel cages, are shown in Figure 3.2 for the columns subjected to sustained concentric loading. Such plastic molds were chosen because they have better precision in dimension than timber formworks fabricated in the laboratory. Moreover, the plastic molds are lightweight and easy to strip, clean, and assemble. As shown in Figure 3.3, three formworks with the same dimension of 5.91 in. x 5.91 in. x 21.3 in., were connected together by screwing 1/4 in. diameter bolts through the holes punched at the ribbed interlocking part of the formwork to obtain the formworks for the slender columns. In order to avoid formwork expansion in the transverse direction caused by the lateral pressure from concrete during its pouring, two 12-in. long steel strap-ties were mounted on the top of the formwork.

Prior to placing steel cage into a formwork, its small gaps were sealed with the quick drying silica gel to prevent water leakage. The formwork was then brushed with an oil-based release agent. The longitudinal reinforcements were supported in the form by steel spacers, which had a length of 2 in. and a cross-section of 0.5 in. by 1 in. The spacers were placed at the two sides and bottom of the concrete mold, as shown in Figures 3.2 and 3.3. In this way, the clear distance between the D9 longitudinal bars to the nearest outer surface of a specimen was maintained as 1 in.

Due to the type of formworks employed in this study, concrete was poured horizontally. It

can be expected that the upper portion of concrete may be slightly weaker than the lower portion. For typical cast-in-place columns, concrete was cast vertically; due to the gravity effects, the concrete strength in the top will be a little lower than the bottom (Ferguson et al., 1988). Because of the reduced scale of the tests, the difference in behavior between horizontally and vertically cast columns was assumed herein to be insignificant.

3.4.2 Concrete Mix

The specimens were cast using the same batch of ready mixed concrete provided by a local supplier. The concrete mix was designed to achieve a 28-day compressive strength of 4000 psi. Based on the role of aggregate in size effect on creep (Bažant and Wittmann, 1983) and to limit this effect in the experiments, the maximum aggregate size was also at 0.5 scale and specified as 3/8 in. for all the tests performed in this study. Table 3.3 summarizes the mix design. The coarse aggregate was gravel and fine aggregate was sand. The concrete mix contained 517 lb of Type V cement per cubic yard with a designed water-cement ratio of 0.64. Details about concrete mix design and properties are shown in Appendix A.

Table 3.3 Concrete mix proportions

Material	Design quantity per cubic yard (lbs)
Coarse aggregate	1310
Fine aggregate	1938
Type V Cement	517
Water	331

3.4.3 Specimen Pouring and Curing

Concrete slump was measured as 5.5 in. when the ready-mixed concrete was delivered to the laboratory. In addition to the eight short column specimens and five longer column

specimens, a total of forty-five concrete cylinders with a dimension of 6 in. x 12 in. were also prepared at the time of concrete pouring. The concrete cylinders were used to measure actual concrete compressive strength immediately before and after the structural testing of specimens. Because of the dry local environment and the low relative humidity inside the laboratory, proper concrete curing was needed. After approximately 5 hours of concrete pouring, cotton fabrics were used to cover all exposed concrete and saturated by water when the concrete was set and hardened. Two layers of plastic sheets were then placed all around the specimens to limit moisture evaporation. The cotton fabrics were kept wet by spraying water daily as necessary. The concrete test cylinders were sprayed with water each and covered by lids.

The daily temperature and humidity inside the air-conditioned laboratory normally changed within a narrow range. The temperature was maintained between 68 and 75°F and relative humidity between 18 to 25%. After 21 days of wet curing, the column specimens and the concrete cylinders were demolded and stored in the laboratory.

3.5 Material Mechanical Properties

3.5.1 Steel Reinforcing Bars

The uniaxial tensile properties of D5 transverse reinforcement and D9 longitudinal bars were tested. Two samples for each size of reinforcement were tested with a gauge length of 1.97 in. Figure 3.4 shows the measured stress-strain response of the tested samples. Because yielding and fracture of one D5 bar occurred outside the gauged region, the ultimate strain of this bar was much lower than that of the other one. However, the discrepancy is not critical because the D5 bars were used as transverse reinforcement and did not yield during the structural tests.

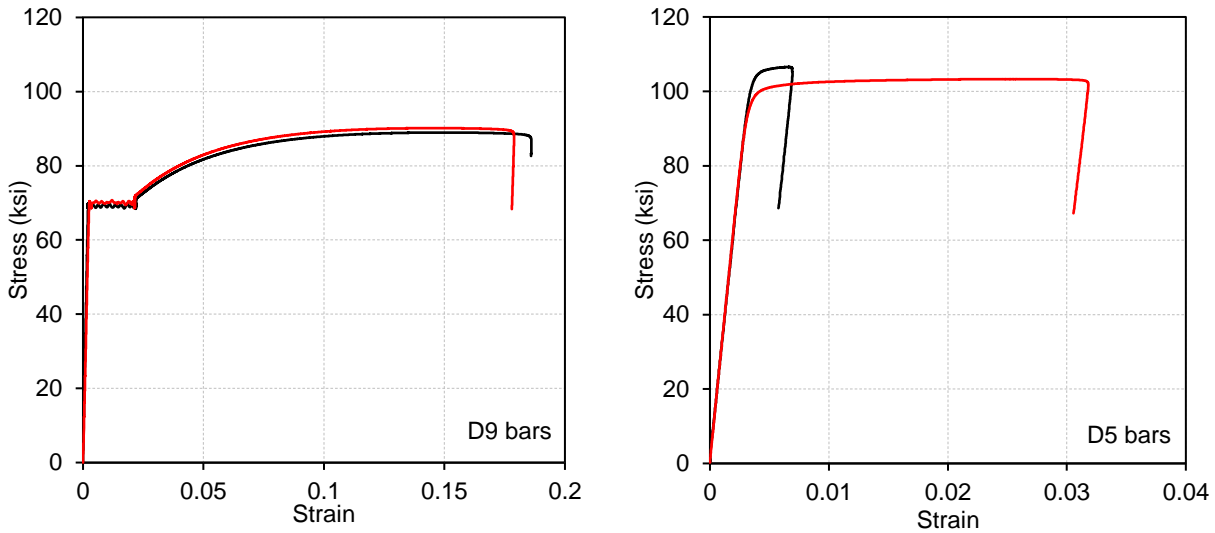


Figure 3.4 Tensile stress-strain response of steel reinforcement.

Table 3.4 summarizes the tensile properties of reinforcing bars. The modulus of elasticity (E_s) was determined based on test data at stresses of 0 and 65 ksi. The average E_s for the D9 and D5 bars was 30189 and 31367 ksi, respectively. As shown in Figure 3.4, the D9 bars had well-defined yield plateaus, making it easy to interpret structural test data. The yield strength (f_y) of each D9 bar sample was determined as the average stress when the strain ranges from 0.0028 to 0.01. The average f_y of the two samples was accordingly determined as 69.5 ksi. The D5 bars presented a gradual change in stiffness when yielding was approached. Thus, the 2% offset method in accordance with ASTM A370 (2018) was used to determine f_y . The average f_y for the D5 bars defined in this way was 104 ksi. The D16 bars used for strengthening purposes at each end of a specimen were not tested because they should not yield during the structural tests.

Table 3.4 Summary of tensile test results for steel reinforcing bars

Bar size	Sample	f_y (ksi)	E_s (ksi)	f_u (ksi)	Ultimate elongation (%)
D9	1	69.1	32826	89.0	18.6
	2	69.9	27552	90.1	17.9
D5	1	106	31241	107	0.7
	2	101	31493	103	3.18

3.5.2 Concrete Compressive Strength

The concrete cylinder compressive strength f_c' was tested in accordance with ASTM C39 (2018) using a concentric loading test machine. In general, the concrete compressive strength was tested by loading three concrete cylinders to failure immediately before or after the start and end of the sustained loading tests. Table 3.5 shows a summary of the measured concrete compressive strengths as a function of concrete age.

Table 3.5 Concrete cylinder compressive strength over time

Concrete age (days)	f_c' (psi)	Test duration (mins)	Average f_c' (psi)
209	4272	6	4311
	4343	5	
	4318	6	
238	4248	4	4322
	4329	5	
	4389	4	
268	4386	5	4336
	4223	9	
	4400	4	
317	4379	5	4315
	4308	5	
	4258	4	
348	4177	5	4198
	4131	5	
	4287	4	
468	4110	7	4010
	3915	5	
	4004	5	
481	3975	2	3895
	3770	2	
	3940	2	
546	3933	2	3850
	3823	2	
	3795	2	
627	4110	2	4069
	4057	2	
	4039	2	
657	3999	2	4036
	3922	2	
	4188	2	

The values of f_c' defined for each specimen at the beginning and end of testing were plotted in Figure 3.5. The dashed line in the figure was the average concrete strength acquired by the concrete cylinder tests. No strength gain due to age was found. Instead, it was seen that the average concrete strength was fairly stabilized between the age of 219 days and 318 days at around $f_c' = 4316$ psi. The maximum f_c' was achieved as 4336 psi at 264 days. After 319 days, the concrete compressive strength experienced a slight decrease by 7.9% until $t = 468$ days. At 468 days, the average f_c' was reduced to 4010 psi. Beyond $t = 468$ days, the average cylinder strength varied in a narrow range. Thus, the average value of f_c' was again considered a constant ($f_c' = 3958$ psi) until $t = 657$ days when the last column test was finished. The decrease of concrete strength over a long term was also observed in the sustained loading experiments carried out by Jenkins (2015) and Kosmatka et al. (2002). The reason for concrete strength decrease over long term was mainly because of different concrete curing method.

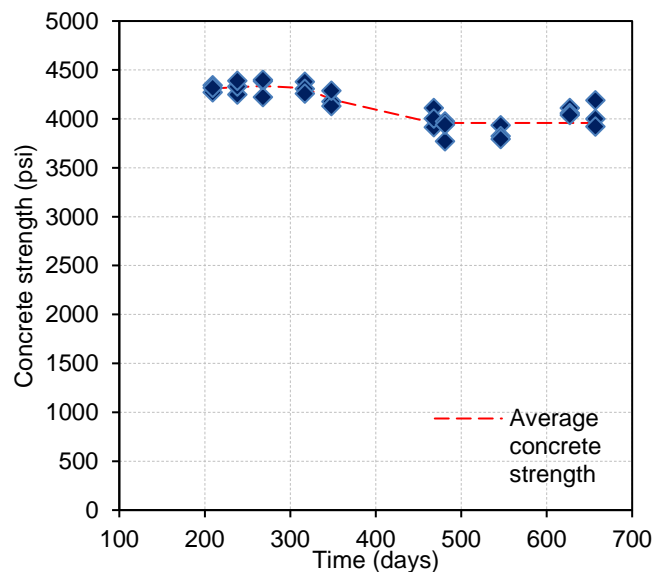


Figure 3.5 Concrete compressive strength versus age.

Figure 3.6 shows the measured compressive stress-strain response of three concrete cylinders after 481 days of concrete casting following the completion of concentric axial loading tests of 8 short columns. These cylinders were tested using the concrete compressive strength test machine, and the strain was measured by strain gauges attached at the mid-height of the cylinders. The average Young's modulus determined at 40% of the peak load was 4054 ksi. The average strain at the peak stress was 0.00197.

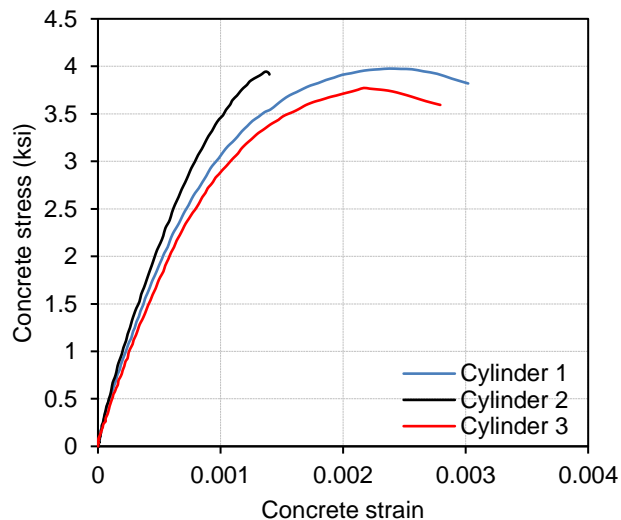


Figure 3.6 Compressive stress-strain relationship for three concrete cylinders at an age of 481 days.

3.6 Test Setup and Instrumentation for Concentric Loading Tests

3.6.1 Test Setup

Figure 3.7 shows the test setup designed and fabricated to allow both short-time and long- sustained concentric loading. Overall, the sustained loads were applied by post-tensioning four high strength steel rods distributed around the four sides of a test specimen. The load-applying and maintaining approaches were conceptually identical to those shown in Figures 1.30 and 1.31 in Section 1.5.5 and employed by Viest et al. (1956) and Green and Breen (1969).

However, in order to apply much greater sustained loads and accommodate load-maintaining devices, a more complex test setup was considered in this study.

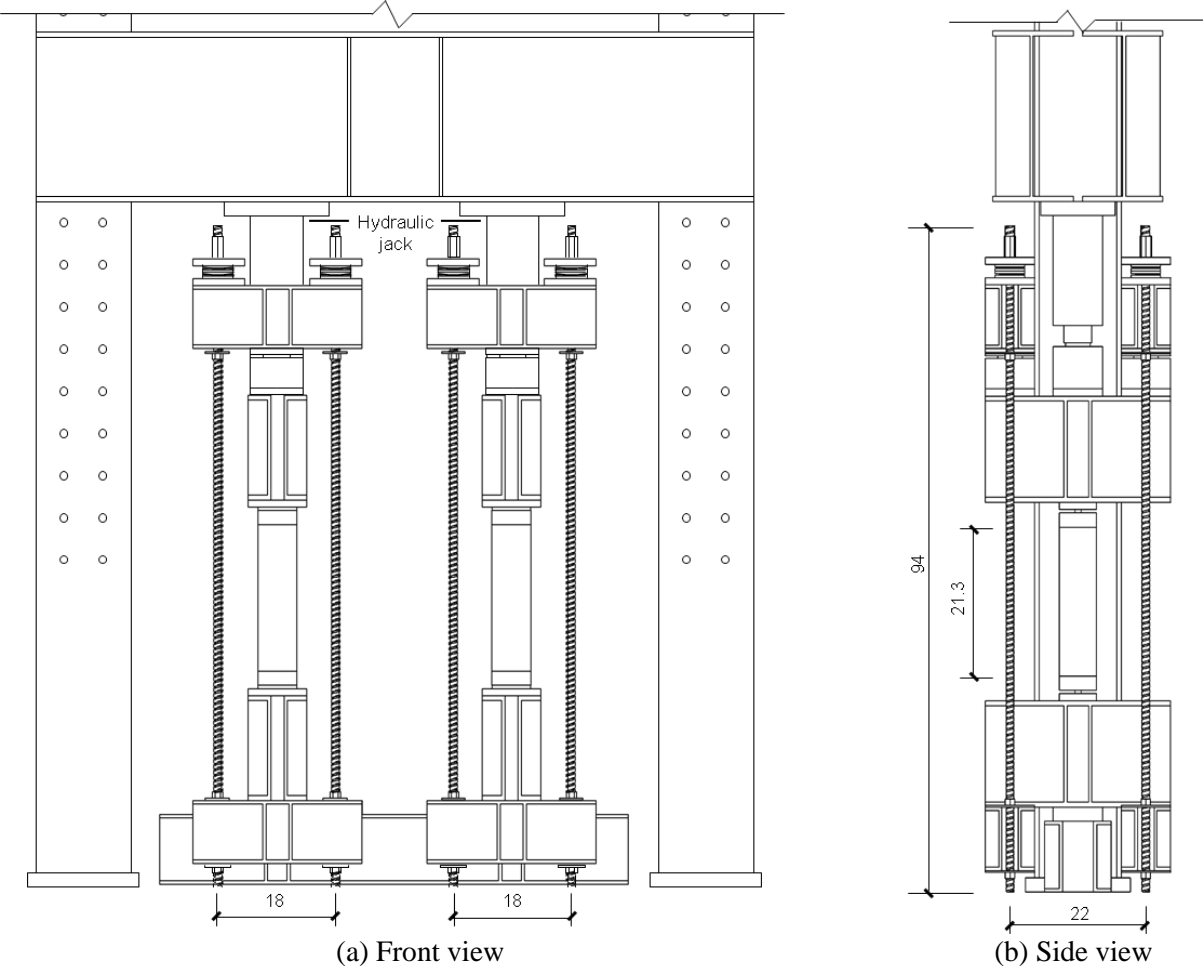


Figure 3.7 Test setup for concentric loading (unit: in.).

Figure 3.8 provides the detailed design of loading frames. To support two specimens simultaneously, a 6 ft. long steel pedestal beam made of two C10x25 channel sections was anchored to the strong lab floor using four 1-in. diameter high-strength threaded steel rods. For each specimen, a 30-in. long steel beam, oriented in the perpendicular direction and made of two C15x40 channel sections, was bolt-connected with the pedestal beam to support the specimen. As shown in Figure 3.8, the load-carrying components installed on the top of specimens were

symmetrically arranged relative to the specimen bottom. The aforementioned steel beams, directly transferring load to the specimen, are termed herein as primary loading beams for convenience.

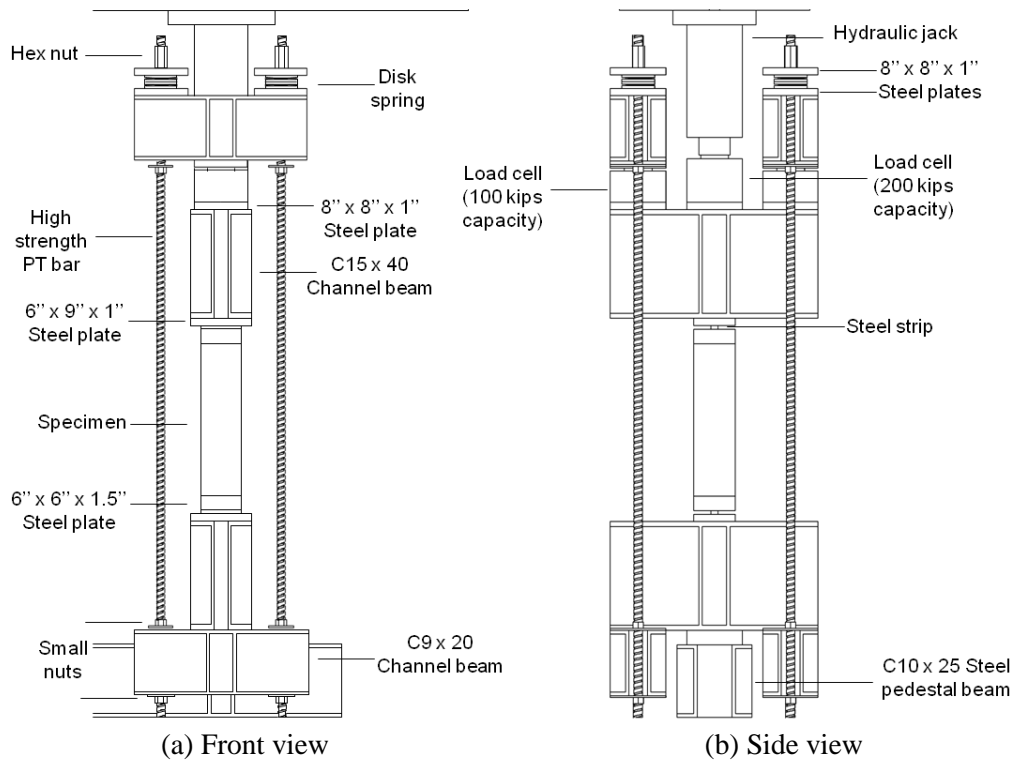


Figure 3.8 Loading frame for columns under concentric loading.

To evenly spread the concentric load to column section, a 1.5-in thick steel end plate was attached to each end of the column. High-strength gypsum cement (hydro-stone) with a minimum compressive strength of 8000 psi was used between the steel plate and specimen end to fill unavoidable voids at the contact. The end plate assemblies used in this experiment were shown in Figure 3.9. To better achieve concentric loading with minimized accidental eccentricity, the specimen was bearing against the steel beam through a steel strip, which was 1-in. wide, 0.5-in. thick, and 6-in. long. The steel strip was situated at the center of specimen top (Figure 3.9),

and bottom ends. To accommodate this steel strip, a 1 in.-wide and 0.25 in.-deep rectangular groove was milled into the center of steel end plate. The groove's middle line was aligned with the centerline of the specimen to ensure that the load can be applied concentrically. The steel strip was seated in the groove at one side and welded to the center of a 6 x 9 x 1 in. steel plate, which was mounted to the primary loading beam.

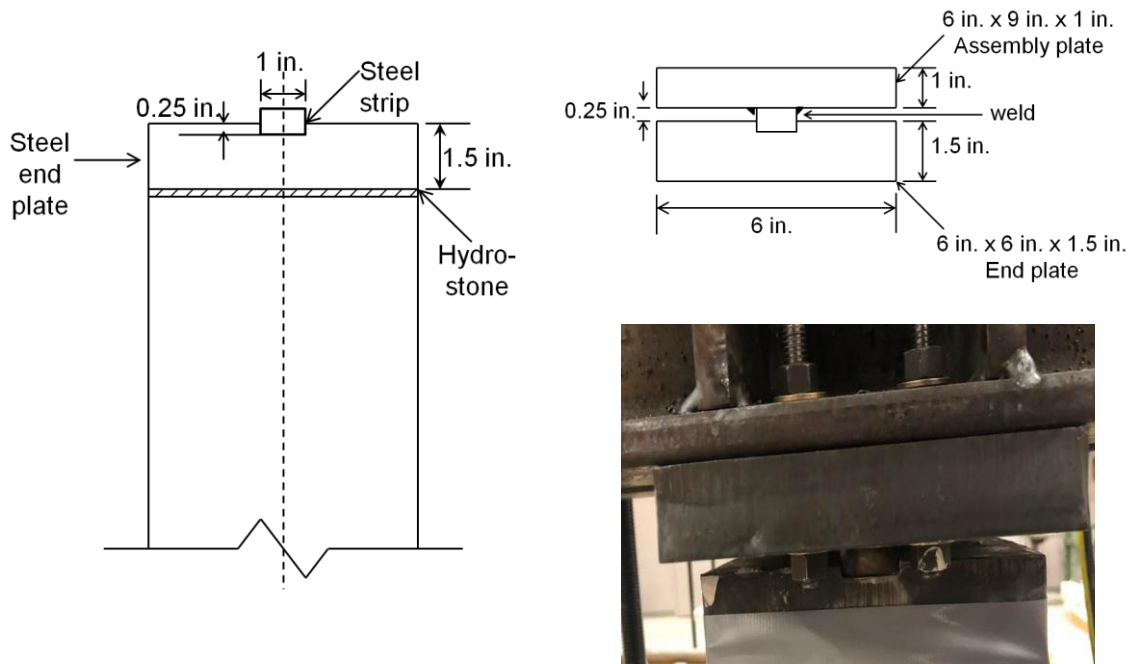


Figure 3.9 Column end regions for concentric loading tests.

Except for Specimens PS and CS, all other six short column specimens were subject to sustained loads. As mentioned previously, the sustained load was applied by tightening the hex nuts situated on the top end of the high-strength post-tensioning rods. These rods had a nominal diameter of 1 in., with a minimum yield strength of 120 ksi, and were fully threaded. The spacing between the post-tensioning rods was 22 in. in one direction and 18 in. in the other direction. As shown in Figure 3.7, to transfer the sustained loads from the four post-tensioning rods to a specimen, they were connected to a total of four 26-in. long steel beams (two on the upper side

and two on the lower side) made of two C9x20 channel sections. These beams, termed as secondary loading beams for convenience, were bolt-connected with the two primary loading beams. To avoid excessive flange local bending and web buckling during loading, the pedestal beam and the primary and secondary loading beams were strengthened by 0.5-in. thick stiffeners at locations where concentrate loads were transferred. All the steel beams and plates were made of A36 steel.

Time-dependent concrete creep, especially due to high compressive stresses introduced into the columns, can significantly decreased posttensioning forces. The sustained loads were maintained by four stackable Belleville disk springs. Viest et al. (1956) and Green and Breen (1969) employed heavy duty coil springs to maintain the applied sustained loads. The springs need to have both enough strength and flexibility. In these experiments, the maximum sustained load at each posttensioning rod was only 28.5 kips. However, in this study, the maximum load experienced by posttensioning rod was estimated as 40 kips prior to the tests. Due to the much higher sustained loads to be applied, disk springs, rather than coil springs, were employed. Based on this strength (40 kips) requirement, disk springs with a 4.75-in. outside diameter, 2.063-in. inner diameter and 0.356-in. thickness was chosen. Each spring had a 0.46-in. overall height, 0.104-in. maximum deflection, and a 58.8 kips maximum allowable load. To easily maintain the applied sustained load during concrete creep, the effective stiffness of the spring assemblies was chosen as approximately $1/8$ of the initial axial stiffness of a column specimen, which was estimated as 4500 kips/in. Accordingly, a total of four disk springs aligned in series, as shown in Figure 3.10, were used at a posttensioning rod. Different from coil springs, disk springs are nonlinear elastic. The overall stiffness provided by all springs at the four posttensioning rods was 565 kips/in. when the four disk springs at a rod was compressed to 0.416 in.

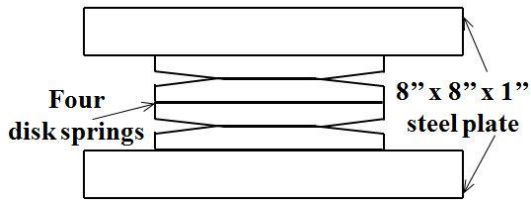


Figure 3.10 Disk spring details.

As shown in Figure 3.8, a steel plate was placed underneath the upper secondary loading beams and held by a nut on a post-tensioning rod. The plate was used to carry the secondary beams when the testing frame was assembled. The plate was lowered down prior to loading the specimen to allow the application of post-tensioning forces and prevent the steel beams on the specimen top from falling down once the specimen was failed. Figure 3.11 shows a picture of the entire test setup after two specimens were installed and ready for testing.

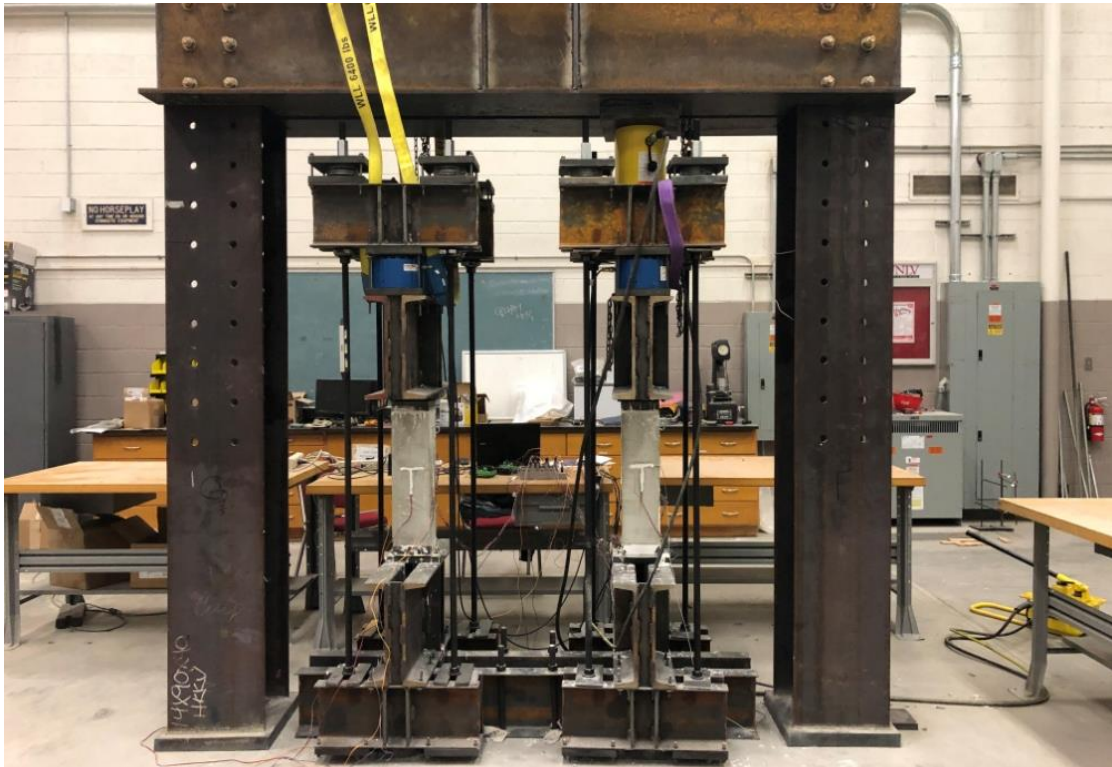


Figure 3.11 Two specimens installed prior to concentric loading tests.

3.6.2 Loading Approach and Procedure

Specimens PS and CS – The plain concrete control specimen, PS, was loaded to failure in a short time (about 10 minutes) at an age of $t_0 = 209$ days. For this purpose, a double-acting general-purpose hydraulic cylinder jack, mounted to the beam of the reaction frame shown in Figures 3.7 and 3.11, was installed. With a 338-kips loading capacity and a 6.63 in. stroke, the loading jack was used to apply a downward force to the upper primary loading beam seated on the top of PS until it failed under compression. The reinforced concrete control specimen, CS, was loaded to failure in a short time (about 91 minutes) at an age of $t_0 = 478$ days. However, the loading was carried out purely by applying post-tensioning forces.

Specimens P77 and P90 – The plain concrete specimens, P77 and P90, were loaded at a concrete age of $t_0 = 238$ and 317 days. The initial short-time loading was first applied up to approximately 80% of the target sustained load (76.3 kips for P77 and 89.3 kips for P90) by tightening the hex nuts on the top of post-tensioning rods; the remaining 20% of the target load was by the hydraulic jack. It took 99 minutes and 96 minutes to complete the initial loading of Specimens P77 and P90. These specimens resisted the sustained loads for 22 days without presenting any sign of failure. They were then unloaded completely for one day to measure the irreversible concrete strains. After that, they were loaded to failure in a short time. During this reloading process, the specimens were first loaded by applying post-tensioning the threaded rod up to the previously applied sustained load and then further loaded to failure by the hydraulic jack.

Specimens C76A, C76B, C98A and C98B – The initial loading of these specimens to the target sustained load was also applied only by tightening hex nuts. The age of concrete at the initial loading was $t_0 = 268, 268, 348,$ and 354 days and the target sustained load was 117 kips

for Specimens C76A and C76B, and 148 kips for Specimens C98A and C98B. The time spent in the initial loading was 93, 106, 94, and 68 minutes for Specimens C76A, C76B, C98A, and C98B, respectively. Knowing that the sustained loads applied to C76A and C76B would never cause a failure, the sustained loading was stopped after 47 days, when the rate of concrete creep became low, which was indicated by a flattened axial strain versus time response. The sustained load applied to C98A and C98B was maintained for 120 days without causing a failure. After the sustained loading has been completed for Specimens C76A, C76B, C98A, and C98B, they were not unloaded; instead, they were loaded in a short time to failure using the hydraulic jack.

3.6.3 Instrumentation

Room temperature and relative humidity – A digital temperature humidity monitor recorded environmental humidity and temperature inside the laboratory during the tests. The data, however, were manually recorded and cannot be transferred or stored in the data acquisition system used for collecting other measurements.

Measurement of deformation – Concrete deformations were measured using strain gauges attached to the column face at mid-height. The concrete strain gauges were applicable for temperatures between -4 to 176°F and had an average resistance of 121 Ohm. The length and width of the strain gauge were 3.15 and 0.12 in., respectively. For each specimen, the axial strain of concrete was measured at all four vertical faces. In addition, for the RC column specimens, the concrete transverse strain was measured at the mid-height of one column face. To obtain a relatively symmetric strain distribution among the four sides of a column specimen, the measured longitudinal concrete strains were used to guide the tightening force applied to the post-tensioning rods during the initial loading to the target sustained loading as well as during

the sustaining loading. During these processes, the longitudinal strains were monitored so that more tightening force was applied to the rods closer to the sides with lower longitudinal strains. For example, if the concrete strain on the right side was smaller than the other three strains, the hex nuts on the two threaded rods on the right side should be adjusted. If the concrete strain in both right and front sides were lower than the other sides of the concrete specimen, the nut on the threaded rod in the front right corner was adjusted.

In each RC column specimen, four steel strain gauges were attached on the steel reinforcement around the column mid-height. Two were attached on longitudinal bars, and the other two on transverse reinforcement. The steel strain gauges had an average resistance of 120.3 Ohm, and the applicable temperature was -103 to 392 °F. The total length and width of strain gauges for steel reinforcement were 0.307 and 0.15 in., respectively. For long-term loading tests, the electrical drift of the sensors could be a concern. However, when the weather outside the laboratory changed during data acquisition, such as the occurrence of rain or sharp decreased in temperature, both the concrete strain gauges and steel reinforcement strain gauges drifted approximately 30 microstrains over time. Due to the relatively small drift, the strain gauge measurements were not adjusted.

Measurement of load – Two 100-kips capacity load cells were placed between the upper primary and secondary loading beams, as shown in Figures 3.7, 3.8, and 3.11. These load cells were used to measure the total post-tensioning force at the front and back sides of a specimen. Load cells can experience creep under sustained loading as well. However, this would cause at most 3% measurement change (Mohamed et al., 2009). To measure the load applied by the hydraulic jack, a 200-kips capacity load cell was placed between the jack and the upper primary loading beam, as shown in Figure 3.7. The measured sustained load was checked at least daily.

To compensate the load drop caused by concrete creep, the sustained load was adjusted by tightening the hex nuts at the top of the post-tensioning rods. This load adjustment was performed daily in the initial days of sustained loading when most of the creep occurred. After that, the time interval for load adjustment was longer. The electrical drift of signal acquired by the load cell due to lab environmental change was small, around 0.1 to 0.2 kips. This amount of change minorly affects the sustained stress level. Therefore, the data recorded by the load cells were not adjusted.

Data collection – All the measured strains and loads were acquired by a National Instruments (NI) data acquisition system together with software LabVIEW. The signals from the load cells and the strain gauges were acquired by NI9219 universal analog input modules inserted into a CompactDAQ chassis. Each module had four channels and permitted a maximum data recording rate of 100 signals/second(s)/channel. The test data were collected at a rate of 1 data/second per channel whenever short-time loading was applied. This sampling rate was also applied to the first 24 hours of sustained loading. After that, the data recording rate during sustained loading was changed to 1 data/20 seconds per channel due to the significantly reduced creep rates.

3.7 Test Setup and Instrumentation for Eccentric Loading Tests

3.7.1 Test Setup

Figure 3.12 shows the test setup used to test the longer columns under eccentric loading. The sustained loads were still applied by mean of four 1-in. diameter fully threaded post-tensioning rods distributed around the four sides of a specimen and spaced at distances identical to those in the concentric loading tests. The mechanism of load transfer was the same as

described previously. The pedestal beam, primary loading beams, and secondary loading beams used in the concentric tests were also employed. However, the test setup for concentrically loaded specimens was modified to apply and maintain eccentric loads and provide extra lateral stability.

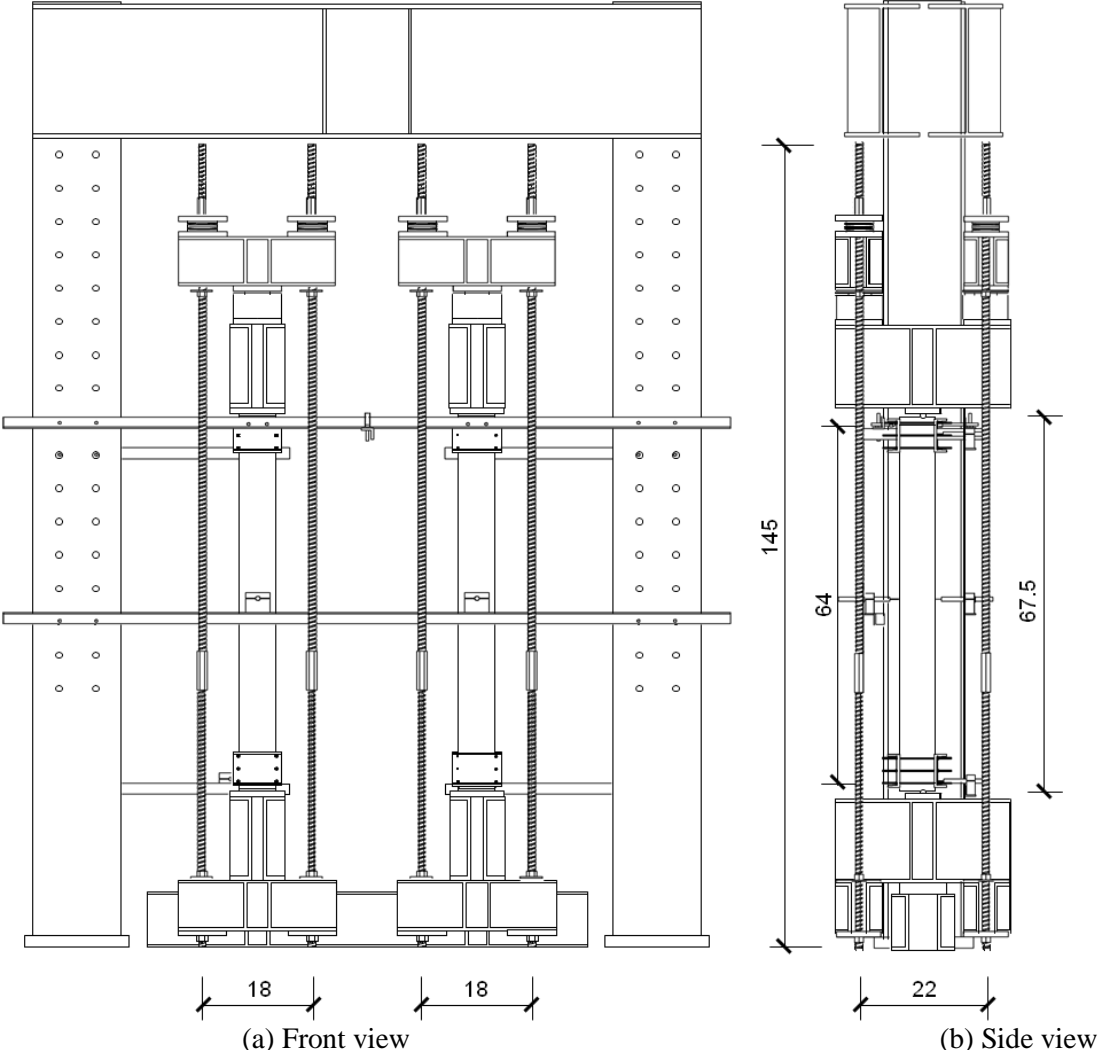


Figure 3.12 Test setup for eccentric loading (unit: in.).

During the short column tests, the sustained loads were applied by tightening the hex nuts at the top of the post-tensioning rods. However, because of the 64-in. length of the longer specimens (the distance between the two loading pins was 67.5 in.), the hex nuts at the upper

ends of the post-tensioning rods were located at a too high position (approximately 11.5 ft) to be easily tightened. Therefore, each rod in the test setup for short column specimens was replaced by two rods, each having a 1-in. diameter and 120 ksi yield strength. The upper rod had right-hand threads and was 94-in. long, whereas the lower rod had left-hand threads and was 48-in. long. The two rods were connected by a 7-in. hex thread adapter in the middle, where tightening force was applied during both short-time loading and sustained loading.

Figure 3.13 provides the detailed design of one set of loading frames. The load-carrying components installed on the specimen top were symmetrically arranged relative to the specimen bottom. High strength gypsum cement was used between the steel plate and the end of specimen to fill unavoidable voids at the contact in all slender column tests. The eccentrically loaded column tests were very sensitive to actual eccentricity. Therefore, some changes were made for the end plate assemblies, as shown in Figure 3.14. The sustained load was transferred by a 1-in. diameter and 6-in. long steel pin instead of the steel strip used in the short column tests. This change allowed the column ends to rotate freely and achieved a pinned-pinned supporting condition. The diameter of steel pins was chosen as 1 in. based on the maximum possible axial load of 100 kips to be applied to the columns. If a smaller diameter was considered, the load capacity of the steel pins may not suffice and there was not enough space for rotation between the end plate and assembly plate. On the other hand, to better achieve an eccentric loading with minimized accidental eccentricity, the steel pin with greater diameter was not a good choice. The steel pin was situated at chosen eccentricity of 1 in. or 1.5 in. away from the center of specimen top (Figure 3.14) and bottom ends. To accommodate this steel pin, a 1 in-diameter and 0.25 in-deep circular groove was milled into the center of steel assembly plate and 1 in. or 1.5 in. apart from the center of steel end plate. The groove centerline was 1 in. or 1.5 in. apart from the

specimen centerline to ensure that the load can be applied eccentrically. The steel pin was seated in the groove at both sides of the steel plates. The assembly plate was mounted to the primary loading beam.

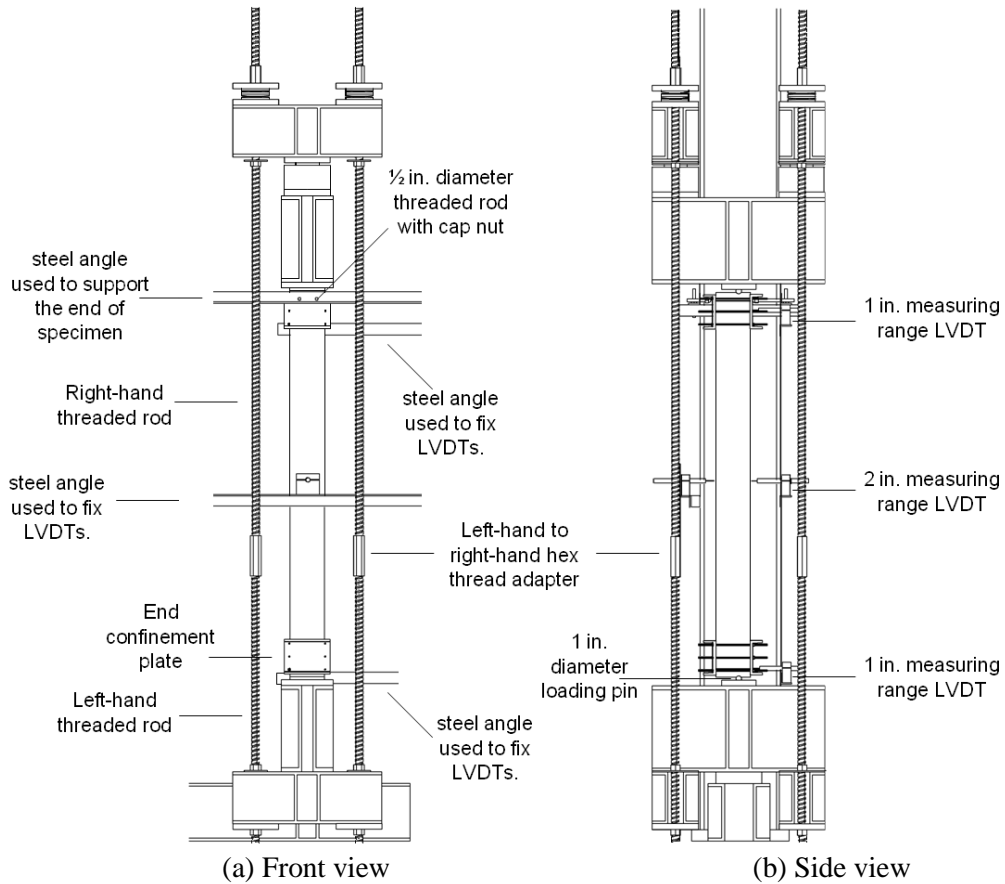


Figure 3.13 Loading frame for columns under sustained eccentric loading.

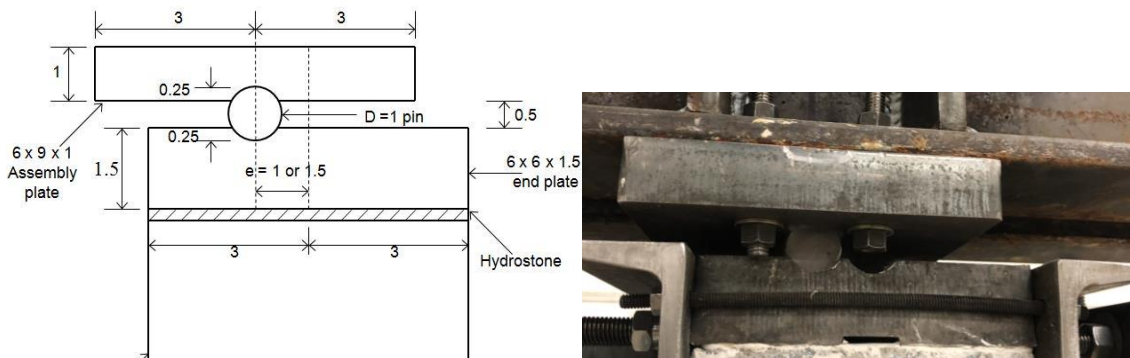


Figure 3.14 End region of columns under sustained eccentric loading.

To prevent relative sliding between the end plate and column end and avoid premature concrete failure, the column ends were confined by two C6x13 steel channel sections, as shown in Figure 3.15. The confinement was fabricated and assembled to each column end region before loading using six 0.25 in. diameter threaded steel rods. Two 10-ft long 2" x 2" x 1/4" steel angles were fixed at both front and back sides of the specimen top end and bolted with the steel reaction frame columns, as shown in Figure 3.12. Two 0.5-in. diameter fully threaded rods with a minimum yield strength of 120 ksi were fixed to each steel angle with bolts along perpendicular direction. A cap nut was screwed at one tip of threaded rod, as shown in Figure 3.16. The two steel angles and the rods with cap nuts were used to reduce sideways movement caused by accidental eccentricity and allow the rotation of column end during loading.



Figure 3.15 Confinement provided at column ends.



Figure 3.16 Lateral support at column upper end.

All the five longer specimens were subject to sustained loads only. Instead of tightening the hex nuts situated on the top of the high-strength post-tensioning rods during the sustained concentric loading, the sustained load during eccentric loading was applied and maintained by screwing the thread adapter located at approximately 4 ft from the ground during the tests. The adapter was 3.25-in. long threads at both ends. The sustained loads were also maintained by four stackable Belleville disk springs, as described previously and shown in Figure 3.10. In all five longer column experiments, the maximum sustained load at each post-tensioning rod was around 24 kips. The effective stiffness of spring assembly was approximately 1/5 of the initial axial stiffness of the longer column specimens, estimated as 2882 kips/in. Figure 3.17 shows a picture of the entire test setup after two specimens was installed and ready for testing.



Figure 3.17 Two specimens installed prior to sustained eccentric loading test.

3.7.2 Loading Procedure

Specimens E98A17, E100B17, and E92A25 – Specimens E98A17, E100B17, and E92A25 underwent three loading stages: (1) the initial loading to the target sustained load, (2) sustained loading for 22, 11, and 28 days without any sign of failure, and (3) reloading to failure in a short time. The age of concrete at the initial loading was $t_0 = 547, 603, \text{ and } 629$ days, and the target sustained load was 86.1, 86.3, and 60.6 kips for Specimens E98A17, E100B17, and E92A25, respectively. The time spent in the initial loading to the target sustained load was 112, 182, and 47 minutes for Specimens E98A17, E100B17, and E92A25.

Specimens E99A17 – Specimen E99A17 underwent only two loading stages: (1) initial short-time loading to 80.5 kips within 59 minutes at the age of $t_0 = 604$ days, and (2) sustained loading for two days because it failed during a load adjustment.

Specimens E77A25 – Specimen E77A25 underwent four loading stages, (1) initial short-time loading to 55 kips within 42 minutes at the age of $t_0 = 628$ days, (2) sustained loading for eleven days, (3) sustained loading for 17 days after increasing the sustained load to that applied to Specimen E92A25 (60.6 kips) on the 12th, and (4) reloading to failure in a short time.

3.7.3 Instrumentation

The load, room temperature, and relative humidity were measured using the same methods as in the concentric loading tests.

Measurement of deformation – Concrete axial deformations were measured using four strain gauges attached to each column face at mid-height. Two strain gauges measured concrete transverse strain at column mid-height, one at compression face and the other one at tension face. One strain gauge was attached to a concrete cylinder during the sustained loading tests to

measure the variation of concrete strain caused by room temperature change. The maximum variation of strain measured by this strain gauge was only 16 microstrains during the sustained load tests. Two strain gauges were attached to the tensile bars at column mid-height. Two additional strain gauges were attached to transverse reinforcement nearest to column mid-height. Moreover, one strain gauge was attached on a D9 reinforcement embedded into a concrete cylinder to measure strain variation of reinforcement inside stress-free concrete. The maximum strain variation in this gauge was only 9 microstrains during the sustained load tests.

Measurement of deflection – Totally four high-accuracy direct current voltage output LVDTs were used to measure column deflections at different locations. As shown in Figure 3.12, two 10-ft long 2" x 2" x 1/4" steel angles were installed with the loading frame at both the front and back sides of the specimen mid-height. These steel angles were used to fix two LVDTs measuring column center deflection at the front and back sides. Another two LVDTs measured column deflection at the top and bottom ends.

Data collection - All the strain and load data were obtained in the same manner as in the concentric loading tests. One NI 9205, a 16-channel universal analog input module, was used to collect displacement data obtained from LVDTs. The test data were recorded at 1 data/second per channel when the specimen was loaded in a short time. Subsequently, the data recording rate changed to 1 data/20 seconds per channel during the sustained loading.

CHAPTER 4

EXPERIMENTAL RESULTS OF COLUMNS SUBJECTED TO CONCENTRIC SUSTAINED LOADING

4.1 Introduction

Eight short square columns, including three plain concrete and five RC columns, with the same slenderness ratio of $H/h = 3.6$, were tested under concentric loading. The tests started at concrete ages greater than 200 days to ensure that the specimens had stabilized concrete strength and shrinkage. Loading duration was chosen based on the test observations and time restraint. This chapter presents the test data of the eight specimens in terms of loading history, axial strain history and creep coefficient, load-strain response and failure mode, and transverse strain history and Poisson's ratio history.

4.2 Behavior of Plain Concrete Columns

4.2.1 Plain Concrete Specimen under Short-Term Loading

The control specimen PS was loaded to failure in approximately 10 minutes at an age of $t_0 = 209$ days. Figure 4.1 shows the load-strain relationship. The load resisted by this specimen and other specimens described in this chapter include a gravity load of 0.85 kips caused by the self-weight of all components sitting on the top of the specimens, such as the primary loading beam, secondary loading beams, load cells, disk springs, and some steel plates. The peak failure load of Specimen PS was 124 kips and very close to 128 kips calculated using Equation (1.25) given in ACI 318-19 (2019) after setting the area of steel reinforcement as zero. The peak stress of PS was 3553 psi, equivalent to $0.83f'_c$. The corresponding axial strain at the peak load was 0.00198. Based on this test, the short-time prism concrete compressive strength, f_{cp} , for the plain

concrete specimens in this study is defined hereafter as

$$f_{cp} = 0.83f_c' \quad \text{Equation (4.1)}$$

where f_c' is the cylinder concrete compressive strength on the day $t = t_0$ when a column test was started.

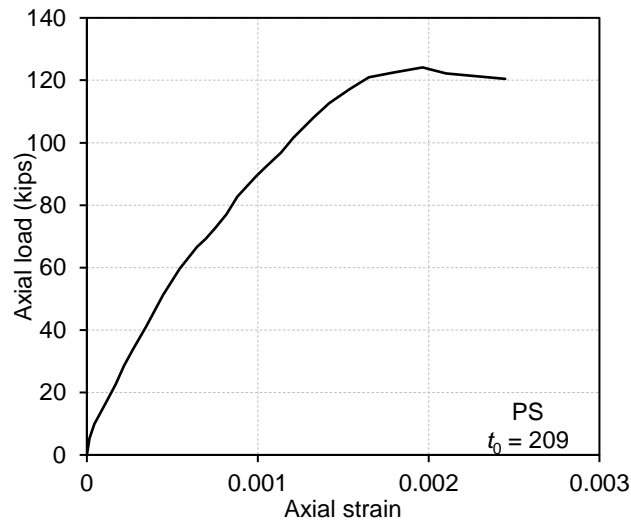


Figure 4.1 Load-strain relationship of Specimen PS during short-time loading test.

4.2.2 Plain Concrete Specimens under Sustained Loading

4.2.2.1 Loading History

In sequence, the plain concrete specimens P77 and P90 underwent the following loading stages: (1) initial short-time loading, (2) sustained loading, (3) complete unloading, and (4) short-time reloading to failure. Figure 4.2 shows the loading history. At $t_0 = 238$ and 317 days, P77 and P90 were loaded to 96.5 and 111 kips within 99 and 96 minutes, respectively. The initial loading caused an axial compressive stress of $\sigma_c = 2768 \text{ psi} = 0.77 f_{cp}$ in P77 and $\sigma_c = 3183 \text{ psi} = 0.90 f_{cp}$ in P90. The loads were then kept for 22 days. As summarized in Table 4.1, during this sustained loading stage, the average load was 95.5 kips for Specimen P77, causing an average sustained stress of $0.77 f_{cp}$. The minimum and maximum sustained loads were 92.6 and 96.6 kips, leading to

a percentage load variation from the average load of -3.0% to 1.2%. The average sustained load for P90 was 111 kips, resulting in an average sustained stress of $0.90f_{cp}$. The maximum and minimum loads were 101.7 and 112.7 kips. The percentage variation from the average load was -8.4% to 1.5%. Thus, the sustained load level was 77% and 90% of the short-time loading capacity for Specimens P77 and P90, respectively. Note that, for each specimen, the largest load drop occurred only during the first day following the initial application of sustained loads. After that, the sustained load was well maintained, as indicated in Figure 4.2. At $t - t_0 = 22$ days, the applied load was released to measure the irreversible concrete strain. After a rest for one day, the specimens were loaded to failure in a short time. The peak load prior to the final failure was 132 kips for Specimen P77 and 133.6 kips for P90.

Table 4.1 Specific loading details for Specimens P77 and P90

Specimen	Duration of loading to target load (mins)	Average sustained load (kips)	Maximum sustained load (kips) and % change	Minimum sustained load (kips) and % change	Peak load (kips)
P77	99	95.5	96.6 (+1.2%)	92.6 (-3.0%)	132
P90	96	111	112.7 (+1.5%)	101.7 (-8.4%)	133.6

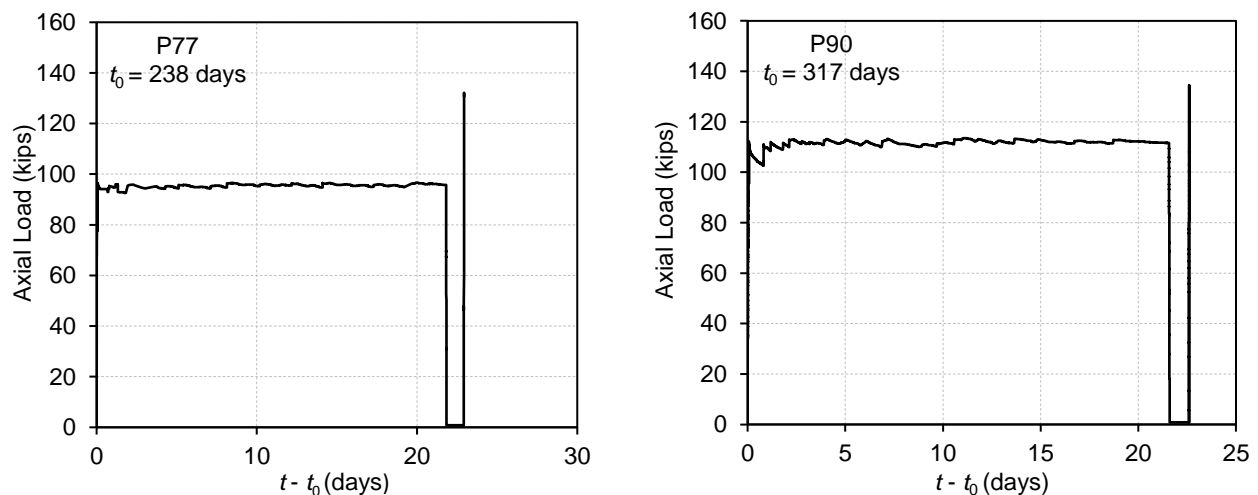


Figure 4.2 Loading history of plain concrete Specimens P77 and P90.

4.2.2.2 Axial Strain History and Creep Coefficient

Figure 4.3 plots the axial compressive strain history for the two tests. Unfortunately, the strain data were lost when Specimen P90 was reloaded to failure after sustained loading. The initial axial strain at the beginning of sustained loading (i.e., the end of initial short-time loading) was 0.000857 for P77 and 0.000985 for P90. During the first day of sustained loading, the concrete axial strain increased rapidly by 35.9% in Specimen P77 and 30.2% in Specimen P90. As the time of sustained loading increased, the rate of strain increase decreased. After 20 days, the strain became stable. Thus, sustained loading was stopped at $t - t_0 = 22$ days, when the axial strain reached 0.00171 and 0.00196 in Specimens P77 and P90, respectively. The ratio of axial strain at the end of sustained loading to that at the start of sustained loading was 2.00 for Specimen P77 and 1.99 for Specimen P90. Because the ratio of axial strain at the end of sustained loading to that at the start of sustained loading of two specimens was almost the same, the effects of sustained load level on the concrete creep in this experiment cannot be noticed. Table 4.2 summarizes the axial strains measured at characteristic loading stages.

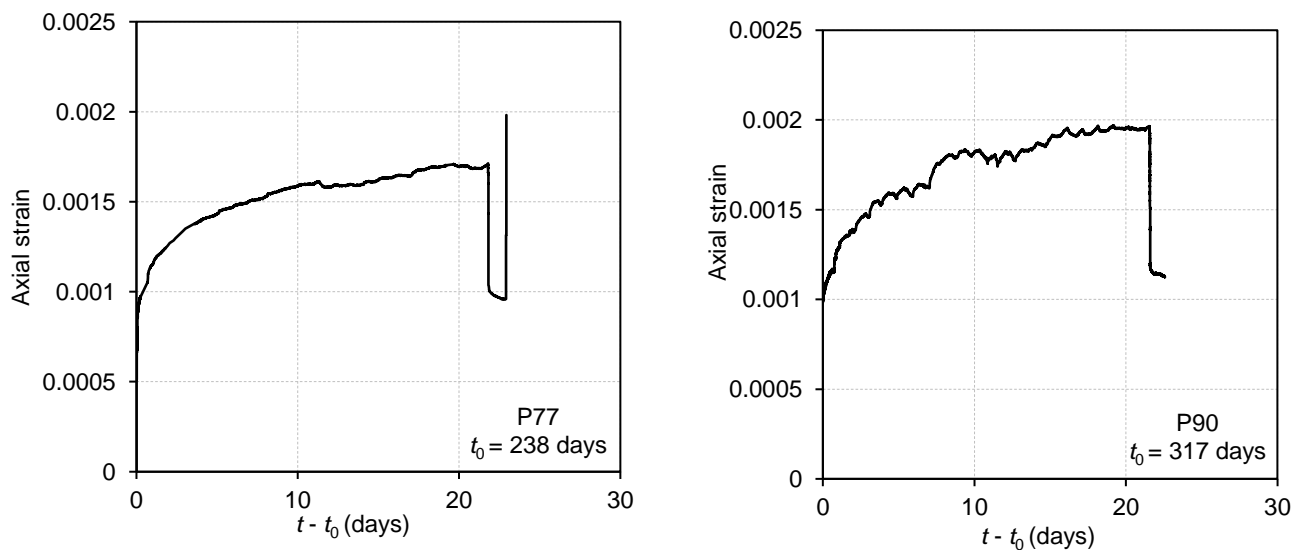
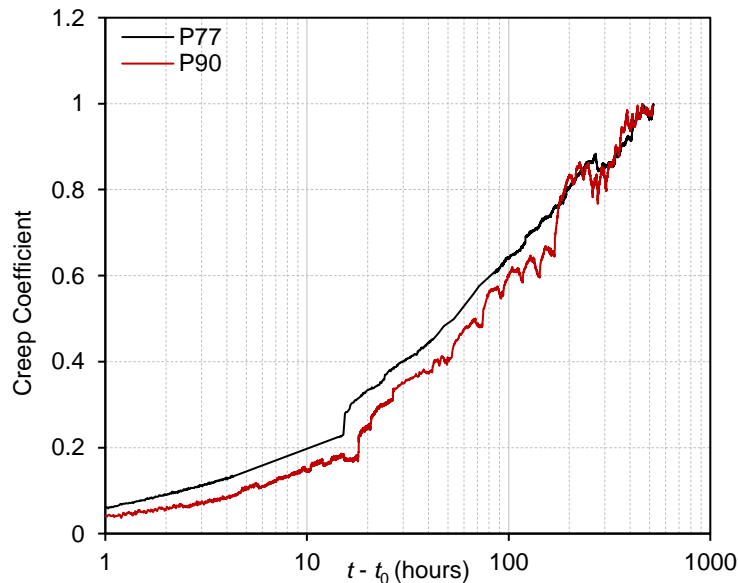


Figure 4.3 Strain history of plain concrete Specimens P77 and P90.

Table 4.2 Characteristic concrete strains of Specimens P77 and P90

Specimen	Strain at the beginning of sustained load	Strain at the end of sustained load	Irreversible strain	Strain change during the unloading	Failure strain at the peak load
P77	0.000857	0.00171	0.000103	0.000076	0.00198
P90	0.000985	0.00196	0.000139	0.000101	—

Figure 4.4 plots the creep coefficient during the sustained loading for Specimens P77 and P90. The creep coefficient was calculated as the ratio of creep strain during the sustained loading to the initial strain at the beginning of the sustained load. Even though the sustained load ratio of P90 was 17% higher than that of Specimen P77, the creep coefficient of P90 was lower than P77 until $t - t_0 = 178$ hours and became similar thereafter. The creep coefficient of P90 was lower than P77 during the first 178 hours because the 79 days difference in loading age (t_0) affected the creep coefficient. After $t - t_0 = 22$ days, the creep coefficient was equal to 1.00 for P77 and 0.99 for P90.

**Figure 4.4** Creep coefficient during sustained concentric loading for Specimens P77 and P90.

4.2.2.3 Stress-Strain Response and Failure Mode

Figure 4.5 shows the stress-strain relationship of Specimens P77 and P90. The red color dashed lines indicate f_{cp} , the short-time prism concrete strength determined using Equation (4.1). f_{cp} was 3582 psi for Specimens P77 for P90. As indicated in Figure 4.5, the peak stress during reloading was 3789 psi, resulting in a 5.8% increase compared to f_{cp} . The peak reloading stress of Specimen P90 is not shown in Figure 4.5 due to the loss of strain data; however, based on the measured peak load shown in Figure 4.2, the peak reloading stress for P90 was determined as 3855 psi, which is 7.5% higher than the short-time strength of $f_{cp} = 3582$ psi. The strength increase in both specimens may be explained by concrete consolidation during sustained loading (Shah and Chandra, 1970). Moreover, based on the test results shown in Figure 4.5, it was found that both the unloading and reloading stiffness were similar to that during the initial loading.

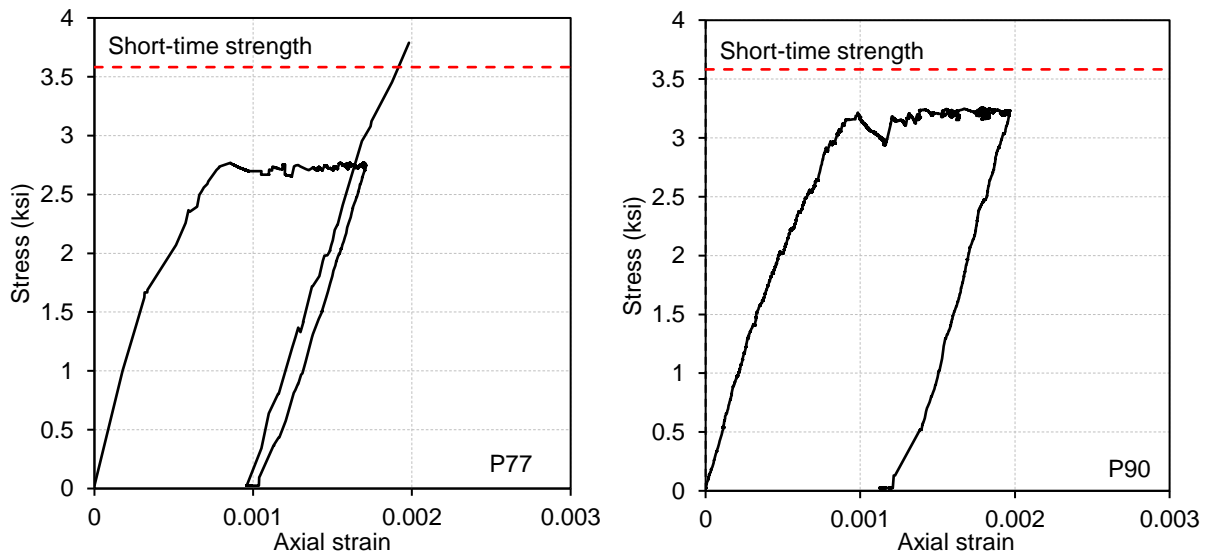


Figure 4.5 Stress-strain relationship of plain concrete specimens P77 and P90 under concentric loading.

The failure of each specimen was sudden and explosive. Figure 4.6 shows the three plain concrete specimens after failure. The Specimen PS shown a splitting failure. For Specimens P77

and P90, the failure was dominated by shear, a failure mode that can also be observed in testing plain concrete (ASTM, 2018), as shown in Figure 4.6. This strength increase in P77 and P90 after sustained loading may be associated with the shift in failure mode.



(a) PS (b) P77 (c) P90

Figure 4.6 Plain concrete specimens after failure.

4.3 Experimental Results of Reinforced Concrete Columns

4.3.1 RC Specimen under Short-Term Loading

The control Specimen CS was loaded to failure in approximately 90 minutes after 478 days of concrete pouring. Figure 4.7 shows the force-axial strain and force-volumetric strain relationships. Figure 4.7 provides the axial strains measured at all four forces. It is seen that the variation among these strains was low, indicating that a relatively symmetric strain response was achieved under the concentric loading. The black color solid line shows load versus average axial strain response. Only the average axial strain will be reported for all other concentric loading

tests.

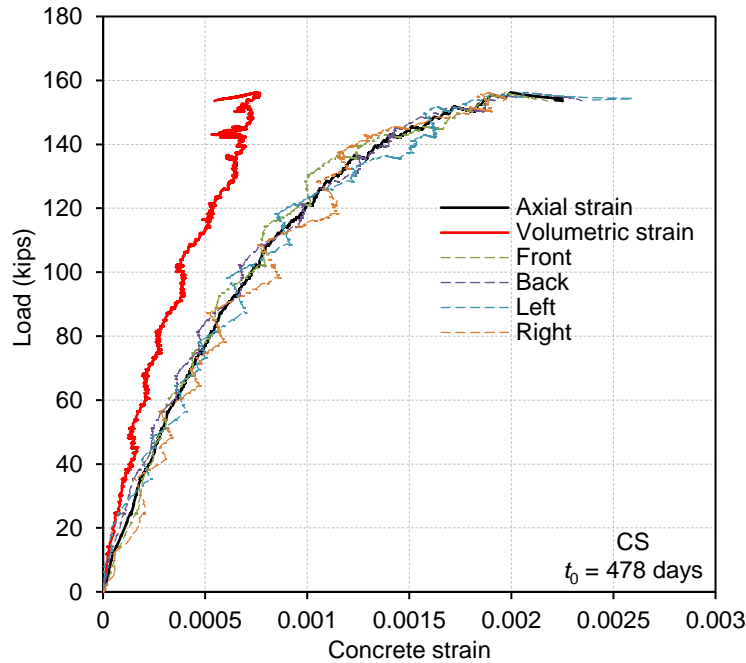


Figure 4.7 Load strain response of CS.

The loading was paused several times to inspect specimen condition, loading system, and data acquisition system. The pause lasted approximately 7 minutes and, when the load approached the failure load, caused a notable increase in axial strain up to 0.000106 accompanied by a slight load drop. This indicates that creep occurred in this short period. However, once the loading was resumed, the specimen showed a greater reloading stiffness than that prior to the load pause. Therefore, the envelop response measured in the test should be close to the load-deformation response of the specimen should it have been loaded continuously. The peak load was 156.3 kips, 7% greater than the nominal short-time loading capacity of 146 kips predicted based on Equation (1.25) given in ACI 318-19 (2019). The greater strength was due to the confinement effects of transverse reinforcement, which is not taken into account by Equation (1.25). The average axial strain at the peak load was 0.00199. The strain at the left side of the

specimen had the maximum value thereafter. At the failure (immediately prior to a sudden load drop), the average axial strain was 0.00225.

The concrete volumetric strain ε_{vol} was evaluated based on test data using the following equation.

$$\varepsilon_{vol} = \varepsilon_{axial} + \varepsilon_{t1} + \varepsilon_{t2} \quad \text{Equation (4.2)}$$

where ε_{axial} is concrete axial strain, ε_{t1} and ε_{t2} are concrete transverse strain in two orthogonal directions and assumed to be equal. Because the transverse strain was measured at only one side of the column, the measured axial strain at this side was used to calculate the volumetric strain. It is seen from Figure 4.7 that, once the applied load has exceeded 149 kips, the volumetric strain kept decreasing, indicating an imminent compressive failure of concrete cover.

Another parameter that can be used to indicate concrete damage condition is Poisson's ratio. Figure 4.8 plots load versus Poisson's ratio of Specimen CS. The value of Poisson's ratios at different loads were determined from the same concrete axial and traverse strains used to evaluate the volumetric strains previously. The measured axial strain was low and fluctuated when the applied load was lower than 40 kips. Accordingly, the values of Poisson's ratio also fluctuated. Therefore, the Poisson's ratio for the applied load lower than 40 kips is not shown in Figure 4.8. In general, the value of Poisson's ratio increased with the applied load. When the load was less than 80 kips, the Poisson's ratio was less than 0.20; when the load reached to 150 kips, the Poisson's ratio was nearly 0.30. At failure, Poisson's ratio measured at the concrete surface reached to approximately 0.4. According to Park and Paulay (1974), the volumetric strain can be a negative value, and the Poisson's ratio may reach 0.5 when concrete fails in compression.

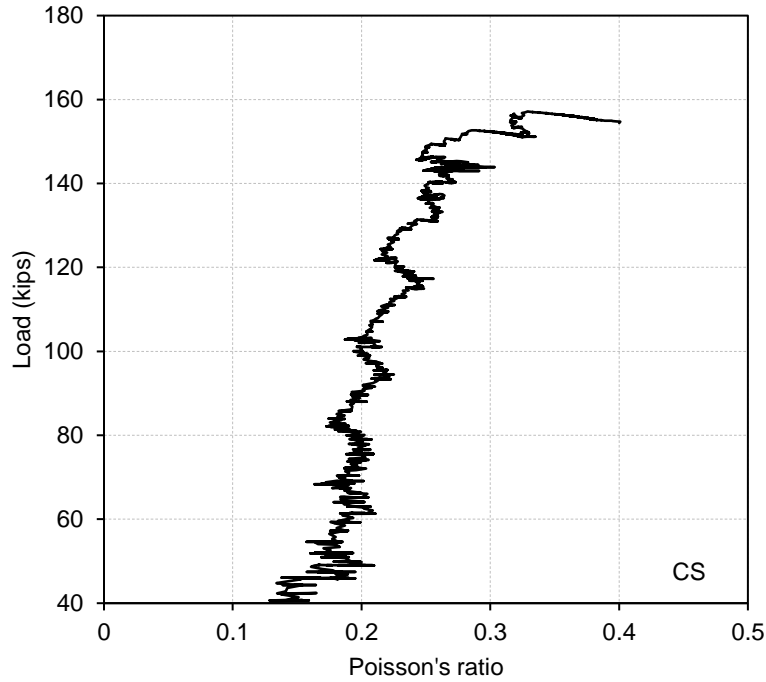


Figure 4.8 Load versus Poisson's ratio response of Specimen CS.

4.3.2 RC Specimens under Sustained Loading

4.3.2.1 Loading History

None of the RC specimens (C76A, C76B, C98A, and C98B) failed during the sustained concentric loading even though the sustained load level was as high as 98% of column nominal short-time capacity in the tests of C98A and C98B. Each specimen underwent the following loading stages: (1) initial short-time loading, (2) sustained loading, and (3) loading to failure in a short time. Figure 4.9 shows the loading history of the four RC columns. Table 4.3 shows the loading details.

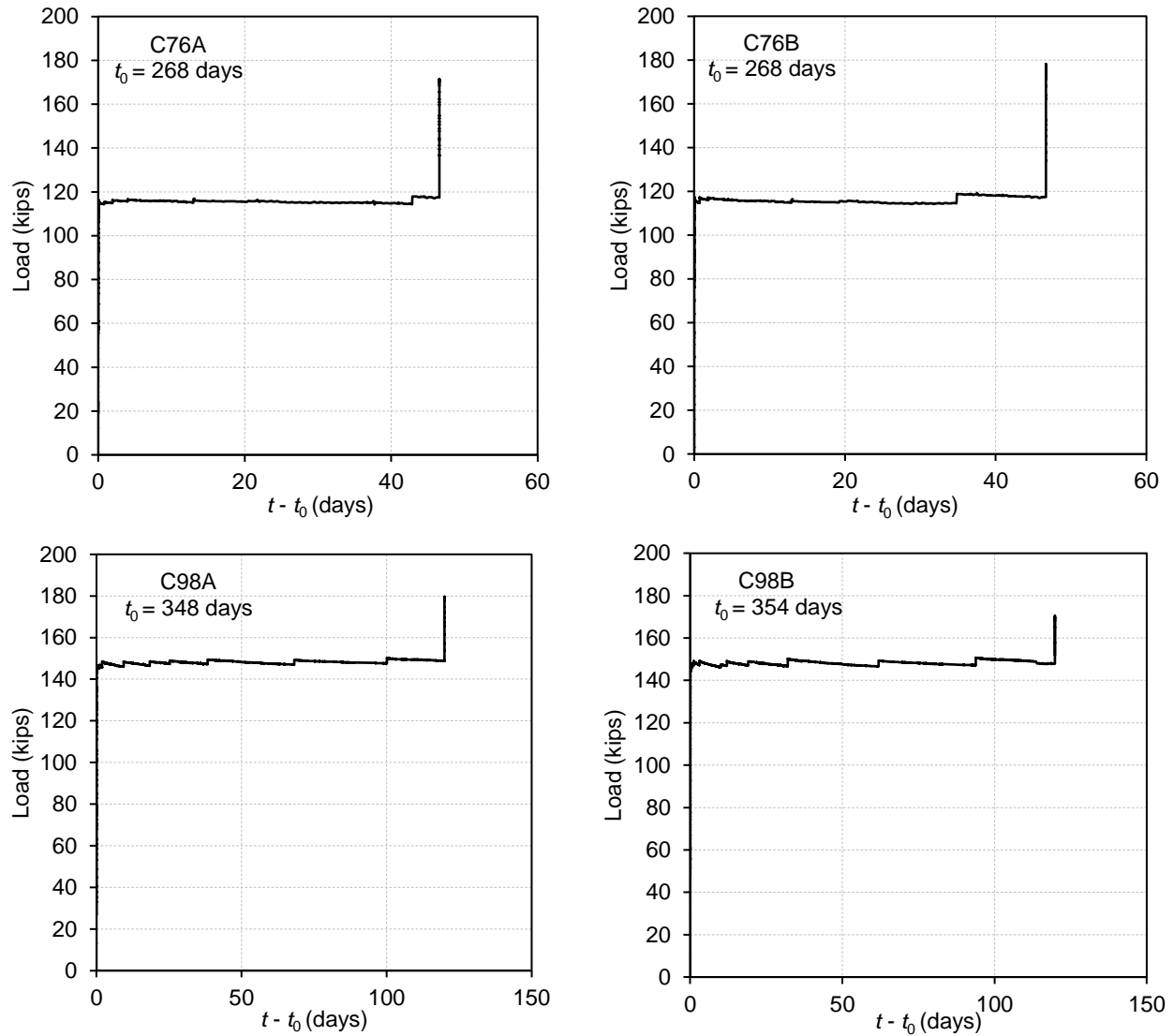


Figure 4.9 Loading history of Specimens C76A, C76B, C98A, and C98B.

Table 4.3 Loading details for Specimens C76A, C76B, C98A, and C98B

Specimen	Duration of loading to target load (mins)	Average sustained load (kips)	Maximum sustained load (kips) and % change	Minimum sustained load (kips) and % change	Peak load (kips)
C76A	93	117	119 (+1.7%)	115 (-1.7%)	172
C76B	106	117	120 (+2.6%)	115 (-1.7%)	179
C98A	94	148	150 (+1.4%)	143 (-3.4%)	180
C98B	86	147	150 (+2%)	144 (-2.0%)	170

At $t_0 = 268$ days, Specimens C76A and C76B were loaded to 116 and 117 kips within 93 and 106 minutes, respectively. The sustained loading of these columns was ended at $t - t_0 = 47$ days because the axial strain became stable. The average sustained load was 117 kips for both Specimens. The average sustained loads were about 76% of the nominal short-time loading capacity evaluated based on ACI 318 (2019), denoted as $N_{u,ACI}$ and indicated by the dashed lines in Figure 4.12. The $N_{u,ACI}$ is calculated by Equation (4.3), where f_c' is determined based on the concrete cylinder compressive strength at the start of sustained loading.

$$N_{u,ACI} = 0.85 f_c' A_c + f_y A_s \quad \text{Equation (4.3)}$$

At $t_0 = 348$ and 354 days, Specimens C98A and C98B were loaded to 146 and 147 kips within 94 and 68 minutes, respectively. Due to the high sustained load, the measured axial strain kept increasing. However, because of time restraint, the sustained loading for these specimens was stopped after $t - t_0 = 120$ days. The average sustained loads were 148 kips and 147 kips for Specimens C98A and C98B respectively, and about 98% of their short-time loading capacity $N_{u,ACI}$, estimated in the same manner for Specimens C76A and C76B.

For each RC column specimen, the largest load drop occurred only during the first day after the application of sustained loads, as indicated in Figure 4.9. The percentage of load drop for all RC specimens were smaller than the plain concrete specimens, indicating that the RC columns could sustain loads better than the plain concrete columns. Moreover, as shown in Table 4.3, the variation of sustained load from the average value was at most 3.4% for each specimen.

4.3.2.2 Axial Strain History and Creep Coefficient

Figure 4.10 plots the concrete average axial strain history for the four tests. Table 4.4 summarizes the concrete strains, including both axial and transverse strains, measured at

characteristic loading stages. The initial axial strain at the beginning of sustained loading was 0.000742, 0.00122, 0.00130, and 0.00148 for Specimens C76A, C76B, C98A, and C98B, respectively. During the first day of sustained loading, the concrete axial strain increased rapidly by 25%, 25%, 36%, and 17% in C76A, C76B, C98A, and C98B. As the loading time increased, the rate of strain increase was reduced. By the end of the sustained loading, the axial strain reached 0.00138, 0.00227, 0.00277 and 0.00315 in C76A, C76B, C98A, and C98B, respectively.

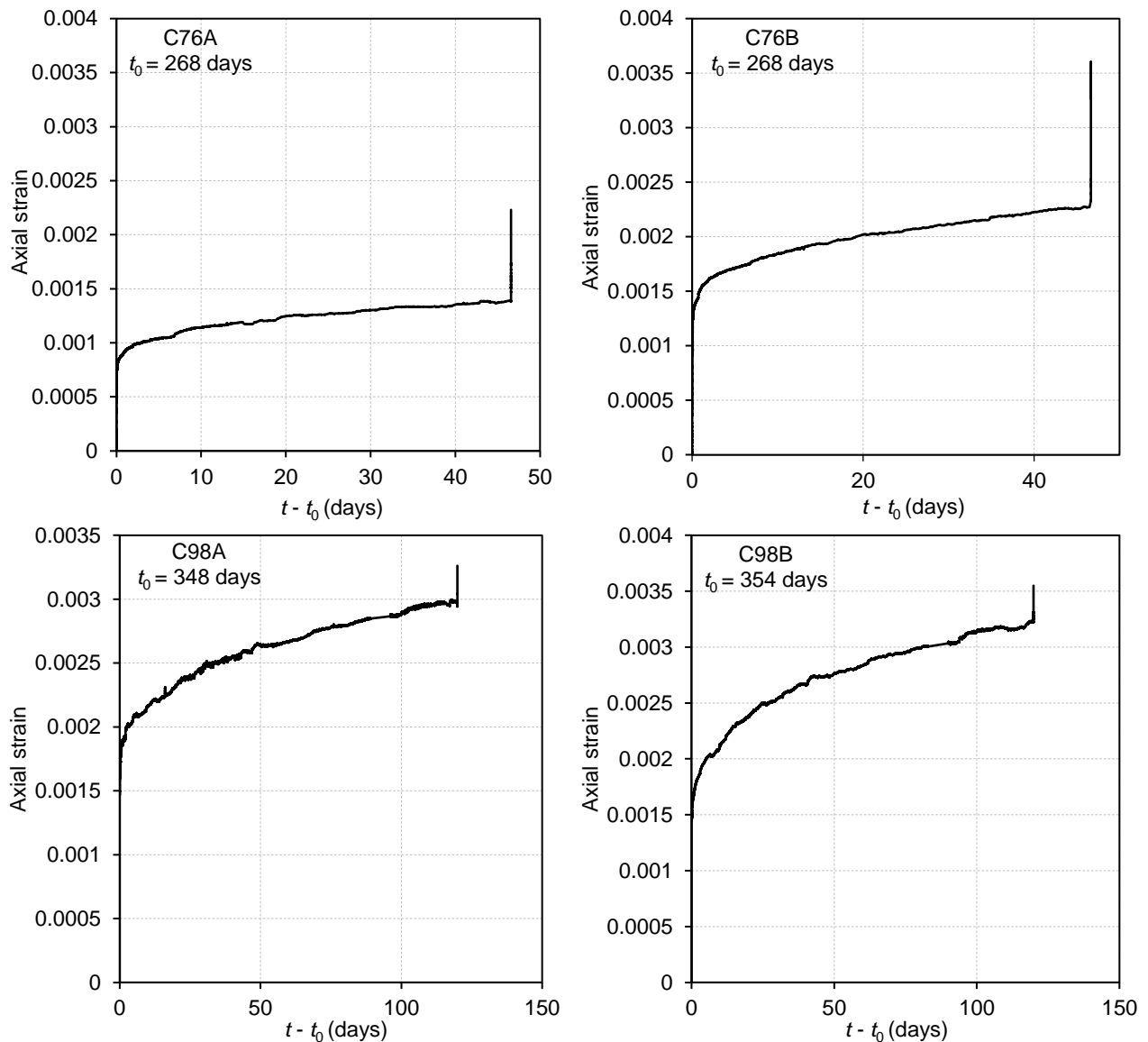


Figure 4.10 Strain history of Specimens C76A, C76B, C98A, and C98B.

Table 4.4 Characteristic concrete strains for Specimens C76A, C76B, C98A and C98B

Test	Axial strain at t_0	Axial strain at end of sustained load	Transverse strain at t_0	Transverse strain at end of sustained load	Axial failure strain at peak load	Transverse failure strain at peak load
C76A	0.000742	0.00138	0.000170	0.000111	0.00221	0.000216
C76B	0.00122	0.00227	0.000277	0.000326	0.00335	0.000767
C98A	0.00138	0.00295	0.000531	0.00169	0.00326	0.00227
C98B	0.00142	0.00323	0.000432	0.00183	0.00355	0.00227

The measured axial strains during the sustained loading contains both creep and shrinkage strains. However, because the specimens were loaded at an age greater than 250 days, most ultimate shrinkage strain of concrete has already been completed prior to the testing. Accordingly, the change in shrinkage strain according to ACI 209 (2008) was negligible compared with the creep strain. More detailed discussions regarding the estimation of shrinkage strains is presented in Section 6.1. Due to the small shrinkage strain increase during sustained loading, a creep coefficient is defined herein as the ratio of measured creep strains during the sustained loading to the axial strain at the beginning of sustained loading.

Figure 4.11 plots the variation of creep coefficient during the sustained loading for Specimens C76A, C76B, C98A, and C98B. For Specimens C76A and C76B, the creep coefficients were nearly the same during the whole sustained concentric loading. At the end of sustained loading ($t - t_0 = 47$ days), the creep coefficient was equal to 0.86 for both columns, even if they had different transverse reinforcement ratios. Thus, the effect of transverse reinforcement ratio on creep coefficient was not obvious for the sustained load level of $P_{\text{sus}}/N_{u, \text{ACI}} = 0.76$. However, for Specimens C98A and C98B, the effects of column transverse reinforcement on creep coefficient was notable, as shown in Figure 4.11. Transverse reinforcement is engaged in confining concrete when concrete axial strain becomes greater than

0.0015 (Sheikh and Uzumeri, 1980). At $t - t_0 = 1$ hour, 1 day, and 7 days, the creep coefficient of C98B ($\rho_t = 0.78\%$), the creep coefficient of C98B was 77%, 51%, and 28% less than the creep coefficient of C98A ($\rho_t = 0.26\%$). Because the sustained loading of C98B started only 6 days later than C98A, the loading age difference should not contribute to the difference in creep coefficient. The creep coefficient discrepancy decreased with time. At the end of sustained loading ($t - t_0 = 120$ days), the creep coefficients were similar: 1.14 for Specimen C98A and 1.13 for Specimen C98B. Moreover, at $t - t_0 = 47$ days (the sustained loading duration of Specimen C76A and C76B), the creep coefficient was 0.88 and 0.82 for C98A and C98B, which is close to the creep coefficient of 0.86 for C76A and C76B. Although the sustained load level for Specimens C98A and C98B was greater than Specimens C76A and C76B, the 80-days difference in loading age (t_0) affected the creep coefficient. The greater loading age caused lower creep strains. However, the greater sustained load level caused greater creep strains. Overall, the creep coefficient for Specimens C98A and C98B was almost the same as Specimens C76A and C76B after experienced the same sustained loading duration ($t - t_0$). On the other hand, Specimens C76A and C76B had different initial axial strain at the end of initial short-time loading but did not cause a significant difference in creep coefficient.

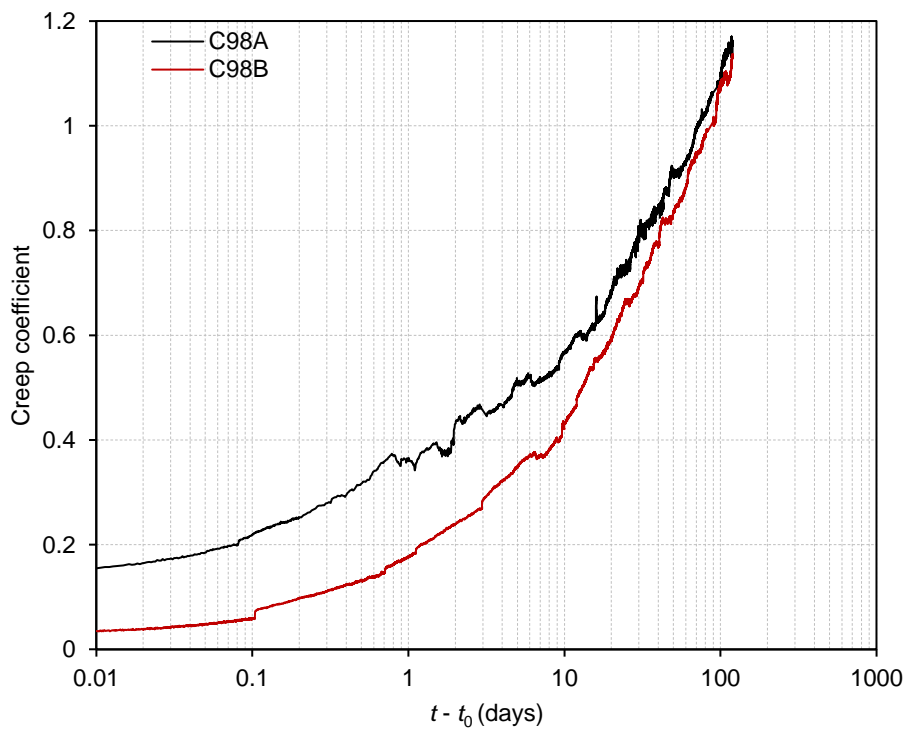
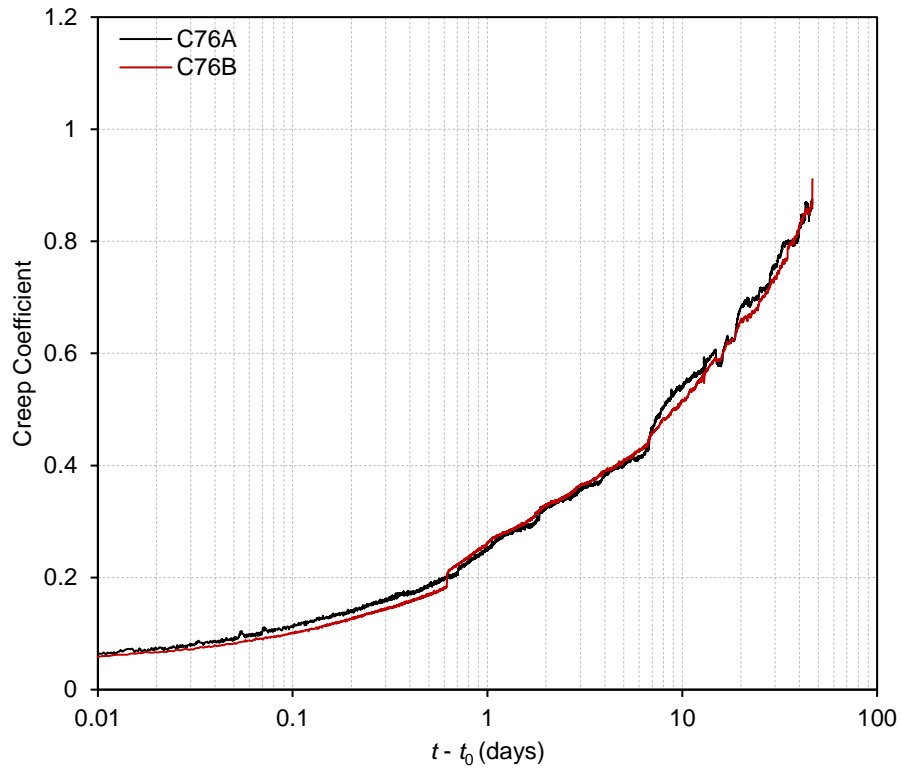


Figure 4.11 Creep coefficient during sustained loading for Specimens C76A, C76B, C98A, and C98B.

4.3.2.3 Load-Strain Response and Failure Mode

Figure 4.12 plots the load-axial concrete strain and load-volumetric concrete strain responses. The blue dashed lines indicate $N_{u,ACI}$, the nominal short-term strength of RC columns, determined based on the cylinder concrete compressive strength at the time of initial loading. The nominal short-term strength was estimated as $N_{u,ACI} = 154$ kips for C76A and C76B, and $N_{u,ACI} = 151$ kips for C98A and C98B.

Due to the greater loads applied to Specimens C98A and C98B, they demonstrated an obvious nonlinear load - axial strain response during the initial short-time loading. The load plateau in Figure 4.12 corresponds to the sustained loading stage. The third portion of a load-strain response corresponds to the final short-time loading to failure after 47 days of sustained loading for Specimen C76A and C76B and 120 days for C98A and C98B. For all RC specimens, the reloading stiffness was slightly greater than the initial loading stiffness. The peak load achieved in this loading stage was 172 kips ($1.12N_{u,ACI}$), 178 kips ($1.16N_{u,ACI}$), 180 kips ($1.19N_{u,ACI}$), and 170 kips ($1.13N_{u,ACI}$) for C76A, C76B, C98A, and C98B, respectively. The results showed that the previously experienced sustained loading did not negatively affect the subsequent axial loading capacity of the RC columns. Instead, on average, the load capacity was increased by 15% due to the sustained loading. This type of strength gain is consistent with the findings made from the tests of plain concrete columns and can be explained by concrete consolidation during the sustained loading. As described in Section 4.2.2.3, sustain loading of 22 days increased the axial strength by 5.8% and 7.5% for Specimens P77 and P90.

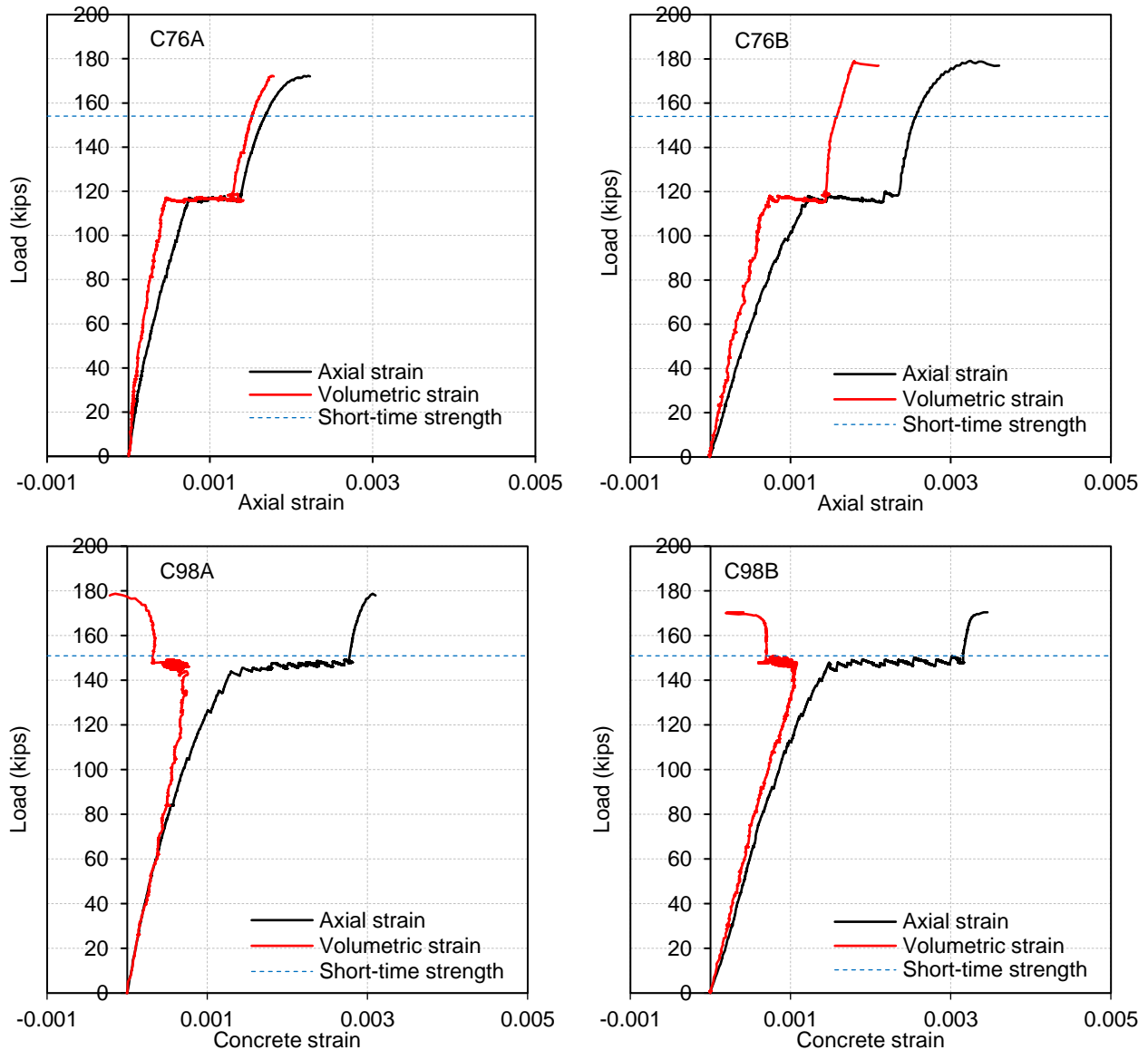


Figure 4.12 Load-strain response of Specimens C76A, C76B, C98A, and C98B.

The concrete strain at the peak load during the reloading process was between $\epsilon_{c0} = 0.00221$ and 0.00346 . Chovichien et al. (1973) suggested Equation (4.4) for estimating this type of strain, which was assumed only as a function of sustained loading time without considering other variables such as concrete age. The measured ϵ_{c0} for Specimens C76A, C76B, C98A, and C98B was about 36%, 5.2%, 18.8%, and 8.2% less than that predicted by Equation (4.4).

$$\varepsilon_o(t) = 0.002 + 0.000851 \log_{10}(t+1), \text{ for } t \leq 730 \quad \text{Equation (4.4)}$$

where t is time under sustained loading (in days).

Concrete volumetric strain in the RC columns was computed in the same way as plain concrete specimens and shown in Figure 4.12. For Specimens C76A and C76B, the volumetric strain consistently increased with the increased axial strains measured along the time of sustained loading. For Specimens C98A and C98B, the volumetric strain initially increased with loads during the initial short-time loading. When the load was approaching the target sustained load, the volumetric strain started decreasing and kept being reduced during the following sustained loading. Thus, the change of volumetric strain depends on the sustained stress level $P_{sus}/N_{u,ACI}$, where P_{sus} is applied sustained load. The trend of volumetric strain bifurcates between $0.76 < P_{sus}/N_{u,ACI} < 0.98$. If $P_{sus}/N_{u,ACI} < 0.76$, the volumetric strain increases as the axial strain increases with time; if $P_{sus}/N_{u,ACI} > 0.98$, the volumetric strain decreases as the axial strain increases with time.

Figure 4.13 shows the five RC specimens after failure. The application of sustained loading has no impact on the failure mode, which was the same as that observed in the short-time concentric loading tests of RC columns with various transverse reinforcement ratios performed by Sheikh and Uzumeri (1980).

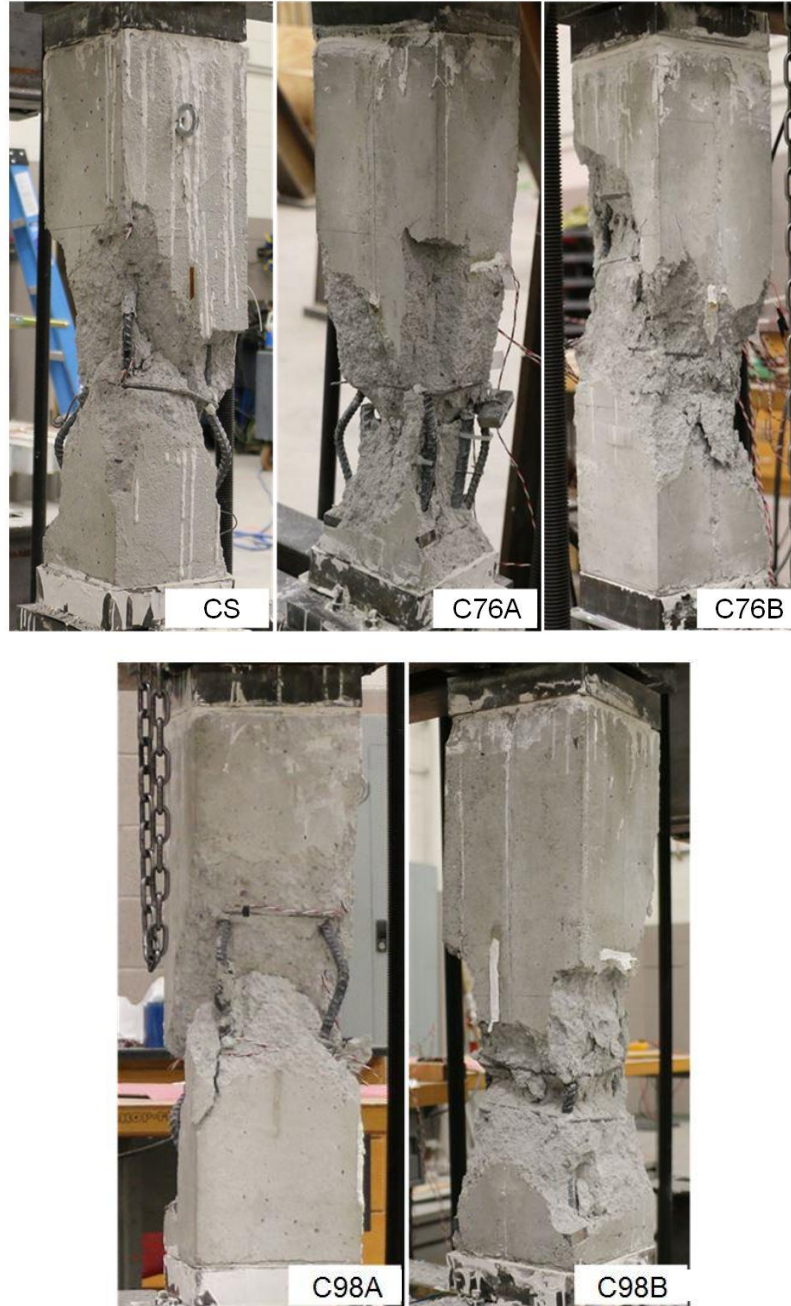


Figure 4.13 RC column specimens after failure.

4.3.2.4 Transverse Strain and Poisson's Ratio History

Figure 4.14 shows the history of transverse strain of concrete cover measured at column mid-height (ϵ_{ct}) during sustained concentric loading with the starting time at ($t - t_0 = 0.01$ days). ϵ_{ct} changed little in Specimen C76B and slightly decreased in Specimen C76A during the

sustained loading. This explains that although the two specimens had different transverse reinforcement ratios, the transverse strain creep response of two specimens was almost the same. In contrast, for Specimen C98A and C98B, the transverse strain ε_{ct} increased over time during the sustained loading. When the time of sustained loading increased ($t - t_0$), the difference between the two creep coefficients was reduced. This phenomenon was consistent with the creep coefficient response shown in Figure 4.11. It is not clear why the transverse reinforcement in Specimen C98B became less effective in restraining the transverse strain of concrete cover as the sustained loading time increased. In addition, the distinctively different transverse strain history under two different levels of sustained load affected the transverse failure strain at the peak load during the following reloading stage, as shown in Table 4.4. The transverse failure strains at the peak load in Specimens C76A and C76B were smaller than in Specimens C98A and C98B.

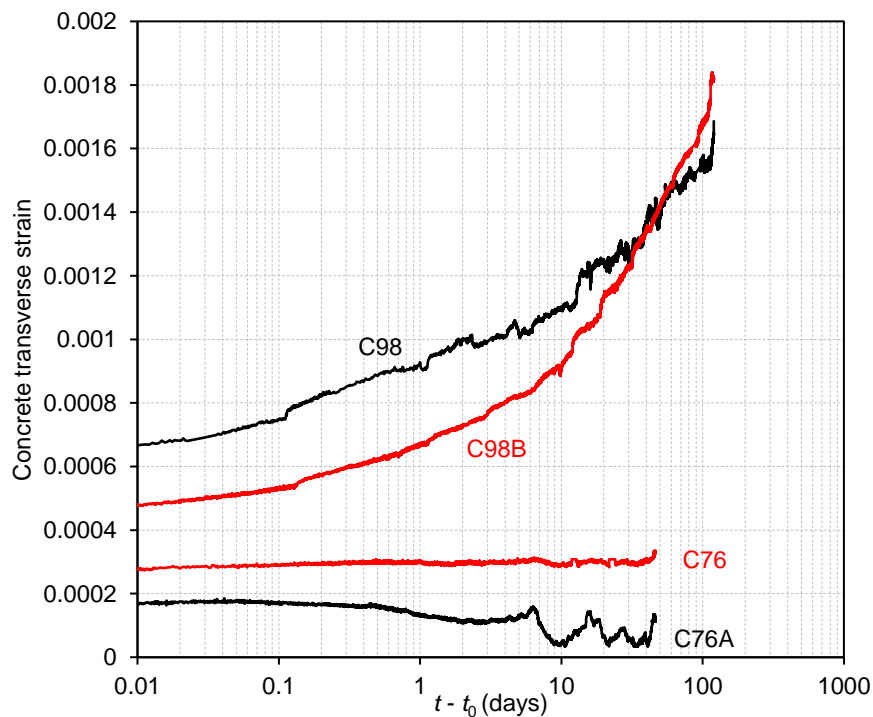


Figure 4.14 Transverse strain history of concrete cover during sustained concentric loading for Specimens C76A, C76B, C98A, and C98B.

Figure 4.15 shows the history of Poisson's ratio (ν) measured at the concrete cover during sustained loading of the four RC specimens with the starting time at ($t - t_0 = 0.01$ days). The Poisson's ratio of concrete cover was calculated based on the ratio of measured transverse strain shown in Figure 4.14 to the measured average axial strain shown in Figure 4.10. The variation trend of Poisson's ratio was similar to that of concrete transverse strain shown in Figure 4.14. For Specimens C76A and C76B, ν was equal to 0.23 at the beginning of sustained loading t_0 and decreased during the sustained loading. For Specimens C98A and C98B, ν was equal to 0.29 and 0.21 at t_0 . After one day of sustained loading, the Poisson's ratio reached 0.37 in Specimen C98A and 0.28 in Specimen C98B. The difference in Poisson's ratio between Specimens C98A and C98B decreased as the sustained loading time increased. Poisson's ratio reached 0.45 in C98A and 0.42 in Specimen C98B at the end of sustained loading after 120 days. The variation trend of ν was consistent with the conclusions made from the tests of young concrete material (Shah and Chandra, 1970; Mazzotti and Savoia, 2002). When the sustained stress level (σ_c / f_c') was greater than 0.8, the Poisson's ratio of concrete increased over time. In contrast, the Poisson's ratio of concrete remained unchanged or even decreased when the sustained load stress level was moderate.

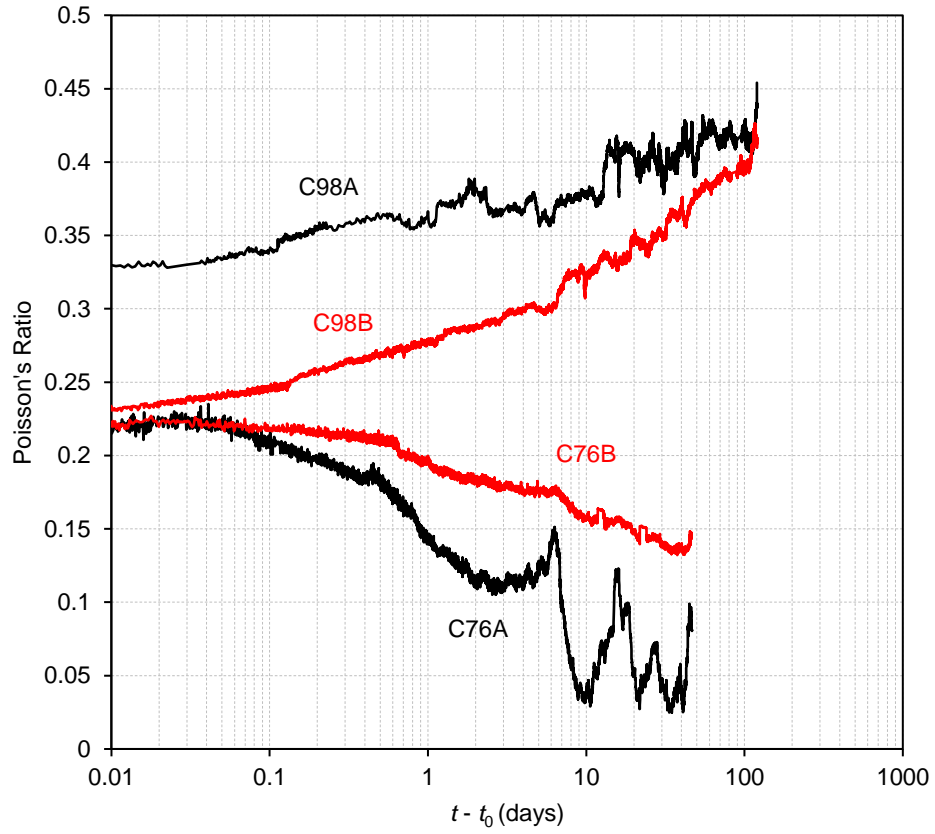


Figure 4.15 Poisson's ratio history during sustained loading for Specimens C76A, C76B, C98A, and C98B.

CHAPTER 5

EXPERIMENTAL RESULTS OF COLUMNS SUBJECTED TO SUSTAINED ECCENTRIC LOADING

5.1 Introduction

Five square columns with the same height-to-width ratio of $H/h = 10.8$ were tested. The tests started at concrete ages greater than 540 days. The sustained loading durations were chosen based on test observations and time restraint. This chapter presents the test data of the five specimens, including loading history, load-strain response, axial and transverse strains, deflection at column mid-height, load-deflection relationship, moment-axial load response, moment-curvature response, creeps for deflection and curvature, concrete transverse strain history, Poisson's ratio history, and failure modes.

5.2 Loading History

Specimens E98A17, E100B17, E77A25, and E92A25 did not fail during the sustained eccentric loading tests. Only one specimen, E99A17, failed during sustained loading. In the specimen designations, E stands for eccentric loading. The number (e.g. 98) represents a percentage ratio of column mid-height moment at the beginning of sustained loading to the unfactored nominal short-time flexural capacity, $M_{u,ACI}$, defined based on the ACI 318-19 (2019) after considering axial force-moment interaction. Specimens E98A17, E100B17, and E92A25 underwent three loading stages: (1) initial short-time loading, (2) sustained loading, and (3) loading to failure in a short time. Specimen E99A17 only experienced the first two loading stages because it failed during a load adjustment after two days of sustained loading. Specimen E77A25 was first loaded to approximately 55.5 kips, which caused a mid-height moment of 0.77

$M_{u,ACI}$ and was maintained for 11 days. The sustained load applied to E77A25 was then adjusted to the same sustained load as in Specimen E92A25 on the 12th day of the sustained loading; the increased sustained loading in this specimen lasted for 17 days.

Table 5.1 shows loading details of the five RC columns subjected to sustained eccentric loading. Figure 5.1 shows loading history. At $t_0 = 547, 603, 604, 628,$ and 629 days, E98A17, E100B17, E99A17, E77A25, and E92A25 were loaded to 86.9, 86.0, 81.3, 81.4, 55.6, and 60.6 kips within 112, 182, 59, 42.2, and 46.6 minutes, respectively. The initial loading caused a column midspan moment M of 104 kip-in ($0.98M_{u,ACI}$), 108 kip-in ($M_{u,ACI}$), 109 kip-in ($0.99M_{u,ACI}$), 95.4 kip-in ($0.77M_{u,ACI}$), 111 kip-in ($0.92M_{u,ACI}$) in E98A17, E100B17, E99A17, E77A25, and E92A25, respectively. During the sustained loading, the average load was 86.1, 86, 80.5, and 60.8 kips for E98A17, E100B17, E99A17, and E92A25. For Specimen E77A25, the average load was 55.9 kips for the first 11 days and 61.8 kips for the remaining 17 days during the second sustained loading stage. For each specimen, the largest load drop occurred during the first day following the initial application of sustained loads. After that, the sustained load was well maintained, as indicated in Figure 5.1. During reloading, the peak load was 92.2, 91.9, 73.0, and 65.4 kips or Specimens E98A17, E100B17, E77A25, and E92A25, respectively.

Table 5.1 Loading details for Specimen E98A17, E100B17, E99A17, E77A25, and E92A25.

Specimen	Time of initial loading (mins)	Average sustained load (kips)	Maximum sustained load (kips) and % change	Minimum sustained load (kips) and % change	Peak load (kips)
E98A17	112	86.1	87.7 (1.9%)	84.2 (-2.2%)	92.2
E100B17	182	86.0	87.5 (1.7%)	84.8 (-1.4%)	91.9
E99A17	59	80.5	81.6 (1.4%)	78.6 (-2.4%)	81.2
E92A25	46.6	60.8	62.6 (3%)	58.5 (-3.8%)	65.4
E77A25	42.2	55.9 (in the first 11 days) 61.8 (for remaining 17days)	57.5 (2.9%) 62.6 (1.3%)	54.6 (-2.3%) 60.9 (-1.5%)	73.0

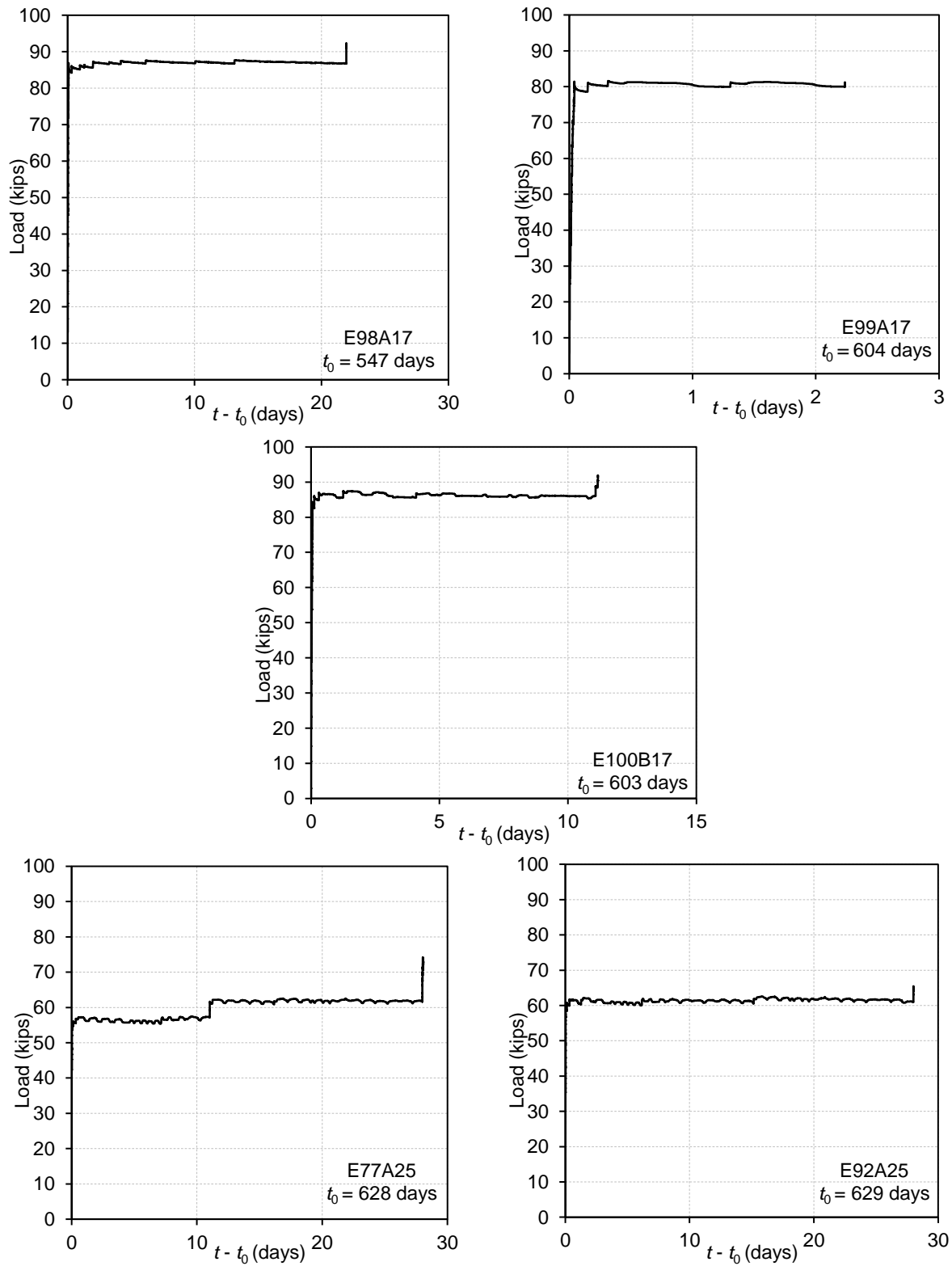


Figure 5.1 Loading history of column specimens subjected to sustained eccentric loading.

5.3 Load-Strain Relationship and Strain History

The axial concrete strain at compression face of Specimen E98A17 and the tensile bar strain in Specimen E77A25 could not be obtained due to strain gauge malfunction. Figure 5.2 shows load versus column mid-height axial strains measured in Specimens E99A17, E100B17, E77A25, and E92A25 at four locations, including tension face, tensile reinforcement, section mid-depth at side faces, and compression face. Positive sign in Figure 5.2 stands for compressive strain. Except for Specimen E77A25, the concrete strain at mid-depth of the side faces was approximately equal to the average of the concrete strains measured at the compression and the tension faces. The measured axial strains indicate that plane section assumption was approximately held during the short-time loading. Moreover, the resultant force of bearing stress at the pin supports was aligned with pin center; otherwise, the measured strain at the tension surface would deviate from the nominal strain calculated by Equation (5.1) for the columns with an elastic response. In Equation (5.1), P is the load measured by the load cell; e is the eccentricity of load; E_c is elastic modulus of concrete; h is the depth of cross section. The strain measurements were used to partially validate the eccentricity ratios defined for the specimens. For Specimens E99A17, and E100B17, the eccentricity ratio was $e/h = 0.17$. When the load was low, columns behaved elastically, and the second order effect of column was negligible. The concrete tensile strain calculated by Equation (5.1) should approximately equal to zero at the beginning of short-time loading when the load P was less than 25 kips. When the load increased, the deflection at the mid-height of the columns increased, making the eccentricity ratio $e/h > 0.17$. The tensile strain was not equal to zero and increased as the load increase. For Specimen E77A25 and E92A25, the initial eccentricity ratio was $e/h = 0.25$. According to Equation (5.1), the initial strain at the tension face should be less than zero. However, based on the plane section

assumption, the axial strain in the tensile reinforcement of columns shall be approximately equal to zero. This was achieved in Specimen E92A25, as shown in Figure 5.2.

$$\varepsilon_t = \frac{P}{E_c h^2} \left(1 - 6 \frac{e}{h}\right) \quad (5.1)$$

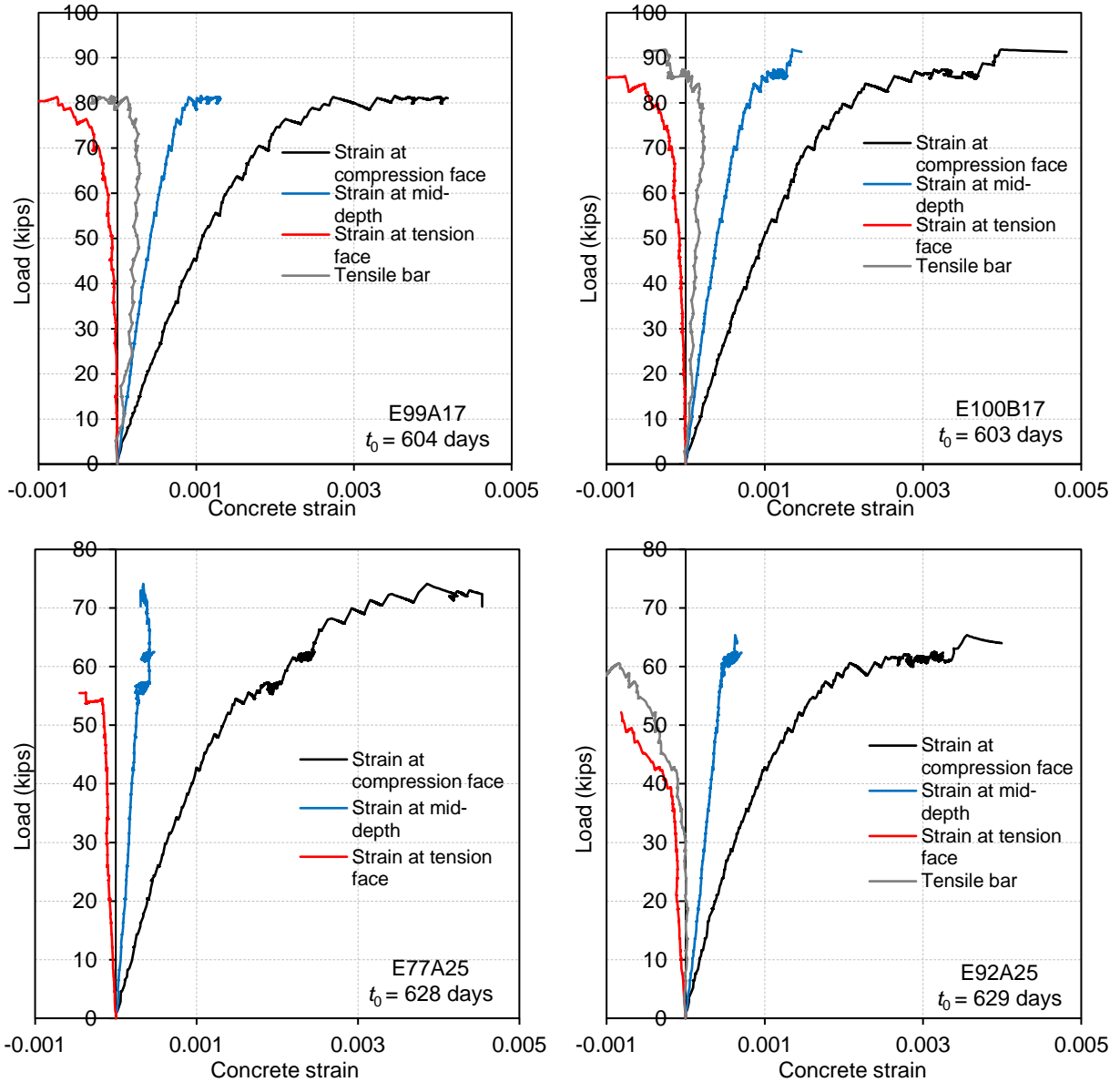


Figure 5.2 Load-strain relationship of Specimens E100B17, E99A17, E77A25, and E92A25.

Figure 5.3 plots the history of concrete strain on the compression face of Specimens E100B17, E99A17, E77A25, and E99A25. Due to concrete cracking, the strain gauges attached to the tension face were broken at 2117, 214.7, 60.6, 42.2, and 31.3 minutes after the load has been applied to Specimens E98A17, E100B17, E99A17, E77A25, and E92A25, respectively.

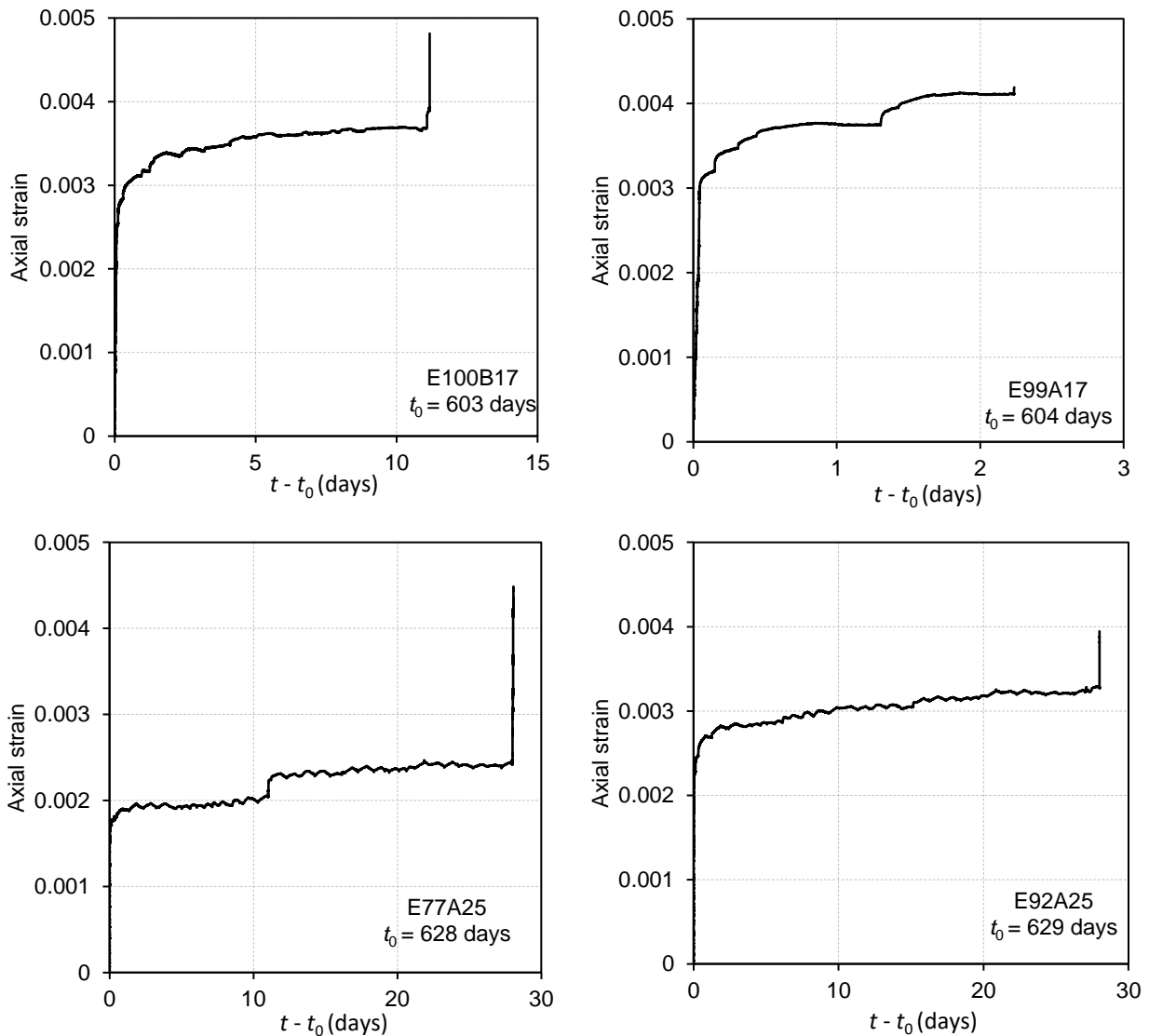


Figure 5.3 Strain history at compression face of Specimens E100B17, E99A17, E77A25, and E92A25.

Table 5.2 summarizes the concrete strains, including both axial and transverse strains, on the compression face of the specimens. The initial axial strain at the beginning of sustained loading was 0.00264, 0.00273, 0.00164, and 0.00208 in Specimens E100B17, E99A17, E77A25, and E92A25, respectively. During the first day of sustained loading, the concrete axial strain increased rapidly by 20.3%, 37.4%, 15.6%, and 29.9% in E100B17, E99A17, E77A25, and E92A25. As the sustained loading time increased, the rate of strain increase was reduced. By the end of the sustained loading, the axial strain reached 0.00368, 0.00242 and 0.00329 in Specimens E100B17, E77A25, and E92A25. At failure, the axial compressive strain reached 0.00482, 0.00417, 0.00454, and 0.00394 for Specimens E100B17, E99A17, E77A25, and E92A25. The axial failure strain of all specimens was close to or exceeded 0.004, which were greater than the failure strains (ranging from 0.00223 to 0.00360 as shown in Table 4.4) of the RC short columns subject to sustained concentric loading.

Table 5.2 Concrete strain at characteristic loading stages of eccentrically loaded columns.

Specimen	Axial strain at beginning of sustained load	Axial strain at end of sustained load	Transverse strain at beginning of sustained load	Transverse strain at end of sustained load	Axial failure strain	Transverse failure strain
E98A17	—	—	0.000719	0.00225	—	0.00323
E100B17	0.00264	0.00368	0.00117	0.00183	0.00482	0.00283
E99A17	0.00273	—	0.00137	—	0.00417	0.00359
E77A25	0.00164	0.00242	0.000306	0.00122	0.00454	0.00208
E92A25	0.00208	0.00329	0.000806	0.00137	0.00394	0.00202

The measured axial strain during sustained loading contains both creep and shrinkage strains. However, because the specimens were loaded at ages greater than 547 days, most ultimate shrinkage strain of concrete was completed prior to the loading. Thus, compared with creep strain, the change in shrinkage strain was negligible according to ACI 209 (2008).

When the peak load was reached, the strains in tensile reinforcement were 0.000381, 0.000259, 0.000321, 0.00468, 0.0017 for Specimens E98A17, E100B17, E99A17, E77A25, and E92A25. Except for Specimen E77A25, all the tensile reinforcements did not yielded ($\varepsilon_y = 0.00230$). Therefore, the failure of Specimens E98A17, E100B17, E99A17, and E92A25 was governed by concrete crushing. Viest et al. (1956) observed that the ultimate concrete strain after experiencing sustained loading may be approximately by superimposing the concrete ultimate strain under short-time loading with the creep strain under sustained loading. This conclusion, however, was made from 12 column tests with only one column loaded at an age greater than 90 days ($t_0 > 90$ days) and thus examined by the test data obtained from this study. For Specimens E100B17, E77A25, and E92A25, after subtracting the creep strains from the ultimate strain after experiencing the sustained loading, the concrete ultimate strain becomes 0.00378, 0.00376, and 0.00273, with an average ultimate strain of 0.00342, which is close to the typical concrete ultimate strains under short-time loading.

5.4 Deflection at Column Mid-height and Load-Deflection Relationship

Figure 5.4 plots the history of mid-height deflection. The deflection at the beginning of sustained loading was 0.198, 0.252, 0.343, 0.216, and 0.322 in. for Specimens E98A17, E100B17, E99A17, E77A25, and E92A25, respectively. During the first day of sustained loading, the deflection increased rapidly by 33.6%, 36.3%, 37.4%, 15.6%, and 29.9% in E98A17, E100B17, E99A17, E77A25, and E92A25. From $t - t_0 = 18$ days for E98A17, 6 days for E100B17, 17 days for E77A25, and 20 days for E92A25, the daily deflection increase become less than 0.002 in. The deflections at the end of sustained loading were 0.425, 0.392, 0.520, 0.326, and 0.503 in. for Specimens E98A17, E100B17, E99A17, E77A25, and E92A25.

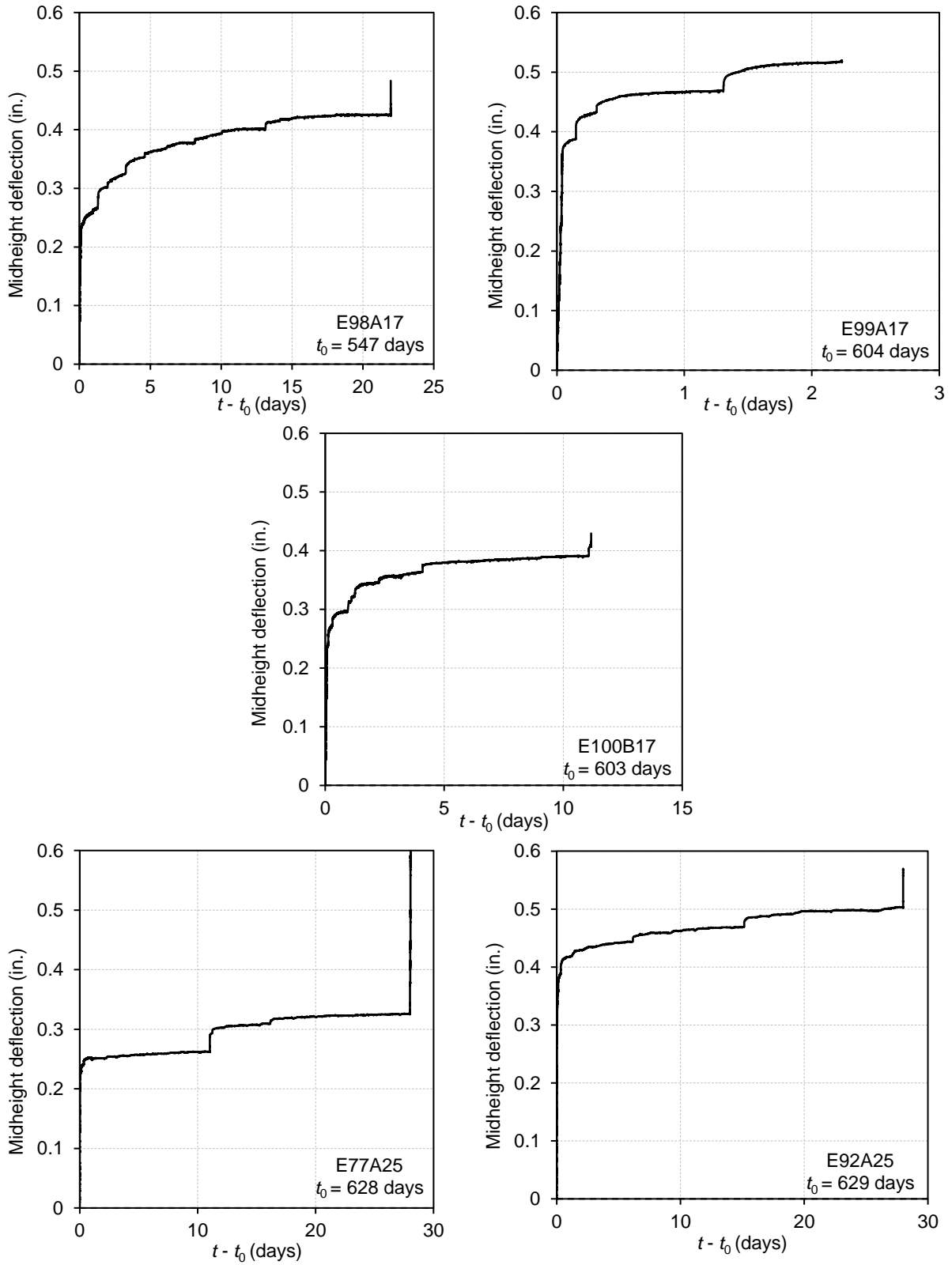


Figure 5.4 Mid-height deflection history of column specimens subjected to sustained eccentric loading.

The percentage increase in mid-height deflection during sustained loading was 115% in 22 days for Specimen E98A17, 55.2% in 11 days for Specimen E100B17, 51.6% in 2 days for Specimen E99A17, 50.9% in 28 days for Specimen E77A25, and 56.2% in 28 days for Specimen E92A25. The mid-height deflection at the peak load was 0.452, 0.413, 0.520, 0.524, and 0.528 in. for Specimens E98A17, E100B17, E99A17, E77A25, and E92A25, respectively.

Figure 5.5 plots the load-deflection relationship for Specimen E98A17, E100B17, E99A17, E77A25, and E92A25. For Specimen E77A25, the sustained load with an average of 55.9 kips was maintained for 11 days, over which the mid-height deflection was increased by 0.047 in. The sustained load was then adjusted to 61.6 kips on the 12th day. The increase in mid-height deflection for the remaining 17 days of sustained loading was 0.0420 in. For Specimen E92A25 with an average sustained load of 60.8 kips, the increase in mid-height deflection for the last 17 days of sustained loading was 0.0389 in., which was approximately equal to the mid-height deflection increase in Specimen E77A25 from the 12th day to the end of sustained loading.

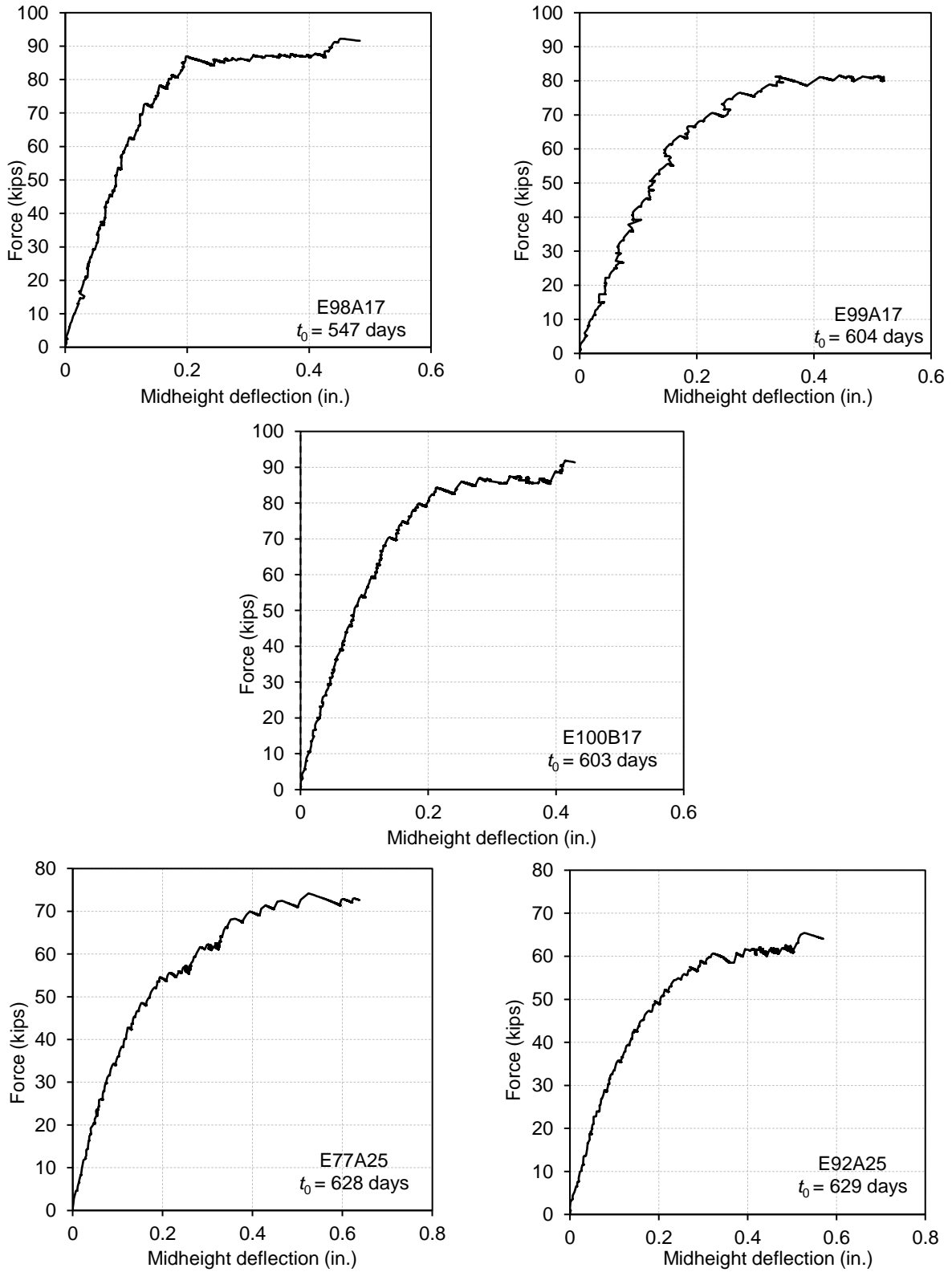


Figure 5.5 Load-deflection relationship of column specimens subjected to sustained eccentric loading.

5.5 Axial Load – Mid-Height Moment Response

Figure 5.6 plots the axial load - moment response at column mid-height for the column specimens subjected to sustained eccentric loading. For comparison purpose, the short-time axial load-interaction diagram (nominal strength) calculated according to ACI 318-19 (2019) was also plotted in Figure 5.6. Table 5.3 summarizes the column mid-height moment at characteristic loading stages.

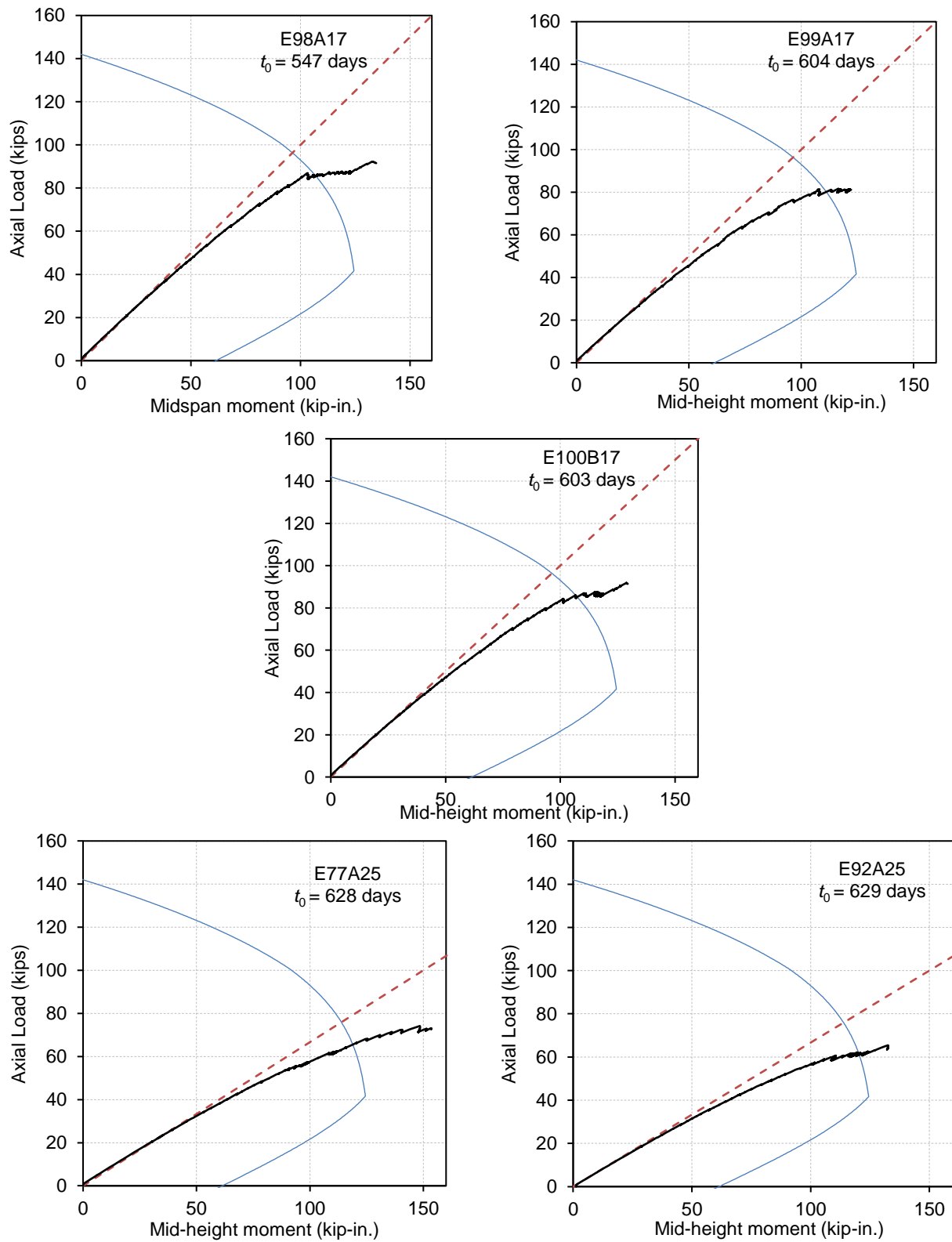


Figure 5.6 Axial load-moment response of column specimens subjected to sustained eccentric loading.

Table 5.3 Mid-height moment at characteristic loading stages of eccentrically loaded columns.

Specimen	M at beginning of sustained load (kip-in.)	M at end of sustained load (kip-in.)	M increase (%) during sustained load	M at peak load (kip-in.)	Nominal strength (M) calculated by ACI 318	Ultimate moment capacity increase (%)
E98A17	103	122	19%	133	100	33%
E100B17	107	118	10%	129	101	28%
E99A17	108	—	—	122	109	12%
E77A25	94	111	18%	149	111	34%
E92A25	109	121	11%	131	117	12%

Specimens E98A17 and E100B17 were subjected to similar average sustained loads (86.1 and 86 kips) and both loaded after 540 days of concrete casting. The average concrete cylinder strength varied in a narrow range after 540 days. The only difference was that Specimens E98A17 and E100B17 were subjected to sustained loading for 22 and 11 days. The column mid-height moment at the peak axial load, $M_u = 1.33M_{u,ACI}$ and $1.28M_{u,ACI}$ for Specimens E98A17 and E100B17. The different sustained loading durations may explain the similar flexural capacity of the two specimens although they had different transverse reinforcement ratios. As described in Chapter 4, for the concentrically loaded RC column CS, the confinement effect enhanced its short-time strength by approximately 10%. However, this effect should be less pronounced in the flexural strength of an eccentrically loaded column. The extra strength of E98A17 and E100B17 beyond $M_{u,ACI}$ can be partially attributed to the strength increase due to the previously applied sustained loads. Specimen E99A17 endured the sustained load for only 53 hours and failed with $M_u = 1.12M_{u,ACI}$ when a load adjustment was made. The extent of strength increase from $M_{u,ACI}$ was the lowest among three columns with an eccentricity ratio of 0.17 due to the short sustained loading period.

Specimen E77A25 with $e/h = 0.25$ was initially loaded to 55.5 kips, resulting in a mid-height moment of $M = 0.77M_{u,ACI}$. At $t - t_0 = 11$ days, the mid-height moment increased by 5.5%.

The load was then increased to 61.6 kips at the 12th day, causing $M = 0.91M_{u,ACI}$. During the second sustained loading of 17 days, the mid-height moment increased by only 2.5%. The low deflection increase in both loading stages made the sustained loading effect almost indiscernible in Figure 5.6. When reloaded, Specimen E77A25 failed at $M_u = 1.34M_{u,ACI}$. Specimen E92A25 was initially loaded to 60.7 kips, resulting in a mid-height moment of $M = 0.92M_{u,ACI}$. The mid-height moment in E92A25 increased by 8.7% at $t - t_0 = 11$ days and 11% after 28 days of sustained loading. During the subsequent reloading, Specimen E92A25 failed at $M_u = 1.12M_{u,ACI}$. Overall, the flexural capacity of all the columns exceeded the computed nominal moment strength, as shown in Table 5.3.

5.6 Moment - Curvature Response

Figure 5.7 plots the moment-curvature relationship of the column specimens. Based on the plane section assumption, the axial strains measured at the mid-depth and compression face were used to calculate column mid-height curvature. The curvature was calculated by Equation (5.2), where ε_c is concrete strain at column compression surface, ε_m is strain at section mid-depth, and h is the depth of column cross section. For Specimen E98A17, because the strain gauge was broken at the compression face, its curvature was determined from the axial strains measured in the tensile reinforcement and the strain at section mid-depth, as shown in Equation (5.3). In Equation (5.3), ε_{st} is the strain of tensile reinforcement and $l_s/2$ is the distance between tensile reinforcement to section mid-depth.

$$\Phi = \frac{\varepsilon_c - \varepsilon_m}{h / 2} \quad (5.2)$$

$$\Phi = \frac{\varepsilon_m - \varepsilon_{st}}{l_s / 2} \quad (5.3)$$

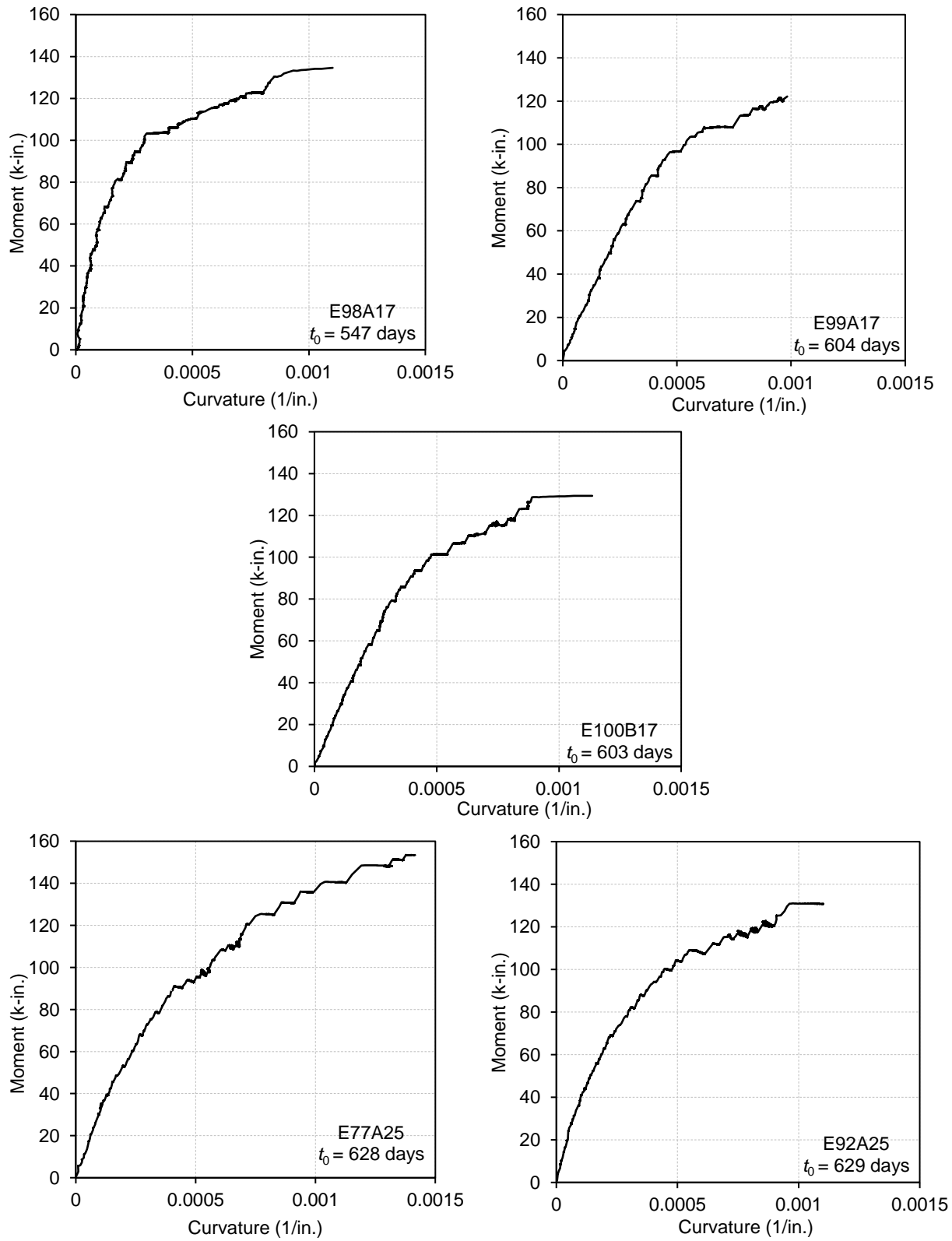


Figure 5.7 Moment-curvature relationship of column specimens subjected to sustained eccentric loading.

The curvature at characteristics loading stages for Specimen E98A17, E100B17, E99A17, E77A25, and E92A25 were summarized in Table 5.4. The curvature at peak load for specimens with eccentricity ratio $e/h = 0.25$ was greater than the specimens with $e/h = 0.17$. The failure curvature of the specimen with a higher transverse reinforcement ratio (E100B17) was greater than that of Specimens E98A17 and E99A17. The sustained loads applied to Specimen E98A17 and E100B17 were the same. For Specimen E98A17, the percentage curvature increase after 11 days of sustained loading was 162%; however, for Specimen E100B17, the increase of curvature after 11 days of sustained loading was only 71.3%. Thus, higher transverse reinforcement ratio can reduce the curvature of specimens during sustained loading.

Table 5.4 Curvature at characteristic loading stages of eccentrically loaded columns

Specimen	Curvature at beginning of sustained load (1/in.)	Curvature at end of sustained load (1/in.)	Curvature at peak load (1/in.)
E98A17	0.000303	0.000799	0.00110
E100B17	0.000566	0.000817	0.00114
E99A17	0.000619	—	0.000983
E77A25	0.000465 0.000605	0.000554 0.000681	0.00143
E92A25	0.000547	0.000892	0.00110

Specimen E98A17 had the greatest flexural stiffness during the initial loading. However, the stiffness of Specimen E100B17 and E99A17 was similar. During the sustained loading, the column stiffness was approximately constant even though concrete creep softened the columns. A secant flexural stiffness during sustained loading was calculated based on the moments and curvatures at the start and end of sustained loading. This stiffness was nearly identical for Specimens E98A17 and E99A17 during sustained loading. For Specimen E100B17, the reduced transverse reinforcement spacing caused the 21% higher stiffness, which contributed to the lower

creep effects discussed in Section 5.7.

For Specimen E77A25, the percentage curvature increase after 11 days of sustained loading was 19.1%. The percentage curvature increase from the 12th day to the end of the sustained loading was 12.6%. For Specimen E92A25, the curvature increase was 49.7% after the first 11 days of sustained loading and 12.7% for the remaining 17 days of sustained loading. Comparing the results of Specimen E77A25 and E92A25 indicate that different sustained load levels greatly affected column curvature in the first 11 days of sustained loading. However, after the sustained load of Specimen E77A25 was adjusted to approximately the same as that of Specimen E92A25, the percentage curvature increase of the two specimens was almost the same. The curvature at peak load was comparable among E98A17, E99A17, E100B17, and E92A25. Specimen E77A25 achieved higher flexural strength and deformation capacity than E92A25, which may be explained by the different sustained loading histories.

5.7 Creep for Deflection and Curvature

Two types of creep were examined: creep of column mid-height deflection representing global deformation and creep of mid-height curvature representing local deformation. The variation of creep coefficient, ϕ , during sustained loading is shown in Figure 5.8 for the specimens with $e/h = 0.17$, and Figure 5.9 for the specimens with $e/h = 0.25$. Even if E98A17 was loaded 57 days earlier than E99A17, they had similar ϕ during the first two days of sustained loading, as shown in Figure 5.8. This indicates that the difference in loading age was not influential for the eccentrically loaded columns, which were already more than 500-days old at the start of testing. E100B17 had the lowest ϕ among the three specimens with $e/h = 0.17$; however, E99A17 quickly failed within three days of loading. On the other hand, after 10 days of

sustained loading, the ϕ for E100B17 was 45% lower for deflection and 67% lower for curvature than E98A17. Thus, for eccentrically loaded columns carrying a high sustained load, increasing transverse reinforcement ratio can reduce creep deformations.

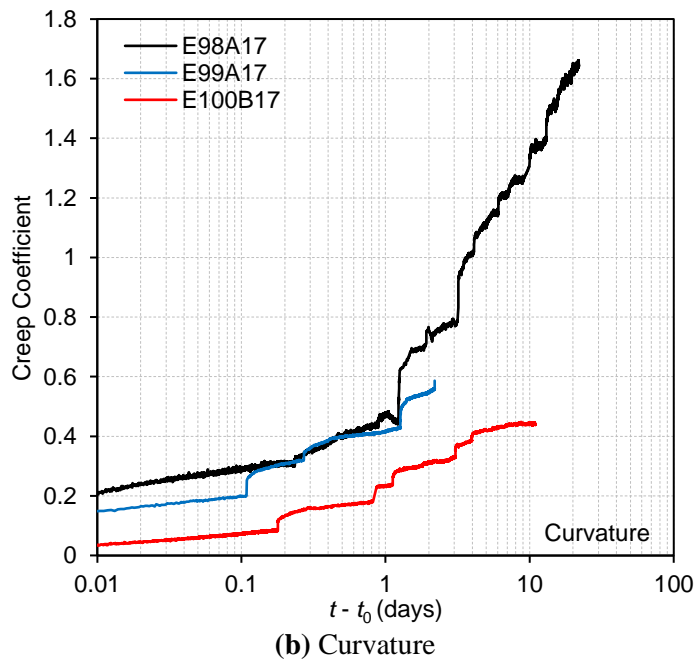
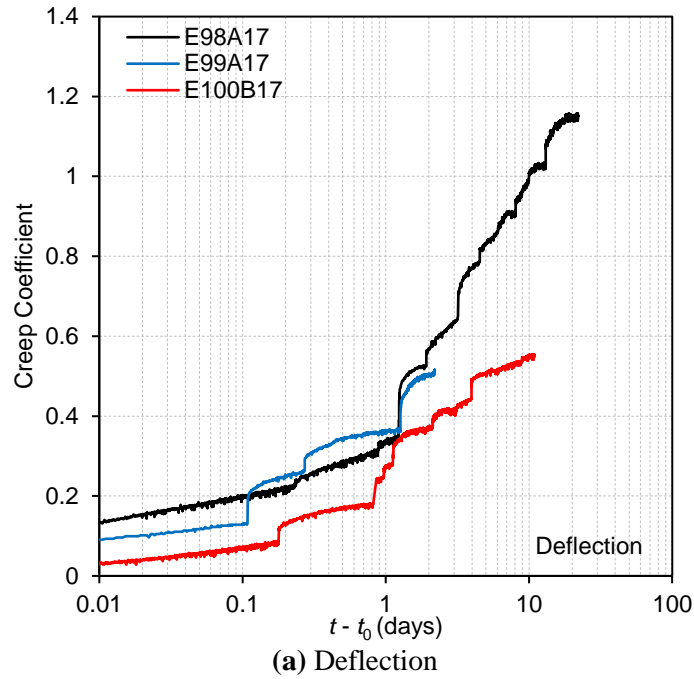
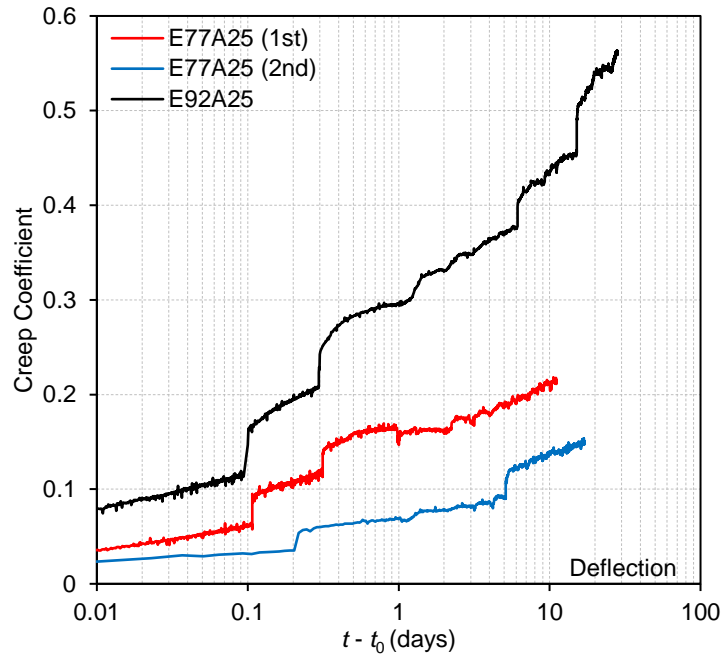
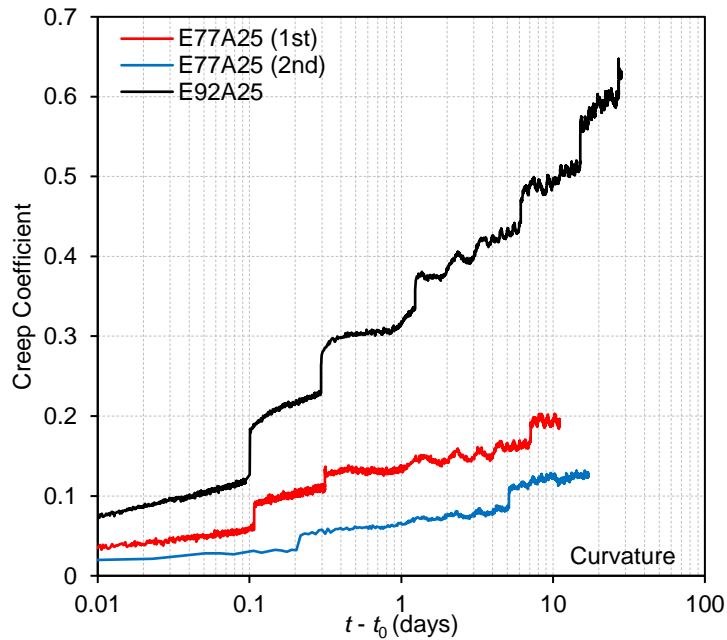


Figure 5.8 Creep coefficient of columns with $e/h = 0.17$.



(a) Deflection



(b) Curvature

Figure 5.9 Creep coefficient of columns with $e/h = 0.25$.

For Specimen E77A25, the creep coefficients were divided into two parts: during the first sustained loading, which started at $t_0 = 629$ days and lasted for 11 days, and during the second sustained loading, which started at $t_0 = 640$ days and lasted for 17 days. Thus, the creep time

histories for the two sustained loading stages are shown separately in Figure 5.9. Due to the lower sustained load, ϕ during the first sustained loading of 11 days was less than 50% of that for Specimen E92A25 loaded with nearly the same duration. For the second sustained loading, even if the load applied to E77A25 resulted in an initial mid-height moment comparable to that of E92A25, the ϕ in terms of both deflection and curvature for E77A25 was lower than in the first sustained loading and much less than that of E92A25. Therefore, the test result of E77A25 indicated that the loading history affect the creep behavior of RC columns – the lower sustained load applied previously reduced the creep deformation caused by the higher sustained load applied later.

5.8 Concrete Transverse Strain History

Figure 5.10 plots concrete transverse strain (ε_{ct}) history at compression face of column mid-height for the column specimens subjected to sustained eccentric loading. Higher level of sustained load caused greater transverse strain. After the initial loading, $\varepsilon_{ct} = 0.00072, 0.00137, 0.00117, 0.00031,$ and 0.00081 in Specimens E98A17, E99A17, E100B17, E77A25, and E92A25, respectively. For Specimen E99A17, ε_{ct} quickly increased to 0.00259 at the end of first day of sustained loading, and $\varepsilon_{ct} = 0.00359$ when this specimen failed during the third day of sustained loading. When E98A17, E100B17, E92A25, and E77A25 failed during reloading, $\varepsilon_{ct} = 0.00323, 0.00283, 0.00202,$ and $0.00208,$ respectively.

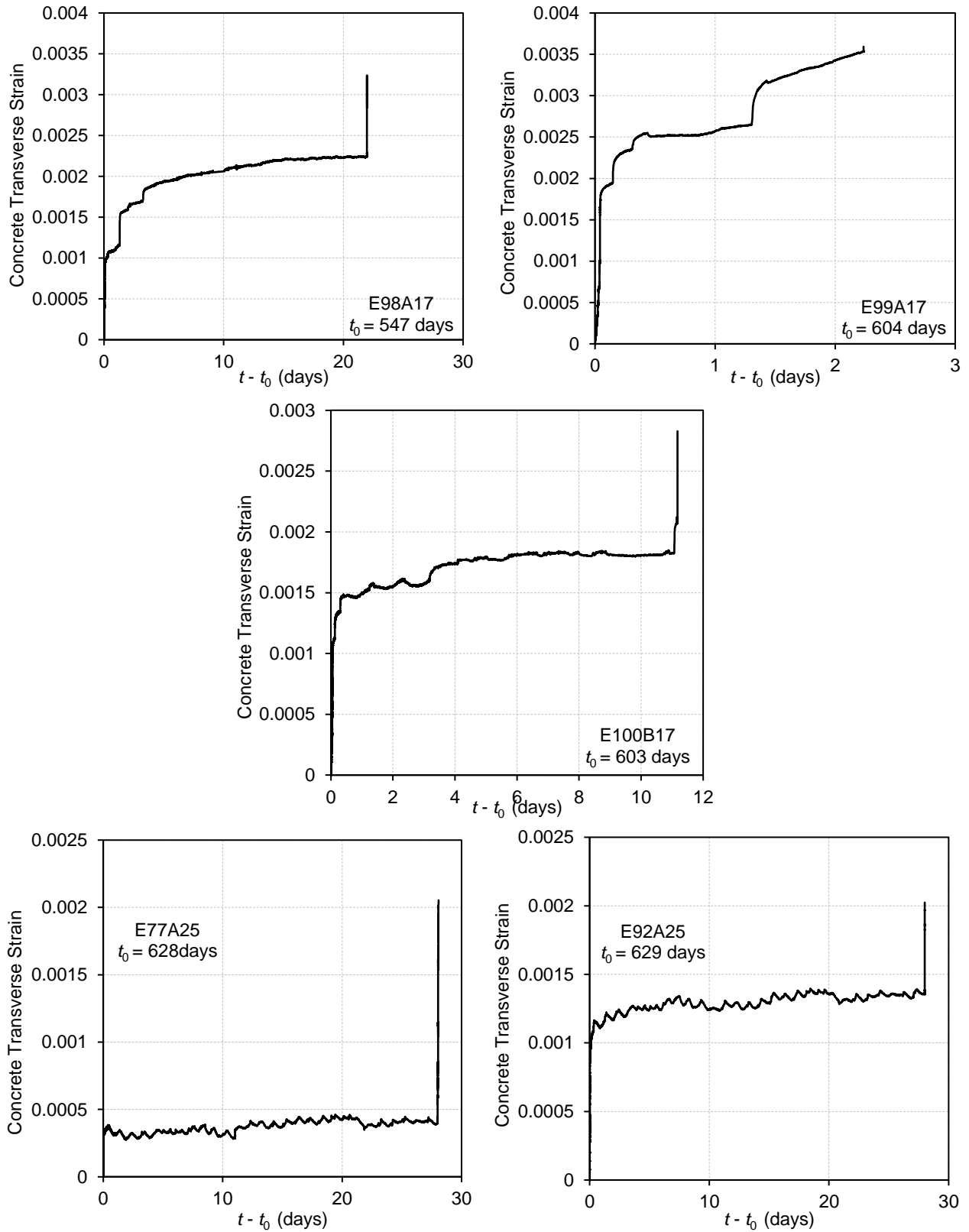


Figure 5.10 Concrete transverse strain history of column specimens subjected to sustained eccentric loading.

5.9 Poisson's Ratio

Poisson's ratio, based on the measured transverse and longitudinal strains at the concrete compression face, was evaluated for four specimens because the axial strain at compression face could not be obtained in Specimen E98A17 due to strain gauge malfunction. Figure 5.10 plots the time history of Poisson's ratio for Specimens E100B17, E99A17, E77A25, and E92A25. After the initial short-time loading, Poisson's ratio $\nu = 0.5, 0.45,$ and 0.39 in Specimens E99A17, E100B17, and E92A25, respectively. Similar to the concentric loading tests described in Chapter 4, the evolution of Poisson's ratio during sustained loading was impacted mainly by transverse strain. After the columns have been subjected to sustained loading for one day, ν increased to $0.48,$ and 0.42 in E100B17 and E92A25; after 3 days, ν became stabilized at around 0.5 in E100B17, whereas ν in E92A25 varied in a narrow range of 0.4 to 0.44 . In contrast, ν quickly increased to 0.69 for Specimen E99A17 after being subjected to sustained loading for one day and kept increasing thereafter. The Poisson's ratio reached 0.86 ($\nu = 0.86$) when Specimen E99A17 failed during the third day of sustained loading. For Specimen E77A25, $\nu = 0.19$ after the initial loading and slightly reduced to 0.14 after 11 days of sustained loading. Even if the sustained load was then increased in the second sustained loading stage, ν showed little change and was equal to 0.17 by the end of sustained loading. When E100B17, E92A25, and E77A25 failed during reloading, $\nu = 0.59, 0.51,$ and $0.46,$ respectively. Table 5.5 summarizes the Poisson's ratio at characteristic loading stages of eccentrically loaded columns.

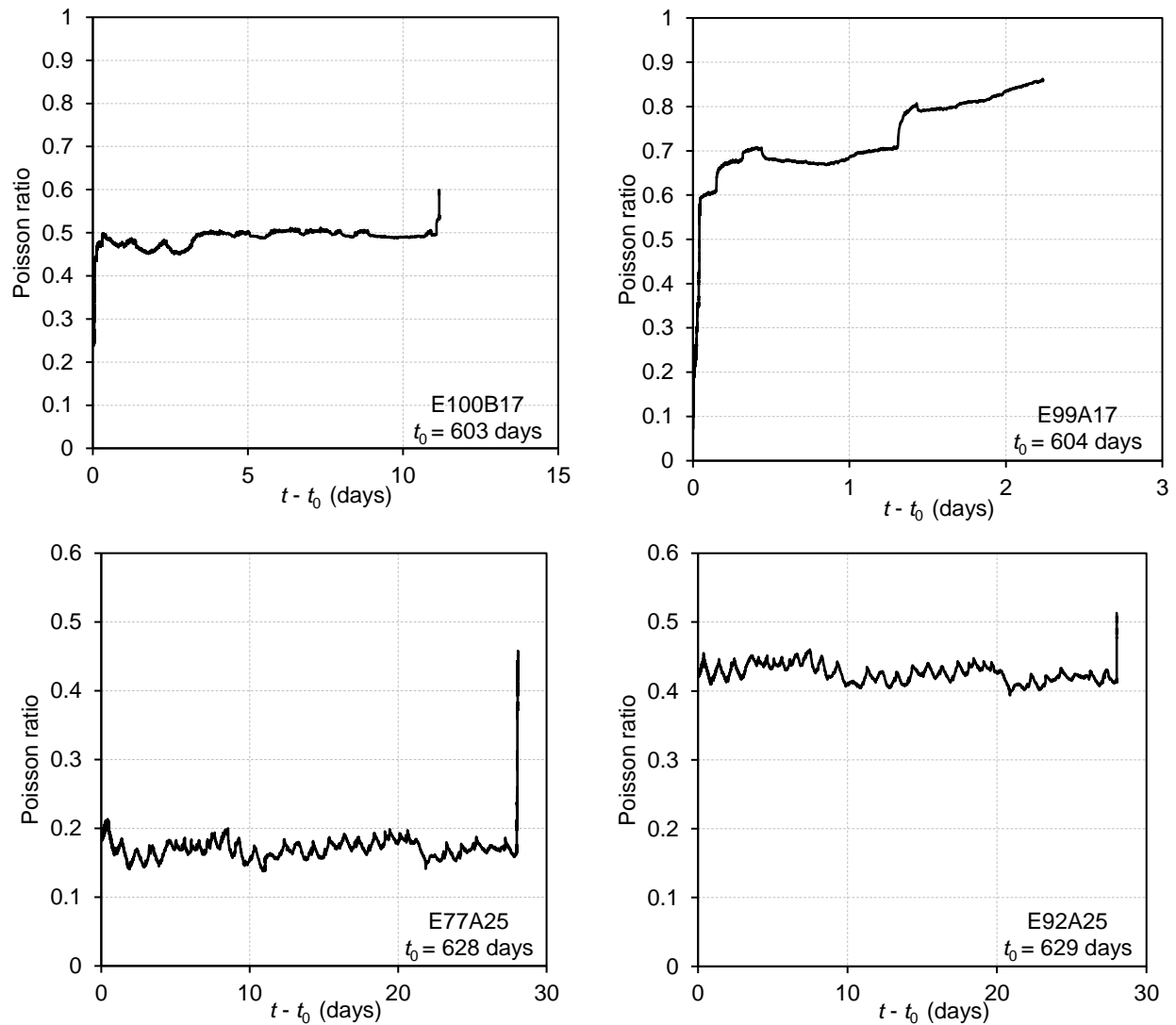


Figure 5.11 Time history of Poisson's ratio in Specimens E100B17, E99A17, E77A25, and E92A25.

Table 5.5 Poisson's ratio at characteristic loading stages of eccentrically loaded columns.

Specimen	at beginning of sustained load (1/in.)	at end of sustained load (1/in.)	at failure (1/in.)
E100B17	0.445	0.496	0.59
E99A17	0.500	—	0.86
E77A25	0.186 0.147	0.140 0.167	0.46
E92A25	0.388	0.415	0.51

It can be concluded from the test results that the change of Poisson's ratio depends on the sustained load level. The trend of Poisson's ratio bifurcates between $0.77 < M_{\text{sus}}/M_0 < 0.92$, where M_{sus} is the moment at the beginning of sustained loading, M_0 is the nominal moment capacity of RC columns. If $M_{\text{sus}}/M_0 < 0.77$, the Poisson's ratio decreased as the axial strain increased with time; if $M_{\text{sus}}/M_0 > 0.92$, the Poisson's ratio increased as the axial strain increased with time.

5.10 Damage and Failure Modes

Figure 5.12 shows the crack pattern and failure mode of the five eccentrically loaded columns. Flexural cracks were not visible during the initial loading and the first day of sustained loading of columns with $e/h = 0.17$. For the columns with $e/h = 0.25$, cracks were noticed in the column mid-height region immediately after the initial loading. The buckling of the column longitudinal bars at mid-height caused the failure of the Specimens E98A17, E99A17, E77A25, and E92A25. However, rebar buckling did not occur for the failure of Specimen E100B17, where the transverse reinforcement spacing was reduced to one third of the other four specimens. The most obvious crack appeared at the mid-height of all five slender columns. Most cracks at the tension face were developed along the location of transverse reinforcements. The failures caused the concrete cover to spall at the compressive zone at the mid-height and the failure zone extended to the mid-depth of the specimens. No columns failed farther from the center region. Specimen E100B17 exhibited an excessive spalling area of the concrete on compression face of the specimen. However, the depth of damaged concrete in the compressive zone was shallow, and the concrete core was well maintained.



E98A17

E99A17

E100B17

E77A25

E92A25

Figure 5.12 Failure modes of column specimens subjected to eccentric loading.

CHAPTER 6

NUMERICAL SIMULATIONS OF COLUMN NONLINEAR CREEP DUE TO SUSTAINED CONCENTRIC LOADING

6.1 Introduction

A numerical method for predicting concrete column creep under high axial sustained stresses and at older loading ages is explored. The method is based on a theoretical framework suggested by Tasevski et al. (2018) for plain concrete, which extended the prediction of linear concrete creep to that of nonlinear concrete creep. For plain concrete, the linear concrete creep is estimated by the GL2000 model. For RC specimens, the linear concrete creep is predicted using an age-adjusted effective modulus method. The experimental results of short column tests described in Chapter 4 are compared with the predictions.

6.2 Strains of Concrete and Reinforcing Bars Due to Shrinkage

Concrete shrinkage is the contraction of hardened concrete mixture due to losing capillary water. Concrete shrinkage begins after concrete pouring and continues during the life of concrete no matter it is loaded or not. In order to acquire the concrete creep strain under sustained load, concrete shrinkage strain should be eliminated from the total strain measured during the sustained loading process. Concrete shrinkage properties were not measured in the experiments. Four models can be used to estimate concrete shrinkage, including ACI 209 (2008), B3 (Bažant and Baweja, 1995, 2000), CEB MC90 (CEB 1999) and GL2000 (Gardner and Lockman, 2001) models. The ACI 209 model, which in general predicts greater shrinkage, is defined in Equations (6.1) through (6.11), where $\varepsilon_{sh}(t, t_c)$ is shrinkage strain at concrete age of t

(in days) measured from the start of drying at t_c (in days). The ACI 209 model is employed to estimate the shrinkage strains of the test specimens subjected to concentric loading.

$$\varepsilon_{sh}(t, t_c) = \frac{(t - t_c)}{f + (t - t_c)} \varepsilon_{shu} \quad (6.1)$$

where f is a parameter defined using Equation (6.2) to address the effect of volume-surface ratio V/S , and ε_{shu} is ultimate shrinkage strain evaluated using Equation (6.3).

$$f = 26e^{0.36(V/S)} \quad (6.2)$$

$$\varepsilon_{shu} = 780 \times 10^{-6} \gamma_{sh} \quad (6.3)$$

where γ_{sh} is defined in Equation (6.4) as the products of $\gamma_{sh,tc}$, $\gamma_{sh,RH}$, $\gamma_{sh,vs}$, $\gamma_{sh,s}$, $\gamma_{sh,\psi}$, $\gamma_{sh,c}$, and $\gamma_{sh,\alpha}$.

$$\gamma_{sh,tc} = \gamma_{sh,tc} \gamma_{sh,RH} \gamma_{sh,vs} \gamma_{sh,s} \gamma_{sh,\psi} \gamma_{sh,c} \gamma_{sh,\alpha} \quad (6.4)$$

In Equation (6.4), $\gamma_{sh,tc}$ is a parameter related to curing times different from 7 days for moist-cured concrete and calculated by Equation (6.5). $\gamma_{sh,RH}$ is calculated by Equation (6.6), where h is environmental relative humidity in decimals. $\gamma_{sh,vs}$ allowing for the effects of V/S -ratio is defined using Equation (6.7). $\gamma_{sh,s}$ is calculated by Equation (6.8), where s is the slump of fresh concrete in inch. $\gamma_{sh,\psi}$ is calculated by Equation (6.9) for $\psi > 50\%$, where ψ is the ratio of fine aggregate to total aggregate by weight expressed as percentage. $\gamma_{sh,c}$ is calculated by Equation (6.10), where c is the cement content in lb/yd^3 . $\gamma_{sh,\alpha}$ is evaluated using Equation (6.11), where α is percentage air content.

$$\gamma_{sh,tc} = 1.202 - 0.2337 \log_{10}(t_c) \quad (6.5)$$

$$\gamma_{sh,RH} = 1.4 - 1.02h \quad (6.6)$$

$$\gamma_{sh,vs} = 1.2e^{-0.12(V/S)} \quad (6.7)$$

$$\gamma_{sh,s} = 0.89 + 0.0041s \quad (6.8)$$

$$\gamma_{sh,\psi} = 0.9 + 0.002 \psi \quad (6.9)$$

$$\gamma_{sh,c} = 0.75 + 0.00036c \quad (6.10)$$

$$\gamma_{sh,\alpha} = 0.95 + 0.008 \alpha \geq 1 \quad (6.11)$$

Based on the actual properties of the specimens (e.g. V/S ratio, mix design, and measured slump), curing approach and time, and the average humidity in the laboratory of 21%, the unrestrained concrete shrinkage strain of each test specimen at the start and end of sustained concentric loading is evaluated and given in Table 6.1. It is seen that, the change in concrete shrinkage during the period of sustained loading is less than 3%. Given that creep deformation was far greater than the change in shrinkage strain, concrete shrinkage effect is neglected when predicting the long-term deformations of the test specimens.

Table 6.1 Concrete and reinforcement strains due to shrinkage

Specimen	P77	P90	C76A	C76B	C98A	C98B
ε_{sh} at start of sustained loading ($\times 10^{-3}$)	0.709	0.742	0.723	0.723	0.751	0.753
ε_{sh} at end of sustained loading ($\times 10^{-3}$)	0.720	0.749	0.741	0.741	0.776	0.777
E_c at start of sustained loading (ksi)	5503	4860	6483	3187	5302	3185
concrete tensile strain ε_{c,t_0} ($\times 10^{-3}$)	—	—	0.037	0.071	0.046	0.074
steel compressive strain ε_{s,t_0} ($\times 10^{-3}$)	—	—	0.686	0.652	0.705	0.679

Concrete shrinkage in the RC columns is restrained by the longitudinal reinforcing bars. Accordingly, tensile strain ε_{c,t_0} is developed in concrete and compressive strain ε_{s,t_0} in steel at $t = t_0$ when sustained loading starts. ε_{c,t_0} and ε_{s,t_0} can be evaluated based on the concept shown in Figure 6.1. If no reinforcement exists, concrete should have an unrestrained shrinkage of ε_{sh} in the $\Delta\varepsilon^-$ direction. However, the concrete shrinkage is restrained by the reinforcement and the

shrinkage of concrete is pulled back a little bit in the $\Delta\varepsilon^+$ direction. ε_{c,t_0} shall be equal to $\varepsilon_{sh} - \varepsilon_{s,t_0}$.

Assuming elastic behavior for both concrete and steel during this process and applying equilibrium, ε_{c,t_0} and ε_{s,t_0} satisfy

$$\varepsilon_{s,t_0} E_s A_s = \varepsilon_{c,t_0} E_c A_c \quad (6.12)$$

where $E_s = 30189$ ksi is the Young's modulus of D9 column longitudinal reinforcement, and E_c is the Young's modulus of concrete at the age of loading, which is calculated based on the concrete stress σ_c and the average concrete longitudinal strain ε_c of RC specimens at a load of 30 kips during the initial short-time loading and shown in Table 6.1. The concrete stress is calculated by Equation (6.13), where P is the measured force, ε_c is measured average concrete longitudinal strain. The strain of steel reinforcement is assumed to be equal to the measured concrete strain.

$$\sigma_c = \frac{P - E_s \varepsilon_c A_s}{A_c} \quad (6.13)$$

Based on Equation (6.12), ε_{c,t_0} and ε_{s,t_0} are calculated using Equations (6.14) to (6.16) for each RC short column and given in Table 6.1.

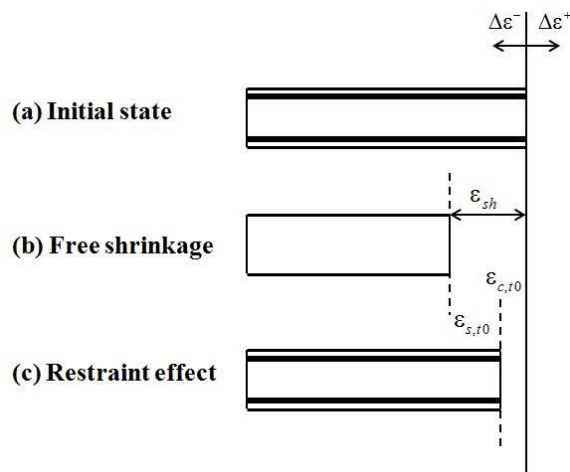


Figure 6.1 Conceptual view of restrained shrinkage behavior of a RC component.

$$\varepsilon_{c,t_0} = \left(\frac{nA_s}{nA_s + A_c} \right) \varepsilon_{sh} \quad (6.14)$$

$$\varepsilon_{s,t_0} = \frac{A_c}{nA_s + A_c} \varepsilon_{sh} \quad (6.15)$$

$$n = \frac{E_s}{E_c} \quad (6.16)$$

6.3 Short-Time Loading Capacity of RC Columns Subjected to Concentric Loading

Because hoops meeting seismic detailing requirements were used in the RC column specimens as transverse reinforcement, the confinement effect is considered. Transverse reinforcement of RC columns confines the lateral expansion of core concrete. Thus, both the compressive strength of concrete core and ductility can be increased, especially under high loads. This is because the confinement effect of transverse reinforcement is more obvious under higher stresses. The degree of confinement effect is influenced mainly by two factors: (1) the amount and shape of transverse reinforcement, and (2) the strength ratio of transverse reinforcement to concrete f_{yt}/f'_c , where f_{yt} is the yield strength of transverse reinforcement and f'_c is concrete cylinder strength at the time of loading. The stress of concrete core and the ultimate load capacity of short reinforced concrete columns are estimated using the model for concrete under low strain rates suggested by Scott et al. (1982), as shown in the following.

$$\rho_t = \frac{2A_{sh}(b''+h'')}{b''h''s} \quad (6.17)$$

$$K = 1 + \rho_t \frac{f_{yt}}{f'_c} \quad (6.18)$$

$$\varepsilon_0 = 0.002K \quad (6.19)$$

where A_{sh} is the area of transverse reinforcement, b'' and h'' are the width and height of core area, s is the clear spacing of the transverse reinforcement, ρ_t is the ratio of the volume of transverse reinforcement to the volume of confined core. For Specimen C76A and C76B, $f_c' = 4,316$ psi over entire sustained loading period; for Specimen C98A and C98B, $f_c' = 4,316$ psi at the start of sustained loading and $f_c' = 4,200$ psi at the end of sustained loading. Then, the concrete core stress σ_{core} can be calculated by Equations (6.20) to (6.24), where $\varepsilon_0 = 0.002$ is used in Equations (6.20) and (6.21).

$$\sigma_{core} = Kf_c' \left[2 \frac{\varepsilon_c}{\varepsilon_0} - \left(\frac{\varepsilon_c}{\varepsilon_0} \right)^2 \right] \quad \text{for} \quad 0 \leq \varepsilon_c \leq \varepsilon_0 \quad (6.20)$$

$$\sigma_{core} = Kf_c' [1 - Z_m(\varepsilon_c - \varepsilon_0)] \quad \text{for} \quad \varepsilon_c \geq \varepsilon_0 \quad (6.21)$$

$$Z_m = \frac{0.5}{\varepsilon_{50u} + \varepsilon_{50h} - \varepsilon_0} \quad (6.22)$$

$$\varepsilon_{50u} = \frac{3 + 0.002f_c'}{f_c' - 1000} \quad (6.23)$$

$$\varepsilon_{50h} = 0.75\rho_t \sqrt{\frac{b''}{s}} \quad (6.24)$$

Figure 6.2 shows an example of the stress-strain curve for the confined and unconfined concrete in Specimen C76B. The stress-strain diagram for unconfined concrete descends rapidly along a straight line after passing the peak load point (ε_c, f_c') . The unconfined concrete is presumed to have no compressive resistance beyond the point at which the descending branch drops to $0.2f_c'$. For confined concrete, the shape of stress-strain curve is similar to that of the unconfined concrete in the rising part. The peak stress Kf_c' is slightly higher than f_c' . The concrete strain at the peak stress equals to ε_0 for the unconfined concrete. However, the stress-strain

diagram for confined concrete descends smoothly along a straight line after passing from the peak load point (ε_0, Kf_c') through the point $(\varepsilon_{20c}, 0.2Kf_c')$, where ε_{20c} is confined concrete strain when $\sigma = 0.2Kf_c'$. The confined concrete is assumed to maintain $\sigma = 0.2Kf_c'$ for all strains in excess of the point at which the descending branch reaches $0.2Kf_c'$. Due to the slope difference between the confined concrete and unconfined concrete at the descending part of the stress-strain curve, the concrete cover loses load capacity quickly when the concrete strain exceeds 0.002. Once the concrete cover fails, the whole RC column should fail very soon because the area of concrete cover accounts for about 50% of the cross section area. Therefore, the strain of $\varepsilon_c = 0.002$ at the peak stress f_c' of the unconfined concrete cover is used in Equation (6.20) to estimate the concrete core stress.

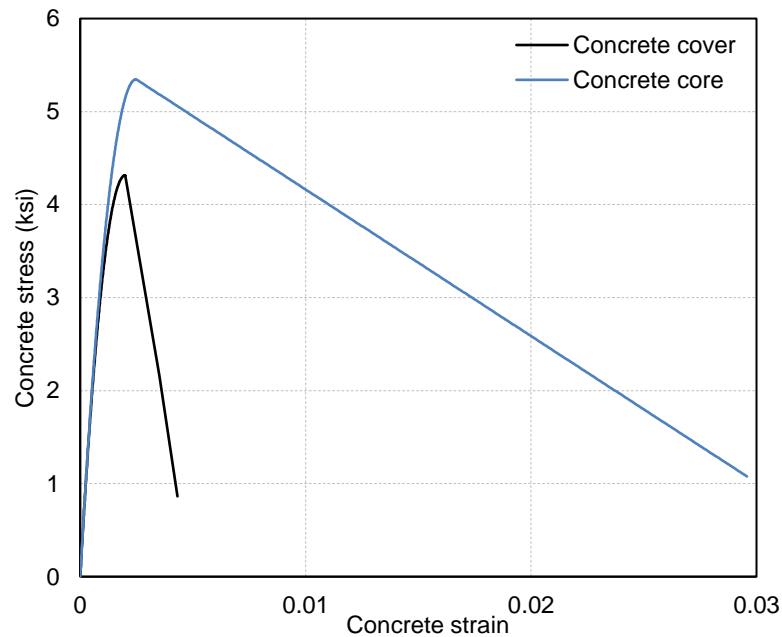


Figure 6.2 Stress-strain relationship for confined and unconfined concrete for Specimen C76B.

After the concrete core stress at $\varepsilon_c = 0.002$ has been determined, the short-time ultimate loading capacity of RC columns, $P_{u,cal}$, is estimated by Equation (6.25). An average concrete ultimate stress $\sigma_{u,cal}$ is then calculated by Equation (6.26). The measured average concrete peak stress σ_u is estimated using Equation (6.27) based on the measured peak load P_u shown in Table 6.2, the force carried by steel reinforcement, and the net concrete area.

$$P_{u,cal} = \sigma_{core} A_{core} + 0.85 f_c' (A_c - A_{core}) + f_y A_s \quad (6.25)$$

$$\sigma_{u,cal} = \frac{\sigma_{core} A_{core} + 0.85 f_c' (A_c - A_{core})}{A_{core} + 0.85 (A_c - A_{core})} \quad (6.26)$$

$$\sigma_u = \frac{P_u - f_y A_s}{0.85 (A_c - A_{core}) + A_{core}} \quad (6.27)$$

where A_c is the net concrete area of column's cross section; A_{core} is the area of concrete core; A_s is total area of column D9 longitudinal reinforcement.

Based on Equations (6.17) to (6.25), the calculated short-time loading capacity of Specimen CS is $P_{u,cal} = 160.9$ kips, only 2.4% greater than the peak load of $P_u = 157.2$ kips measured during the short-time loading. Table 6.2 summarizes the concrete core stress σ_{core} at $\varepsilon_c = 0.002$, the calculated average concrete ultimate stress $\sigma_{u,cal}$ at $\varepsilon_c = 0.002$, the calculated ultimate loading capacity $P_{u,cal}$, the average measured concrete peak stress σ_u at the measured peak load P_u , and the measured peak load P_u after experiencing sustained load for Specimens C76A, C76B, C98A, and C98B. The purpose of calculating an average concrete stress at failure is to determine the difference between the estimated average ultimate stress $\sigma_{u,cal}$ under short-time load and the concrete peak stress σ_u after experience the sustained load of the RC specimens. The average concrete stress is important to determine the stress ratio used to predict

nonlinear concrete creep, which is discussed later in Section 6.4.2. It is seen that the average peak stress σ_u is 0.1%, 3.1%, and 7.4% lower than $\sigma_{u,cal}$ for Specimens C76A, C76B, and C98B, respectively. However, for Specimen C98A, σ_u is 6.9% greater than $\sigma_{u,cal}$. In general, compared with the short-term loading capacity of RC specimens, the change in capacity after experiencing sustained load is small.

Table 6.2 Calculated and measured loading capacity of RC specimens

Specimen	C76A	C76B	C98A	C98B
σ_u (ksi)	4.552	4.766	4.750	4.464
P_u (kips)	172.3	179.1	178.6	169.5
σ_{core} (ksi)	4.774	5.450	4.657	5.326
$\sigma_{u,cal}$ (ksi)	4.558	4.916	4.442	4.795
$P_{u,cal}$ (kips)	172.5	183.9	168.8	180.0

6.4 Simulations of Column Creep under High Sustained Concentric Loading

6.4.1 Simulating Creep of Plain Concrete Columns

Constitutive models capable of describing the behavior of RC components subjected to high-level sustained loads are needed to reliably predict the near-collapse response of RC frame structures overstressed by excessive gravity loads. As described previously, research on concrete creep under high sustained stresses was very limited because concrete creep was considered mainly as a serviceability issue. As a result, most concrete creep prediction models concentrated on linear concrete creep. A few existing models for predicting nonlinear creep of concrete under high sustained load are reviewed in Section 1.6.3.2. Among them, the model developed by Tasevski et al. (2018) provides a theoretical framework allowing to predict nonlinear concrete creep more conveniently than the other models. This model was verified by the results of the

authors' own experiments and those performed by Rüsç (1960), Awad (1971), Smadi et al. (1982), and Iravani et al. (1998).

The theoretical framework developed by Tasevski et al. (2018) was based on the experimental observations and a set of hypotheses, extending the prediction of linear concrete creep to that of nonlinear concrete creep. However, the method used to calculate the linear concrete creep can be defined by the users. Three existing methods (ACI 209 model, CEB MC90-99 model, and GL2000 model) for predicting linear concrete creep are chosen in this section. Concrete creep is predicted based on the framework suggested by Tasevski et al. (2018) described in Equation (1.15) in Section 1.6.3.2, with some modifications.

In the experiments of this study, concrete stress varied during the sustained loading due to stress redistribution between steel and concrete, load drop, and load adjustment. Thus, as shown in Equation (6.28), a term of $(\sigma_{c,i} - \sigma_{c,i-1}) / E_{cmt_0}$ is added to the formulations suggested by Tasevski et al. (2018) to explain the instantaneous concrete strain change at a time step, i , in the numerical simulations.

$$\varepsilon_c(t) = \varepsilon_0 + \sum_{i=1}^n \left[\varepsilon_0 \left(1 + \eta \left(\frac{\sigma_{c,i}}{f_{c,i}} \right) \phi(t_i, t_0) \right) - \varepsilon_0 \left(1 + \eta \left(\frac{\sigma_{c,i-1}}{f_{c,i-1}} \right) \phi(t_i, t_0) \right) \right] + \frac{\sigma_{c,i} - \sigma_{c,i-1}}{E_{cmt_0}} \quad (6.28)$$

where ε_0 is concrete strain at the beginning of sustained load measured by the concrete strain gauges along column axial direction; i indicates the i th step; $\sigma_{c,i}$ is concrete stress at the i th step, determined based on the measured load, the force carried by the longitudinal reinforcement, and the area of concrete cross section A_c ; t_0 is concrete age at the beginning of sustained load (in days); E_{cmt_0} is mean modulus of elasticity of concrete when sustained loading started at age t_0 ;

$\sigma_{c,i} / f_{c,i}$ is the sustained stress ratio at the i th step; η is a parameter defining the effects of sustained load level, which is described later.

Based on the stress-strain relationship of Specimens P77 and P90 shown in Figure 4.4, the elastic modulus of concrete during sustained loading almost did not change. For simplicity, the change in instantaneous concrete strain during a time step is calculated by the ratio of change in sustained stress during this time step to the elastic modulus of concrete (E_c) at the start of sustained loading (t_0), which is provided in Table 6.1.

The total number of time steps shown in Equation (6.28), n , is consistent with the number of time steps collecting data during the experiments and at least 2,000 time steps for each specimen. After experiencing sustained loading, the peak load of the plain concrete Specimens P77 and P90 increased by 6.6% and 8.6%, as compared with the short-time peak failure load of Specimen PS. In Equation (6.28), $f_{c,i}$ is concrete cylinder strength at the i th step and was assumed to increase linearly proportional to the sustained loading time. Coutinho (1977) found that (1) sustained loading increased concrete compressive strength by 2% to 14% with different loading ages and sustained load levels, (2) higher sustained loads caused a higher concrete strength increase, (3) higher loading age t_0 caused faster concrete strength increase, and (4) concrete strength increase was usually completed within three days if the loading age t_0 was greater than three months.

In Equation (6.28), $\sigma_{c,i} / f_{c,i}$ means the ratio of sustained stress $\sigma_{c,i}$ to the short-time concrete compressive strength $f_{c,i}$. The sustained stress ratio $\sigma_{c,i} / f_{c,i}$ affects the nonlinear concrete creep. All the specimens tested in this study were square columns rather than concrete cylinders. According to ACI 318 design code (2019), the ultimate concrete stress should be $0.85f'_c$ rather than f'_c for plain concrete columns, where f'_c is concrete cylinder strength. Figure

6.3 shows a comparison of creep prediction results of using $0.85f'_c$ and f'_c to define the concrete short-time strength in stress ratio.

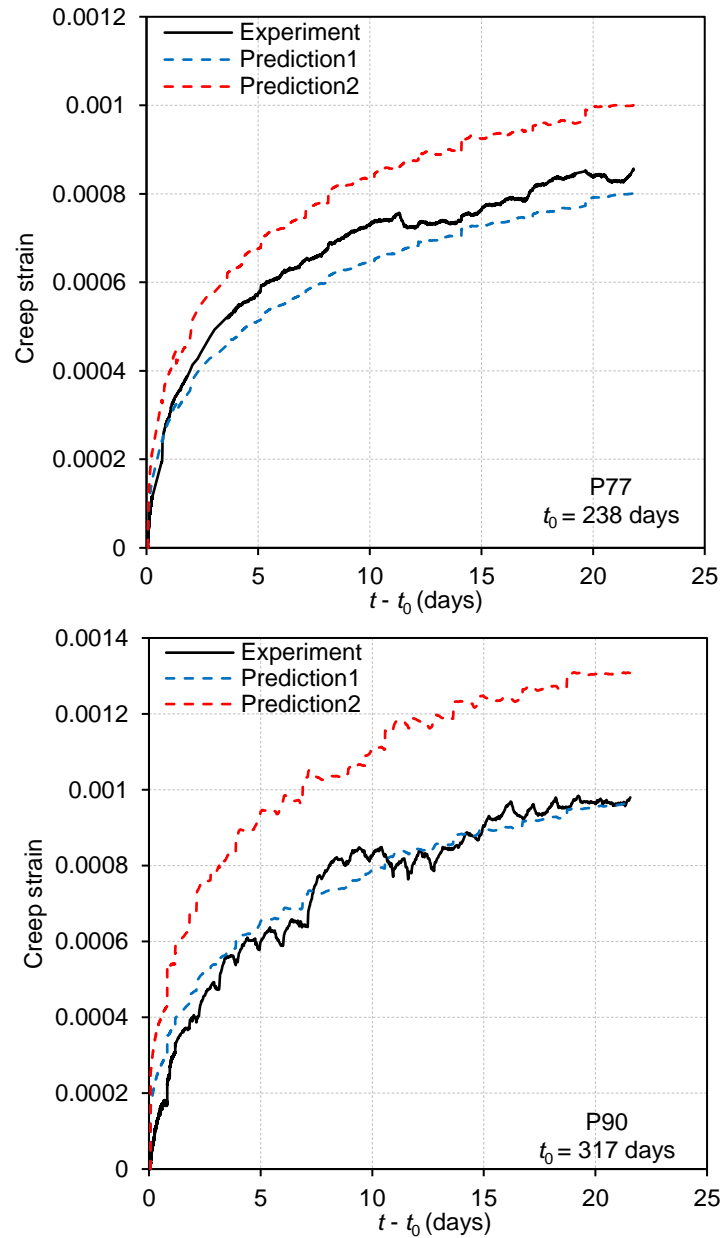


Figure 6.3 Comparison of predicted and measured creep strains with two different methods defining sustained stress ratio for Specimens P77 and P90.

The red dashed line is the creep prediction using $\sigma_{c,i}/(0.85f_{c,i})$ as the sustained stress ratio and GL2000 model to calculate linear creep coefficient. The blue dashed line is the creep prediction using $\sigma_{c,i}/f_{c,i}$ as the sustained stress ratio. The reason for using GL2000 model to calculate the linear creep coefficient is explained later. For Specimen P77, the concrete creep strain difference between the predicted and experimental results at the end of sustained loading is -6.1% and 17.2% for using $\sigma_{c,i}/f_{c,i}$ and $\sigma_{c,i}/(0.85f_{c,i})$ as the sustained stress level to calculate concrete creep strain. For Specimen PC90, the concrete creep strain difference between the predicted and experimental results at the end of sustained loading is -1.6% and 33.6% for using $\sigma_{c,i}/f_{c,i}$ and $\sigma_{c,i}/(0.85f_{c,i})$ as the sustained stress level to calculate concrete creep strain. Therefore, the predicted creep strain results using the $\sigma_{c,i}/f_{c,i}$ as the sustained stress level show better agreements with the experimental results.

For the ACI 209 model, the linear concrete creep coefficient $\phi(t_i, t_0)$ in Equation (6.28) can be calculated directly by Equation (1.2) in Section 1.6.3.1. However, for GL2000 and CEB MC90 model, the linear concrete creep coefficient $\phi(t_i, t_0)$ in Equation (6.28) can be calculated by a 28-day linear creep coefficient $\phi_{28}(t_i, t_0)$ as shown in Equation (6.29) given in GL2000 model or Equation (1.6) given in the CEB MC90 model. $\Phi(t_c)$ in Equation (6.29) is calculated by Equation (6.30). For concrete specimens loaded after 28 days of concrete pouring, the linear creep coefficient $\phi(t_i, t_0)$ at the beginning of sustained load (t_0) and the i th time step in Equation (6.28) can be calculated by Equation (6.31) in order to apply the GL2000 and CEB MC90 models. The ratio of $E_{cm,t_0} / E_{cm,28}$ is calculated by Equation (6.32), as recommended by CEB Bulletins (1999). $E_{cm,28}$ is the mean elastic modulus of concrete at 28 days, which was not

measured in the experiments of this study. $E_{cm_{t_0}}$ is the elastic modulus of concrete at t_0 , the value of $E_{cm_{t_0}}$ is the same as the E_c shown in Table 6.1.

$$\phi_{28}(t_i, t_0) = \Phi(t_c) \left[2 \frac{(t_i - t_0)^{0.3}}{(t_i - t_0)^{0.3} + 14} + \left(\frac{7}{t_0} \right)^{0.5} \left(\frac{(t_i - t_0)}{(t_i - t_0) + 7} \right)^{0.5} + 2.5 \cdot (1 - 1.086h^2) \left(\frac{t_i - t_0}{(t_i - t_0) + 77(V/S)^2} \right)^{0.5} \right] \quad (6.29)$$

$$\Phi(t_c) = \left[1 - \left(\frac{(t_0 - t_c)}{(t_0 - t_c) + 77(V/S)^2} \right)^{0.5} \right]^{0.5} \quad (6.30)$$

$$\phi(t_i, t_0) = \phi_{28}(t_i, t_0) \frac{E_{cm_{t_0}}}{E_{cm_{28}}} \quad (6.31)$$

$$E_{cm_{t_0}} = E_{cm_{28}} \exp \frac{s}{2} \left(1 - \sqrt{\frac{28}{t_0}} \right) \quad (6.32)$$

where the value of s is the same as that in Table 1.2; t_c is the age of concrete when drying starts at the end of moist curing (days); V/S is volume-surface ratio; h is relative humidity expressed as a decimal.

As shown in Equation (6.28), nonlinear creep is calculated by applying an amplification factor $\eta(\sigma_{c,i}/f_{c,i})$ to the linear concrete creep $\phi(t_i, t_0)$. This factor is evaluated using Equations (6.33) and (6.34).

$$\eta \left(\frac{\sigma_{c,i}}{f_{c,i}} \right) = 1 + 2\eta_\tau(t_i, t_0) \left(\frac{\sigma_{c,i}}{f_{c,i}} \right)^4 \quad (6.33)$$

$$\eta_\tau(t_i, t_0) = \left(1 - \log \left(\frac{t_i - t_0}{t_m + t_i - t_0} \right) \right)^n \quad (6.34)$$

After experiencing sustained loading, the strength of plain concrete specimens P77 and P90 was increased by 6.6% and 8.6% from the expected short-time axial loading capacity P_0 ,

respectively. P_0 is estimated using Equation (6.35), where f'_c is the concrete cylinder strength and A_c is the cross section of a plain concrete specimen.

$$P_0 = 0.85f'_cA_c \quad (6.35)$$

It is assumed that the peak load of a plain concrete specimen after experience sustained loading can still be calculated by Equation (6.35); however, concrete cylinder strength (f'_c) increased due to sustained loading over time. Three existing models described in Section 1.6.3.1, including GL2000, ACI 209, and CEB MC90, are used to calculate the linear creep coefficient $\phi(t_i, t_0)$ in Equation (6.28). Then, Equations (6.28) through (6.34) are applied to simulate the creep strains of two plain concrete specimens subjected to sustained concentric loading. The simulation result for Specimen P77 is plotted in Figure 6.4.

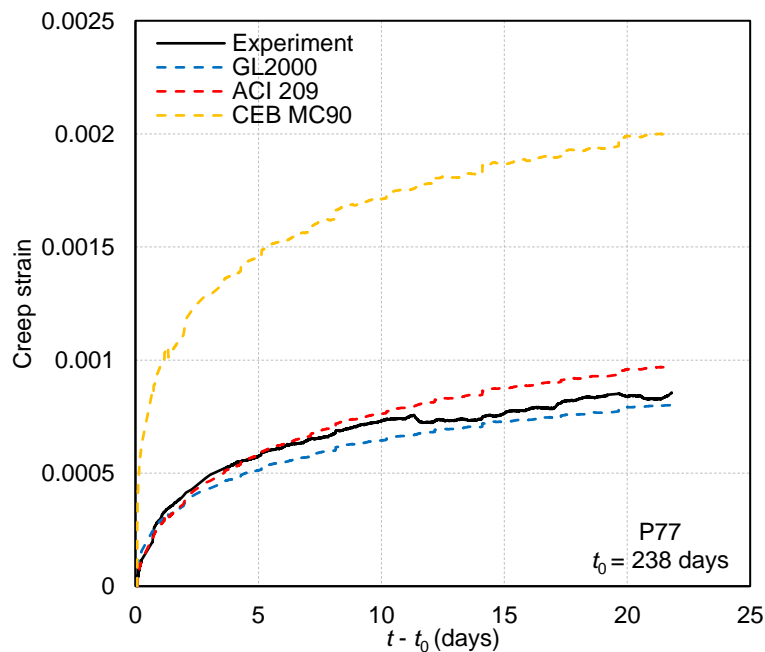


Figure 6.4 Comparison of predicted and measured creep strains for Specimen P77.

In the first 10 days of sustained loading, the creep strain predicted by using ACI 209 model to calculate $\phi(t_i, t_0)$ is better than using the GL2000 model. However, by the end of sustained loading, the difference of concrete creep between the predicted and experimental results at the end of sustained loading is -6.1%, 13.8%, and 135% for using the GL2000, ACI 209, and CEB MC90 model to calculate $\phi(t_i, t_0)$, respectively.

The axial creep strain of Specimen PC90 during the sustained loading is also predicted by Equation (6.28) as shown in Figure 6.5. This time, the simulation result using the GL2000 model to calculate the linear creep coefficient $\phi(t_i, t_0)$ is better than using the other two models during the entire sustained loading.

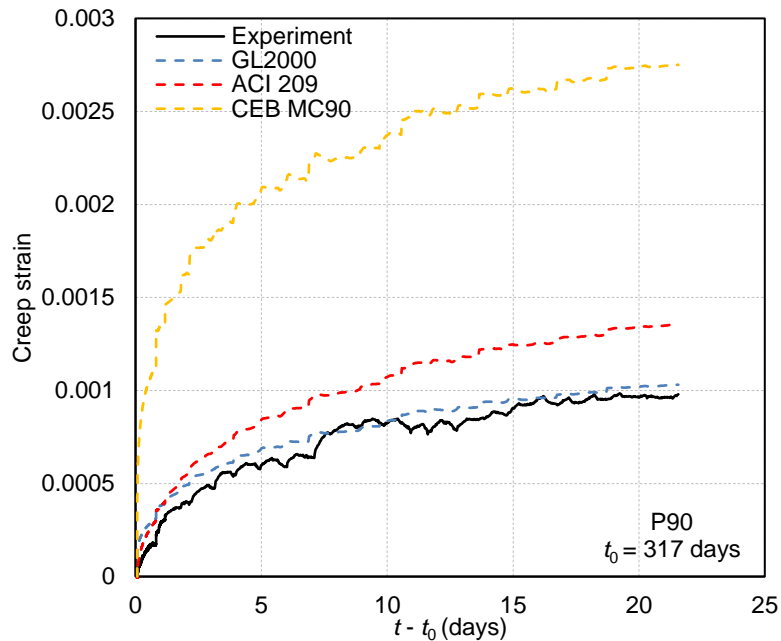


Figure 6.5 Comparison of predicted and measured creep strains for Specimen P90.

As shown in Figure 6.5, the difference in the predicted and measured creep strains at the end of sustained loading is -1.6%, 31.3%, and 167% for using GL2000, ACI 209, and CEB

MC90 models to calculate $\phi(t_i, t_0)$, respectively. Overall, applying the GL2000 model to calculate $\phi(t_i, t_0)$ better predicts the concrete creep strain for the plain concrete columns tested in this study. Therefore, the GL2000 model is chosen to calculate the linear creep coefficient $\phi(t_i, t_0)$ for the RC column specimens, as described in Section 6.4.2.

6.4.2 Simulating Creep of Reinforced Concrete Columns

Very limited research has been conducted on simulating the creep behavior of RC columns under high sustained loads. Concrete creep strain in the longitudinal direction is assumed to be the same as the strain in longitudinal reinforcement. The elastic modulus of steel reinforcement (E_s) is generally five to ten times greater than that of concrete (E_c). Concrete creep causes extra compressive strains in the longitudinal bars. Under the same creep strain increment, the stress increase in longitudinal bars is much higher than in concrete. For the four short RC column experiments in this study, the load was well maintained during the sustained loading. Stress was reduced in concrete and increased in the longitudinal bars until they yielded. As a result, a portion of the elastic strain in concrete was recovered under the sustained loads. Therefore, under the same level of sustained load (P_{sus}/P_0), the stress redistribution between concrete and reinforcement in a RC column caused the concrete creep strain to be smaller than in a plain concrete column. The stress redistribution between concrete and longitudinal reinforcement in Specimens C76A, C76B, C98A, and C98B is shown in Figure 6.6. No yielding occurred in the longitudinal reinforcement by the end of sustained loading for Specimen C76A. For Specimens C76B, C98A, and C98B, the longitudinal reinforcement yielded 2.8 days, 4.8 hours, and 5.3 hours after the beginning of sustained loading. The maximum and minimum axial

forces carried by concrete during sustained loading were 100 and 90.8 kips in C76A, 95 and 86.2 kips in C76B, 122 and 117 kips in C98A, 123 and 117 kips in C98B.

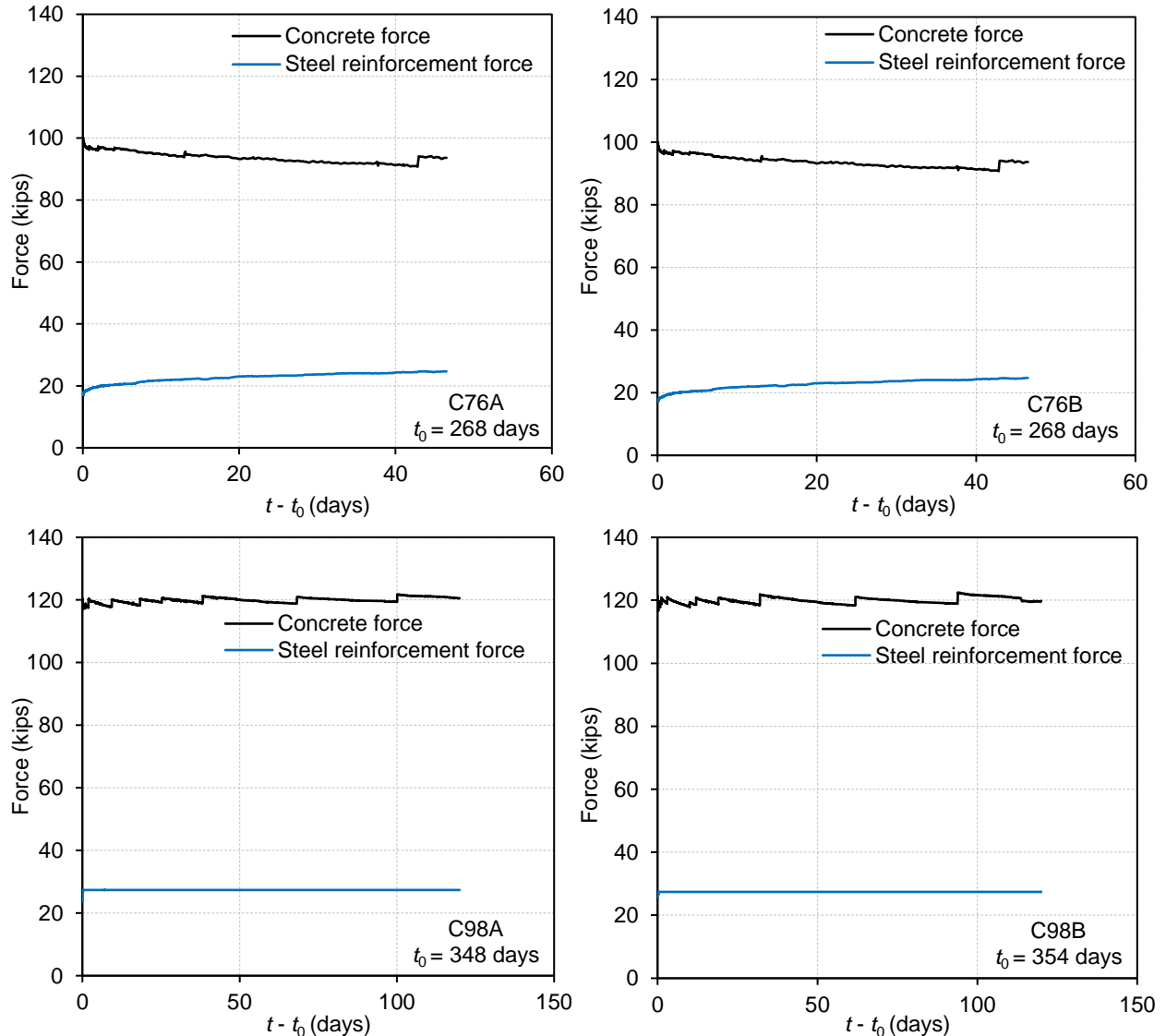


Figure 6.6 Variation of axial forces resisted by concrete and longitudinal reinforcement during sustained loading of Specimens C76A, C76B, C98A, and C98B.

This study extends the linear creep prediction model, an age-adjusted effective modulus method, proposed by Neville (1996) for axially loaded RC columns with a sustained stress level $\sigma < 0.4f_c'$ to RC columns under high sustained stresses. The experiments conducted in this

study indicated that the shapes of the creep coefficient time-history curves for the RC column specimens and the plain concrete column specimens were similar, as shown in Figures 4.4 and 4.12. The variation of creep coefficient of the RC specimens was almost proportional to the variation of creep coefficient of plain concrete specimens after experiencing the same duration of sustained loading. Therefore, it is assumed that the creep strain of a RC column under high sustained load can be calculated by extending linear creep to nonlinear creep for a RC column following the concept proposed by Tasevski et al. (2018) as well.

In the linear creep model for RC columns developed by Neville (1996), two coefficients were introduced in addition to linear concrete creep prediction. One coefficient was the ratio of a transformed area, A_{tr} , to an age-adjusted transformed area, A_{traa} . A_{tr} at the start of sustained loading was defined by Equation (6.36), in which n , the modular ratio between longitudinal reinforcement and concrete at t_0 , is defined by Equation (6.37). The effect of force redistribution between concrete and longitudinal reinforcement during sustained loading was reflected using an age-adjusted effective modulus $E_{caa}(t, t_0)$ calculated by Equation (6.38) and an age-adjusted transformed area A_{traa} calculated by Equation (6.39). The age-adjusted elastic modular ratio of longitudinal steel reinforcement to concrete, n_{aa} , in Equation (6.39) can be calculated by Equation (6.40). The second coefficient was aging coefficient $\chi(t_0)$ addressing the reduction of compression force in concrete due to creep and calculated by Equation (6.41).

$$A_{tr} = A_c + (n-1)A_s \quad (6.36)$$

$$n = \frac{E_s}{E_{cm t_0}} \quad (6.37)$$

$$E_{caa}(t, t_0) = \frac{E_{cmt_0}}{1 + \chi(t_0) \left(\frac{E_{cmt_0}}{E_{cm28}} \right) \phi(t_i, t_0)} \quad (6.38)$$

$$A_{traa} = A_c + (n_{aa} - 1)A_s \quad (6.39)$$

$$n_{aa} = \frac{E_s}{E_{caa}(t, t_0)} \quad (6.40)$$

$$\chi(t_0) = \frac{t_0^{0.5}}{1 + t_0^{0.5}} \quad (6.41)$$

After the coefficients in the linear creep model for reinforced concrete have been determined, the nonlinear creep under high sustained loads is calculated by applying the theoretical framework developed by Tasevski et al. (2018), as shown in Equation (6.42). The GL2000 model (Gardner 2004) is chosen to calculate the linear creep coefficient $\phi(t_i, t_0)$. The definitions of coefficients of ε_0 , $\eta(\sigma_{c,i} / f_{cav,g,i})$, E_{cmt_0} , and $(\sigma_{c,i} - \sigma_{c,i-1}) / E_{cmt_0}$ are the same as those in Equation (6.28); however, the definition of concrete strength, $f_{c,i}$, in Equation (6.28) is modified as $f_{cav,g,i}$ to define the sustained stress ratio, as shown in Equation (6.42). The initial value of $f_{cav,g,i}$ at $t = t_0$ used in Equation (6.42) is the same as $\sigma_{u,cal}$ in Table 6.2. The loading age t_0 in the experiments was greater than three months and the average concrete strength increased by 7.5% for Specimens P77 and P90; therefore, concrete short-time compressive strength is assumed to increase linearly with respect to sustained loading time during the first three days of loading when the 7.5% strength increase was achieved. After 3-days loading, due to the lack of experimental data, the short-time strength is assumed to be unchanged. In Equation (6.42), E_{cmt_0} is modulus of elasticity of concrete when sustained loading started at age t_0 . For RC specimens, E_{cmt_0} is calculated by Equation (6.43), where P is the measured total load, E_s is the elastic

modulus of longitudinal reinforcement, ε_c is measured average concrete longitudinal strain, A_s is the total area of column D9 longitudinal reinforcement, and A_c is the net concrete area. The value of E_{cmt0} was the same as E_c shown in Table 6.1.

$$\varepsilon_c(t) = \varepsilon_0 + \sum_{i=1}^n \left[\varepsilon_0 \left(1 + \eta \left(\frac{\sigma_{c,i}}{f_{cavg,i}} \right) \phi(t_i, t_0) \right) - \varepsilon_0 \left(1 + \eta \left(\frac{\sigma_{c,i-1}}{f_{cavg,i-1}} \right) \phi(t_i, t_0) \right) \right] \left[\left(\frac{A_{tr}}{A_{raa}} \right) \chi(t_0) + \frac{\sigma_{c,i} - \sigma_{c,i-1}}{E_{cmt_0}} \right] \quad (6.42)$$

$$E_{cmt_0} = \frac{(P - E_s \varepsilon_c A_s) / (A_c)}{\varepsilon_c} \quad (6.43)$$

The predicted creep strains based on Equation (6.42) for Specimens C76A and C76B are plotted in Figure 6.7. The predicted creep strains are close to the experimental results over the entire sustained loading period for both specimens. At the end of 47 days sustained loading, the predicted creep is 5.6% and 4.4% lower than the creep measured in the experiment of C76A and C76B, respectively. The predicted creep strain calculated by Equation (6.42) for Specimens C98A and C98B are plotted in Figure 6.8. The predicted creep strain results are greater than the experimental results from the beginning of sustained load for both specimens. The possible reason is that the transverse reinforcement affects concrete creep earlier under the higher sustained load level. According to Sheikh and Uzumeri (1980), the transverse reinforcement was engaged in confining concrete when concrete axial strain became greater than 0.0015. The axial strain of Specimen C98A and C98B was 0.00130 and 0.00148 at the beginning of sustained loading, but exceeded 0.0015 after 1 and 0.15 hour of sustained load in Specimen C98A and C98B. For Specimen C76A, the axial strain was less than 0.0015 even at the end of sustained load. For Specimen C76B, although the axial strain exceeded 0.0015 after 0.8 days of sustained load, the axial strain at the end of sustained loading was 0.00228, which was only 52% greater than 0.0015. The strain at the end of sustained loading was not exceeded 0.0015 a lot. Therefore,

the predicted strain of Specimen C76B was close to the measured strain as well, even though the confinement effect due to transverse reinforcement engaged in Specimen C76B.

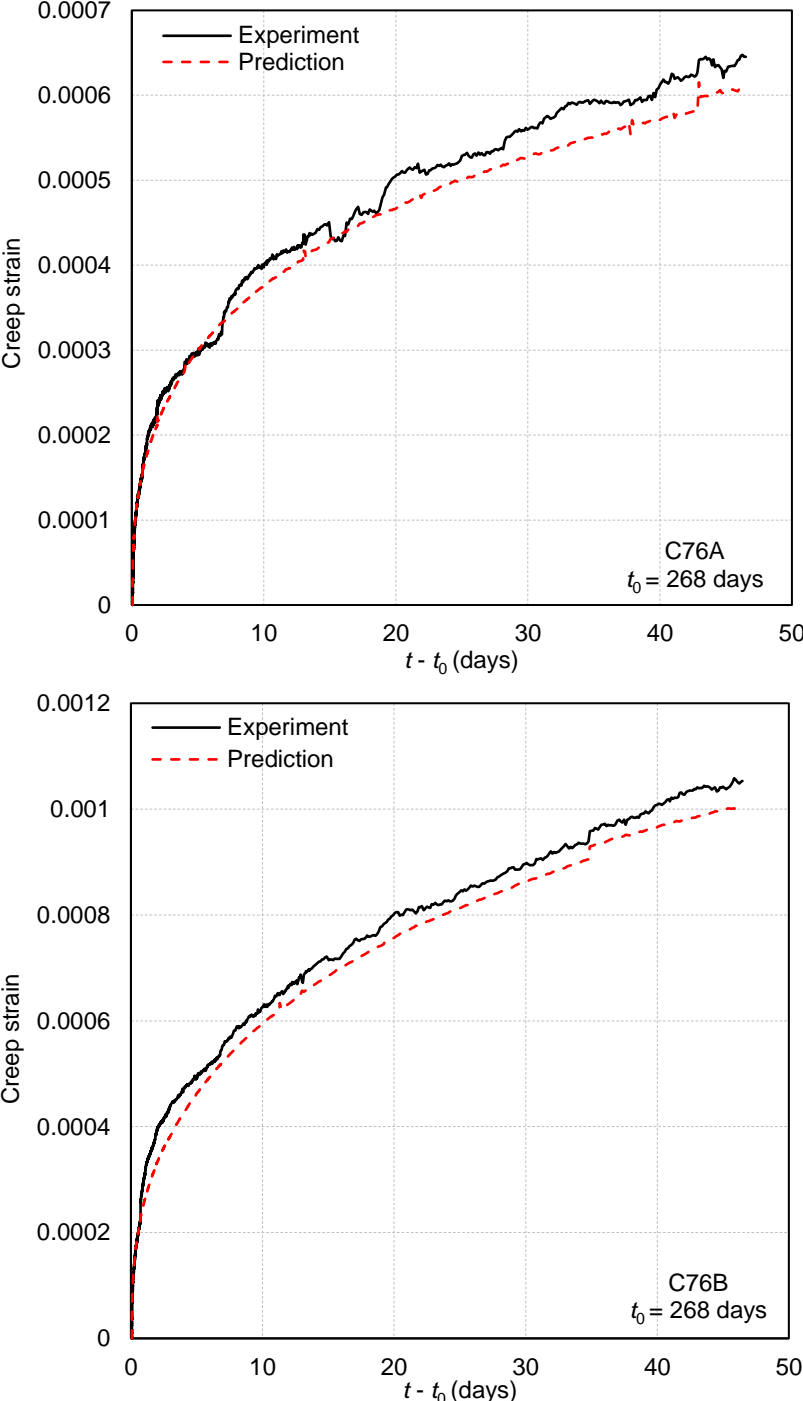


Figure 6.7 Comparison of predicted and measured creep strains for Specimens C76A and C76B.

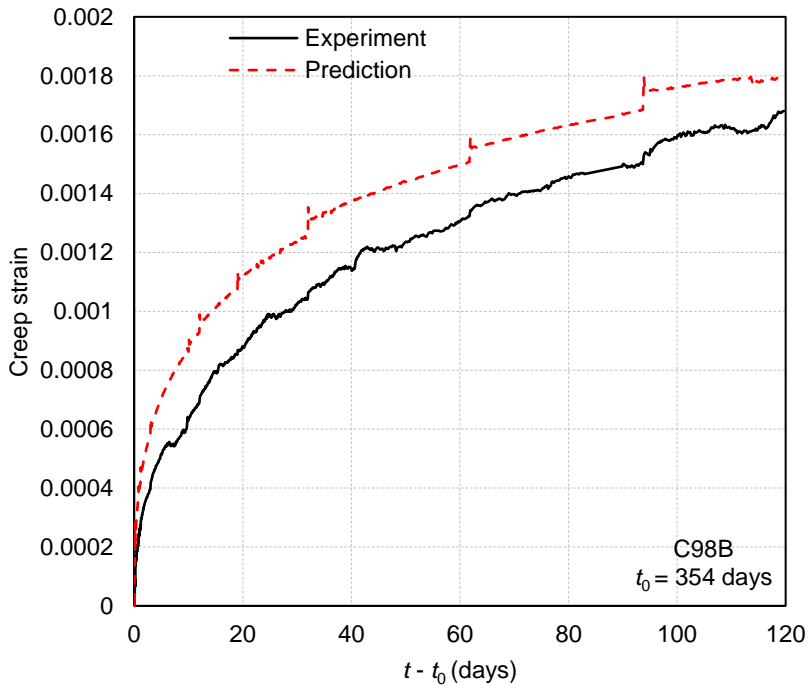
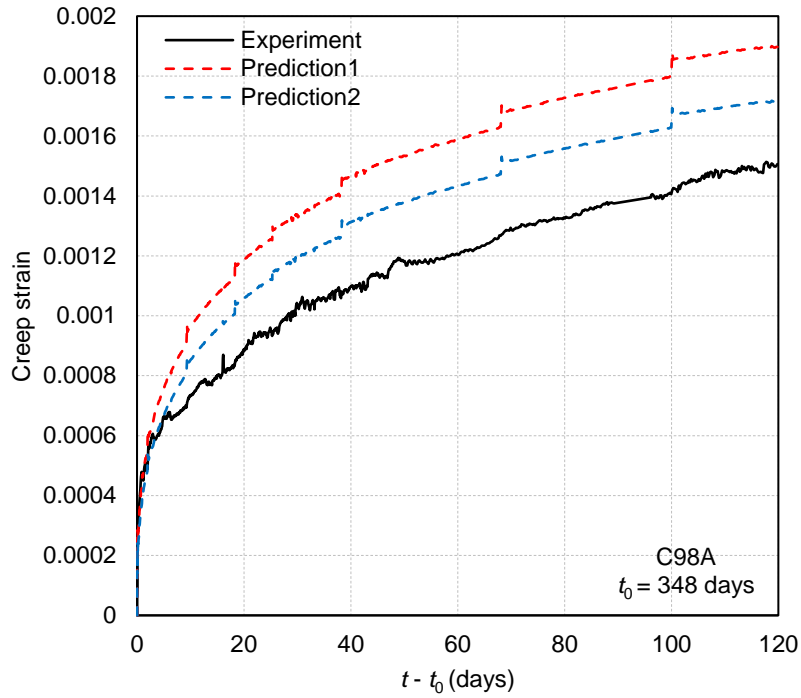


Figure 6.8 Comparison of predicted and measured creep strains for Specimens C98A and C98B.

As shown in Figure 6.8, after 20 days of sustained loading, the difference between the predicted and measured creep strains almost remained unchanged for Specimens C98A and

C98B. Among the four RC column specimens, the average measured concrete stress σ_u at the peak load P_u is greater than the calculated average concrete ultimate stress $\sigma_{u,cal}$ for Specimen C98A, as shown in Table 6.2. The red dashed line in Figure 6.8 shows the predicted strain, which uses $\sigma_{u,cal}$ as the initial value to calculate the stress ratio $\sigma_{c,i-1} / f_{cavg,i-1}$ in Equation (6.42). The blue dashed line is the predicted strain using σ_u as the initial value to calculate the stress ratio $\sigma_{c,i-1} / f_{cavg,i-1}$ in Equation (6.42). For Specimen C98A, the predicted creep is 26% and 13.9% greater than the measured creep strain at the end of sustained load using $\sigma_{u,cal}$ and σ_u as the initial value to calculate sustained stress ratio $\sigma_{c,i-1} / f_{cavg,i-1}$, respectively. For Specimen C98B, the predicted creep strain is 18.2% greater than the measured creep strain at the end of sustained load. Based on the creep prediction results for the four RC specimens, the possible reasons for the predicted strain greater than the measured strain were, (1) column transverse reinforcement can restrain concrete creep growth under high sustained stresses, especially in the early stage of sustained loading, (2) the longer sustained loading duration ($t - t_0$) was, the greater concrete strength (f_c') enhancement.

CHAPTER 7

SUMMARY AND CONCLUSIONS

7.1 Summary

The overall goal of this research was to identify the behavior of aged reinforced concrete (RC) columns under high sustained loads no less than 75% of nominal short-time loading capacity. Four tasks were fulfilled: (1) characterizing the behavior of RC columns under high sustained concentric loads, (2) characterizing the behavior of RC columns under high sustained eccentric loads, (3) examining the effects of column transverse reinforcement on creep, and (4) examining the use of a nonlinear creep model for concentrically loaded columns under sustained high stresses.

For the first task, eight square columns with a height-to-width ratio of 3.6 were tested under concentric axial loading after 209 to 478 days of concrete casting. The specimens included three plain concrete columns used to provide fundamental material behavior under sustained high stresses and to interpret the test results of five RC columns. Two control specimens, including one plain concrete column and one RC column, were loaded to failure in a short time. The other six specimens underwent three loading stages: (1) initial short-time loading, (2) sustained loading, and (3) reloading to failure in a short time. Two plain concrete specimens were subjected to 22-days sustained loads at 77% and 90% of column short-time strength. Two RC specimens with different transverse reinforcement ratios, 0.26% and 0.78%, were subjected to sustained loading for 47 days; the sustained loads for both specimens were equal to 76% of column short-time strength. Another two RC specimens with different transverse reinforcement ratios, 0.26% and 0.78%, were subjected to sustained loading for 120 days; the sustained loads for both specimens were equal to 98% of column nominal short-time strength. Test data of the

eight specimens were analyzed in terms of load-strain response, transverse strain history, Poisson's ratio history, and failure modes.

For the second task, five longer RC columns with a height-to-width ratio of 10.8 were tested under sustained loading with two eccentricity ratios of 0.17 and 0.25 after 547 to 629 days of concrete casting. The specimens included four RC columns with a lower transverse reinforcement ratio of 0.26% and one with a higher transverse reinforcement ratio of 0.78%. Among them, three specimens underwent three loading stages: (1) initial short-time loading, (2) sustained loading, and (3) reloading to failure in a short time. The initial short-time loading caused the column mid-height moment to reach to 92% to 100% of short-time moment capacity and the sustained loading lasted for 11 to 28 days. One specimen underwent two loading stages because it failed after two days of sustained loading. The column mid-height moment at the beginning of sustained loading reached 99% of nominal short-time moment capacity. The last specimen was initially loaded to approximately 77% of short-time moment capacity for 11 days; then the sustained load was increased and maintained for 17 days. The experimental data of the five RC columns were examined in terms of strain history, deflection at column mid-height, load-deflection relationship, load-moment relationship, moment-curvature response, creeps for deflection and curvature, Poisson's ratio evolution, and failure modes.

For the third task, the effects of column transverse reinforcement on creep were examined by comparing the experimental results between the specimens with comparable sustained load level, loading age, and eccentricity ratio but different transverse reinforcement ratios. The test data regarding peak load, creep coefficient, and Poisson's ratio were used to determine the effects of column transverse reinforcement on the behavior of columns under sustained eccentric loading. The test data about the increase in column mid-height moment, creep coefficients for

deflection and curvature, concrete transverse strain, and flexural stiffness were used to examine the effects of the transverse reinforcement.

For the fourth task, a numerical method for predicting the nonlinear creep of aged concrete columns under sustained high axial stresses was explored. The method was based on an existing theoretical framework for plain concrete, which extended the prediction of linear concrete creep to that of nonlinear concrete creep. The linear creep model most suitable for using this framework was calibrated based on the test data of plain concrete columns obtained in this study. The calibrated concrete creep model for plain concrete was then combined with an age-adjusted effective modulus method to predict the nonlinear creep of RC columns.

7.2 Conclusions

7.2.1 Concentric Loading

The following observations and conclusions were made from the tests of concentrically loaded columns:

- Aged concrete columns demonstrated quite strength to carry high sustained loads. None of the concentrically loaded columns failed under the high sustained loads as high as 98% of nominal short-time strength.
- For all concentrically loaded RC specimens, the reloading stiffness after being subjected to sustained loading was slightly greater than the initial loading stiffness.
- A higher column transverse reinforcement ratio resulted in reduced creep deformation. Under concentric loading, the beneficial effect of transverse reinforcement was prominent during the early sustained loading stage but diminished over time.

- The Poisson's ratio of concrete increased over time when the sustained stress was higher than 90% of short-time strength, but remained unchanged or even decreased when the sustained load level was moderate. Same trend was found for concrete transverse strain response. For two specimens loaded with 76% of column short-time strength, although they had different transverse reinforcement ratios, the concrete transverse strain response remained unchanged or even decreased. However, for specimens loaded with 98% of column short-time strength, the transverse strain increased over time during the sustained loading.
- Previously applied sustained loading increased the residual short-time loading capacity of columns on average by 6.6%. The combined effects of sustained loading and transverse reinforcement confinement increased the axial strength of concentrically loaded RC columns by 12% to 19%.

7.2.2 Eccentric Loading

The following observations and conclusions were made from the tests of eccentrically loaded columns:

- No column failed during eccentric loading if the moment at column mid-height after initial loading was no more than 92% of short-time flexural strength.
- The combined effects of sustained loading and transverse reinforcement confinement increased the flexural strength of eccentrically loaded columns by 11% to 33%, as compared with the column short-time moment capacity defined by ACI 318 design code after considering axial force-moment interactions. The moment at the peak axial load increased by 33% and 28% for the specimens loaded with the same eccentricity ratio but different transverse reinforcement ratios of 0.26% and 0.78%.

- The variation rate of concrete Poisson's ratio can be taken as an indicator of column safety condition under sustained loads. No failure occurred during either concentric or eccentric loading if the Poisson's ratio of concrete cover increased only slightly or decreased. In contrast, the column that failed during sustained eccentric loading experienced a fast increase in Poisson's ratio when the failure was approaching.
- Due to concrete creep, the flexural stiffness at column critical section during sustained eccentric loading was much lower than that prior to application of sustained loading. The flexural stiffness during sustained loading was approximately constant for all RC columns. For the column with higher transverse reinforcement ratio, the flexural stiffness was about 20% higher than the columns with lower transverse reinforcement ratio.
- The test of an eccentrically loaded column experiencing two sustained load levels indicated that the previously applied lower sustained load reduced creep under the higher sustained load applied later.
- Even though RC columns experienced different loading histories, the compressive strain of concrete at failure was approximately equal to the sum of creep-induced strain during sustained loading and the ultimate strain of concrete under short-time loading.

7.2.3 Numerical Simulations of Column Nonlinear Creep

The following conclusions were made from the numerical simulations:

- The creep strain under high sustained concentric loading can be predicted by the combination of a theoretical framework suggested by Tasevski et al. and the linear concrete creep prediction model GL2000. By the end of sustained loading, the difference of concrete creep

between the predicted and experimental results was less than 7% for the plain concrete specimens subjected to sustained loads of 77% and 90% of their short-time strength.

- For RC columns specimens, the creep strain under concentric loading was predicted by considering an age-adjusted effective modulus. For the two RC columns loaded to 76% of their short-time strength, the difference between the measured and predicted creeps at the end of sustained loading was less than 6%. For the two specimens loaded with 98% of column short-time strength, the predicted creep was 26% and 18% greater than the measured creep at the end of sustained loading.
- The predicted creep being greater than the measured one under the highest sustained loads was likely because (1) transverse reinforcement can restrain concrete creep under high sustained stresses, especially in the early stage of sustained loading, and (2) the longer sustained loading duration, the greater concrete short-time strength enhancement, thereby causing a decreased sustained stress ratio.

7.3 Suggestions for Future Research

The following topics are suggested for future research:

- More experiments are needed to further examine the effects of transverse reinforcement on concrete creep of aged RC columns, especially for concentrically and eccentrically loaded columns subjected to sustained loads greater than 90% of short-time load-carrying capacity.
- The experimental results obtained in this study indicated that concrete creep is restrained by column transverse reinforcement under high sustained loads. This restrained effect is

suggested to be explicitly considered in the future modeling approach for the creep of RC columns.

- System-level numerical simulations using nonlinear creep models extensively validated by experiments are suggested to understand the complicated damage evolution process in a near-collapse RC structure under high sustained loads.

APPENDIX A

COMPRESSIVE STRENGTH OF CYLINDRICAL CONCRETE SPECIMENS



611 WEST BONANZA ROAD - LAS VEGAS NV 89106 - (702) 932-3915 OFFICE (702) 932-3977 FAX

COMPRESSIVE STRENGTHS OF CYLINDRICAL CONCRETE SPECIMENS (ASTM C39) LABORATORY TRIAL BATCH

CLIENT INFORMATION

CLIENT:	Nevada Ready Mix / Service Rock Products	REPORT DATE:	
PROJECT NAME:	Misc. Laboratory Testing	PROJECT NO:	12051834
CONTRACTOR:	N/A		

FIELD INFORMATION

DESIGN CRITERIA	SAMPLE	FIELD TESTS
SUPPLIER: NRM / SRP	SAMPLE DATE: 12/5/2018	SLUMP: (IN) 5.50
MIX DESIGN: 2503	SAMPLE TIME: 1:30 PM	MIX TEMP: (°F) 69
STRENGTH: 2500		AIR TEMP: (°F) 72
SACK FACTOR: 5.50	BATCH SIZE: 1.89 cf	AIR CONTENT: (%) 1.9
W/C RATIO: 0.64	RECEIVED: 12/6/2018	UNIT WEIGHT: (PCF) 152.0
AGG SIZE: (IN) 3/8		CURE METHOD: LAB
FLY ASH: % 0		LOW HIGH
SLUMP: (IN) 4.0 - 6.0	CYLINDER SIZE: 4 x 8 6 x 12	INITIAL CURE TEMPERATURE: 72 72
	NO OF CYLINDERS: X 18	(°F)

CONCRETE MIX SPECIFICATIONS

DESIGN CRITERIA	MATERIALS	WEIGHTS (SSD)
AIR CONTENT: 2.0	CEMENT TYPE: V	CEMENT LBS/YD: 517.0 Lbs.
UNIT WEIGHT: 151.7	ADMIXTURES: 322N @ 4.0 oz/cwt	FLY ASH LBS/YD: 0.0 Lbs.
STRENGTH: 2500		SAND LBS/YD: 1938.4 Lbs.
W/C RATIO: 0.64		3/8" LBS/YD: 1310.3 Lbs.
SET NO: 12051834		

CYLINDER ID	DATE TESTED	DIAMETER (IN)	AGE (DAYS)	AREA (SQ IN)	MAX LOAD (LBS)	COMPRESSIVE STRENGTH (PSI)	PERCENT	TYPE	TECH
12051834-B	12/12/2018	4.01	7	12.63	29520	2340	94%	3	EC
12051834-C	12/19/2018	4.01	14	12.63	39830	3150	126%	3	EC
12051834-D	12/26/2018	4.01	21	12.63	43740	3460	138%	3	EC
12051834-E	1/2/2019	4.01	28	12.63	46610	3690	148%	5	EC
12051834-F	1/9/2019	4.01	35	12.63	48310	3830	153%	5	EC
12051834-G	1/16/2019	4.01	42	12.63	52780	4180	167%	3	EC
12051834-H	1/23/2019	4.01	49	12.63	53500	4240	170%	3	EC
12051834-I	1/30/2019		56						
12051834-J	2/6/2019		63						

REMARKS: Each 'Age' is the average of two cylinders

28 DAY AVERAGE: 3690



Fracture Type

TESTS ARE PERFORMED IN GENERAL ACCORDANCE WITH ASTM C-31, C-39, C-78, C-138, C-143, C-172, C-173, C-192, C-231, C-617, AND C-1066

REVIEWED BY: **MTC**
Materials Testing Corporation

[Signature]
Elu Chavez
Quality Control Manager

APPENDIX B

CONCRETE MIX DETAILS



Contractor: PENTA Building Group
Project: Caesar's Forum Meeting Center

Date: December 3, 2018

Mix Number:	P4033F	
Strength:	4000 psi @	28 Days
Slump:	4" +/- 2"	
Description:	3/8 inch Pump/Place Mix	
Batch Plant:	Lone Mtn / Arville / Bonanza	
Aggregate Source:	Lone Mountain	
Application:	Slab on Metal Deck	

MIX PROPORTIONS

MATERIALS	% USED	SP. G.	ABS VOL	WEIGHTS	COMPLIANCES	SOURCE
Cement Type V	6.50 Sk.	3.150	2.176	427.7 Lbs	ASTM C 150	Mitsubishi
Fly Ash Type F	30 %	2.320	1.265	183.3 Lbs	ASTM C 618	Headwaters
Concrete Sand (SSD)	50 %	2.791	9.070	1579.7 Lbs	ASTM C 33	Lone Mountain
Size #4 (1 1/2"x 3/4")	0 %	2.816	0.000	0.0 Lbs	ASTM C 33	Lone Mountain
Size #67 (3/4"x #4)	0 %	2.829	0.000	0.0 Lbs	ASTM C 33	Lone Mountain
Size #89 (3/8"x #16)	50 %	2.830	9.070	1601.8 Lbs	ASTM C 33	Lone Mountain
Water Design	36.5 GALS.	1.000	4.878	304.4 Lbs	ASTM C 94	LVVWD
ADMIXTURES						
Pozzoloth 322N	4.00 oz/cwt			24.44 Ozs	ASTM C 494 (Type A)	BASF
Glenium Type F	(Optional)				ASTM C 494 (Type A & F)	BASF
2.0 % Air in Design			0.540			
TOTALS			VOLUME: 27.000	4097 Lbs/Cu. Yard		

C-33 Date: July 2018

AGGREGATE GRADATIONS

SIEVE	Size #4 0 %	Size #67 0 %	Size #89 50 %	SAND 50 %	COMBINED GRADING
2"	100.0				100.0
1 1/2"	97.0				100.0
1"	48.0	100.0			100.0
3/4"	10.0	97.0			100.0
1/2"	2.0	67.0	100.0		100.0
3/8"	1.0	40.0	93.0	100.0	96.5
#4	1.0	5.0	43.0	100.0	71.5
#8		2.0	12.0	95.0	53.5
#16			3.0	60.0	31.5
#30				32.0	17.0
#50			2.0	16.0	9.0
#100				9.0	5.5
#200	0.5	0.9	0.9	3.8	2.4

Methods: All concrete will be batched, transit mixed and transported according to ASTM C 94. This mix was proportioned based on project specifications as provided by the customer. Materials Testing Corporation is not responsible for any criteria not submitted for consideration in mix proportioning.

Maximum W/C Ratio: 0.50
Maximum Gallons/Sack: 5.62

Plastic Unit Weight: 151.73 Lbs/Cu Ft
Maximum Gallons/Cwt.: 5.97



Materials Testine Corporation

Elu Chavez

Elu Chavez
Quality Control Manager

Notes: For Extended or Accelerated Set Times and Temperature Control:
add BASF Delvo Stabilizer or BASF Pozzoloth NC534
Maximum Slump: * 10 inch slump with the addition of High Range Water Reducer

REFERENCE

- ABAQUS (2014). ABAQUS Inc., *ABAQUS Standard User's Manual*, 6.14 Edition.
- ACI Committee 209. (2008). "Guide for Modeling and Calculating Shrinkage and Creep in Hardened Concrete." *ACI 209.2R-08*, American Concrete Institute, Farmington Hills, MI, 44 pp.
- ACI Committee 318. (2019). "Building Code Requirements for Structural Concrete and Commentary." *ACI 318-19*, American Concrete Institute, Farmington Hills, MI.
- Asiaone News (2016). "30 years after hotel New World collapse, volunteers at scene look back," March 13, 2016.
- ASCE. (2016). "Minimum Design Loads for Buildings and Other Structures (ASCE 7-16)." American Society of Civil Engineers, Reston, VA., USA, 2016.
- ASTM International, ASTM C39/C39M (2018). "Standard Test Method for Compressive Strength of Cylindrical Concrete Specimens," *Annual book of ASTM standards 2018*, West Conshohocken, PA: American Society for Testing and Materials.
- Awad, M. E. and Hilsdorf, H. K. (1971). "Strength and deformation characteristics of plain concrete subjected to high repeated and sustained loads," Report, Structural Research Series, University of Illinois, vol. 372, February 1971, 266 p.
- Barpi, F. and Valente, S. (2002). "Creep and fracture in concrete: A fractional order rate approach," *Engineering Fracture Mechanics*, vol. 70, no. 5, pp. 611-623.
- Bažant, Z. P. (1975). "Theory of Creep and Shrinkage in Concrete Structures: A Précis of Recent Developments," *Mechanics Today*, Vol.2, pp. 1-93, Pergamon Press.
- Bažant, Z. P. and Oh, B. H (1983). "Crack Band Theory for Fracture of Concrete," *Materials and Structures*, 16(3), 155-177.
- Bažant, Z. P. and Wittmann F. H. (1983). "Creep and Shrinkage in Concrete Structures," John Wiley & Sons, 374 pp.
- Bažant, Z. P. and Chern, J. C. (1985). "Concrete creep at variable humidity: constitutive law and mechanism," *Materials and Structures*, 18(1), pp. 1-20.

- Bažant, Z. P. and Chern, J. C. (1985). "Strain softening with creep and exponential algorithm," *Journal of Engineering Mechanics*, 111(3), pp. 391-415.
- Bažant, Z. P. and Prasannan, S. (1989). "Solidification theory for concrete creep. I: Formulation," *Journal of Engineering Mechanics*, 115, pp. 1691-1703.
- Bažant, Z. P. and Prasannan, S. (1989). "Solidification theory for concrete creep. II: Verification and application," *Journal of Engineering Mechanics*, 115, pp. 1704-1725.
- Bažant, Z. P. (1995). "Creep and Shrinkage Prediction Model for Analysis and Design of Concrete Structures - Model B3," *Materials and Structures*, 28, pp. 357-365.
- Bažant, Z. P. and Baweja, S., (1995). "Creep and Shrinkage Prediction Model for Analysis and Design of Concrete Structures - Model B3," *Materials and Structures*, 28, pp. 357-365
- Bažant, Z. P. and Baweja, S. (1996). "Creep and Shrinkage Prediction Model for Analysis and Design of Concrete Structures: Model B3-Short Form," *ACI Special Publication*, SP-194, pp. 85-100.
- Bažant, Z. P., Hauggaard, A. B., Baweja, S. and Ulm, F. J. (1997). "Microprestress-solidification theory for concrete creep. I: Aging and drying effects," *Journal of Engineering Mechanics*, 123, pp. 1188-1194.
- Bažant, Z. P., Hauggaard, A. B. and Baweja, S. (1997). "Microprestress-solidification theory for concrete creep. II: Algorithm and verification," *Journal of Engineering Mechanics*, 123(1997), pp. 1195-1201.
- Bažant, Z. P. and Baweja, S., (2000). "Creep and Shrinkage Prediction Model for Analysis and Design of Concrete Structures: Model B3," *The Adam Neville Symposium: Creep and Shrinkage-Structural Design Effects*, SP-194, A. Al-Manaseer, ed., American Concrete Institute, Farmington Hills, MI, pp. 1-83
- Bažant, Z. P., Gianluca, C. and Luigi, C. (2004). "Temperature Effect on Concrete Creep Modeled by Microprestress-Solidification Theory," *Journal of Engineering Mechanics*, 130(6), pp. 691-699.
- Bažant, Z. P., Luzio, G. D. (2004). "Nonlocal microplane model with strain softening yield limits," *International Journal of Solids and Structures*, 41(24-25), pp. 7209-7240.

- Bockhold, J and Stangenberg, F (2004). "Modeling of nonlinear creep of concrete [Modellierung des nichtlinearen Kriechens von Beton]," *Beton- and Stahlbetonbau*, vol. 99, no. 3, pp. 209-216 (in German).
- Carlos Aquino, Masumi Inoue, Hiroaki Miura, Maki Mizuta, and Takahisa Okamoto. (2010). "The Effects of Limestone Aggregate on Concrete Properties," *Construction and Building Materials*, Vol. 24, No. 12, December 2010, pp. 2363-2368
- Carol I. and Murcia J. (1989). "A model for the non-linear time-dependent behaviour of concrete in compression based on a Maxwell chain with exponential algorithm," *Materials and Structures*, vol. 22, no. 3, pp. 176-184.
- CEB Bulletin. (1999). "Structural Concrete — Textbook on Behaviour, Design and Performance. Updated Knowledge of the CEB/FIP Model Code 1990," *fib Bulletin 2*, V. 2, Federation Internationale du Beton, Lausanne, Switzerland, pp. 37-52.
- Challamel Noël, Lanos Christophe, and Casandjian Charles. (2005). "Creep failure in Concrete as Bifurcation Phenomenon," *International Journal of Damage Mechanics*, 14(1), 5-24.
- Chovichien Vinit, Gutzwiller Martin J., and Lee Robert H. (1973). "Analysis of Reinforced Concrete Columns Under Sustained Load," *ACI Journal Proceedings* Vol. 70, No. 62, October 1973, pp. 692-700.
- Comite Euro-International Du Beton. (2012). "CEB-FIP model code 2010." Thomas Telford, Lausanne, Switzerland.
- Coutinho, A. Sousa. (1977). "A contribution to the mechanism of concrete creep," *Materials and Structures*, 10 (1), 3-16
- Dat, P. X., and Hai, T. K. (2013). "Experimental Study of Beam-Slab Substructures Subjected to a Penultimate-Internal Column Loss," *Engineering Structures*, V. 55, pp. 2-15.
- DoD (Department of Defense). (2013). "Design of Buildings to Resist Disproportionate Collapse".
- Deryagin, B. V., ed. (1963). *Research in surface forces*, Consultants Bureau, New York, 190.
- Eldukair, Z.A. and Ayyub, B. M. (1991). "Analysis of Recent US Structural and Construction Failures." *Journal of Performance of Constructed Facilities*, 5(1), 57-73.

- El-Kashif KF and Maekawa K. (2004). "Time-dependent nonlinearity of compression softening in concrete," *Journal of Advanced Concrete Technology*, vol. 2, no. 2, pp. 233-247.
- Eom Tae-Sung, Chang-Soo Kim, Xin Zhang and Jae-Yo Kim. (2018). "Time-Dependent Deformations of Eccentrically Loaded Reinforced Concrete Columns," *International Journal of Concrete Structures and Materials*, vol.12, no.76, pp. 1-12.
- Factly news. (2019). <https://factly.in/more-than-13000-lost-lives-in-structure-collapses-in-the-last-5-years/>
- Ferguson, P. M., Breen, J. E., and Jirsa, O. J. (1988). "Reinforced Concrete Fundamentals," 5th Edition, Wiley, 768 pp.
- Furlong W. Richard and Ferguson M. Phil. (1966). "Tests of Frames with Columns in Single Curvature," *Reinforced Concrete Columns in Symmetrically Loaded Frames*, pp. 55-73.
- Gardner, N. J., and Lockman, M. J. (2001). "Design Provisions for Drying Shrinkage and Creep of Normal Strength Concrete," *ACI Materials Journal*, V. 98, No. 2, Mar.-Apr., pp. 159-167.
- Gardner, N. J. (2004). "Comparison of Prediction Provisions for Drying Shrinkage and Creep of Normal Strength Concretes," *Canadian Journal for Civil Engineering*, V. 31, No. 5, Sept.-Oct., pp. 767-775.
- Geymayer, H. G. (1970). "The Effect of Temperature on Creep of Concrete: A Literature Review," U. S. Army Engineer Waterways Experiment Station, Vicksburg, Mississippi.
- Green, R. and Breen, J. E. (1969). "Eccentrically Loaded Concrete Column under Sustained Load," *ACI Journal*, 66(11), 866-874.
- Green, R. and Breen, J. E. (1984). "Eccentrically Loaded Concrete Columns: 15 Years of Sustained Load," *IABSE congress report*, 911-918.
- GSA (General Service Administration). (2003). "Disproportionate Collapse Analysis and Design Guidelines for New Federal Office Buildings and Major Modernization Projects," Washington, DC.
- Hellesland J and Green R. (1972). "A stress and time dependent strength law for concrete", *Cement and Concrete Research*, vol. 2, no. 3, pp. 261-275.

- Iravani, S. and MacGregor, J. G. (1998). "Sustained Load Strength and Short-Term Strain Behavior of High-Strength Concrete," *ACI Structural Journal*, 95(5), 636-647.
- Jenkins, Ryan W. (2015). "Improved procedures for the design of slender structural concrete columns," Doctoral Thesis, Purdue University, West Lafayette, Indiana, USA 223 p.
- Kaltakci, M. Y., Arslan, M. H., Korkmaz, H. H., and Ozturk, M. (2007). "An Investigation on Failed or Damaged Reinforced Concrete Structures under Their Own-weight in Turkey," *Engineering Failure Analysis*, 14(6), 962-969
- Kaltakci, M. Y., Mehmet Kamanli, Murat Ozturk, M. Hakan Arslan and Husnu Korkmaz. (2013). "Sudden Complete Collapse of Zumrut Apartment Building and the Causes," *Journal of Performance of Constructed Facilities*, 27(4), 381-390.
- Kosmatka, Steven H., Kerkhoff, Beatrix, and Panarese, William C. (2002). "Design and Control of Concrete Mixture," 15th Edition, EB001, PCA Engineering Bulletin EB 001, Portland Cement Association, Skokie, IL, 2002.
- Li, Z. X., and Qian, J. C. (1989). "Creep Damage Analysis Its Application to Nonlinear Creep of Reinforced Concrete Beam," *Engineering Fracture Mechanics*, 34(4), 851-860.
- Liu, J. R. (2014). "Progressive Collapse Analysis of Older Reinforced Concrete Flat Plate Building Using Macro Model." Doctoral Thesis, University of Nevada, Las Vegas, Las Vegas, Nevada, USA 190 p.
- Luzio, G. Di. (2007). "A symmetric over-nonlocal microplane model m4 for fracture in concrete," *International Journal of Solids and Structures*, 44(13), 4418-4441.
- Luzio, G. Di. (2009). "Numerical model for time-dependent fracturing of concrete", *Journal of Engineering Mechanics*, vol. 135, no. 7, pp. 632-640.
- Luzio, Giovanni. Di and Cusatis Gianluca. (2012). "Solidification-microprestress-microplane (SMM) theory for concrete at early age: Theory, validation and application," *International Journal of Solids and Structures*, 50(1), 957-975.
- Mazzotti, C. and Savoia, M. (2002). "Nonlinear Creep, Poisson's Ratio, and Creep-Damage Interaction of Concrete in Compression," *ACI Structural Journal*, 99(5), 450-457.
- Mazzotti Claudio and Savoia, Marco. (2003). "Nonlinear Creep Damage Model for Concrete under Uniaxial Compression," *Journal of Engineering Mechanics*, 129(9), 1065-1075.

- Mohamed, M. I., Hasan, E. H., and Aggag, G. (2009). "Study of Creep Behavior of Load Cells," *Measurement*, 42(7), 1006-1010.
- Muller, H. S., and Hilsdorf, H. K. (1990). "General Task Group 9," *CEB Comité Euro-International du Béton*, Paris, France, 201 pp.
- MustShare News (2016). "15 Facts You Never Knew About The Collapse Of Hotel New World," March 16, 2016.
- Neville, A. (1996). "Properties of Concrete." John Wiley and Sons, New York.
- NU Database of Laboratory Creep and Shrinkage Data. (2017).
Link:<http://www.civil.northwestern.edu/people/bazant/>.
- Orton, S. L., and Kirby, J. E., (2013). "Dynamic Response of a RC Frame under Column Removal," *Journal of Performance of Constructed Facilities*, V. 28, No. 4, pp. 1-8.
- Papa, E., Taliercio, A., and Gobbi, E. (1998). "Triaxial Creep Behavior of Plain Concrete at High Stresses: A Survey of Theoretical Models," *Materials and Structures*, 31, 487-493.
- Park, R. and Paulay, T. (1974). "Reinforced Concrete Structures" 1st edition, A WILEY-INTERSCIENCE PUBLICATION, 17 pp.
- Park, T.W. (2012). "Inspection of Collapse Cause of Sampoong Department Store," *Forensic Science International*, 217, 119-126.
- Qian, K., and Li, B. (2012). "Slab Effects on Response of Reinforced Concrete Substructures after Loss of Corner Column," *ACI Structural Journal*, Vol. 109, No. 6, pp. 845-855.
- Richart, F. E., and Brown, R. L. (1934). "An Investigation of Reinforced Concrete Columns," Bulletin, NO. 267, University of Illinois, Engineering Experimental Station, Urbana, June 1934.
- RILEM TC 107-CSP. (1998). "Measurement of Time-Dependent Strains of Concrete," *Materials and Structures*, 31, 507-512.
- Ruiz M. Fernández, Muttoni, A. and Gambarova P.G. (2007). "Relationship between nonlinear creep and cracking of concrete under uniaxial compression," *Journal of Advanced Concrete Technology*, 5(3), 383-393.

- Rüsch, H. (1960). "Research toward a General Flexural Theory for Structural Concrete," *ACI Journal Proceedings*, 57(7), 1-28.
- SAP2000 (2014). Computer and Structures, Inc, *CSI Analysis Reference Manual*
- Sasani, M., Bazan, M., and Sagioglu, S. (2007). "Experimental and Analytical Progressive Collapse Evaluation of an Actual Reinforced Concrete Structure," *ACI Structural Journal*, 104(6), 731-739.
- Scott B. D., Park, R., and Priestley, M. J. N. (1982). "Stress-Strain Behavior of Concrete Confined by Overlapping Hoops at Low and High Strain Rates," *ACI Journal Proceedings*, 79(2), January-February 1982, 13-27
- Shah, Surendra. P. and Chandra, S. (1970). "Fracture of concrete subjected to cyclic and sustained loading," *ACI Journal Proceedings*, 67(10), 816-827.
- Sheikh Shamim A. and Uzumeri S. M. (1980). "Strength and Ductility of Tied Concrete Columns," *Journal of the Structural Division*, Vol. 106, NO. 5, May 1980, pp. 1079-1102.
- Smadi, Mohammad. M, Floyd O. Slate, and Arthur H. Nilson. (1985). "High-, Medium-, and Low-Strength Concrete Subject to Sustained Overloads - Strains, Strengths, and Failure Mechanisms," *ACI Journal*. 82-58, 657-664.
- Smadi, Mohammad. M., Floyd O. Slate, and Arthur H. Nilson. (1986). "Shrinkage and Creep of High-, Medium-, and Low-Strength Concretes, Including Overloads," *ACI Materials Journal*. 84-M25, 224-234.
- Stöckl, S. (1972). "Strength of concrete under uniaxial sustained loading," *ACI Special Publication*, 34, 313-326
- Su, Y., Tian, Y., and Song, X. (2009). "Progressive Collapse Resistance of Axially-Restrained Frame Beams," *ACI Structural Journal*, 106 (5), 600-607.
- Tasevski D, Ruiz M. Fernández and Muttoni A. (2018). "Compressive strength and deformation capacity of concrete under sustained loading and low stress rates", *Journal of Advanced Concrete Technology*, vol. 16, no. 8, pp. 396-415.
- Tasevski D, Ruiz M. Fernández and Muttoni A. (2019). "Assessing the compressive strength of concrete under sustained actions: From refined models to simple design expressions", *Structural Concrete*, vol. 20, pp. 971-985.

Thean, L. P., Vijiaratnam, A., Lee, Seng-Lip and Broms, Bengt Baltzar. (1987). "Report of Inquiry into the Collapse of Hotel New World," *Singapore National Printers*.

Theconstructor.org. <https://theconstructor.org/concrete/concrete-creep/6224/>.

The New York Times. (1986). "Singapore Toll Put at 33," March 22, 1986
<https://www.nytimes.com/1986/03/22/world/singapore-toll-put-at-33.html?n=Top%2FNews%2FWorld%2FCountries+and+Territories%2FSingapore>.

Viest, I. M., Elstner, R. C., and Hognestad, E. (1956). "Sustained Load Strength of Eccentrically Loaded Short Reinforced Concrete Columns," *ACI Journal Proceedings*, 52(3), 727-754.

Wardhana, K. and Hadipriono, F. (2003). "Study of Recent Building Failures in the United States," *Journal of Performance of Constructed Facilities*, 17(3), 151-158.

Wearne, Philip. (2000). "Collapse: when buildings fall down." New York: TV books.

Wei Ya, Guo Weiqiang, Liang Siming. (2016). "Microprestress-solidification theory-based tensile creep modeling of early-age concrete: Considering temperature and relative humidity effects," *Construction and Building Materials*, 127(1), 618-626.

Wendner, R. Hubler, M.H, and Bažant, Z. P. (2015). "Optimization Method, Choice of Form and Uncertainty Quantification of Model B4 Using Laboratory and 23 Multi-decade Bridge Databases," *Materials and Structures*, 48(4), 771-756.

Wendner, R. Hubler, M.H, and Bažant, Z. P. (2015). " Statistical Justification of Model B4 for Multi-Decade Concrete Creep Using Laboratory and Bridge Databases and Comparisons to Other Models," *Materials and Structures*, 48(4), 815-833.

Wittmann F. H. and Zaitsev J (1972). "Behavior of hardened cement paste and concrete under sustained load", in Society of Materials Science Conference on the Mechanical Behavior of Materials, vol. 4, pp. 84-95.

Wittmann F. H. (1982). Creep and shrinkage mechanics. In: Bažant, Z. P., Wittmann, F. H. (Eds.), *Creep and Shrinkage of Concrete Structures*. John Wiley & Sons Ltd., pp. 129-161.

WIKIPEDIA https://en.wikipedia.org/wiki/Progressive_collapse.

Xiao, Y., Kunnath, S., Li, F. W., Zhao, Y. B., Lew, H. S., and Bao, Y. (2015). "Collapse Test of Three-Story Half-Scale Reinforced Concrete Frame Building," *ACI Structural Journal*, V. 112, No. 4, July-Aug., pp. 429-438.

- Yi, W., He, Q., Xiao, Y., and Kunnath, S. K. (2008). "Experimental Study on Progressive Collapse-Resistant Behavior of Reinforced Concrete Frame Structures," *ACI Structural Journal*, 105 (4), 433-439.
- Zhou F.P (1992). "Time-dependent crack growth and fracture in concrete," Doctoral Thesis, Lund Institute of Technology, Sweden 132 p.
- Zijl, G.P.A.G. van, R. de Borst and J.G. Rots. (2001). "A numerical model for the time-dependent cracking of cementitious materials," *International Journal for Numerical Methods in Engineering*, 62(1), 637-654.

CURRICULUM VITAE

Graduate College
University of Nevada, Las Vegas

Wenchen Ma
wenchen.ma2014@gmail.com

Degrees:

Bachelor of Science in Civil Engineering, 2014
Beijing Jiaotong University, Beijing, China

Master of Science in Civil Engineering, 2016
Northeastern University, Boston, Massachusetts, USA

Dissertation Examination Committee:

Committee Chair, Dr. Ying Tian, Ph.D.
Committee Member, Dr. Nader Ghafoori, Ph.D.
Committee Member, Dr. Samaan Ladkany, Ph.D.
Committee Member, Dr. Ryan Sherman, Ph.D.
Graduate College Representative, Dr. Zhiyong Wang, Ph.D.

Publications:

Chunyu Zhang, Wenchen Ma, Xiang Liu, Ying Tian, Sarah L. Orton. (2019). "Effects of high temperature on residual punching strength of slab-column connections after cooling and enhanced post-punching load resistance", *Engineering Structures*, Vol. 199. accepted

Wenchen Ma, Ying Tian, Hailong Zhao, Sarah L. Orton. "Time-Dependent Behavior of Aged Reinforced Concrete Columns Subjected to High Sustained Loads", *Journal of Structural Engineering*, under review